University of Southampton

Faculty of Engineering, Science and Mathematics

School of Chemistry

OPTOFLUIDIC BRAGG GRATING SENSORS FOR CHEMICAL DETECTION

By

RICHARD MARK PARKER

Thesis for the degree of Doctor of Philosophy

September 2010

UNIVERSITY OF SOUTHAMPTON

ABSTRACT

FACULTY OF ENGINEERING, SCIENCE AND MATHEMATICS
SCHOOL OF CHEMISTRY

DOCTOR OF PHILOSOPHY

OPTOFLUIDIC BRAGG GRATING SENSORS FOR CHEMICAL DETECTION

By Richard Mark Parker

This thesis reports the development and potential applications of direct UV written Bragg grating refractometers for detection of chemical analytes.

The technique of direct UV writing uses the localised refractive index increase of a photosensitive planar glass layer upon exposure to a tightly focussed UV beam to fabricate a wide range of integrated optical devices. One such device, the Bragg grating, can be used as an optical sensor for changes in refractive index.

This thesis reports upon the advancements made to such optical Bragg grating devices towards the development of practical “lab-on-a-chip” microfluidic chemical sensors. This has been achieved through improvements in the fabrication processes and the inclusion of a high-index overlayer, shown to enhance the sensitivity by over an order of magnitude. A novel method for compensating for fluctuations in temperature is introduced; with it demonstrated that this technique can be applied towards the fabrication of an athermal Bragg grating device. The encapsulation of such highly sensitive refractometers within a microfluidic channel allows for real-time measurements of the dynamic composition of a fluid. This technology has been further developed to allow for chemical reactions to both occur, and to be monitored upon the microfluidic sensor surface. It is also demonstrated that using such a functionalised surface allows for chemical specificity to be introduced to these highly sensitive optical sensors, with examples of both copper and sodium selective sensors presented.

Table of Contents

Acknowledgements

There are many people to whom thanks are due for the help and inspiration they have gave me, over the course of my PhD.

First and foremost, I would like to thank my supervisors, Dr. Martin Grossel and Prof. Peter Smith. Through their combined guidance I was given the freedom to set my own goals and seek out my own solutions to problems, but at the same time I have always been able to turn for them for support and advice. Bringing their collective strengths together gave this interdisciplinary project the firm foundations necessary for it to flourish.

I am extremely grateful to all the past and present members of the two research groups that I had the pleasure of working with, but I specifically would like to thank Dr. James Gates, without whose tutorage, support and friendship the work presented here would not have been possible. James, through his unending patience, inspired advice and tireless enthusiasm made the daunting challenge of entering the new and unknown field of photonics an exciting experience.

I would like to thank all the support staff at the School of Chemistry and the Optoelectronics Research Centre; from the technicians maintaining the world-class facilities through to the administration teams who ensure everything runs smoothly.

Finally, thank you to my parents, family and friends for their unwavering support and understanding that encouraged me through the high points and supported me through the low points over the course of my PhD studies.

Notation

AFM	Atomic force microscopy
AOM	Acousto-optic modulator
ASE	Amplified stimulated emission
ATR	Attenuated total reflectance
BPM	Beam propagation method
CCD	Charge-coupled device
CNC	Computer numerically controlled
CVD	Chemical vapour deposition
DGW	Direct grating writing
DNA	Deoxyribonucleic acid
EDFA	Erbium doped fibre amplifier
ES	Electrospray mass spectroscopy
FDM	Finite difference method
FEM	Finite element method
FITC	Fluorescein isothiocyanate
FMM	Film mode matching
FHD	Flame hydrolysis deposition
FWHM	Full width half maximum

GPIB	General purpose interface bus
IR	Infrared
LPG	Long-period grating
MP	Melting point
MZI	Mach-Zehnder interferometer
NA	Numerical aperture
NMR	Nuclear magnetic resonance
NOV	Neutral oxygen vacancy
ODC	Oxygen deficient centre
OSA	Optical spectrum analyser
PDMS	Polydimethylsilane
PECVD	Plasma enhanced chemical vapour deposition
PM	Polarisation maintaining
Ppm	Parts per million
SAM	Self-assembled monolayer
SERS	Surface enhanced Raman spectroscopy
SMF	Single mode fibre
SPR	Surface plasmon resonance
TE	Transverse electric
TM	Transverse magnetic
UV	Ultraviolet
v/v	Volume in volume
WDM	Wavelength division multiplexing
wt%	Weight percent

1. Introduction

1.1 Introduction

From monitoring industrial processes and environmental change to detecting pathogens and biomedical diagnosis, sensors play an essential role in modern life, with the US demand for chemical sensors alone projected to surpass $5 billion by 2012 [1].

Integrated optics focuses on fabricating devices that miniaturise and integrate multiple photonic functions within a single smart device, while microfluidic networks enable small-scale fluid control and analysis. The emerging field of optofluidics combines integrated optics and microfluidics with one of the most common applications novel “lab-on-a-chip” devices. Optofluidics lends itself to the field of optical sensors; allowing for the development of smaller, more powerful and cost-effective devices that are changing the future of sensor design.

Furthermore, the low cost, small size and integrated nature allows for optofluidic sensors to be deployed in a wide range of applications including use within hazardous environments where traditional electronics cannot be used for safety reasons.

1.2 Integrated Optics

The goal of integrated optics is to develop miniaturised optical devices of high functionality on a common substrate. The concept of integrated optics was introduced in 1969 when Miller proposed the development of “laser beam circuitry” [2]. It was shown that in principle resonators, couplers and other functions could be realised in a single device through the use of embedded dielectric waveguides. Since that time the optical component market has grown significantly with the use of

integrated devices becoming increasingly attractive. The laser beam circuits proposed by Miller are now referred to as planar lightwave circuits, planar waveguides and also commonly by the somewhat ambiguous term, waveguides.

Many parallels can be drawn between the field of integrated optics and the microelectronics industry, although contemporary integrated optics is still far behind its electronic counterpart. Unlike electronic integration where silicon is the dominant material, integrated optical circuits have been fabricated from a variety of material systems. These systems are typically based on silica-on-silicon, silicon-on-insulator, various polymers and semiconductor materials (used to make semiconductor lasers such as gallium arsenide, lithium niobate and indium phosphide). Each different material system provides different advantages and limitations, making the choice of substrate dependent on the function to be integrated.

As with electronic integrated circuits, photolithography is the dominant fabrication technique and is used to pattern wafers for etching and material deposition [3]. Optical integrated circuits employ a broad range of optical components, based on the miniaturisation of bench-top devices found in conventional free-space optics. The range of components required on a device ranges from power splitters, optical amplifiers, and optical modulators through to filters, lasers and detectors, all linked by optical waveguides, an analogous interconnect to the electrical wire. This contrasts strongly to electronic systems where the primary component is the transistor. With the variety of different materials and fabrication techniques required, these optical devices are more difficult to realise on a single chip.

Photonic integrated circuits can allow optical systems to be made more compact and with higher performance than with discrete optical components. They also offer the possibility of integration with electronic circuits to provide increased functionality [4].

1.3 Optical Device Applications

The market for integrated optical devices has traditionally been focussed around the telecommunication industry, where high consumer demand for network bandwidth and flexibility has driven technological development. The optical telecommunication industry is currently in a state of growth, which is driven by

several factors including an increase in demand for high-definition multimedia information over the internet and a change of global dynamics [5] including the emergence of strong eastern economies [6].

The rapidly expanding demand for higher bandwidth services in the commercial and consumer sectors is starting to strain the ageing infrastructure. Telecommunication networks are being enhanced to meet with an ever increasing demand by upgrading traditional electronic systems to optical devices (the recent push by BT and Virgin Media for optical fibre to the home being one such example [7]) and increasing the number of existing optical fibres. This increasing desire to switch to an all-optical network (except at the end nodes) will provide improved economy, flexibility, robustness and speed. For this to be achieved it is necessary to convert the current optical-electronic-optical network switches to integrated optical devices. To this end, the principal focus of much research into integrated optical components has been towards applications in the telecoms industry.

1.3.1 Telecommunications

The vast amount of optical telecommunication transmission is achieved through silica-based optical fibres. The low optical loss of such optical fibres allows them to transmit large amounts of information over very long distances (1000's of km). To coincide with silica's spectral regions of low loss (and the available light sources), specific telecommunication windows exist. The most common window being the infrared C-band window from 1530 to 1565 nm wavelength, this spans a spectral range in silica of low loss sitting between regions of absorption and Rayleigh scattering. This window also takes into consideration a hydroxide resonance, associated with 1400 nm wavelengths.

Despite the low loss of optical fibre, no material is perfectly transparent, with the infrared signal attenuated as it travels along the optical fibre. The advent of the erbium doped fibre amplifier (EDFA) has allowed for the broadband amplification in this spectral window, increasing the range of optical telecommunication networks while eliminating complex and inefficient conversion and electronic amplification stages.

Network capacity has been increased by developments in optical fibre and light sources that have extended this spectral window from 1460 to 1600 nm, however it

has been shown that this can be extended even further using “zero water peak” fibre, achieved through fibre drying [8]. Network capacity can also be increased by either laying additional optical fibre or increasing the density of channels that exist within the telecom window. Channels are defined in the wavelength regime using a system known as Wavelength Division Multiplexing (WDM) [9]. WDM channels are spaced to avoid inter-channel interference. These are decided by taking into consideration the guard band for the laser sources and the modulation bandwidth used for each wavelength. The bandwidth is assigned to take into account temperature effects and ageing. Typical bandwidths of 0.4 nm to 1.6 nm are employed, corresponding to 50 GHz and 200 GHz respectively, at 1550 nm wavelengths. The key feature of WDM is that the discrete wavelengths form an independent set of carriers which can be separated, routed, and switched without interfering with one another.

However, as with most fields, there are many secondary applications that have benefited from this investment. At the forefront of this are optical sensors, covering a wide range of stimuli from physical properties such as pressure [10] or temperature [11] through to targeted detection of biological and chemical species [12]. Optical-based sensors are of particular interest as they possess advantages which include immunity to electro-magnetic interference, high sensitivity, and the potential for mass production.

1.3.2 Sensors

A sensor is a device that measures a physical quantity and converts it into a signal which can be read by an observer or by an instrument. A wide range of sensors exist today for monitoring physical, chemical or biological changes. For good performance, a sensor should:

- be sensitive to the measured property,
- be insensitive to any other property likely to be encountered in its application,
- be incapable of influencing the measured property,
- have a large dynamic range.

Physical sensors monitor physical changes within their environment and have a huge expanse of applications ranging from large-scale structural monitoring of bridges and

skyscrapers [13, 14] to the small-scale monitoring of temperature of an integrated optical [15] or electrical chip. Optical physical sensors are currently increasing in popularity in the physical sensor market, previously dominated by electrical devices. A notable example being the increasing use of optical fibre based sensors in civil engineering, used as a tool for monitoring stresses in both new and old constructions [16].

While physical parameters are often easier to separate, for biological and chemical sensors the scope and variety of potential measurand parameters is much higher, with much greater risk of interference between the sensor and its environment.

The chemical sensor market contains a variety of competing technologies, however these can be generalised into four main categories [17]:

- Chromatography chemical sensors involve the separation of complex mixtures and include standard techniques found in analytical chemistry, such as high pressure liquid chromatography (HPLC) [18] and capillary electrophoresis [19].
- Mass sensors involve the detection of mass (or mechanical modulus) changes upon a surface [20], generally the detection is characterised by a shift in resonance frequency, e.g. the resonance of a cantilever [21].
- Electrochemical sensors involve the detection of an electrical signal [22] and monitor electrical change, such as resistance [23].
- Optical devices detect changes in the electromagnetic waves as they interact with a chemical.

The majority of commercial optical chemical sensors are based on free space optics, such as spectrometers and refractometers. However there is a growing subset that exploits optical fibre [24] or integrated optical structures for detection [25]. The compact nature and ability to combine multiple functions into a single device lend integrated optical sensors towards lab-on-a-chip applications, a field of research that focuses on replicating an entire laboratory process or system on a single small-scale chip[26, 27]. The transition to compact analytical devices will allow samples to be analysed at the point of need rather than in a centralised laboratory [27] revolutionising fieldwork and point-of-care medical diagnostics.

Lab-on-a-chip devices have many advantages over large-scale systems, including:

- low fluid volume consumption, generating less waste with lower reagent costs and with a reduction in the required sample volume for diagnostics.
- faster analysis and response times, due to short diffusion distances, fast heating, high surface-to-volume ratios and small heat capacities.
- better process control through faster feedback (as a result of faster analysis).
- compact systems.
- massive parallelisation allowing for high-throughput analysis.
- lower fabrication costs through mass production and use of existing fabrication techniques from the microelectronics industry leading to cost-effective disposable chips.
- a safer platform for chemical, radioactive or biological analysis, through reducing the quantities of hazardous material and containing it within closed systems.

However, there are some disadvantages associated with lab-on-a-chip devices, primarily due to the lack of development in this new technology. These can include:

- physical and chemical effects that become more dominant as the scale diminishes, such as: capillary forces, surface roughness and the chemical interaction of the device material on reaction processes.
- detection principles that may not always scale down in a positive way, leading to low signal-to-noise ratios.
- microfabrication processes may lack the precision to produce the desired structures uniformly and reproducibility.

Optical sensors often exhibit greater sensitivity and faster readings than conventional sensing methods [28]. They have the advantage of immunity to electromagnetic and radio frequency interference and an inability to create sparks, allowing for implementation in explosive environments. Generally, the materials from which they are made can function under adverse temperature, pressure, toxicity or corrosive atmospheres that would otherwise rapidly erode metals.

The market for chemical sensors is large, with the US market alone predicted to surpass $5 billion by 2012 [1]. While biosensors will continue to be the largest type of

chemical sensor, overall growth will also be supported by technological advances that allow for price reduction, sensor miniaturisation and greater precision, all of which expand the use of chemical sensors into new markets or applications. Demand for chemical sensors based on emerging technologies is predicted to see the fastest gains with optical sensors seeing the greatest growth of all sensor types. It is expected [1] that they will continue to benefit from their high sensitivity, stability, immunity to interference and product improvements such as reduced size and enhanced ruggedness.

Integrating optics within microfluidic systems to form "lab-on-a-chip" optofluidic devices is an emerging technology at the forefront of sensor design [29]. The work presented here focuses on the development of such an optical sensor system from a simple refractometer towards a working integrated optical chemical sensor.

1.4 Aim of Research

This PhD thesis investigates direct UV grating written integrated optical devices, for potential telecom and sensing applications. Direct UV grating writing is a fabrication technique for the definition of both waveguide and Bragg gratings in a one-step process. The system consists of a dual UV laser-beam set-up, beneath which a photosensitive silica-on-silicon composite sample is translated. Exposing these Bragg gratings to the environment provides a refractometer that can be applied to a wide range of sensor applications.

The original aim of this PhD thesis was to develop direct UV written devices for chemical detection, by bringing together elements of supramolecular chemistry, integrated optics and microfluidics. The aims of this PhD thesis have been met through the development of several novel direct UV written components/devices that has culminated in a lab-on-a-chip sensor that uses the supramolecular interaction of the crown ether moiety to enhance the sensor response to the presence of a specific cation; all within a microfluidic flow cell allowing continual sampling of a feedstock. This holistic proof-of-concept device is competitive with rival approaches in terms of sensitivity, robustness and practicality, while offering specific advantages of its own.

This work has yielded several journal publications [30-33] and data that have been presented at several national and international conferences (a complete bibliography is detailed in Chapter 11.4).

1.5 Thesis Synopsis

Following from this introduction to integrated optical devices, a theoretical understanding of optical waveguide and Bragg grating operation is tackled in Chapter 2. In this, the fundamental physical concepts describing light propagation through a medium and how this forms the basis of an optical lightwave circuit are defined. These are used to introduce the concepts of the optical slab and channel waveguide structures. For channel waveguides numerical examples of mode-solving algorithms are discussed including the film mode matching (FMM) method in preparation for later chapters where a commercial FMM algorithm (Fimmwave) has been used by the author to model the guided modes of the presented waveguide systems. Chapter 2 concludes by exploring the concept and spectral response of optical Bragg gratings.

Starting from the fabrication of the silica-on-silicon platform by chemical vapour deposition, the method of optical device fabrication is addressed in Chapter 3. This chapter covers the theory and history of direct UV writing, comparing it to other competing methods of fabrication, including photolithography and direct femtosecond writing. This includes the considerations of the composition required for direct UV writing, including the introduction of germanium as a UV-photosensitive dopant combined with the proposed mechanisms for this photochemical effect. The dual-beam direct UV writing technique is described including methods of grating design to achieve apodised Bragg grating structures. The chapter concludes by with a discussion of the optical characterisation of Bragg grating structures.

Chapter 4 provides an overview of chemical sensing and focuses upon effective refractive index-based evanescent field sensors; introducing examples of such device structures developed around surface plasmon resonance (SPR) sensors, Mach-Zehnder interferometers (MZI) and Bragg reflector refractometers.

This overview introduces the Bragg grating sensors presented in Chapter 5. Enhancements to the sensitivity of such devices are discussed, including improvements to the fabrication process, waveguide design and alternative geometries. The concept of a high-index overlayer for Bragg grating sensors is introduced, with an examination of the sensitivity limit of such a device shown.

Chapter 6 introduces the concept of reconfigurable optical Bragg gratings for telecoms applications, whereby a photoresponsive polymer is used to tune the Bragg response of the optical device.

To develop these systems into practical chemical sensors, robust and reliable referencing is necessary to remove the effects of physical changes. Chapter 7 outlines several approaches to temperature referencing and their application in fabricating an athermal Bragg grating.

Chapter 8 focuses on the development of the microfluidic system and bulk sensing of fluid transitions within these small scale channels, highlighting unexpected observations. With the groundwork laid, the final chapters focus upon the development of these integrated optical refractometers into optofluidic chemical sensors, including a discussion of chemically functionalising the sensor surface and the effect this has on both the sensitivity and selectivity of these systems. Here it will be shown that these sensors are capable of selectively detecting small concentrations of an analyte within a fluid flow system.

Experimental methods, procedures and chemical synthesis are discussed in greater detail in the experimental chapter (Chapter 12) that follows the main discussion.

2. Theory and Analysis

2.1 Introduction

This chapter summarises the theoretical basis and analysis techniques that can be applied to integrated optical circuits. There are many good texts which cover this topic in depth [9, 34-38] and so the purpose of this chapter is to complement the literature and provide sufficient summary to introduce the work presented in this thesis.

This chapter introduces the theory behind optical waveguides, introduces Maxwell's equations and applies these to a weakly guiding waveguides. Using this theory, analytical and numerical techniques, the analysis of waveguide structures and Bragg gratings are described.

2.2 Refractive Index, Dispersion and the Kramers-Kronig Relationship

To summarise the theoretical basis of the optical lightwave circuits presented here, it is first necessary to introduce several physical concepts relating to the propagation of light through a medium.

The phase velocity of light (often simply referred to as the velocity of light) is defined as the rate at which the phase of a wave propagates through space. This can be thought of as the speed at which the phase of any one frequency component of the wave travels, as illustrated in Figure 2.1 where over the interval Δt the wave has propagated by Δx, giving a phase velocity equal to $\Delta x/\Delta t$ in the x-direction.

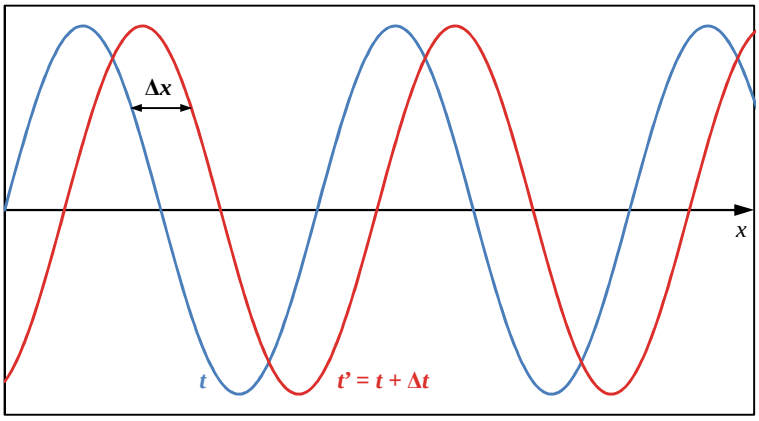

Fig. 2.1 Illustrating phase velocity. In a time Δ*t* the position corresponding to a given point on the wave travels a distance Δ*x* = cΔ*t*.

The phase velocity can differ from the group velocity, which is defined as the rate at which changes in amplitude (the envelope of the wave) propagate. In this way, the group velocity can be considered the velocity at which energy or information is conveyed along the wave.

2.2.1 Refractive index

The refractive index of a conventional medium is a measure for how much the speed of light is reduced within that medium. The refractive index, *n*, is defined as the ratio of the phase velocity, *c* of a wave in a reference medium, typically a vacuum, to the phase velocity, v_p in the medium itself. In the case of light, it can be given by:

$$n = \frac{c}{v_p} = \sqrt{\varepsilon_r \mu_r} \qquad (2.1)$$

where ε_r is the material's relative permittivity, and μ_r is its relative permeability. The relative permittivity of a material is determined by the ability of the material to polarise in response to an applied electric field and as such the refractive index of a molecule should be determined by its polarisability. Similarly, the relative permeability can be defined by the degree of magnetisation that a material obtains in response to an applied magnetic field. Both permittivity and permeability are given relative to free space, such that:

$$\varepsilon_r = \frac{\varepsilon}{\varepsilon_0} \quad \text{and} \quad \mu_r = \frac{\mu}{\mu_0} \qquad (2.2)$$

where ε_0 is the permittivity of free space, and μ_0 is permeability of free space. For most naturally occurring materials, μ_r is very close to 1 at optical frequencies.

While refractive index is almost exclusively positive, recent research has also demonstrated the existence of negative refractive index, which can occur if the real parts of both permittivity and permeability have simultaneous negative values. This can be achieved with periodically constructed negative index metamaterials, the resulting negative refractive index offers the possibility of exotic phenomena such as the superlens [39] – a lens that can go beyond the diffraction limit.

Refractive index is also frequency dependent and varies according to the frequency of radiated light. Measurements are normally taken using the characteristic yellow doublet of a sodium source at a wavelength of 589.8 nm (the Fraunhofer "D" line) denoted as n_D. Therefore, the cited values of refractive indexes, such as 1.33 for water, are based on measurements with yellow light at a wavelength of 589.8 nm It should also be noted that temperature also affects refractive index and literature values are based on a standard temperature, such as 25 °C.

2.2.2 Dispersion

In optics, dispersion is the phenomenon in which the phase velocity of a wave depends on its frequency, or alternatively when the group velocity (the rate at which the envelope of the wave propagates) depends on the frequency.

The most familiar example of dispersion is a rainbow, in which dispersion causes the spatial separation of white light into components of different wavelengths. However, dispersion also has an effect in many other circumstances: for example, group velocity dispersion causes pulses to spread in optical fibres, degrading signals over long distances.

There are generally two sources of dispersion: material dispersion and waveguide dispersion. Material dispersion comes from a frequency-dependent response of a material to waves. This can have both a desirable or undesirable effect in optical applications. The dispersion of light by glass prisms is used to construct spectrometers, while in a lens dispersion can cause chromatic aberration, degrading images in microscope objectives. Waveguide dispersion occurs when the speed of a wave in a waveguide (such as an optical fibre) depends on its frequency for geometric reasons and is independent of any material dispersion. In general, both types of dispersion may be present, although they are not strictly additive.

In general, the refractive index is a function of the wavelength, λ of the light, thus $n = n(\lambda)$. The wavelength dependence of a material's refractive index is usually quantified by an empirical formula, the Cauchy or Sellmeier equations.

From Snell's law (as discussed later in Section 2.3.1) it can be seen that the angle of refraction of light in a waveguide depends on the refractive index of the prism material. Since that refractive index varies with wavelength, it follows that the angle that the light is refracted by will also vary with wavelength, causing an angular separation known as angular dispersion.

Because of the Kramers–Kronig relations (Section 2.2.3), the wavelength dependence of the real part of the refractive index is related to the material absorption, described by the imaginary part of the refractive index (the extinction coefficient).

If, as with most transparent materials, the refractive index decreases with increasing wavelength the medium is said to have normal dispersion. Conversely, if the index increases with increasing wavelength the medium has anomalous dispersion.

2.2.3 Complex refractive index

The dispersion of a material can be calculated from its respective absorption spectra, using the Kramers-Kronig relation. The Kramers–Kronig relations are mathematical properties, connecting the real and imaginary parts of a complex function. To understand the formulism of the Kramers-Kronig relationship the complex nature of refractive index ought to be first understood. The refractive index of a medium $n(\lambda)$ can be split into a real dispersive part $\underline{n}(\lambda)$ and an imaginary absorption part $\kappa(\lambda)$, formulated as:

$$n(\lambda) = \underline{n}(\lambda) - i\kappa(\lambda) \qquad (2.3)$$

where, $\underline{n}$ is dispersion and κ is the extinction coefficient (it should be noted that this differs from the molar extinction coefficient, α, more commonly discussed in Chemistry), which indicates the amount of absorption loss (or gain) when the electromagnetic wave propagates through a material.

The spectral form of absorption can be mathematically interpreted by considering an electron bound to the nucleus to be analogous to a small mass bound to a bigger

mass by a spring. If the system is driven by a (light)wave, $E_0e^{i\omega t}$ the resulting oscillations can be approximated as a damped force oscillator. Therefore, considering an electron of mass m_e and charge e, there is a resonance at ω_0, with a particular viscous drag, γ formulated as:

$$m_e \frac{d^2x_e}{\partial t^2} + m_e\gamma \frac{dx_e}{\partial t} + m_e\omega_0^2 x_e = eE_0e^{-i\omega t} \qquad (2.4)$$

From Equation 2.4 and applying electomagnetic identities for an electron density N, gives absorption, α, in the form of a complex Lorentzian:

$$\alpha = \frac{Ne^2}{4\epsilon_0 cm_e}\left[\frac{\gamma/2}{(\omega_0-\omega)^2+(\gamma/2)^2}\right] \qquad (2.5)$$

This description of imaginary refractive index is inherently linked to the real part through the Kramers-Kronig relationship [40]. The significance of this relationship is that it relates the refractive index at a particular frequency (or wavelength) to the absorption at other wavelengths. This treatment draws heavily on the mathematics of the complex treatment of signals and is not essential to the work presented here.

However, the interrelationship between n and κ can be understood by considering an excited atom that vibrates at the frequency of the light that excited it and re-emits this energy as light of that frequency. The delay in re-emission retards the time taken for light to travel through a material, thus increasing n. Absorption is affected by the relative phase of the light that is re-emitted with respect to the incident light. This relative phase shift will produce interference with the original light, with destructive interference observed as absorption. This is illustrated in Figure 2.2, where it is shown that an absorption peak has a corresponding change in refractive index.

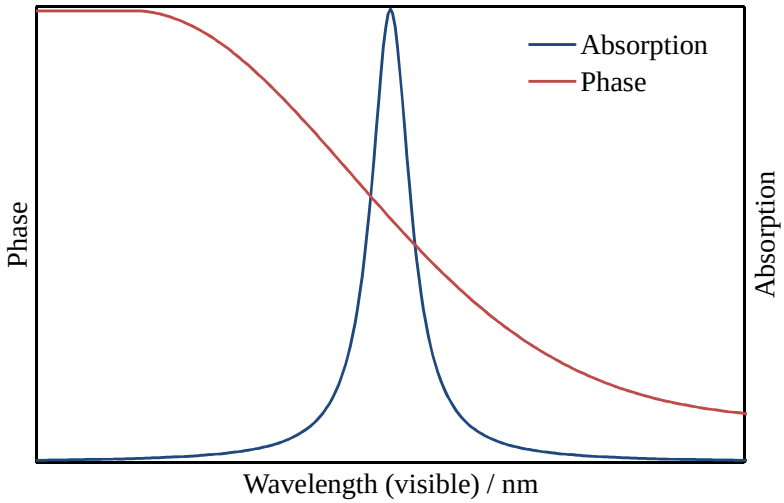

Fig. 2.2 An illustration of the relationship between absorption and refractive index [41].

2.3 Optical Waveguides

The field of integrated optics relies on the principle of controlling and guiding the path of light through optical circuitry. An optical integrated circuit is much like its electronic analogue, with a network of optical components designed to work together to achieve a function. Information transfer between these components is achieved by one of the most fundamental structures of an optical circuit, the optical waveguide. Just as electronic circuits manipulate current with wires and conducting strips, waveguides are used analogously to manipulate the path of light in an integrated optical circuit.

A waveguide is defined as a structure capable of guiding the flow of electromagnetic energy in a direction parallel to its axis. In the context of this work, the waveguide structures are designed to transmit electromagnetic waves in the short infrared wavelength region (telecoms C band, 1530-1560 nm).

2.3.1 Light incident upon a boundary

An optical waveguide can simply be considered as a structure that confines and directs wave propagation by channelling light between two interfaces. Thus, to understand the optical waveguide it is first necessary to understand the interaction of light incident upon a boundary.

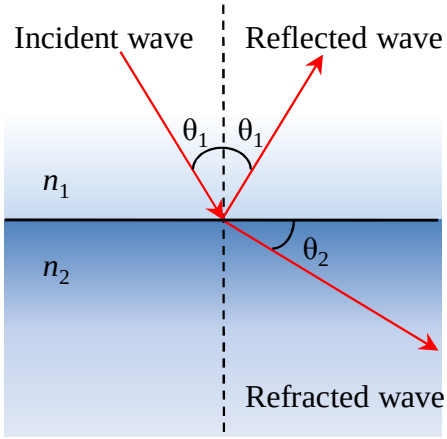

Fig. 2.3 Reflection and refraction at a planar interface,

As illustrated in Figure 2.3, when light interacts with a planar boundary, reflection and refraction occur. Snell's law [34] states that the angles of reflection and refraction of an incident electromagnetic wave are related by:

$$n_1 \sin\theta_1 = n_2 \sin\theta_2 \qquad (2.6)$$

where θ_1 and θ_2 are the angles of incidence and refraction respectively, n_1 and n_2 are the refractive indices of the material on either side of the boundary. For the case $n_1 > n_2$ and where the angle of incidence is given by $\theta_i = \sin^{-1}(n_2/n_1)$, the angle of refraction is $\pi/2$ and the refracted wave travels along the interface between the media. This value of θ_i is known as the critical angle and any incident angle greater than this will result in no transmitted wave, only total internal reflection, i.e. 100 % of the light is reflected. However when $n_1 < n_2$, the angle of refraction can never equal $\pi/2$ and total internal reflection is impossible [34].

2.3.2 Planar waveguides

Using the principle of total internal reflection a planar waveguide can be constructed by confining a sheet of high refractive index material (core) between two sheets of lower refractive index material (cladding), such that the light is trapped within the plane of the waveguide, as illustrated in Figure 2.4. This trapping results in propagation along the *z*-axis, parallel to the plane of the waveguide.

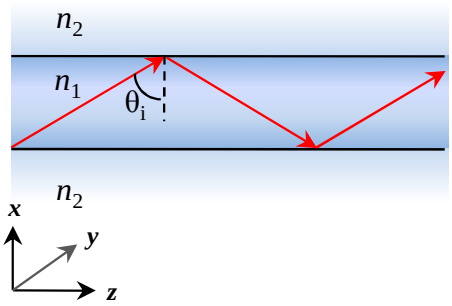

Fig. 2.4 Light guided by total internal reflection in a planar slab waveguide.

While this would imply that any lightwave with an angle of incidence greater than the critical angle for total internal reflection will be confined, for the majority of waveguides there is a discrete set of angles greater than the critical angle that corresponds to successive boundary reflections having phase fronts which coincide. These discrete set of angles can be thought of as a discrete set of characteristic waves, referred to as the supported eigenmodes of the waveguide (or simply "modes"). These modes are transverse field distributions that maintain the same distribution and polarisation invariantly during propagation along the waveguide axis. The effective refractive index of the propagating mode is the average refractive index experienced by the mode as it traverses along the waveguide. It is found that the effective index of a slab waveguide is lower than that of the core layer, indicating the mode is not tightly confined to the core but has an evanescent 'tail' propagating into the cladding. It is this property that is exploited in the development of optical sensors described in this thesis.

2.3.3 Channel waveguides

The simple case of the planar (or "slab") waveguide, discussed above, is not the most practical waveguide design, as it only has confinement of the propagating lightwave in the *x*-direction. By adding a second degree of confinement along the *y*-axis a channel waveguide can be formed (Figure 2.5). As with the planar case, guided modes are found to have an effective refractive index below that of the core, so therefore $n_{clad} < n_1$.

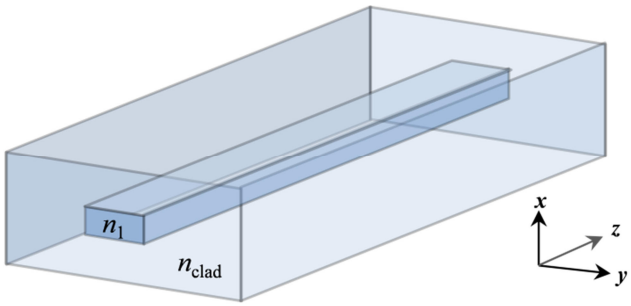

Fig. 2.5 A rectangular channel waveguide.

Several possible geometries for channel waveguides exist which confine the light in two dimensions. These can be categorised as diffused, rib and buried channel waveguides, as shown in Figure 2.6. The waveguide geometry used is generally dependent upon the material and method of fabrication [36], however the work presented within this thesis will focus on buried waveguide structures fabricated by direct UV writing.

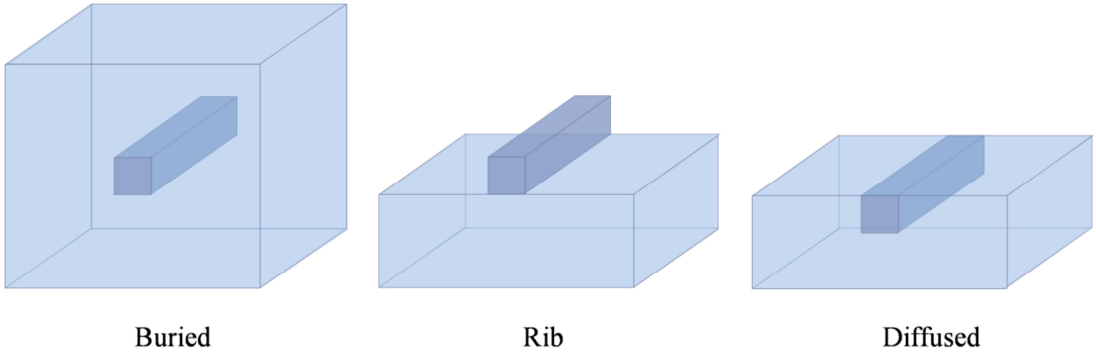

Fig. 2.6 The three basic geometries that support channel waveguides; buried, rib and diffused structures.

2.3.4 Maxwell's equations

So far, light within a waveguiding structure has been described classically, with only consideration of the interaction of a lightwave at a boundary through reflection and refraction. However, a photon within a waveguide can also be described in a similar manner to a "particle in a box" in quantum mechanics, with certain discrete wavefunctions (eigenmodes) supported within this box. This discrete set of supported modes gives rise to a discrete series of effective refractive indices supported by the waveguide, much like the energy levels for a particle in a box.

If the barrier is finite, then the wavefunction may not be fully confined within the box, but may exist outside. The probability of finding the particle outside the box can be modelled as an exponential decay. In the case of a weakly-guiding

waveguide this gives rise to the "evanescent tail" of the guided mode, a property heavily exploited in optical sensors (Chapter 4). Furthermore by describing this finite potential well in two dimensions and considering the symmetry of the well, it is possible to explain the existence of different polarisation states as a pair of discrete orthogonal modes.

Maxwell's equations irrefutably hold the solution to all problems in electrodynamics. Indeed the foundation of waveguide theory is bound together by four equations published by Maxwell in 1873. These equations can be used to explain quantitatively the concepts outlined above, which while not necessary for the comprehension of the work detailed in later chapters, has been included in the following section for completeness. The following sections introduce the Helmholtz equations and the approximations of a weakly-guiding waveguide. The key conclusions that can be drawn from these are that only discrete modes are supported within the waveguide and that these can be split into the transverse electric mode and the transverse magnetic mode. In an asymmetric waveguide these orthogonal polarisation modes are exhibited as birefringence. This property is exploited in Chapter 7 to develop an athermal Bragg grating.

The evolution with time, *t*, of the Electric field **E**(*t*) and magnetic field **H**(*t*), in a medium of magnetisation density **M**(*t*) and polarisation density **P**(*t*) can be described by the following Maxwell's equations:

$$\nabla \text{ x } \mathbf{E}(t) = -\mu_0 \frac{\partial \mathbf{H}(t)}{\partial t} - \frac{\partial \mathbf{M}(t)}{\partial t} \tag{2.7}$$

$$\nabla \text{ x } \mathbf{H}(t) = J_f(t) + \varepsilon_0 \frac{\partial \mathbf{E}(t)}{\partial t} + \frac{\partial \mathbf{P}(t)}{\partial t} \tag{2.8}$$

$$\nabla . \varepsilon_0 \mathbf{E}(t) = \rho_0(t) - \nabla . \mathbf{P}(t) \tag{2.9}$$

$$\nabla . \mathbf{H}(t) = -\nabla . \mathbf{M}(t) \tag{2.10}$$

μ_0 is the permeability of free space, ε_0 is the permittivity of free space, $\rho(t)$ is the charge density and $J_f(t)$ is the free current density, which relates to all charges not associated with the polarisation density **P**(*t*).

From these equations the full vectorial Helmholtz equations for the electric field can be derived (the full derivation can be found in " Introduction to Fiber Optics", by Ghatak [34]):

$$\nabla^2\mathbf{E} + \nabla\left(\frac{1}{n^2}\nabla n^2.\mathbf{E}\right) - \varepsilon_0\mu_0 n^2\frac{\partial^2\mathbf{E}}{\partial t^2} = 0 \qquad (2.11)$$

and in a similar manner, the magnetic field can be considered to obtain:

$$\nabla^2\mathbf{H} + \frac{1}{n^2}\nabla n^2 \text{ x } (\nabla \text{ x } \mathbf{H}) - \varepsilon_0\mu_0 n^2\frac{\partial^2\mathbf{H}}{\partial t^2} = 0 \qquad (2.12)$$

Note that these equations cover the situation where the permittivity depends upon position, as would occur within a waveguide. If the permittivity does not depend on position then these equations would yield the wave equation for a uniform material. The full vector Helmholtz equations are used in numerical mode solving techniques (such as those discussed subsequently in Section 2.3.7) and have been described here for completeness, however many waveguides display so called 'weakly guiding' characteristics that result in the simplification of this full vectorial equation into a scalar equation.

The full derivation of these equations from Maxwell's equations and a more thorough discussion of their implications is given in Chapter 7 of "Introduction to Fiber Optics", by Ghatak [34]. To further aid in the comprehension of these equations, a summary of the *del* operator, ∇, and the corresponding vector product, *curl* (∇x), and scalar product, *div* (∇.), are given in the appendix.

2.3.5 Weakly guiding waveguides

The guided modes of a waveguide are a set of solutions that fulfil the total internal reflection condition and require the waveguide core to have a higher refractive index than the surrounding cladding. For many waveguides, the refractive index contrast between the core and cladding varies by only a small amount, ~0.3 %. These types of waveguides are referred to as 'weakly guiding' waveguides. The term weak in this context is not a reflection on the ability of the waveguide to guide light but merely that the refractive index contrast is small.

With the optical mode not confined to the core, but evanescently propagating into the cladding, a weakly guiding waveguide can be used to develop an optical evanescent field sensor. Further, such a waveguide structure is compatible with coupling to an optical fibre, a similar weakly guiding waveguide, allowing for incorporation into an

optical network. The drawback of using a weakly guiding structure is that the increased complexity of the mode makes the system much harder to model.

Following the treatment in Ghatak [34], we can ask what happens to the electromagnetic field at the boundary. This can be understood through further consideration of Maxwell's equations [34], from which the following six equations can be derived:

$$i\beta E_y = -i\omega\mu_0 H_x \tag{2.13}$$

$$\frac{\partial E_y}{\partial x} = -i\omega\mu_0 H_z \tag{2.14}$$

$$-i\beta H_x - \frac{\partial H_z}{\partial x} = i\omega\epsilon_0 n^2(x) E_y \tag{2.15}$$

$$i\beta H_y = i\omega\epsilon_0 n^2(x) E_x \tag{2.16}$$

$$\frac{\partial H_y}{\partial x} = i\omega\epsilon_0 n^2(x) E_z \tag{2.17}$$

$$-i\beta E_x - \frac{\partial E_z}{\partial x} = -i\omega\mu_0 H_y \tag{2.18}$$

where *x*, *y* and *z* refer to the vector field components along the *x*, *y* and *z* dimensions respectively, as indicated in Figure 2.3, relative to the slab waveguide propagating along the *z*-axis and β is the propagation constant of the supported mode.

Consideration of these equations for light in a planar waveguide confined in the *x*-direction, propagating along the *z*-axis, results in two sets of solutions. Equations 2.13-2.15 involve only E_y, H_x and H_z and Equations 2.16 - 2.18 involve only E_x, E_z and H_y, meaning there are two independent sets of solutions to Maxwell's equations. One of these sets will correspond to non-vanishing values of E_y, H_x and H_z and vanishing values of E_x, E_z and H_y. The mode solutions in this instance are known as Transverse Electric (TE) as the electric field component, E_y is in the plane of the waveguide. For the alternative set of solutions the vanishing and non-vanishing terms are swapped with the magnetic field component, H_y in the plane of the waveguide, producing a set of modes known as Transverse Magnetic (TM).

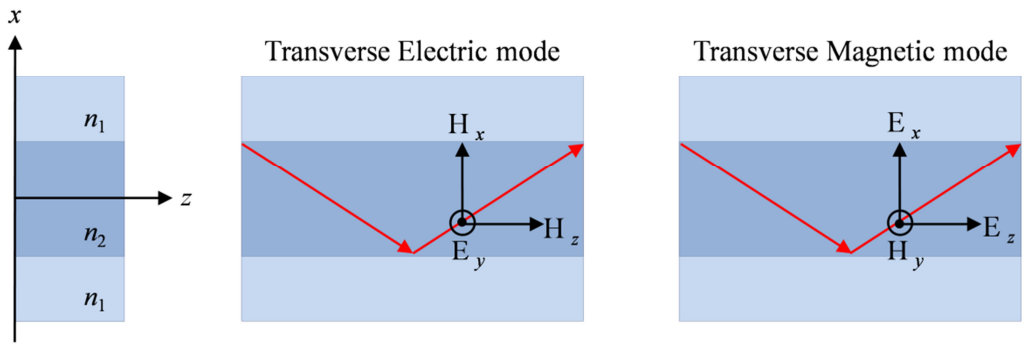

Fig. 2.7 The field components for the transverse electric (TE) and transverse magnetic (TM) optical modes.

The physical interpretation of the two sets of solutions are one set of modes with its electric field (E) oscillating in the *y*-plane and the other with its magnetic field (H) oscillating in the *y*-plane (Figure 2.7). From Maxwell's equations; at the boundary between the cladding and the core, the modes must be both continuous and smooth, i.e. for the TE mode: E_y and its derivative with respect to *x* must be continuous at the interface, resulting in quantisation of the modes allowed within the waveguide. For a well-guided mode, the electric field is mostly confined to the core but decays exponentially out into the cladding region. It is this evanescent field that is used in optical sensing applications.

Polarised light launched into the waveguide either parallel or perpendicular to the plane will only propagate exclusively in either the TE or TM mode, depending on the launch. However launching polarised light at an intermediate angle will not propagate in an intermediate polarisation mode but a ratio of the orthogonal TE and TM modes will be supported. Importantly these modes cannot be orthogonal in both **E** and **B** and so are not equivalent to simple ideas of polarisation in free space.

Figure 2.8 illustrates the differences between this pair of orthogonal polarisation modes of an optical waveguide when in a highly birefringent environment, compared to a symmetric environment. The gradient maps represent the intensity (proportional to the square of the electric field strength) of the guided mode across a 15 x 15 µm cross-section of the waveguide, with a central square core of dimension 5.6 µm, located between layers of cladding. (As discussed in Section 2.3.7, this modelled data was obtained using Fimmwave, a commercial numerical mode solver, based upon the waveguide system presented in Chapter 5).

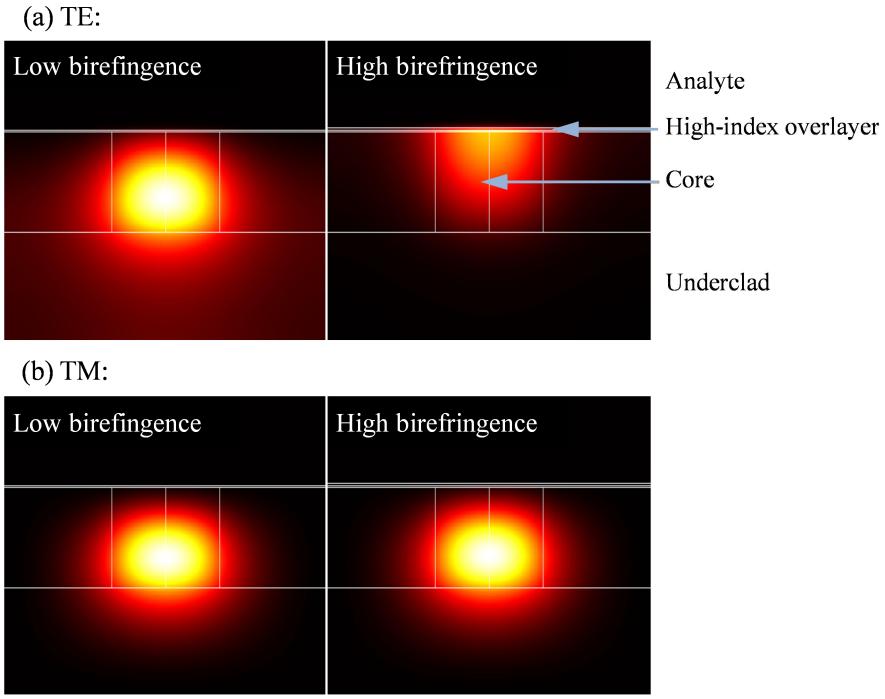

Fig. 2.8 Modelled intensity maps for the TE and TM modes of a waveguide sensor, showing the greater penetration of the TE mode into an analyte than for the corresponding TM mode in the birefringent system.

When in a symmetric environment the intensity distributions of the two orthogonal modes within the core of the waveguide are similar, with a Gaussian intensity profile in all directions. However when the birefringence of the system is increased through removal of the overclad and replacing it with a material of high refractive index, as illustrated in Figure 2.8, the intensity distribution of the two modes differs significantly. While the TM mode remains mostly unchanged, the TE mode is pulled up towards the surface, with most of the power distributed near the surface. In the context of optical sensors, this results in a greater penetration of the evanescent field of the guided mode into the analyte for the TE mode than for the TM.

It is because of the differing responses of these two orthogonal modes that the polarisation state of the optical input must be considered and defined when constructing a planar waveguide circuit for optical sensing. The properties and applications of birefringence within asymmetric waveguides will be discussed in the context of Bragg gratings in Section 2.4.3 and Chapter 7.

2.3.6 The Effective index method

The effective index method is one of several techniques for analysing weakly guiding two-dimensional optical waveguide structures [34, 36]. The method assumes that the refractive index can be split into separate *x* and *y* dependencies. Under these assumptions it operates by simply repeating the planar optical waveguide analysis.

The effective index method splits the problem into a series of one-dimensional planar waveguide structures. The first step of the method calculates the effective indices along the *x* dimension, as if they constituted to an individual planar waveguide, as is illustrated in Figure 2.9 for a buried waveguide structure. Once the effective indices, n_{eff} are calculated for the *x*-dimension, they are used to build another one-dimensional structure in the *y*-dimension. From these an overall effective index approximation can be made.

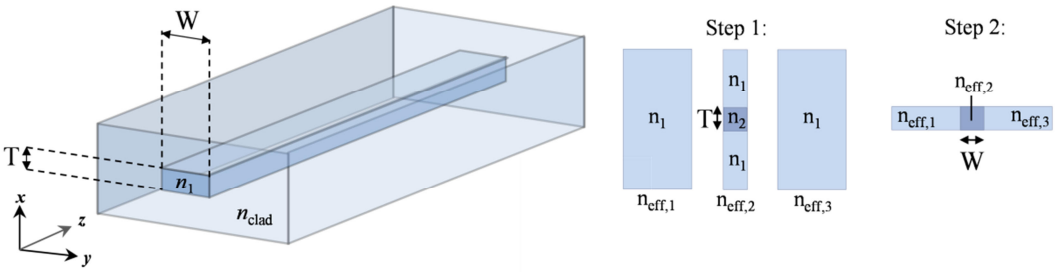

Fig. 2.9 Calculation steps necessary to find the effective index of a buried waveguide, using the effective index method

2.3.7 Numerical mode solving

The treatment of photonic waveguide modes has so far considered analytic solutions. The effective index method and other such approximations are idealised solutions for weakly guiding modes and remain accurate for only very simple waveguide geometries. The geometries of real world waveguides, such as ones containing thin index layers, are much more complicated and often require a full vectorial treatment. Numerical solutions to a waveguide's mode are required in these situations where there is no simple analytical solution. With the rapid increase in inexpensive computing power, numerical tools have become common place in industry and academia, where they are used to optimise and test design parameters of integrated circuits.

The solution accuracy gained by a numerical technique relative to the required computational processing (speed) and memory has traditionally been an important

factor for consideration. However, with exponentially increasing sophistication of modern computers the processing and memory requirements are becoming less important. Today, most mode solving algorithms can be executed on a desktop computer. This is a contributing factor as to why the popularity of certain mode solving techniques has increased at the expense of others.

Numerical methods are encountered in three main areas of photonic waveguide modelling; these include mode solving, beam propagation and network simulation. Waveguide modelling was carried out in this work using mode solving techniques for the calculation of the effective indices of buried and exposed channel waveguides.

Most numerical mode solving techniques operate by subdividing the space into sections which can be more readily solved than the whole problem head on. The list of mode solving techniques that can solve the full vectorial Helmholtz Equation in this manner is an extensive one [42, 43]. The numerical methods that can find the eigenmodes of an arbitrary waveguide include Finite Difference Method (FDM), Finite Element Method (FEM), Beam Propagation Method (BPM) based mode solvers and Film Mode Matching (FMM). The modes in this thesis are solved using a commercial mode solving package called Fimmwave, which is based upon a Film Mode Matching (FMM) method.

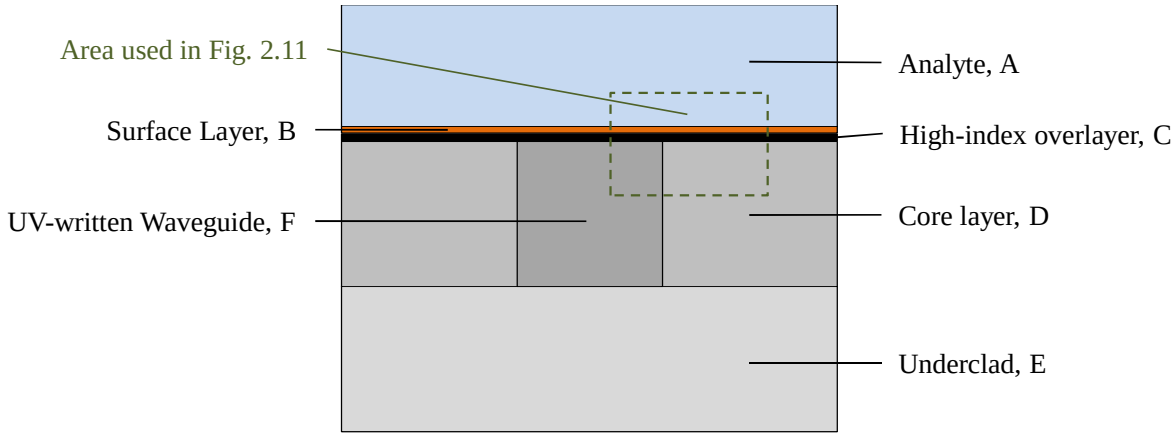

Fig. 2.10 The cross-sectional area of an exposed waveguide design for use in a sensor. The cross-section includes an analyte A, two possible surface layers of arbitrary thickness B, C and a core layer D with a slightly higher index than the underclad E with a UV written waveguide approximated as a rectangle F.

The Finite Difference Method (FDM) has been a very successful numerical technique for mode solving [42, 43] because of the simplicity of its formulation. The

basic operation of this method is to replace the partial derivatives of Helmholtz equations (Equations 2.11-2.12) with finite difference equations. This is achieved by setting up a grid of nodes onto the cross section of the waveguide (a typical waveguide cross section to be modelled is illustrated in Figure 2.11). Approximations of the partial differential equations at a node can then be made by considering the finite differences between it and its nearest neighbours. The simplest way of doing this is considering the four nearest neighbours from which either full vectorial [44], semi-vectorial [45, 46] or scalar formalisms can be made. FDM is relatively straight-forward to program compared to other numerical techniques and so can have an associated lower development cost. However its disadvantage is that it has difficulty discriminating certain structures, due to the technique regularly subdividing space, rather than having an adaptive subdivision of space.

The Finite Element Method (FEM) was first reported by Yeh in 1975 [47] and is now considered to overshadow the FDM of numerical mode solving due to its versatility. It overcomes the discrimination issue associated with FDM as its elements can take the forms of various shapes. This is a computationally taxing technique but with the evolution of desktop computational power FEM has found increased popularity in industry and academia. The elements in FEM are non-overlapping and usually take the form of triangles [9]. The field over each element is then expressed in terms of a low degree interpolating polynomial weighted by the field values at the nodes of each element. This is then evaluated from the linear summation of the fields over each element. The limitation of this technique arises when modes are close to cut-off. For these modes the field extends beyond the core and many more elements and thus computational resources are required to maintain accuracy

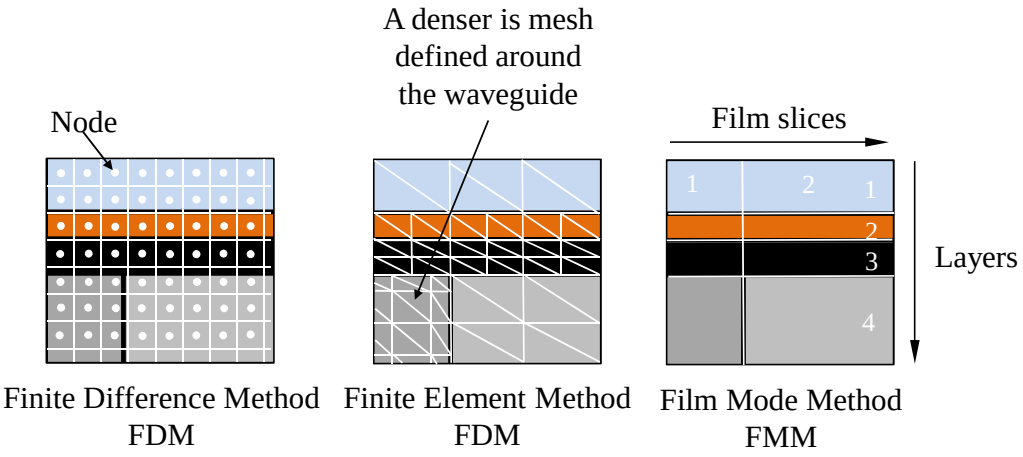

Fig. 2.11 A comparison of the three mode solving methods: finite difference, finite element and film mode, for a region of the waveguide illustrated in Figure 2.10. The FMM method can additionally take advantage of any symmetry present to reduce the computational load.

The waveguide modes are solved in this work using a commercial mode solving package called Fimmwave*, which is based upon a Film Mode Matching (FMM) method reported by Sudbo [48, 49]. This full vector mode solver can be faster and more accurate than alternative methods based upon FDM and FEM. The algorithm used in FMM inherently subdivides the geometry up into areas of refractive index chunks, illustrated in Figure 2.11, giving an advantage when the waveguide is made up of large sections of uniform refractive index. The larger the regions of uniform refractive index are the less subdivisions exist, resulting in fewer calculations. The subdivision occurs by splitting up the geometry into a sandwich of slices (m=1,2,...M), each considered to be cut from a film waveguide, with layer (n=1,2,...N). It must be noted that just as with some FEM and FDM algorithms, the Fimmwave package can take advantage of symmetries in device geometry to reduce the required number of calculations.

Subsequent to FMM subdivision of space, the supported modes of the defined structure are obtained by the algorithm by collecting the modes that have the same wavevector along the propagation dimension and matching the field distributions at the slice interfaces by adjusting the modal amplitudes in each film. The power of the FMM compares fairly well against alternative FEM and FDM for application in this work.

Another useful numerical method in waveguide design is the beam propagation algorithm [9, 37]. While not used directly in this work, this can be used to simulate the

* FIMMWAVE is a product of Photon Design.

evolution of a guided mode and is particularly useful in structures whose index profile is dependent upon the length propagated. Examples of such structures include tapered waveguide, X-couplers, Y-splitters and multimode interference (MMI) devices[37]; all of which have been fabricated using direct UV writing. However due to the slowly varying envelope approximation used in the method it is limited to low-index waveguides.

2.4 Bragg Gratings

Wave propagation in a periodic medium is a well-studied phenomenon. The diffraction of X-rays by a crystal lattice being a classic example [50]. Bragg diffraction occurs when electromagnetic radiation or particle waves with wavelength comparable to atomic spacings are incident upon a crystalline sample. The waves are scattered in a specular fashion by the atoms in the system, and undergo constructive interference in accordance to Bragg's law. For a crystalline solid, the waves are scattered from lattice planes separated by the interplanar distance, *d*. Where the scattered waves interfere constructively; they remain in phase since the path length of each wave is equal to an integer multiple of the wavelength. The path difference between two waves undergoing constructive interference is given by $2d\sin\theta$, where θ is the scattering angle. This leads to Bragg's law which describes the condition for constructive interference from successive crystallographic planes (*h,k,l*) of the crystalline lattice:

$$\Rightarrow n\lambda = 2d\ sin\,\theta \qquad (2.19)$$

Bragg gratings in waveguides are only different in the sense that light is confined in the transverse direction so the interactions are one-dimensional.

2.4.1 The optical waveguide Bragg grating

A Bragg grating is an optical wavelength filter (a “wavelength selective mirror”) created by the periodic modulation, Λ of the effective refractive index of a waveguide.

Gratings can fall into two categories, long-period gratings [51], known as transmission gratings and short-period gratings, known as reflection gratings or Bragg gratings [52, 53]. Long-period gratings are typically sub-millimetre in period and couple specific wavelengths of light from forward propagating guided modes into other forward-

propagating cladding or core modes. Cladding modes typically lose energy through absorption and scattering, resulting in a transmission dip at wavelengths corresponding to the coupled light condition. In contrast, short-period gratings have a sub-micrometre period, where mode coupling occurs between counter-propagating modes. This results in a reflected peak as well as a transmission dip for the coupled wavelength (Figure 2.12). This work will focus upon the fabrication and application of short-period gratings.

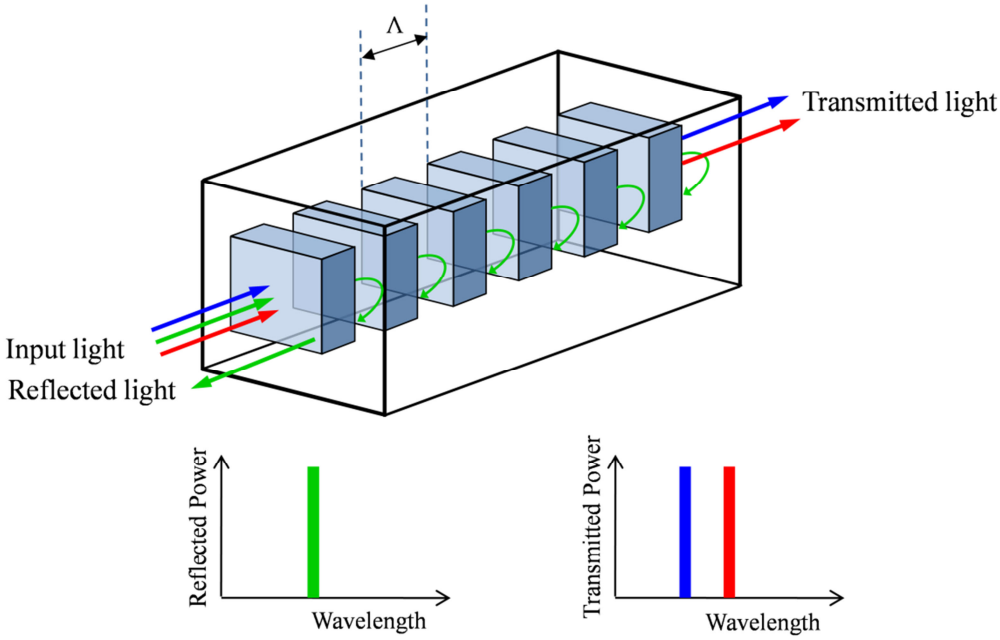

Fig. 2.12 A schematic of a short-period Bragg grating, showing the reflected and transmitted response to a broadband source.

This effective index modulation can be achieved by either variation of the refractive index or the physical dimensions of the guiding core. At each change of refractive index a reflection of the propagating light occurs. The repeated modulation of the refractive index results in multiple reflections of the light travelling through the waveguide. The period of refractive index modulation relative to the wavelength of the light determines the relative phase of all the reflected signals. At the Bragg wavelength, all reflected signals are in phase and add constructively resulting in a back reflected signal centred about the Bragg wavelength. Light reflected at other wavelengths adds destructively and as a result these wavelengths are transmitted through the Bragg grating.

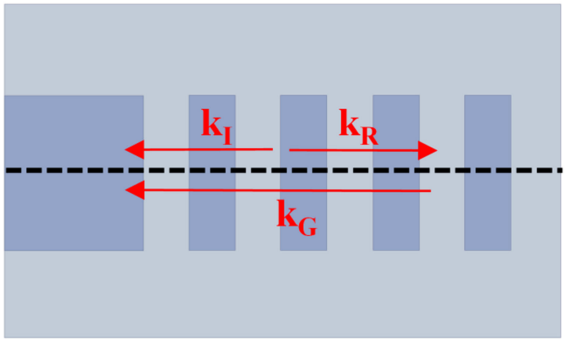

Fig. 2.13 The incident, diffracted and grating wavevectors of a Bragg grating.

The periodic structure of a Bragg grating can be interpreted as having a wavevector component, $\mathbf{k}_G$ (Figure 2.13), where the wavevector of an electromagnetic wave has magnitude equal to the wave number ($|k| = {}^{2\pi}/_{\lambda}$) and in the direction of propagation of the wave. If this wavevector component matches the wavevectors of forward-propagating, $\mathbf{k}_I$ and counter-propagating modes, $\mathbf{k}_R$, the Bragg condition is satisfied, defined as:

$$\mathbf{k}_R = \mathbf{k}_I + \mathbf{k}_G$$
$$\Longrightarrow \; \boldsymbol{n\, sin(\theta_C) = n\, sin(\theta_F) + m\, \frac{\lambda}{\Lambda}} \qquad (2.20)$$

where m is the diffraction order of the grating, as depicted schematically in Figure 2.14:

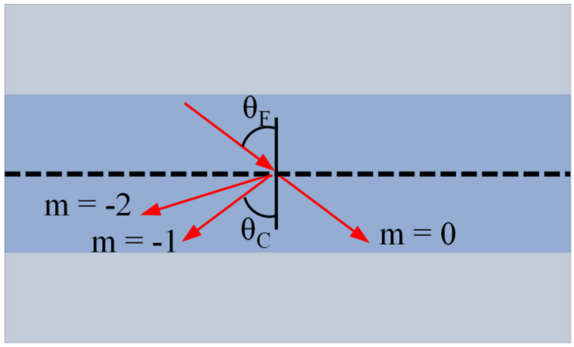

Fig. 2.14 The diffraction of light by a Bragg grating.

Considering first order diffraction (m = -1) coupling a forward-propagating mode into an equal but counter-propagating mode, the Bragg condition is satisfied by $k_R = k_I$ and Equation 2.20 can be rewritten as:

$$- n_{\text{eff}} = n_{\text{eff}} - \frac{\lambda}{\Lambda}$$
$$\Rightarrow \; \lambda = 2\, n_{\text{eff}}\, \Lambda \qquad (2.21)$$

Equation 2.21 defines the Bragg condition, with the wavelength which satisfies this expression known as the Bragg wavelength. The Bragg wavelength can be changed through either variation in the effective index of the mode and/or the period of the grating.

For the fabrication of the direct UV written structures included in this work, the effective index of the waveguide is defined by the photosensitivity enhancement of the germanosilicate glass layer. While this could be controlled through manipulation of the fluence of the UV laser beam (see Section 3.4) it is more effective to alter the period of the Bragg grating, as discussed in Section 3.6.1.

Bragg grating refractometers use the Bragg relation to indirectly measure the response of an exposed grating to changes in the refractive index of its environment. This is achieved through detecting changes in the Bragg wavelength, corresponding to changes in effective index.

2.4.2 Bragg grating structures

A Bragg grating can be considered to be a uniformly periodic structure, which has a sharply-defined beginning and endpoint. Often, either through design, fabrication, or actuation the Bragg grating will deviate somewhat from a uniformly periodic structure. If a grating's refractive index (or pitch) varies slowly over its length, it is defined as being chirped, while if a grating's fringe visibility changes with position, the grating is defined as being apodised (Figure 2.15). Furthermore phase-shifts can be introduced into the Bragg grating by refractive index modulation and result in sharp spectral dips.

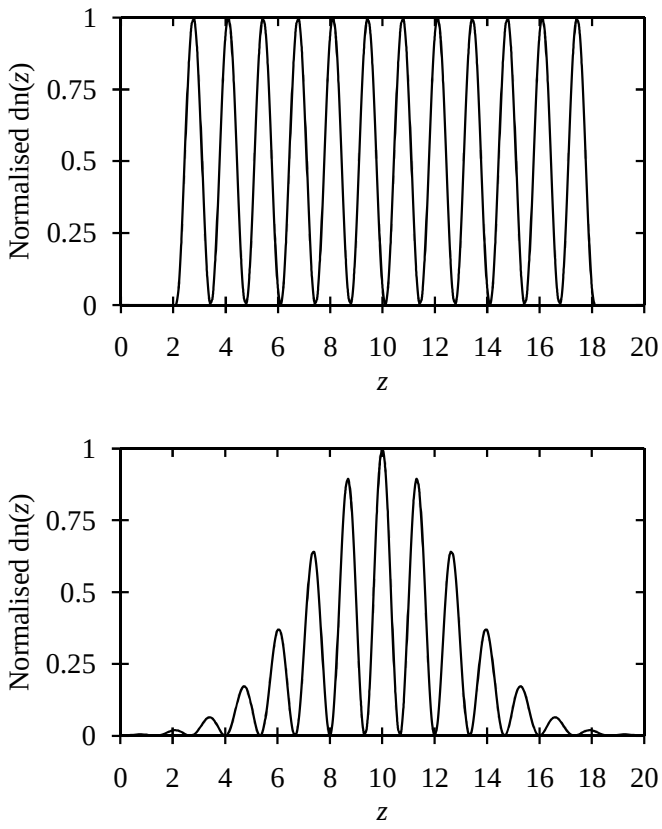

Fig. 2.15 The refractive index profiles of a uniform and Gaussian apodised Bragg grating.

A good approximation to the spectral response of a grating can be achieved through taking the Fourier Transform of the spatial structure, e.g. a uniform grating has a 'top hat' form and so transforms into a 'sinc' function, while a Gaussian apodised grating structure transforms into a Gaussian function (Figure 2.16). For a more detailed analysis of a grating's spectral form, including temporal components, co-directional coupled mode theory is usually applied [34, 36].

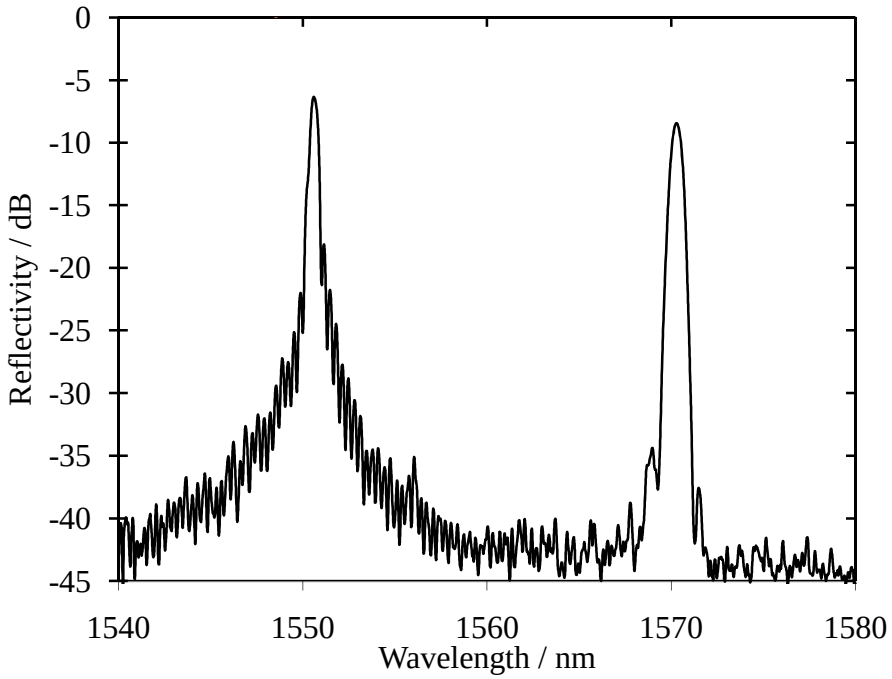

Fig. 2.16 The reflectance spectrum of a waveguide containing a uniform Bragg grating (centred at 1550 nm) and a Gaussian apodised Bragg grating (1570 nm), demonstrating the high side-lobe suppression.

2.4.3 Birefringence

Birefringence is the splitting of a lightwave into two or more separate rays when passing through an anisotropic medium. A uniform, circular waveguide core surrounded by uniform refractive index on all sides will have no birefringence. In the case of the UV written structures presented in this work, the symmetry can be broken for a number of reasons. Firstly, if the three layer structure is not perfectly index matched, the waveguide cladding refractive index will not be uniform in all directions. Secondly, the geometry of the waveguide cross section depends on the writing beam. A non-symmetric beam profile, incorrectly focussed crossed beams or a beam with too high or low fluence can all result in a refractive index increase that varies either in the vertical or horizontal direction. Further, it should be noted that the fabrication of the three layer guiding structure leaves the material inherently under compressive stress. As this stress is anisotropic, it leaves the substrate inherently birefringent.

For a symmetric waveguide the two distinct modes TE and TM, discussed in Section 2.3.5, will experience the same effective index profile. However, if (as is the case for the structures discussed in this work) the waveguide is asymmetric, the modes will propagate into the index profile differently resulting in different effective

indices. Incorporating a Bragg grating into a waveguide allows a simple means of measuring this birefringence as, by the Bragg condition (Equation 2.31), if the effective refractive index varies for different polarisations then so will the corresponding Bragg wavelength [38].

Each of these two orthogonal modes can be guided independently by launching polarised light either parallel or perpendicular to the plane of the sample. However if unpolarised light is used, both modes will be simultaneously supported by the waveguide. Normally the birefringence is small but can still lead to broadening of the Bragg peak, making it necessary to select a single polarisation. However, using the method proposed in Chapter 5 to enhance the sensitivity, the peaks can be separated spectrally and the birefringence can be used for self-referencing, as will be introduced in Chapter 7.

2.4 Summary

This chapter has introduced the concept of refractive index. This has been applied to optical waveguides and Bragg gratings, the fabrication of which will be discussed in the subsequent chapter.

The theory behind these devices, developed from Maxwell's equations, has been introduced and the conditions for waveguide confinement discussed. Guided mode solutions, for TE and TM polarisations, have been considered using an analytical technique. However, for more complicated waveguide geometries, analytical techniques are generally not sufficient and so numerical mode solving techniques have been explored for this means. Finally the principle behind Bragg gratings has been introduced and the necessity to engineer these to produce a refractive index sensor has been discussed.

3. Fabrication

3.1 Introduction

Fabrication on the sub-micron scale is inherently expensive, often requiring the use of complex techniques and clean-room conditions. To control the cost of developing integrated optical devices it is common to develop upon the existing and relatively cost-effective technologies found within the microelectronics fabrication industry. This has led to a wide range of integrated optical devices being developed either directly around the silicon wafer platform or through silica-on-silicon systems. This adoption of the techniques developed for microelectronics processing has the added advantage of the potential integration of both photonic and microelectronic operations onto the same silicon chip [54-57].

The fabrication techniques commonly used for definition of integrated optical circuits within a silica-on-silicon platform are deposition, photolithography and etching. While these techniques are suitable for the large-scale fabrication found in the microelectronics industry the need for controlled clean-room conditions, precise unique lithography masks and aggressive etchants makes them less suitable for rapid prototyping and small-scale fabrication (100's to 1000's of devices).

This PhD thesis focuses on integrated optical devices that have been fabricated by direct UV grating writing, an alternative technique that can be undertaken outside of the clean-room and which does not require photolithography. Direct UV grating writing is a relatively new method used to fabricate a wide range of integrated optical devices in a germanium-doped silica-on-silicon wafer. The technique is based on the localised refractive index increase of a photosensitive planar glass layer through exposure to a tightly focussed UV beam.

3.2 Silica-on-Silicon Platform

A planar waveguide, as discussed in the previous chapter, can be constructed by confining a sheet of high refractive index material (core) between two sheets of

lower refractive index material (cladding), such that the light is trapped by total internal reflection within the plane of the waveguide. Such a structure can be formed from the deposition of three layers of silica onto a silicon substrate (Fig. 3.). For the device to guide light within the central core it must have a higher refractive index than the surrounding cladding; this is achieved by controlled doping of the silica layers with germanium, boron or phosphorous.

The typical structure fabricated for direct UV writing contains two layers deposited onto the thermal oxide (silica) surface of the silicon wafer, where the thermal oxide is used directly as the lower cladding. The thickness of the core is typically 3-7 µm, which ensures transverse single mode operation when UV written at telecoms wavelengths. The cladding layers are typically 14 – 20 µm in thickness, to exceed the maximum penetration depth of the evanescent tail of the first-order guided mode. An exception to this is the "topless" wafer, so called because the upper cladding layer is not deposited; this leaves the evanescent tail of the guided mode propagating out of the silica surface and exposed to the environment.

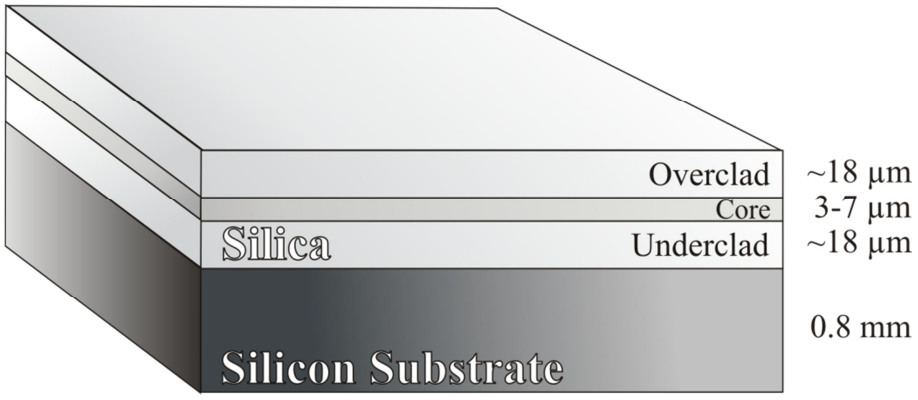

Fig. 3.1 Schematic of the silica-on-silicon substrate.

The first stage of fabrication involves the growth of a thermal oxide layer upon a standard silicon wafer that aids the adhesion of the subsequently deposited silica layers. Thermal oxide growth is achieved by a similar method to that used in the microelectronics industry, whereby the silicon wafers are heated in a furnace containing water vapour at ~1100°C. However, the oxide thicknesses required are up to a hundred times thicker than those traditionally encountered and take several weeks to grow to the desired thickness of up to 14 µm.

Upon this thermal oxide film doped silica is deposited using a derivative of the Chemical Vapour Deposition (CVD) technique, Flame hydrolysis Deposition (FHD).

The FHD process is briefly outlined below, with the relative advantages and disadvantages over Plasma Enhanced Chemical Vapour Deposition (PECVD) discussed [38, 58, 59].

3.2.1 Flame Hydrolysis Deposition, FHD

Flame Hydrolysis Deposition is a common technique used to deposit doped silica glass upon a silicon wafer. FHD is a two-step process, whereby a glass soot layer is first deposited upon the surface of the oxidised silicon wafer, followed by a subsequent heat treatment step to consolidate this soot layer to a glass [60, 61] (Figure 3.2).

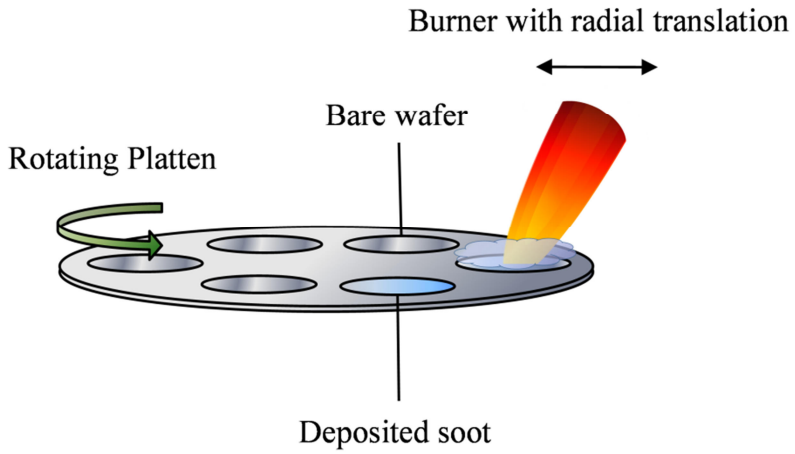

Fig. 3.2 A schematic of the deposition of FHD silica upon a silicon wafer.

The precursors for FHD are required to be halide based. The soot layer is formed by the oxidation of these halide precursors, primarily silicon tetrachloride ($SiCl_4$), within an oxygen-hydrogen flame. The direct oxidation of silicon tetrachloride occurs principally at the centre of the flame, where temperatures reach 2000 °C. However, if the temperature falls below 1200 °C hydrolysis becomes dominant. The resulting products are the solid silica soot and hydrochloric acid vapour. The direct oxidation and hydrolysis reactions of silicon tetrachloride are:

Direct Oxidation: $SiCl_4 + O_2 \rightarrow SiO_2 + 2Cl_2$

Hydrolysis: $SiCl_4 + 2H_2O \rightarrow SiO_2 + 4HCl$

Phosphorus, boron and germanium dopants can also be added to the silica by introducing the corresponding halides i.e. phosphorus oxychloride ($POCl_3$) or

phosphorous trichloride (PCl_3), boron chloride (BCl_3) and germanium chloride ($GeCl_4$) respectively, the reactions in each instance being:

Germanium: $GeCl_4 + O_2 \rightarrow GeO_2 + 2Cl_2$

Phosphorus: $2POCl_3 + 3H_2O \rightarrow P_2O_5 + 6HCl$

Boron: $4BCl_3 + 6H_2O \rightarrow 2B_2O_3 + 12HCl$

Successive silica layers are deposited onto the oxidised wafer, with different concentrations of the relevant dopants. At typical telecoms wavelengths, silica that is doped with germanium or phosphorus has an increased refractive index, whilst silica doped with boron has a decreased refractive index. By careful manipulation of the indices of the respective silica layers a planar waveguide structure is formed. Phosphorous is known to reduce the melting point of the doped silica and so the phosphorus concentration is increased with each layer, such that the concentration in the overclad layer is much greater than that of the underclad. This helps to keep the integrity of the previous layers when consolidating the subsequent soot layer. The germanium dopant has the added benefit of increasing the photosensitivity of the glass to ultraviolet light, a phenomenon exploited in the fabrication of channel waveguides within this thesis.

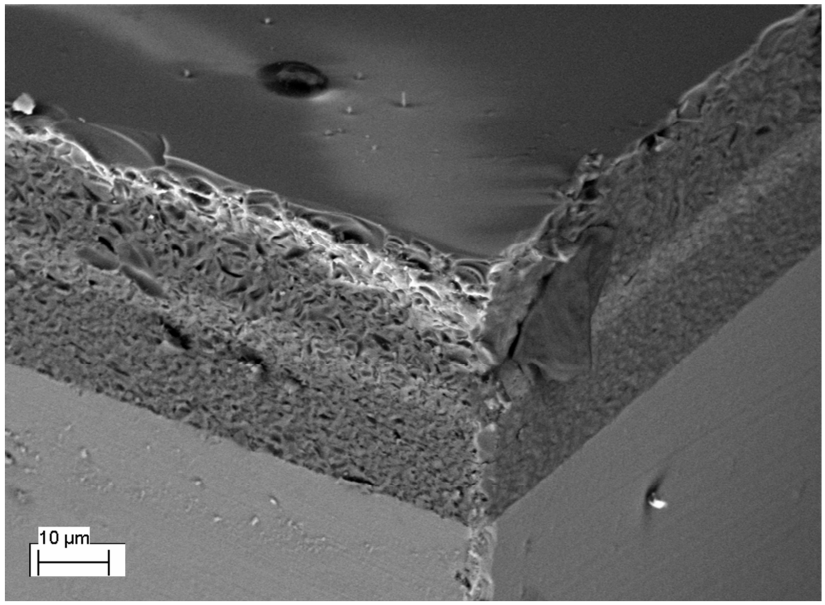

Fig. 3.3 A SEM image of the layered FHD silica-on-silicon substrate (courtesy of Dr J. Gates [62]).

The refractive index of the core layer can either be matched to that of the cladding layers ($\Delta n = 0$) or it can be raised above that of the cladding layers ($\Delta n \neq 0$). While

the latter has the advantage of prefabricating a slab waveguide within the layered silica structure, it can lead to less symmetric channel waveguides with more confined evanescent tails, making them less sensitive to external stimuli. Throughout this work both structures were used, however an index-matched core was favoured.

As a result of the fire in the Mountbatten building on 30th October 2005, the wafers used in this work were fabricated using the FHD process by a company known at the time of thesis publication as the Centre for Integrated Photonics (CIP), formerly BT Laboratories, Ipswich.

3.2.2 Plasma Enhanced Chemical Vapour Deposition, PECVD

An alternative approach to FHD is the use of plasma to assist in chemical deposition, a technique known as Plasma Enhanced Chemical Vapour Deposition (PECVD). This was used to deposit the layered silica required for the first demonstration of direct UV written planar silica-on-silicon waveguides by Svalgaard [63].

PECVD is an established process for layer deposition found in many industries including microelectronics and photonics [64]. Gaseous chemical precursors, commonly silane and nitrous oxide, are introduced into the PECVD chamber and form part of a plasma through collisions with charged particles, accelerated by an radio-frequency electric field. This reactive plasma interacts with the surface of the chamber and the silicon wafers, where energy is dissipated and absorption may occur. Despite reaching the surface of the silicon wafer, the charged particles do not become chemically bonded until a further reaction with other absorbed species on the surface occurs [38].

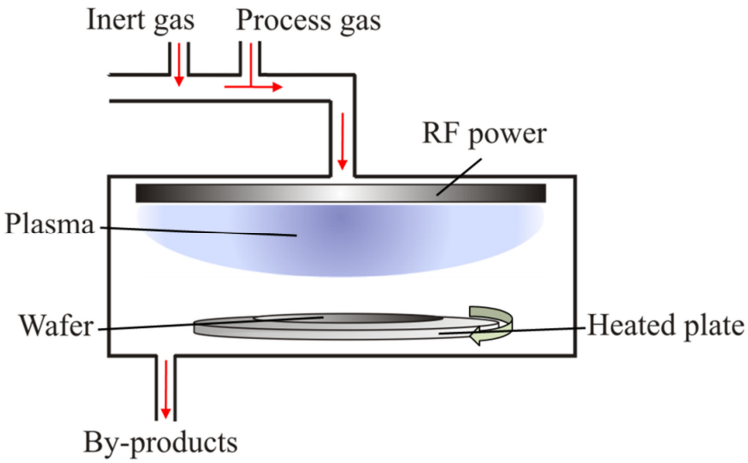

Fig. 3.4 A schematic of the PECVD process.

The deposition of PECVD silica typically results in the inclusion of free or bonded hydrogen and nitrogen within the silica lattice. This can result in the formation of -OH, -H and –NH sites within the silica that can produce high optical losses of 3-10 $dBcm^{-1}$ at telecoms wavelengths [65, 66]. These high losses can be reduced using a thermal annealing process (several hours at 1100 °C) but this negates many of the benefits of low temperature deposition achieved through PECVD. With careful process control and exclusion of nitrogen, optical losses can be reduced down to 0.2 $dBcm^{-1}$ without the need for high temperature annealing [67].

PECVD does not require that the precursor be halide-based, allowing for a much greater selection of viable dopants to be deposited than with FHD. However, this benefit is countered by the restrictions on the maximum deposition thickness of PECVD of a single run, with deposition steps of germanium-doped silica in excess of 5 µm found to result in blistering [38]. With the thickness of cladding layers required to be greater than 14 µm to exceed the maximum penetration depth of the evanescent tail of the first order guided mode, multiple deposition runs would be required to overcome blistering. This would make the technique more labour intensive and expensive than FHD.

3.3 Photosensitivity

The technique of Direct UV grating writing is based on the localised refractive index increase induced within a photosensitive planar glass layer through exposure to a tightly focussed UV beam. The photosensitive material detailed in this work is germanium-doped silica (germanosilica). Under sufficient exposure to UV light, germanosilica undergoes physical changes that result in an increase in the refractive index. The integrated optical devices fabricated for this work utilise this localised index change to write optical structures within the germanium-doped glass with a focussed UV beam.

3.3.1 Photosensitivity of germanosilica

The first observations of a photoinduced refractive index change in germanosilica were reported by Hill and co-workers in 1978 [68, 69]. 488 nm light from an argon ion laser was launched into narrow core optical fibres heavily doped with germanium. They observed that over a one metre length of fibre, the launched laser light would gradually become reflected, with the loss of transmitted light occurring over minute

timescales. This phenomenon was the result of the establishment of a standing wave along the core of the fibre. The points of high intensity along the fibre photoinduced a periodic refractive index change of 10^{-6} in the germanosilica, forming a Bragg grating structure. This structure was self-enhancing, leading to the 100 % Bragg reflection observed.

Bragg grating structures have become commonly used for telecommunication and sensing applications. However, as the Bragg wavelength of Hill's device reflected limited wavelengths outside the telecoms window, it had limited applications. Furthermore, the strength of the index modulation was relatively weak, requiring long grating lengths to achieve sufficient reflected power, making them impractical for localised sensing.

Investigations into the photosensitivity of germanosilica by Lam and Garside [70] revealed that the magnitude of the photoinduced refractive index change depended upon the square of the power of the source. From this, it was deduced that a two-photon process was occurring; meaning that 244 nm wavelength light can be used to induce a strong refractive index change.

Photosensitivity is described as being quasi-permanent as although the lifetime is long, annealing at temperatures below that required to reflow glass can remove the induced index change. Typical annealing conditions to achieve erasure are 800ºC for 30 minutes.

It is understood that the exposure of germanosilica to UV light results in the bleaching of absorption defects [71]. It was discovered by Meltz [72] that exposure to UV light in the region 240 – 250 nm directly results in index changes [73]. These wavelengths correspond to photon energies that match an absorption peak associated with germanium defects within the silica lattice. Direct stimulation of germanosilica with such wavelengths can improve the induced refractive index change by three orders of magnitude (~10^{-3}).

3.3.2 Defects in germanosilica

Defects are present in both pure amorphous silica and doped silica, such as germanosilica. The idealised structure of pure silica is tetrahedral, with each silicon atom linked to four further silicon atoms by oxygen bridges (Figure 3.5). However

within this structure defects can occur during fabrication. Oxygen deficiency is one such cause of these defects. Defects that result from this oxygen deficiency are labelled Oxygen Deficient Centres (ODC). A specific ODC is the Neutral Oxygen Vacancy (NOV), where two silicon atoms are bound directly without an oxygen bridge, as illustrated in Figure 3.5.

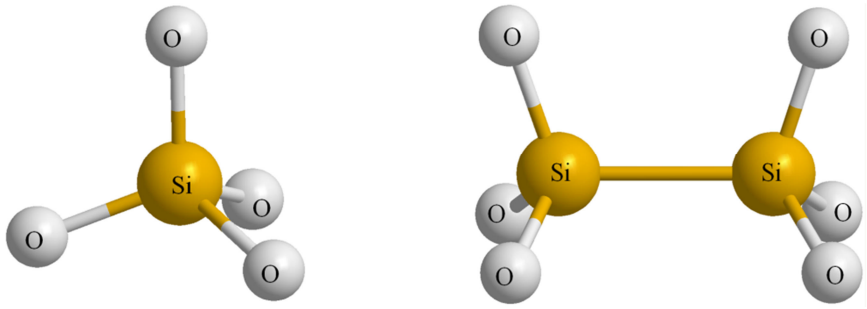

Fig. 3.5 The tetrahedral structure of amorphous silica (left) and a neutral oxygen vacancy defect within a silica lattice (right).

Germanium has the same valency as silicon, allowing for germanium substitution within the silica lattice without significant disruption to the structure. Germanium within the lattice can exist in two main forms; a Ge(1) centre corresponds to a germanium atom bound through oxygen to four silicon atoms or a Ge(2) centre, corresponding to a germanium atom bound through oxygen to three silicon atoms and one germanium. The presence of germanium in the lattice results in germanosilica forming a further two types of NOV defects, corresponding to silicon-germanium and germanium-germanium direct bonding (absorption at 245 nm). In addition to NOV defects, germanium can also form the Ge^{2+} defect in germanosilica, a bi-valent species (absorption at 241 nm). These germanium specific defects are illustrated in Figure 3.6, below:

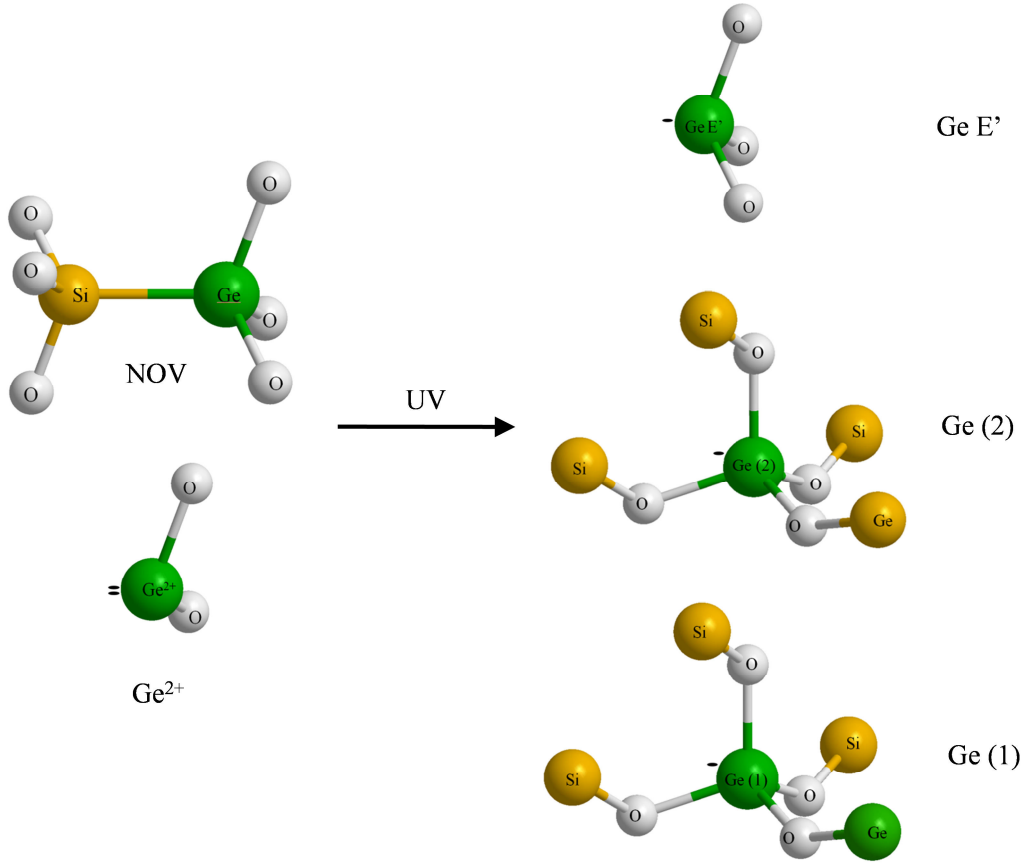

Fig. 3.6 Common point defects of germanosilica thought to be responsible for photosensitivity. ODCs (left) which are believed to absorb around 244nm and produce the GeE' defect and liberate electrons which are captured to form Ge(1) and Ge(2) sites (right).

Both NOV and Ge^{2+} defects demonstrate absorptions between 240-245 nm [72] and are understood to contribute to the photosensitivity of germanosilica glass. Photosensitivity theories suggest that the exposure of germanosilica to UV light at these wavelengths changes the concentration of ODCs within the lattice. Exposure to UV excites electrons; for the case of the NOV defect the excitation of the Si-Ge bonding electron and subsequent release breaks the direct bond creating a GeE' centre. The released electron then may either recombine immediately with the GeE' centre, to give recombination luminance or it may diffuse through the lattice. The electron may eventually become trapped at a Ge(1) or Ge(2) centre to form $Ge(1)^-$ and $Ge(2)^-$ defects respectively (Figure 3.6).

The change from the diamagnetic (where all electrons spins are paired) ODC defects to paramagnetic defects (where unpaired electrons exist) is widely thought to be responsible for the observed photoinduced change in refractive index. However, conversion of ODCs to the paramagnetic defects is predicted, using the Kramers-Kronig relation to be responsible for refractive index changes around an order of

magnitude less than is observed in experimentally achieved results. It is therefore apparent that this simple defect model does not represent the full complexity of photosensitivity [74-76]. Possible explanations proposed have included additional thermal effects and stress modification [77-79]. Densification is a thermally driven process that also results in a refractive index change. This phenomenon arises as a result of absorption in the silica lattice being converted into thermal energy. At high power densities this will result in local heating sufficient to sinter, melt or even ablate the germanosilica.

3.3.3 Hydrogenation

A further development was made by Lemaire in 1993 [80], whereby high pressure was used to diffuse a high concentration of hydrogen into the silica substrate, which on exposure to ultraviolet light led to a significant permanent index change in germanium-doped optical fibre. In this work it was shown that the change in refractive index of germanosilica glass was enhanced by an order of magnitude ($\Delta n = 10^{-2}$) through loading the samples with hydrogen gas at high pressures (~120 bar). There is a limit to the concentration of germanium that can be present within the silica lattice before excessive loss is introduced into the device. The advantage of this technique over further doping is that after exposure the hydrogen out-diffuses, restoring the glass to its prior state.

This enhancement to the photosensitivity through hydrogenation is believed to occur through two mechanisms. The first is a result of hydrogen interacting with GeO_2 sites within the lattice. The proposed reaction occurs through thermal or photovoltaic triggering resulting in the breaking of a germanium-oxygen bond forming Si-OH and an ODC. The second mechanism for enhancement is believed to be a result of the hydrogen acting as a photobleaching catalyst.

The increase of hydroxide bonds formed at defects within the glass increases absorption in the telecoms window, increasing the optical loss of the material [81, 82]. This disadvantage can be overcome by alternatively diffusing deuterium gas into the sample. Like hydrogen, deuterium enhances the induced index change of the germanosilica glass. However, the interaction on exposure to UV results in the formation of -OD bonds instead of -OH bonds. As the mass of deuterium is greater than hydrogen the resonant frequency of the -OD bonds is lower than for -OH bonds,

this shifts absorption to higher wavelengths, such that between 1300-1600 nm there are no absorption peaks [82].

Prior to direct UV writing the germanium-doped silica wafers in this work were hydrogenated for a minimum of 5 days at 120 bar. Hydrogen was selected over deuterium as the reduction in absorption did not justify the increase in cost over the short propagation lengths used (typical samples were 20-40 mm in length, resulting in a maximum transmitted path length of 80 mm). Photosensitivity in the hydrogenated FHD wafers used in this work was observed to induce a refractive index change of 5 x 10^{-3} to 2 x 10^{-2} [37]. This resulted in the ability to directly UV write weakly-guiding waveguides and Bragg gratings.

3.3.4 Hydrogen out-diffusion

While hydrogen will readily diffuse into silica, it will also as readily out-diffuse at room temperature and pressure, reducing the enhancement to the photosensitivity over time (with notable changes to the photosensitivity for timescales greater than thirty minutes). The rate of hydrogen out-diffusion can be reduced by lowering the thermal energy of the system.

Diffusivity, also referred to as the diffusion coefficient, is defined as the rate at which diffusing substances traverse between opposite faces of a unit cube with unit concentration difference between them, expressed in Equation 3.1:

$$D = D_0 \, e^{\left(-\frac{E}{RT}\right)} \tag{3.1}$$

where D_0 is a pre-exponential factor, E is the diffusion activation energy, values for which can be obtained experimentally (~40 kJmol^{-1} [81]), R is the gas constant (8.3 JK^{-1}mol^{-1}) and T is the absolute temperature. From the literature [83] it is known that the 1/e decay time, τ_{UV} can be expressed as:

$$\tau_{UV} = -\ln(\alpha)\, \tau_0 \, e^{\frac{E}{R}\left[\frac{1}{T} - \frac{1}{T_0}\right]} \tag{3.2}$$

where α is the concentration of hydrogen and τ_0 is the decay time at temperature T_0. This can be interpreted graphically through extrapolating accepted values [83] for silica-on-silicon wafers, as shown in Figure 3.7 below:

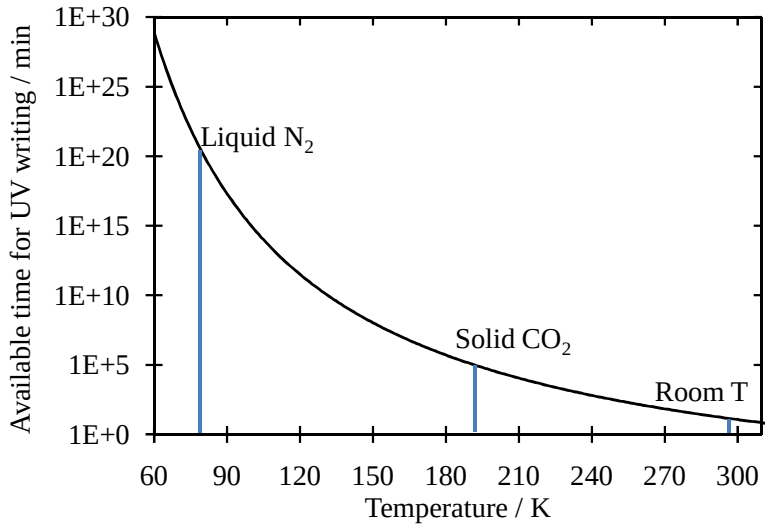

Fig. 3.7 The temperature dependency of available time for UV writing (1/e decay time, extrapolated from data obtained by Svalgaard [83]).

As indicated in Figure 3.7, out-diffusion can be overcome by transporting and storing hydrogenated samples in liquid nitrogen (77 K) or dry ice (194 K) until the sample is used. At these reduced temperatures the direct UV writing time increases from ~30 minutes at room temperature to days. In this way the sample is only warmed to room temperature during the writing process, with out-diffusion effects minimal under typical direct UV writing durations.

For more complex integrated optical circuits or samples written at high fluence (see Section 3.4 for a definition of fluence) temperature reduction during both the transportation and direct UV writing steps is desirable. One method of temperature reduction that has been demonstrated during UV writing was the use of a cold chuck [37]. This system kept the samples at -33 °C during writing and overcame issues of ice formation and condensation, increasing writing time from ~15 minutes to over 10 hours.

Out-diffusion can be controlled by locking the hydrogen in the germanosilica structure through heating to high temperature [84, 85]. There are two ways of achieving this, either through thermal hypersensitisation or high temperature flashing. Thermal hypersensitisation occurs for temperatures of the order of 400 °C [85], high temperature flashing, also known as OH-flooding [84, 86], occurs for temperatures of the order of 1100 °C. However, high temperature flashing can result in a significant increase in optical loss at 1400 nm wavelengths. This increase in associated loss is a

result of the formation of additional hydroxyl species in the germanosilica that have an absorption peak near 1380 nm [86].

Hypersensitisation can also be achieved through UV exposure (355 nm), achievable through the use of a laser or standard UV sterilisation lamps [87, 88].

For the work presented here, the simple nature of the optical circuits fabricated resulted in direct UV writing times of less than thirty minutes. For these devices it was found that storage and transportation in liquid nitrogen was sufficient to prevent significant out-diffusion without the need for further treatment.

3.4 The Direct UV Writing Process

Direct UV writing takes full advantage of the photosensitivity of germanosilica to fabricate integrated optical circuits. Although the direct writing technique was used as early as 1974 to produce single mode waveguides in polymer layers [89], the technique was predominantly developed by Svalgaard [90] and is now an established methodology to fabricate a wide range of integrated optical circuits in silica-on-silicon wafers [91, 92].

The technique is based on the highly localised refractive index increase of the photosensitive planar glass layer when exposed to a tightly focussed laser beam. As discussed previously, a three layer silica-on-silicon wafer is used, with the central core doped with germanium. If the UV laser is focussed into this photosensitive core layer there is a local refractive index change. Translation of the sample relative to this beam with a set of high precision translation stages allows two-dimensional refractive index structures to be defined into the germanosilica. This technique does not require photolithographic or subsequent processing under clean-room conditions (Figure 3.8).

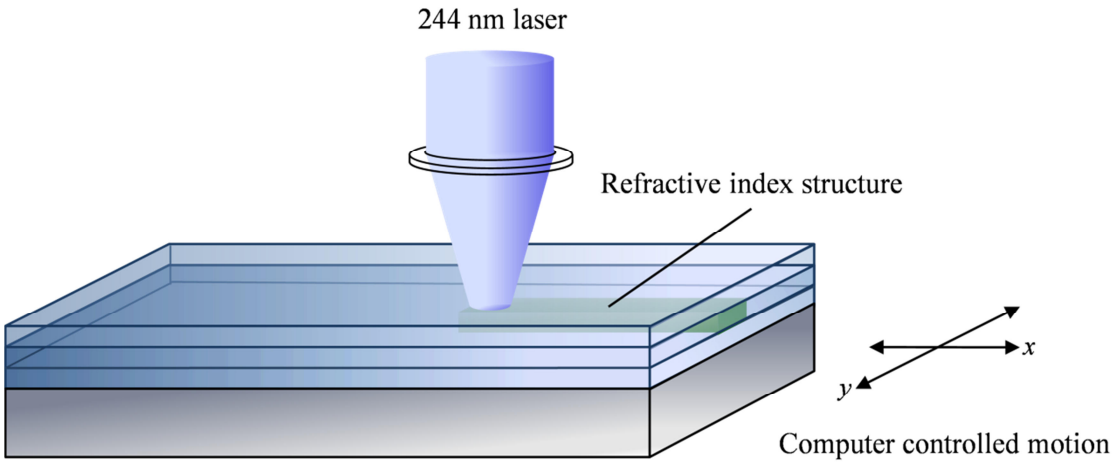

Fig. 3.8 UV writing into the core layer of a silica-on-silicon wafer.

In Svalgaard's early work [63] 514.5 nm wavelength radiation from an Argon-ion (Ar^+) laser was frequency doubled to produce 257.25 nm radiation. Whilst the 514.5 nm line has the highest output power from the Ar^+ laser, the 488.0 nm line can be frequency doubled to a wavelength within the germanosilica absorption bands, corresponding to a strong refractive index change. The optical circuits detailed in this thesis were written using frequency doubled 488.0 nm from an Argon-ion laser to produce 244.0 nm UV-radiation.

The refractive index contrast of these UV written structures have been demonstrated to be as high as 2 x 10^{-2}, but are more commonly in the order of 5 x 10^{-3}or lower. The refractive index change photoinduced into the germanosilica depends upon the total number of incident photons on a point during the UV writing process. The number of incident photons will be dependent not only on the power and focus of the laser beam, but also the translation speed. To quantify and regulate the degree of exposure, the concept of fluence, F is used; this is defined in Equation 3.3:

$$F = \frac{I_{UV}\, d}{v} \qquad (3.3)$$

Fluence, F (kJ cm^{-2}) is a measure of the energy delivered to the sample and is dependent on the UV power and the translation speed, v (cm s^{-1}). UV power is represented by the multiplication of the average power density of the writing spot, I_{UV} (kW cm^{-2}) and the spot diameter, d (cm, with the typical 1/e width of the spot ~7 µm).

As a technique, direct UV writing provides a straight forward route towards rapid prototyping of optical channel waveguides. Once suitable three layer substrates are available, all layout work is carried out in software before the UV exposure is performed. Furthermore as the core layer is protected by cladding layers clean-room conditions are not required during the writing process.

Complex or large devices can require long fabrication times, as each waveguide segment must be written one after the other rather than in the 'parallel' fashion allowed by photolithography. The minimum feature size that may be defined by direct UV writing is determined by the focus spot size and the resolution and accuracy of the translation stages. In a very general sense UV writing is well suited to the production of small to medium volumes where rapid development, design flexibility and low initial investment (i.e. no photolithographic masks) are a priority. For medium to volume production, the ability to simultaneously fabricate multiple devices with high repeatability makes photolithographic methods more appealing.

3.5 Competing Techniques to Direct UV Writing

Direct UV writing is a relatively new technique [63] for defining integrated optical circuits, competing directly against established technologies such as photolithography and etching. For completeness a brief overview of these techniques and their merits and weaknesses compared to direct UV writing are included in the following section.

Direct UV writing is not the only direct writing technique. In recent years there has been an increased interest in femtosecond (fs) lasers to directly write both waveguides and gratings in bulk transparent materials, including fused silica glass.

3.5.1 Photolithography and etching

Photolithography, also referred to as optical lithography, is a technique that has been used for many years in the microelectronics industry. However, it has recently crossed over into the photonics industry for the fabrication of integrated optical circuits [3].

To fabricate integrated optical circuits, first a higher index silica layer (typically germanosilica) is deposited onto a thermal oxide-coated silicon wafer (Step 1). A photoresist (a photoresponsive polymer that cross-links under UV illumination, such

as the commercial epoxy-based photoresist "SU-8" [93]) is then spun onto the surface of the device. This is selectively exposed to UV light through a mask, to transfer the desired circuit design onto the surface. The unexposed photoresist is then washed away to leave the desired design (Step 2). The developed photolithographic design is then etched using a wet/dry etch technique to define the circuit structure (Step 3). An additional CVD run is usually applied to add a relatively low refractive index cladding layer to protect the circuit and shield it from external stimuli (Step 4) [55].

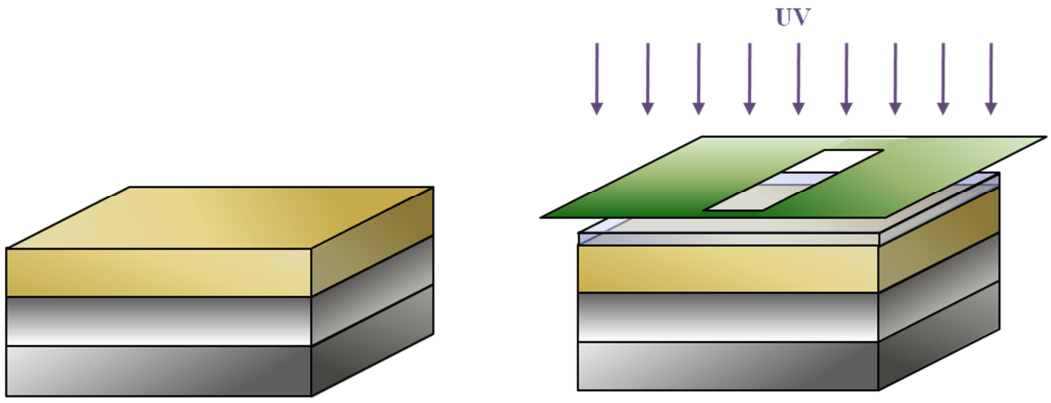

STEP 1:

Thermal oxide growth and PECVD/FHD layer deposited.

STEP 2:

Photoresist spun onto silica, mask aligned and sample UV exposed.

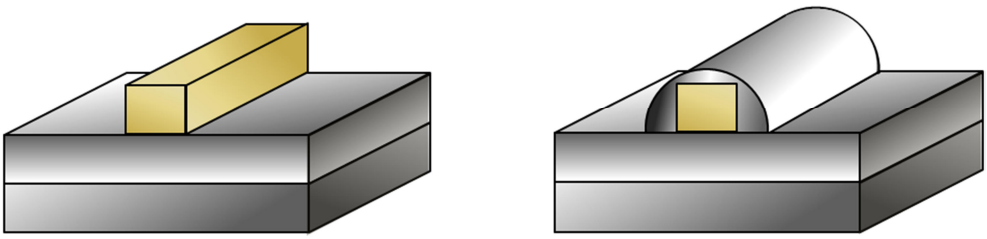

STEP 3:

Photoresist developed and device etched.

STEP 4:

Overclad deposition using PECVD or FHD.

Fig. 3.9 The photolithography and etching technique for optical circuit fabrication [55].

The advantage of photolithography is that it is a cost efficient means for mass production, with the ability to fabricate multiple devices in parallel. However, when considering small device numbers (i.e. for rapid prototyping and small scale fabrication of 100's to 1000's of devices) the cost of the technique becomes prohibitively time consuming and expensive, with alterations in the unique photoresist mask requiring a new mask to be designed and fabricated. Furthermore the resolution of the structures produced is limited by the quality of the mask

manufacture and the UV exposure. Current capabilities allow rectangular cross section waveguides of the order of a few hundred nanometres to be defined and etched [94]. While for direct UV written devices germanium doping is important to introduce photosensitivity, the primary reason for doping the core layer with germanium in this technique is to raise the refractive index over that of the surrounding cladding layers.

3.5.2 Direct femtosecond writing

The first demonstration of direct femtosecond writing was made by Davis in 1996 [95]. Femtosecond writing operates by focusing a near-infrared femtosecond laser into a glass substrate. The high energy density at the focus causes localised densification, leading to a positive change in the refractive index as large as 0.035. Waveguides can be fabricated by translating the sample relative to the laser beam with Bragg gratings fabricated by actively modulating the exposure [96].

The femtosecond writing technique is similar in principle to that used in direct UV writing, in terms of focusing a laser into a material to induce a refractive index change. However, the physical writing process does not rely on photosensitivity but nonlinear effects within the material. This allows femtosecond writing to write three-dimensional circuits, thus, in many different bulk materials it has an advantage over two-dimensional UV writing [97]. The disadvantage of femtosecond writing in relation to UV writing is that the laser system required for fabrication is much more expensive and temperamental in terms of stability. In addition, as the field is still relatively new there are several issues that are still to be addressed, including the slow rate of writing and the propagation loss of the resulting waveguide.

3.6 Direct UV Grating Writing

The direct UV grating writing (DGW) technique is a derivative of the Direct UV writing process, developed at the Optoelectronics Research Centre. The method has the added flexibility of simultaneous waveguide and Bragg grating definition [98]. Direct UV grating writing in this way allows the production of a broad range of optical devices based around combinations of customisable Bragg gratings and channel waveguides.

3.6.1 Direct UV grating writing

Direct UV grating writing (DGW) is an established technique for defining both channel waveguides and Bragg gratings [98]. The technique is achieved through splitting the single UV laser beam into two interfering beams to give an inherent interference pattern, illustrated in Figure 3.10. The advantages of this direct UV grating writing technique over other methods of introducing Bragg gratings is that the grating is not overwritten on top of a pre-existing channel (as is often the case for fibre Bragg gratings [72]) and by controlling the laser modulation, different period gratings can be fabricated without the need for altering the alignment of the system.

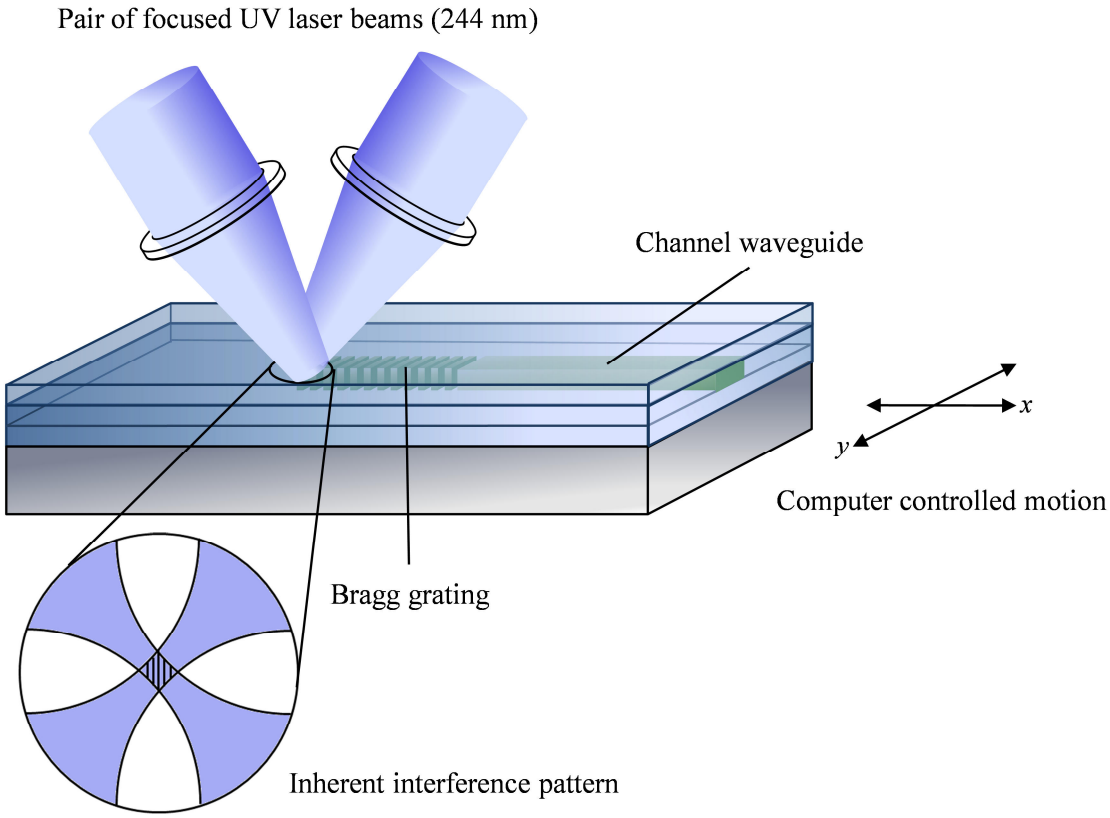

Fig. 3.10 A schematic of the direct UV grating writing of a channel waveguide containing a Bragg grating into germanium doped silica-on-silicon substrate.

The focussed, coherent beams produce an interference pattern, with a period defined by the angle between the two beams (Figure 3.10). Using precision air-bearing stages to translate the wafer under the focussed beams, it photosensitises the underlying core layer analogously to the single beam in Direct UV writing (Section 3.4), resulting in the fabrication of channel waveguides. However, by modulating the writing beam during sample translation such that the inherent interference pattern

stamps periodically upon itself, the fabrication of Bragg gratings can also be achieved.

Controlled modulation of this interference pattern allows for both the grating and the channel structure to be formed simultaneously using the same photosensitive material response. As the grating and channel structure result from the same index change mechanism, the contrast of the grating can be controlled without affecting the strength of the waveguide. This grating writing technique is highly flexible allowing for a wide range of grating periods and profiles to be written with the same setup system that is ideal for rapid prototyping of devices [99].

To write Bragg gratings in the telecoms C band, 1530-1565 nm, the angle of the two beams must be aligned to match the periodicity required. Considering the effective index of the guided mode in a UV written waveguide to be ~1.445, an intrinsic period of ~540 nm is required (as dictated by the Bragg condition; Equation 3.4). The crossing angle between the two beams, θ, required to achieve this period, Λ, can then be calculated [58]:

$$\lambda = 2\, n_{eff}\, \Lambda \tag{3.4}$$

$$\theta = 2\, arcsin\left(\frac{\lambda_{UV}}{2\Lambda}\right) \tag{3.5}$$

where λ_{UV} is the wavelength of the UV laser. For an intersecting angle of 26° an intrinsic period of 542 nm is established, corresponding to a Bragg reflected wavelength of 1566 nm. The system focuses the dual beams to a spot of diameter ~4 µm, using a pair of identical lenses of numerical aperture (NA) 0.18 and focal length 40 mm. The focussed beam contains approximately 7 periods.

The concept is similar to the side exposure with dual UV beam technique used in fibre Bragg grating fabrication [72], although this technique uses a much smaller spot than the ~100 µm diameter spot size used for fibre. The smaller spot size limits the channel waveguides to a single guided mode and allows for greater control when engineering a Bragg grating structure.

The free space optical set-up for the direct UV grating writing system is illustrated in Figure 3.11. It consists of a frequency doubled argon-ion laser emitting typically 80 mW of continuous wave 244 nm UV light. After leaving the laser head, the output

beam is directed into an Acousto-Optic Modulator (AOM) that amplitude modulates the beam. After this arrangement the power of the laser has reduced to approximately 40-50 mW. The beam is then sent through a series of mirrors to above the translation stages, where it passes through a beam splitter to produce two identical beams. These are then focussed (using a pin hole for alignment) onto a point on the surface to produce the interference pattern.

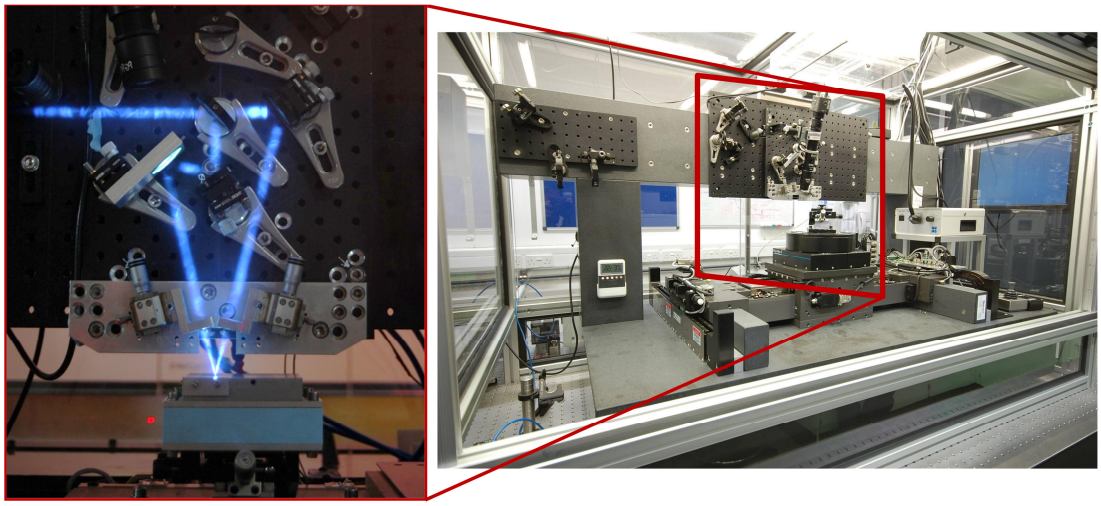

Fig. 3.11 A photograph of the dual beam direct UV grating writing into a photosensitive layer showing the beam path, left; and the full system illustrating the high precision 4-axis stages, right (courtesy of Dr J. Gates [62]).

To write the Bragg grating structure into the photosensitive core, a high level of positional accuracy is required. This is achieved through computer-controlled air-bearing translation stages, with ~10 nm of positional accuracy. The positional translation is controlled by G-code, a standard CNC (computer numerically controlled) software tool allowing for full automation of the writing process. A typical fluence of 20 $kJcm^{-2}$ (relating to a translation speed of 0.2 mm/min) has been used in this thesis to write Bragg grating optical circuits. The AOM is necessary to modulate the intensity of the laser beam, which when coupled with the translation of the sample, imprints the Bragg gratings.

So far it has been described that imprinting a Bragg grating, of a particular period, can be achieved through using a specific crossing angle between the two UV beams. This would imply that to write multiple gratings at multiple wavelengths this angle would have to be adjusted for each grating, much like changing the mask in photolithography. However the direct UV writing system can overcome this limitation and access a variety of grating periods around the intrinsic period without

altering the angle of the cross beams. This allows for Bragg gratings to be written with different periods along a single waveguide in a single process. This is achieved through detuning the imprinted interference pattern.

Detuning operates by introducing an additional displacement, Δ added to or subtracted from the inherent period of the interference pattern, Λ, giving a Bragg grating period of $\Lambda \pm \Delta$. There is a limit to how far the period can be shifted, as the greater the intrinsic interference pattern is detuned, the weaker the reflectivity of the grating becomes. However, using this detuning technique around a single crossing angle (~26 °) the telecommunication E, S, C, L, and U bands have all been accessed [100]. The result of this is a spectral window spanning from wavelengths of 1400 nm up to 1700 nm.

The variables that can be manipulated across the length of a grating include duty cycle, pitch and refractive index. The deviation of these variables across a grating's length affects its spectral response. Changes in these variables may also be the result of an external response, i.e. chemical or physical exposure or be engineered into the grating.

3.6.2 Duty cycle

When light moves from a medium of a given refractive index n_1 into a second medium with refractive index n_2, both reflection and refraction of the light may occur. By considering the average refractive index of the Bragg grating and the channel waveguide as two distinct media meeting at an interface; the greater the refractive index contrast at this interface, the greater the degree of unwanted reflected light (as described by Fresnel reflection), leading to increased optical loss.

Impedance (index) matching a Bragg grating to the waveguide leading up to it, such that the average index across the interface is the same significantly improves the reflected Bragg spectrum. In terms of Bragg grating fabrication, the duty cycle is the fraction of the distance of a single period for which the laser is on (Figure 3.12). By adapting the fluence such that the duty cycle is taken into consideration, the channel and grating can be successfully index matched.

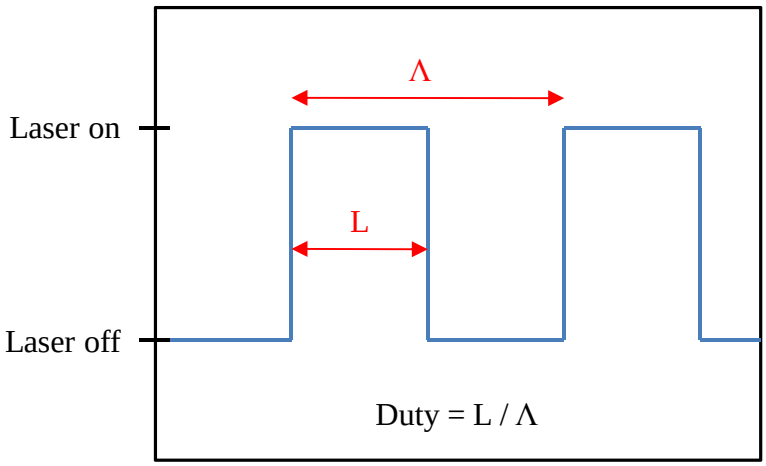

Fig. 3.12 The duty cycle of the laser.

A duty cycle of one corresponds to the laser being continuously on, resulting in a channel waveguide being written. Correspondingly a duty cycle of zero results in no index structure being written into the germanosilica.

For impedance matching to occur, the lower the duty cycle the higher the index contrast must be [58]. However, this higher index contrast requires a higher fluence and with laser power a constant, by Equation 3.3, the structure must take longer to write. This has the associated issue of the hydrogen out-diffusing, reducing the index contrast achievable in the photosensitive layer.

There is a maximum achievable index change limited by the photosensitivity of the core layer and as such an optimum duty cycle exists for the highest reflected power. Previous investigations into this suggest optimum duty cycle of 0.35 [58]. However, it is understood that this value is very much dependent upon the wafer used and the fluence at which the waveguides are written. The duty cycle for Bragg gratings in this work was set at 0.5 for fluences of 20 $kJcm^{-2}$.

3.6.3 Grating engineering

As discussed previously, the spectral response of a Bragg grating can be approximated by the Fourier Transform of its physical shape. Uniform Bragg gratings have a physical shape that can be approximated by a ‘top-hat’ function, with the expected spectral response approximating to a ‘sinc’ function. The spectral side lobes associated with uniform Bragg gratings can become problematic, especially for gratings that are close spectrally, complicating the extraction of a grating’s individual spectral information.

Apodisation suppresses the spectral side lobes of the uniform grating spectrum. There are different types of apodisation [52], but the work presented here focuses on Gaussian apodisation. The Fourier Transform of a Gaussian function is expected to have an approximately Gaussian response. Therefore, a grating written with the physical structure of a Gaussian is expected to have an approximately Gaussian spectral response, as observed in Figure 3.13.

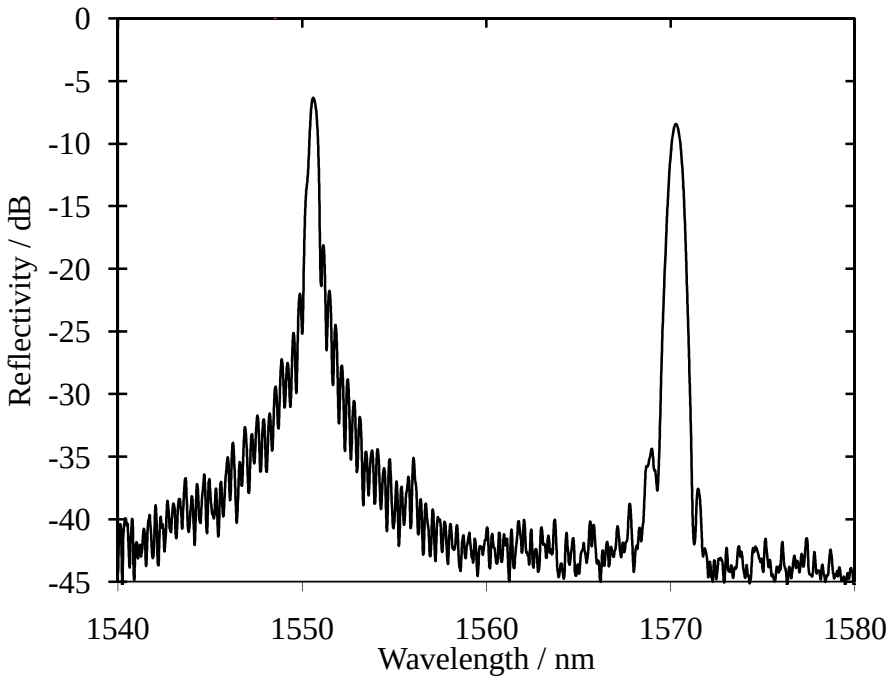

Fig. 3.13 The experimental reflection spectrum of a uniform Bragg grating (centred at 1550 nm) and a Gaussian apodised Bragg grating (centred at 1570 nm).

Over each consecutive period the average refractive index of a Gaussian apodised grating must remain constant; otherwise unwanted spectral fringes can arise as a result of Fabry-Perot resonances, whereby light becomes trapped in an optical cavity formed between peripheral sections [52, 101]. To achieve period-averaged refractive index for a Gaussian-apodised Bragg grating, both the duty cycle and the induced index change are given a Gaussian profile, demonstrated in Figure 3.14.

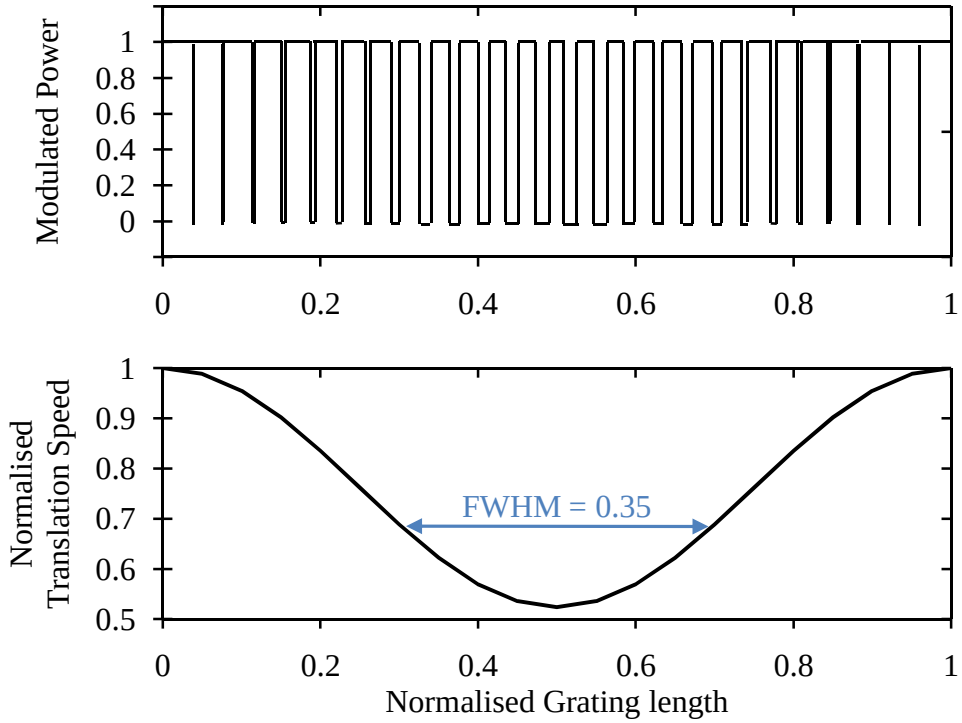

Fig. 3.14 The fluence variation used to achieve a constant period averaged refractive index.

For the grating response to be truly Gaussian, the grating would need to be infinite in length. Limiting the physical Gaussian grating structure does result in spectral cropping of the Gaussian form, with the deviation from an idealised Gaussian increasing as the structure is shortened. It was observed experimentally that a Gaussian-apodised grating with a FWHM set to 35 % of the grating's length gave significant side-lobe suppression, for typical grating lengths written, without compromising grating strength or introducing spectral ringing [101].

Grating engineering is not limited to modifying the apodisation of a Bragg grating, other more complex grating structures can also be written (Chapter 2.4.2), including chirped Bragg gratings and phase-shifted gratings, as shown in Figure 3.15:

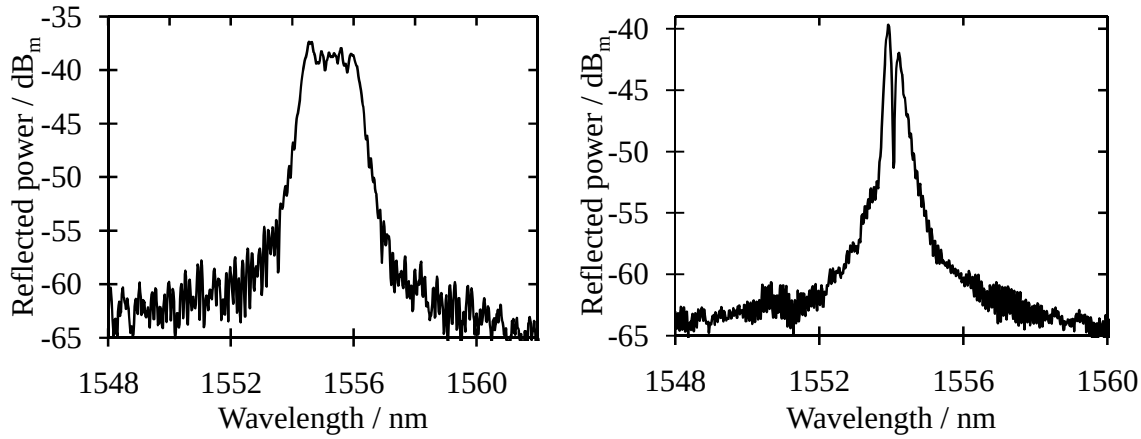

Fig. 3.15 The spectral response of a linearly chirped Bragg grating (left) and a phase-shifted Bragg grating (right).

3.7 Device Characterisation and Packaging

Once an optical circuit has been UV written, the integrity of the waveguides and the spectral response of the written Bragg gratings are characterised. This process tests if the device has been successfully written and is used to calibrate grating properties such as reflectivity, birefringence and effective index before undertaking any post-writing fabrication steps, such as etching or deposition.

The in-diffused hydrogen will begin to diffuse out from the moment the sample is removed from the hydrogen loading chamber and by the time it has been UV written and characterised, typically 3 hours later, the hydrogen is depleted. Negligible differences have been observed for samples characterised 3 hours after writing and several weeks after writing. Therefore, no annealing stage has been applied to the fabricated devices post direct UV writing.

Characterisation is achieved by aligning an optical fibre linked to an interrogation system to the direct UV written waveguide. A fibre coupled helium-neon (HeNe) laser source (~633 nm wavelength) is first used to align the respective waveguides via a single-mode optical fibre. This is achieved by visual inspection of the transmitted red light, and the alignment adjusted via a 3-axis stage until the guided mode is observed. The light source is then switched to an amplified stimulated emission (ASE) broadband infrared source and launched down the same fibre into the UV written waveguide. Depending upon the Bragg condition of the grating, the light is either coupled back into the launch fibre through reflection or transmitted and can then be coupled out through an additional optical fibre. The alignment is further

refined through focusing the transmitted broadband light (1400 – 1600 nm) through a lens to image the end facet upon a CCD camera. To couple the transmitted light out of the device, a similar process is used on the output side of the planar waveguide.

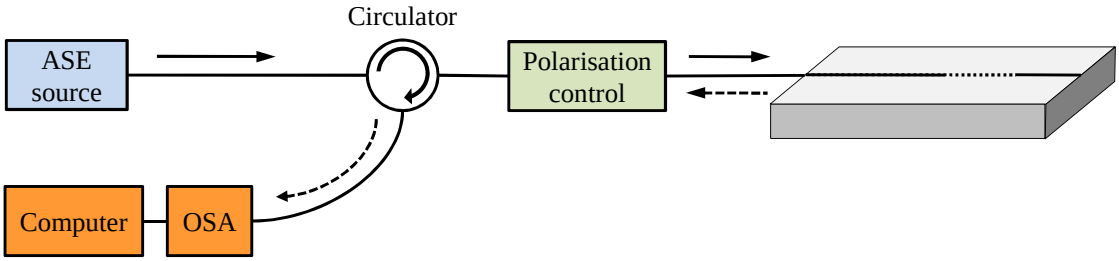

Fig. 3.16 A schematic of the optical interrogation system.

After alignment the reflection and transmission spectra can be measured using an optical interrogation system similar to that depicted in Figure 3.16. A circulator or coupler delivers the broadband light reflected from the optical waveguide circuit to an Optical Spectrum Analyser (OSA), where the reflected Bragg spectrum can be analysed. At this point fine tuning of the alignment takes place to maximise the signal-to-noise ratio of the Bragg response. Spectral data were collected from the OSA and transferred to a computer running Labview software via a GPIB (General Purpose Interface Bus) connection. The Labview data interpretation algorithm (originally written by J. C. Gates [62]) fitted a Gaussian profile (Equation 3.6) to the reflected spectrum using a least squares method. Understanding the form of the Bragg grating, the central Bragg wavelength (*c*), bandwidth (*d*), amplitude (*b*) and background intensity (*a*) could be inferred.

$$\mathrm{P} = a + b \exp\left[-\left(\frac{\lambda - c}{d}\right)^2\right] \qquad (3.6)$$

where P is the reflected power and λ is the wavelength.

This demonstrates the need for a good Gaussian profile from the UV written Bragg grating. If the spectral response is not a true Gaussian, the algorithm will not be able to achieve a good fit and this in turn will lead to worse resolution of the grating parameters, including the central Bragg wavelength used to determine changes in refractive index in sensors. Poor spectral response or a weak reflection from a grating leads to increased noise with the potential for the Bragg wavelength to jump dramatically as spectral fringes move across the Bragg peak.

For long term interrogation, the optical fibre can be replaced with an optical fibre pigtail. A pigtail consists of an optical fibre with one facet mounted into a silicon V-groove while the other is fitted with a fibre connector. This can then be permanently attached to the UV written device using an optical grade UV-curing epoxy. The resulting packaged device is sufficiently robust to withstand larger temperature differentials, mild solvent exposure and prolonged constant use.

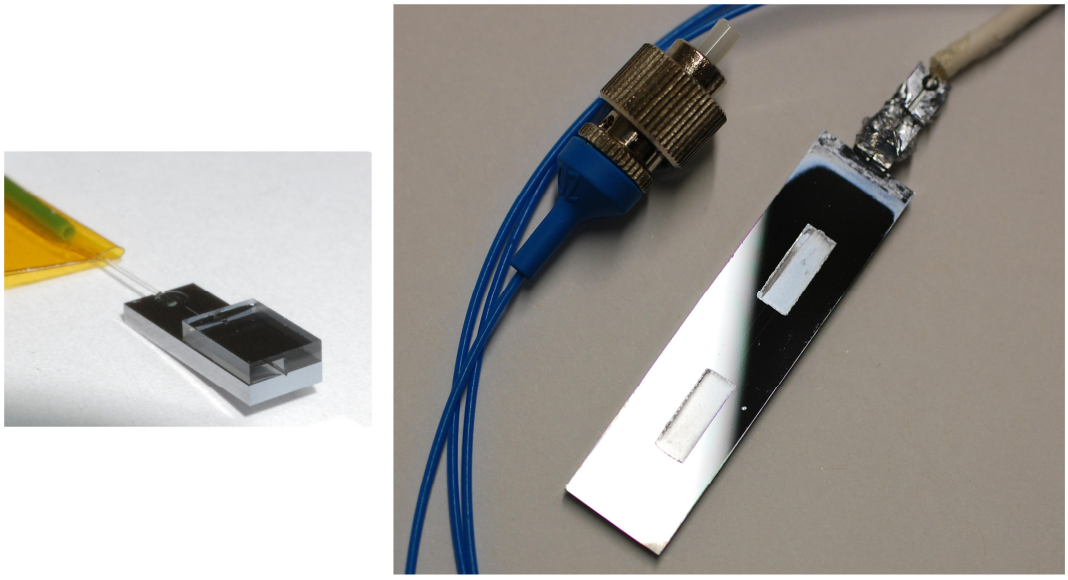

Fig. 3.17 The optical fibre pigtail, mounted within a silicon V-groove (left) and the pigtailed integrated optical device with two etched sensor regions (right).

The asymmetry that arises in the channel waveguide from the differing refractive index profile along the plane and across the FHD layers leads to birefringence between the orthogonally polarised Transverse Electric (TE) and Transverse Magnetic (TM) modes. When characterising a reflected Bragg spectrum it is important to distinguish between TE and TM modes as these modes can exhibit differential responses to analysis. There are two main methodologies to separate and individually interrogate these two modes, as discussed below.

To selectively choose a particular polarisation, the input light itself must firstly be polarised (for an unpolarised source this can be achieved through the use of a fibre polariser). The polarisation state launched into the device can then be controlled through using a standard single mode fibre (SMF) and a polarisation controller. The polarisation within the device can be monitored by focusing the transmitted light from the device's end face through a free space polariser and upon a CCD camera. The polarisation controller can then be adjusted to selectively minimise the imaged

light to align the output to a particular polarisation. However as the polarisation is wavelength dependent, it is only possible to ensure the polarisation at the wavelength of the output polariser is correct.

Alternatively, polarisation maintaining (PM) components can select distinctive polarisations launched into a planar waveguide. Similarly to above, a PM polariser can be introduced into the system (Figure 3.16) with a low return loss of > 60 dB. A PM polariser differs from a conventional fibre polariser in that the output of the polarising element is launched aligned either parallel or perpendicular to the axis of a PM fibre. This maintains the polarisation from the PM polariser through the PM pigtail to the planar waveguide ensuring that the light launched into the waveguide is set to one polarisation. The input polarisation can then be rotated between the two orthogonal states using either a linear or a 90° rotated fibre connector. The main advantage of this technique is that it removes the need to restrict movement of the optical fibre interconnects to maintain the correct polarisation.

The PM polariser method was introduced into the characterisation set-up for this work where studies of the birefringence were of interest as these required reproducible and robust methods of switching between the two polarisation states.

3.8 Accuracy and Stability of the Bragg Measurement

The direct UV writing system can produce strong Bragg gratings with good quality Gaussian responses in the reflectance spectrum. This allows for a good Gaussian fit to determine the central Bragg wavelength. For an unetched grating this is certainly true with sub-picometre resolution of the Bragg wavelength achievable. In these cases most “noise” on a temporal trace of the Bragg wavelength exists in the form of wavelength drift, however this is normally caused by the high sensitivity of the Bragg grating tracking changes in physical properties – most commonly temperature, rather than an uncertainty in the measurement. These effects can be normalised through use of a reference such as a thermocouple or through comparison with a reference Bragg grating, such techniques are discussed in detail in Chapter 7.

For an etched evanescent-field sensor the fluctuations in Bragg wavelength increase. This can be due to fabrication flaws – such as a rough or uneven surface that can lead to fringes or deformation of the Bragg response – leading to poor fitting, or

surface fouling. Deposition on the sensor surface of particulates or precipitates while in use can also lead to corruption of the Bragg response, again increasing the "noise" on the signal and showing the need to consider fouling within microfluidic sensor design.

Graphs where multiple readings have been taken and combined have been fitted with error bars and unless otherwise stated, the error bars given represent the standard deviation for a series of measurements. When measuring a constant condition the fluctuations in Bragg wavelength due to optical and electrical noise (plus fitting) is typically less than one picometre; this is far smaller than the line widths on graphs. As such all graphs showing a raw trace of the Bragg wavelength have error bars too small to show, any fluctuations represent real physical or chemical effects being detected by the grating. Noise present within the reflectance spectra present is not due to the OSA and represents genuine spectral artefacts.

3.9 Summary

Silica-on-Silicon substrates for direct UV grating writing are fabricated by a FHD process. The technique of Direct UV grating writing is based upon on the localised refractive index increase induced within a photosensitive planar glass layer through exposure to a tightly focussed UV beam. This photosensitivity is introduced through doping the core layer with germanium, which can be further enhanced by hydrogenating the sample at a pressure of 120 bar for approximately one week.

The direct UV grating writing technique allows for a combination of waveguide and Bragg gratings to be defined simultaneously into the substrate. This process relies on a photoinduced index change of 5×10^{-3} in the germanosilica core layer of the waveguide. These Bragg gratings can be written from 1400 nm to 1700 nm by detuning and modulating the inherent interference pattern produced by the overlap of two focussed coherent UV laser beams.

The reflectance spectrum in the infrared region can be analysed remotely by commercial telecoms test and measurement equipment via a fibre pigtail, allowing the sub-picometre resolution of the central wavelength of the Bragg peak.

Direct UV grating writing in this way allows for the production of a broad range of optical devices based around combinations of customisable Bragg gratings and

channel waveguides. This has an advantage over photolithographic and etching techniques, as it allows for rapid prototyping and reduced cost for small scale fabrication.

4. Evanescent Field Sensing

4.1 Introduction

Integrated optical devices are being increasingly used for chemical and biochemical sensing applications. These devices have principally been developed in the slip-stream of optical telecommunication technology and the success of optical fibre sensors.

The first optical chemical sensors were based on the measurement of changes in a compound's absorption spectrum and were developed for the measurement of carbon dioxide and oxygen concentration [102]. Since then a large variety of optical methods have been used in chemical sensors and biosensors including ellipsometry, spectroscopy (luminescence, phosphorescence, fluorescence, Raman), interferometry, spectroscopy of guided modes in optical waveguide structures (grating coupler, resonant mirror), and surface plasmon resonance. In these sensors a desired quantity is determined by measuring the refractive index, absorbance or fluorescence properties of analyte molecules or a chemo-optical transducing medium [12, 103-105].

Integrated optical chemical sensors typically operate through monitoring a perturbation of an evanescent field as a result of the presence of a chemical or biological species [106]. Perturbations in the evanescent field can be monitored through a change in effective index, absorption (imaginary part of effective index) or luminescence. These techniques cover a huge range of different devices that have been reviewed in many books and journal articles [106, 107]. The following work focuses upon effective index-based evanescent field sensors, which generally operate in an interference-based regime. Examples of such device structures include Mach-Zehnder interferometers (MZI), ring resonators and Fabry-Perot resonators [108].

Typically the refractive index resolutions of these interferometric devices are up to the order of 10^{-8} [107, 109]. The most well-known representatives of this class are grating couplers (including Bragg reflectors) [110] and Surface Plasmon Resonance (SPR) [111] based devices, of which the interference mechanisms of both are not immediately obvious. While SPR devices and grating coupler-based devices typically have lower sensitivities compared to other interference based devices (~10^{-6}), their advantage lies in the fact that they have a large dynamic range and are less sensitive to variations in supplied optical power. These strengths allows for the deployment of such optical devices into real-world sensor applications.

4.2 Surface Plasmon Resonance (SPR) Sensors [111]

The potential of surface plasmon resonance (SPR) for characterisation of thin films [112] and monitoring processes at metal interfaces [113] was recognized in the late seventies. In 1982 the use of SPR for gas detection and biosensing was demonstrated by Nylander [114, 115] and Liedberg [116]. Since then SPR sensing has been an area of active research within the optical sensing community. A great deal of work has been done in the exploitation of SPR for optical biosensing where SPR has shown a great potential for affinity biosensors, allowing real-time analysis of bio-specific interactions without the use of labelled molecules. The SPR sensor technology has been commercialised by several companies and has become a leading technology in the field of direct real-time observation of biomolecular interactions.

4.2.1 Plasmons [117]

Plasmons can be described classically as an oscillation of free electron density against the fixed positive ions in a metal. This can be visualised by a cube of metal placed in an external electric field. If the electric field is to the right, electrons will move to the left side (uncovering positive ions on the right side) until they cancel the field inside the metal. If the electric field is then switched off the electrons move to the right, repelled by each other and attracted to the positive ions left bare on the right side. They will oscillate back and forth at the plasma frequency until the applied energy is lost through resistance or damping. Plasmons are a quantisation of this type of oscillation.

Plasmons play a large role in the optical properties of metals. Light of frequency below the plasma frequency is reflected, because the electrons in the metal screen the

electric field of the light. Above the plasma frequency the electrons cannot respond fast enough and light is transmitted. In most metals, the plasma frequency is in the ultraviolet, making them reflective in the visible range. Some metals, such as copper and gold, have electronic interband transitions in the visible range, whereby specific wavelengths are absorbed resulting in their distinct colours.

4.2.2 Surface plasmons

Surface plasmons are those plasmons that are confined to surfaces and that interact strongly with light resulting in a polariton (a quasiparticle that results from of the mixing of a photon with an excitation of a material) [117]. They occur at the interface of two media with dielectric constants of opposite signs; often a material with a positive dielectric constant and a negative dielectric constant (typically a metal). A surface plasmon resonance is a charge-density wave associated with an electromagnetic wave, the field vectors of which reach their maxima at the interface and decay evanescently into both media.

In order to excite surface plasmons in a resonant manner, electrons or photons are used. The incoming emission source has to match its impulse to that of the plasmon. In the case of TM polarised light, this is possible by passing the light through a block of glass to increase the wavenumber (and the impulse), and achieve resonance at a given wavelength and angle. While TM polarised light can result in a periodic surface charge-density, TE polarised light possesses only an electric field component parallel to the surface and hence is unable to induce the surface charge-density wave necessary for electronic surface plasmons or display any angular dependence [117].

Typical metals that support surface plasmons are silver and gold [118], but metals such as copper, titanium or chromium are also known to be applicable. Owing to high loss in the metal, the surface plasmon wave propagates with high attenuation in the visible and near-infrared spectral regions. The electromagnetic field of the surface plasmon wave is distributed in a highly asymmetric fashion and the vast majority of the field is concentrated in the dielectric. A surface plasmon wave propagating along the surface of silver is less attenuated and exhibits higher localization of electro-magnetic field in the dielectric than for gold.

A typical experimental system for generating surface plasmon resonance is shown below (Figure 4.1), where the metal film is evaporated onto a glass prism. The

surface is illuminated through the glass, and an evanescent wave penetrates through the metal film. At a particular wavelength and illumination angle the light is coupled to the plasmon at the outer side of the film and there is absorption.

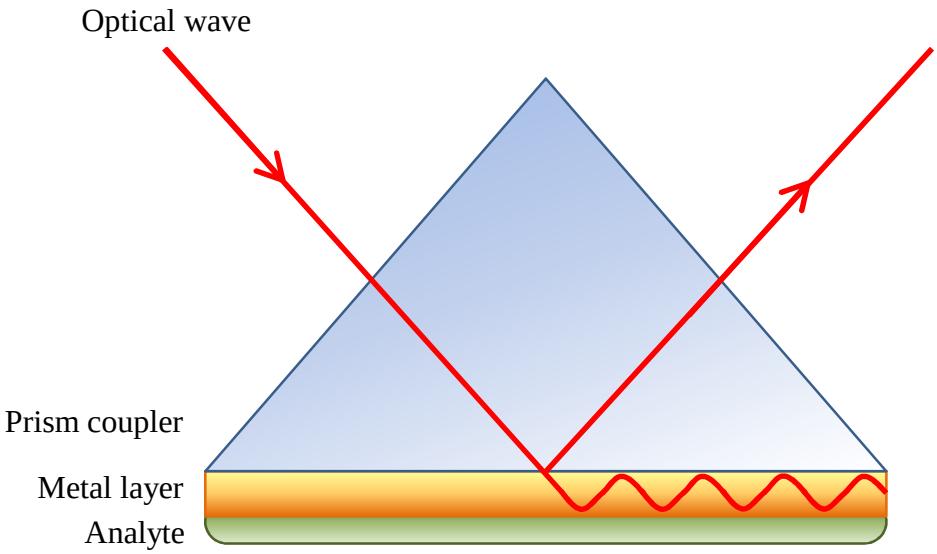

Fig. 4.1 The Kretschmann attenuated total reflectance (ATR) configuration for Surface Plasmon Resonance.

4.2.3 Using surface plasmons in sensing

Surface plasmons have been used to enhance the surface sensitivity of several spectroscopic measurements including fluorescence [119], surface enhanced Raman scattering (SERS) [120], and second harmonic generation [121, 122]. However, in their simplest form, SPR reflectivity measurements can be used to detect molecular adsorption, including polymers, DNA or proteins.

It is common that the angle of the reflection minimum (absorption maximum) is measured. This angle changes in the order of 0.1 ° during thin (about nm thickness) film adsorption. In other cases the changes in the absorption wavelength are followed. The mechanism of detection is based on the adsorbing molecules causing changes in the local index of refraction, changing the resonance conditions of the surface plasmon waves. The sensor sensitivity, stability, and resolution depend upon properties of both the optical system and the transducing medium. While the selectivity and response time of the sensor are primarily determined by the properties of the transducing medium.

Sensitivity of SPR sensors is defined as the derivative of the monitored SPR parameter (e.g. resonant angle, intensity or wavelength) with respect to the parameter

to be determined (refractive index, thickness of a thin overlayer concentration, etc.). The sensitivity of SPR-sensing devices has been widely studied [123-127]. The sensitivity of SPR angular interrogation-based sensors to changes in the refractive index has been found to increase with decreasing operation wavelength [127], conversely, the sensitivity of SPR refractive index sensors using wavelength interrogation and intensity measurement increases with the wavelength [126]. In addition, SPR sensors based on wavelength interrogation and intensity measurement may benefit from using silver as an SPR-active metal instead of gold [125, 126]. Typical values [111] for different SPR systems vary from refractive index changes of 2×10^{-4} for intensity measurements on grating coupler-based SPR sensors to 5×10^{-7} for angular interrogation on prism coupler-based SPR sensors measured at 630 nm wavelength, and an analyte of index 1.32.

Sensor resolution is the minimum change in the parameter to be determined which can be resolved by a sensing device. The sensor resolution depends upon the accuracy with which the monitored SPR parameter can be determined by the specific sensing device and as such is limited by sensor system noise. The noise in SPR-sensing devices has been systematically studied including an analysis of the influence of temperature, the light source, and photodetector noise on SPR sensor resolution [128, 129].

Another important parameter of an SPR sensor is its operating range, which is the range of values of the parameter to be determined that can be measured by the sensor. While the operating range of intensity measurement-based SPR sensors is naturally limited by the limited width of the SPR dip, the operating range of angular and wavelength interrogation-based SPR sensors can be made much wider. In principle, the operating range of these sensors is determined by the detection system, more specifically by the angular or spectral range covered by the optical system-angular position detector array or spectrum analyser, respectively. However, there is a trade-off between the dynamic range and resolution of these sensors.

4.2.4 Waveguide surface plasmon resonance sensor

The use of optical waveguides in SPR sensors provides numerous attractive features such as a simple way to control the optical path in the sensor system, small size and ruggedness. The process of exciting a surface plasmon wave in an optical

waveguide-based SPR-sensing structure is, similar to that in the Kretschmann ATR coupler, shown in Figure 4.1. A lightwave is guided by the waveguide and, entering the region with a thin metal overlayer, it evanescently penetrates through the metal layer. If the surface plasmon wave and the guided mode are phase-matched, the light wave excites a surface plasmon wave at the outer interface of the metal that penetrates up to 200 nm into the analyte [130]. The sensitivity of waveguide-based SPR devices is approximately the same as that of the corresponding ATR configurations. Despite increased design constraints compared to bulk prism-based SPR-sensing devices, all the main SPR detection approaches have been implemented in waveguide SPR sensors.

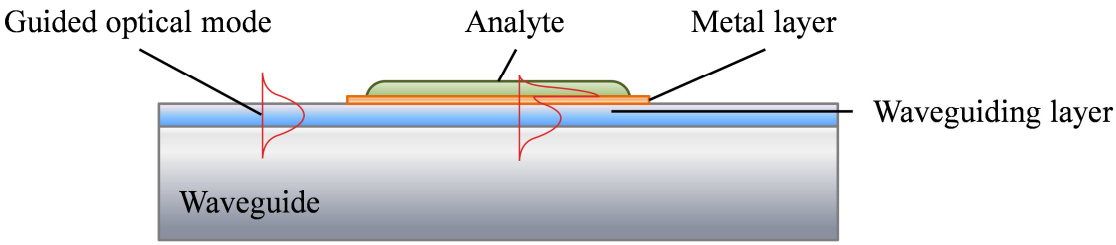

Fig. 4.2 A schematic of an optical waveguide based surface plasmon resonance sensor, illustrating the evanescent wave at the metal surface.

Currently, optical fibre SPR probes present the highest level of miniaturisation of SPR devices, allowing for chemical and biological sensing in inaccessible locations where the mechanical flexibility and the ability to transmit optical signals over a long distance make the use of optical fibres very attractive. The use of optical fibres was first proposed by Jorgenson and Yee [131]. They used a wavelength interrogation technique and formed an SPR sensing structure using a conventional polymer-clad silica fibre. The cladding was partly removed and an active metal layer deposited symmetrically around the exposed section of the core. This approach allowed construction of miniaturised optical fibre SPR probes with a limited interaction area of ~10 mm along the fibre. This fibre optic SPR sensor is capable of detecting variations in the refractive index from 1.2 to 1.4 with a resolution up to 5×10^{-5} at higher refractive indices of analyte with a resonant wavelength resolution of 0.5 nm [131], however this can be improved by raising the refractive index of the core layer [132].

Integrated optical waveguide SPR sensors appear promising for the development of multichannel sensing devices on one chip with the potential for efficient referencing and multi-component sensor analysis of complex samples. Research into integrated

optical waveguide SPR sensors was pioneered by researchers at the University of Twente in the late eighties [133]. Since then, various groups have developed SPR-sensing devices using slab [134, 135] and channel [136, 137] single-mode integrated optical waveguides. Similar to single-mode optical fibre SPR sensors, the integrated optical SPR-sensing devices exhibit a rather limited operating range. Various possibilities for tuning the operating range of the sensor have been explored, such as using waveguides fabricated in low refractive index glass [136], a buffer layer [135], a high refractive index overlayer [138] and more complex multi-layer structures [139, 140]. However, all the approaches that introduced additional layers were found to yield less sensitive SPR sensing devices because of the lower concentration of electromagnetic field in the analyte.

4.2.5 Chemical sensing using surface plasmon resonance

While in specific systems of limited complexity variations in the concentration of analyte may be determined by directly measuring refractive index using an SPR sensor (e.g. monitoring distillation processes [141]), most chemical SPR sensors are based on the measurement of SPR variations due to adsorption or a chemical reaction of an analyte at the surface, resulting in changes in its optical properties. The surface of these sensors is usually composed of gold, which is a well-documented substrate for surface functionalisation and sensitivity enhancement. The applications of such a system include monitoring of the concentration of vapours of hydrocarbons, aldehydes and alcohols by adsorption in polyethylene glycol films [142], monitoring of vapours of chlorinated hydrocarbons by adsorption in polyfluoroalkylsiloxane [143], detection of vapours of tetrachloroethene [144] by adsorption in a polydimethylsiloxane (PDMS) film, and detection of vapours of aromatic hydrocarbons by their adsorption in Teflon films [145]. It has been also demonstrated that SPR sensing devices using palladium as an SPR-active metal can effectively detect molecular hydrogen because of intense adsorption [146, 147]. Recently a sensitive sensor for nitrogen dioxide detection utilizing chemisorption of NO_2 molecules on a gold SPR active layer has been reported [148]. SPR structures have also been exploiting the interaction between the analyte molecules and the transducing layer allowing toluene detection via copper and nickel phthalocyanine [149]. The use of SPR for detection of ammonia vapour using the reaction of ammonia with a bromocresol purple film has been also reported [150]. Combined with anodic

stripping voltammetry, the SPR method has been utilised for the detection of copper and lead ions [151, 152].

4.2.6 Advantages and disadvantages of surface plasmon resonance

Surface plasmon resonance sensors offer good sensitivity to changes in refractive index. While silver yields a better evanescent field enhancement of the sensing surface, gold is typically used for SPR sensors. This preference is pragmatically based on the greater stability, biological compatibility and the ease of controlled functionalisation that a gold surface offers. A potential solution to this shortcoming is through use of a bimetallic silver–gold film for surface plasmon excitation. This has been shown to enhance the sensitivity by a factor of two without compromising on the integrity of the surface [153].

Through well-known thiol based coupling reactions surface functionalisation with both chemical and biological agents is possible. This, combined with the relatively short penetration depth of the evanescent tail of the surface plasmon, allows for the changes in refractive index detected to be associated with a specific target binding at the surface, with little interference from bulk environmental changes. The technology has been well refined and many variations upon the SPR sensor can be purchased commercially today.

However, there are several drawbacks with using SPR. The nature of evanescent field sensing limits the potential range of refractive indices detectable, where indices greater than the waveguide core will couple out into cladding modes. Referencing of physical effects is also necessary, but is not always straight forward, often for temperature referencing a second SPR sensor is required, increasing not only the redundancy, but the cost and size of the system.

4.3 Mach-Zehnder Interferometer (MZI) Sensors

The Mach–Zehnder interferometer (MZI) is an optical device used to determine the relative phase shift between two collimated beams from a coherent light source. The apparatus is named after the physicists Ludwig Mach and Ludwig Zehnder. The integrated optical Mach-Zehnder interferometer is an evanescent refractometer whose surface may be modified to render it sensitive to specific chemical species. Mach–Zehnder devices generally show high sensitivity, are straightforward to design

and fabricate and can be very tolerant of manufacturing error. In principle the Mach-Zehnder interferometer is more sensitive than waveguide surface plasmon resonance based sensors because it does not employ coupling to a lossy waveguide, although exploitation of this enhanced sensitivity may require the sensitive region to be longer.

4.3.1 Integrated optical Mach-Zehnder interferometers

Mach-Zehnder interferometers can be fabricated in integrated optical circuits using a wide variety of waveguide fabrication techniques. Typically, the input waveguide is split equally into two arms using a splitter before recombining into a single waveguide to the detector. This results into an output, P_{out} that depends on the phase difference, $\Delta\varphi$ of both beams in the combination area. It is this phase difference that is used for interrogation in Mach Zehnder interferometer based sensors [109].

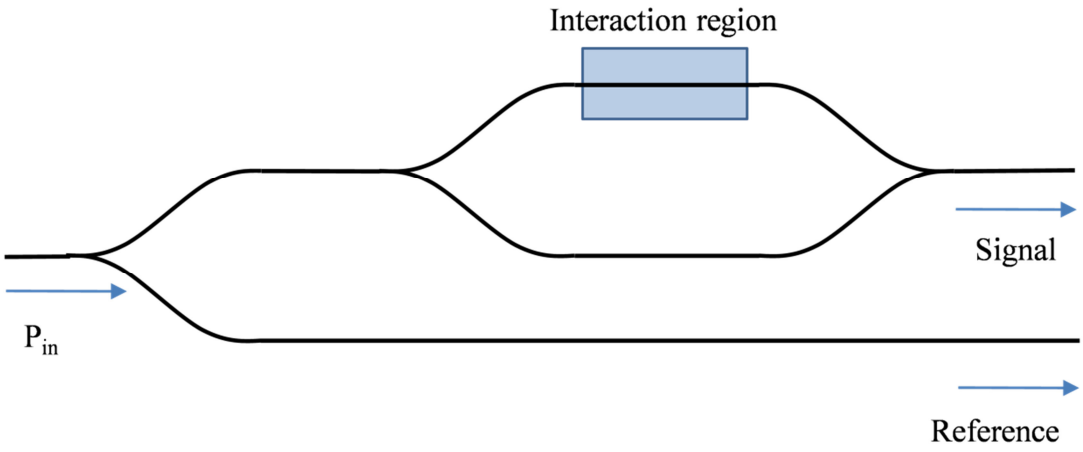

Fig. 4.3 Schematic of an experimental Mach-Zehnder integrated optical device with an additional reference channel to allow compensation for input power fluctuations and coupling efficiency [154].

If the structure is fabricated such that the waveguides are buried, there will be no phase difference in the two beams, yielding constructive interference. However if the waveguide core is exposed to the environment through removal of this overclad, the evanescent tail of the guided mode will interact with the media above it. Changes in the refractive index of this medium will alter the effective path-length of the two beams, resulting in a phase difference between them. From this phase shift, the change in refractive index can be derived, forming a refractometer. Typically one arm will be exposed to the analyte, becoming the “sensor”, while the other will remain covered to give a constant reference for this phase shift, as shown in Figure

4.3. An additional reference channel can also be included to compensate for input power fluctuations and coupling efficiency [154].

4.3.2 Mach-Zehnder Interferometers for sensor applications

There are many examples of Mach-Zehnder sensors for biological [155-157] and chemical sensing applications [109, 158]. Much like SPR sensors, these systems utilise a surface functionalisation to induce specific interactions at the surface. This allows for the differentiation between bulk changes in refractive index and the change induced by the presence of specific species.

It has been shown that the sensitivity limit of a Mach-Zehnder interferometric sensor can be enhanced further with an overlayer of a high index material that acts to pull the guided mode further into the analyte (see Chapter 5.5 for a discussion on the use of high index overlayers). Quigley [154] has demonstrated a highly sensitive refractometer with a detection limit better than 5×10^{-7} through use of a 30-nm-thick high index overlayer of tantalum pentoxide, an order of magnitude improvement over the uncoated MZI sensor.

4.3.3 Advantages and disadvantages of Mach-Zehnder interferometers

Mach-Zehnder interferometers have the highest sensitivity to refractive index change of all the techniques discussed within this chapter. By using a comparative measurement many physical properties can be negated allowing for precise measurements of the analyte in question, as with SPR this can be made specific through functionalisation of the surface, in the case of silica-based systems this is typically achieved through silane chemistry. For accurate negation of these physical effects, such as temperature, the two arms of the splitter must be in close proximity with good thermal conductivity between the two [109], limiting the design of the sensor. This can be overcome through careful design of the dimensions of the two waveguides, as described by Guha [159], however this requires an intimate knowledge of the system to be studied and precise fabrication of the waveguides. The changes in refractive index are derived from monitoring the relative output power, allowing for continual measurement, unlike techniques based upon scanning wavelength.

While Mach-Zehnder interferometers have many strengths, their susceptibility to changes in the optical power of the system makes them more susceptible to misreading without suitable power referencing. The inability to measure the

refractive index directly, introduces the requirement that their output must be continuously monitored, with any pause in measurement leading to uncertainty in the measured value of refractive index. Changes in the measured refractive index must also be of a timescale compatible with the interrogation system or again the absolute refractive index value may be lost. Furthermore it is more complicated to network multiple interferometers into a single device than for other sensor systems as each interferometer must be interrogated directly requiring parallel outputs and/or detectors.

4.4 Optical Fibre Sensors

The applications of fibre optics to analytical systems and sensors are numerous, taking advantage of many different properties of their waveguiding structure and low optical loss. The simplest application is in optical spectroscopy, where they enable it to be performed at sites inaccessible to conventional spectroscopy, over large distances, or even at multiple points along the fibre. However, the waveguide structure of fibre optics enables less common methods of interrogation, in particular evanescent wave spectroscopy.

Commercial optical fibres are available with transmissions over a wide spectral range, allowing for use with a wide range of light sources. Current limitations are not so much in the transmissivity of the fibre, but in the background fluorescence inherent of most of the materials used in fabrication, in particular plastic. With much of this occurring at or near the UV region there is a trend toward long-wave sensing where background signals from the fibre are less significant. Typical applications are in sensing gases and vapours, medical and chemical analysis, molecular biotechnology, marine and environmental analysis, industrial production monitoring, bioprocess control, and the automotive industry.

Fibre optic sensors are based on either direct or indirect sensing techniques. In the first, the intrinsic optical properties of the analyte are measured, for example its refractive index, absorption, or emission. While in the second, the colour or fluorescence of an immobilised indicator or label is monitored. In recent years, fibre bundles also have been employed for purposes of imaging, for biosensor arrays (along with encoding), or as arrays of non-specific sensors whose individual signals may be processed via artificial neural networks (these non-integrated approaches to

optical sensors are discussed further in Section 4.6). As mentioned in Section 4.2.4, SPR sensors fabricated from an optical fibre have been shown to be highly effective at both direct measurements of properties such as refractive index and for detection of biological species through stimulation of a surface layer upon binding [160].

Wolfbeis [103] has written a thorough review of fibre optic sensors for chemical and biological applications detailing the different approaches necessary for different analyte types and the novel structures applied in these systems. As this thesis is focussed upon chemical sensing, a brief overview of the approaches used is given in the following subsections, however for brevity biosensing is omitted. Although it must be noted that optical fibres are frequently used for biosensing and much like their SPR or Mach-Zehnder analogues, they rely upon the use of enzymes, antibodies, nucleic acids and whole cells to induce and detect specific interactions at the sensor surface.

4.4.1 Sensors for gases, vapours and humidity

Hydrogen, along with flammable alkanes, is the analyte where safety considerations have led to a substantial amount of research in terms of fibre optic sensing. Since hydrogen gas does not display intrinsic absorptions or emissions that could be used for simple optical sensing it is always detected indirectly. Hydrogen interacts strongly with metallic palladium and platinum films and with tungsten oxide, resulting in both spectral changes and an expansion of the material. This effect has been applied to fabricate a hydrogen sensor based on a palladium coated side-polished single mode fibre [161].

In contrast to hydrogen or oxygen, methane and other hydrocarbons are almost exclusively sensed via their intrinsic absorption in the near-infrared or via Raman scattering. An example fibre optic Raman sensor was reported for sensing ethanol and methanol in gasoline or water [162]. It employed a frequency doubled 532 nm Nd:YAG laser and a specially designed fibre optic Raman probe that enabled online determination of the sample constituents without employing an expensive infrared fibre.

Oxygen sensing remains an area where fibre optic chemical sensors are quite successful. Oxygen is almost exclusively sensed by virtue of the quenching effect it exerts on certain fluorophores. Cao [163] demonstrated the sensing of oxygen gas

down to 0.6 % through use of the reversible quenching of a methylene blue dye encapsulated within a silica sol-gel, coated onto a side-polished multi-mode fibre.

Numerous materials have been shown to work in optical humidity sensors, including Nafion films (a sulphonated tetrafluoroethylene based co-polymer developed by DuPont), which when doped with crystal violet (a triarylmethane dye) responds to humidity by a change in its reflectance [164]. Relative humidity between 0 and 0.25% was determined with the respective sensor, with a detection limit as low as 0.018 % relative humidity, defined as the percentage of the concentration of water vapour in the gas to the saturated concentration at the same temperature and pressure (equal to ~ 4 ppm volume concentration) in process gases such as nitrogen and hydrochloric acid. The response was fully reversible (with some hysteresis) in dry nitrogen. *N*-confused porphyrins immobilised within Nafion films undergo a water-induced tautomerism that forms the basis of a novel type of fibre optic, relative humidity sensor that exhibits long-term stability and a linear response over the humidity range from 0 to 4000 ppm [165].

4.4.2 Sensors for pH and ions

Optical sensing of pH remains to be of great interest even though all optical sensors suffer from cross sensitivity to ionic strength. While pH fibre optic sensors are commercially available, sensing of pH values below 1 and above 12 still represents a substantial challenge. In most cases, optical pH sensors respond over a limited range of pH only.

Martin *et al* [166] described a new organic pH indicator dye (mercurochrome) that was immobilised in a sol-gel matrix placed at the end of an optical fibre that enabled measurement of pH in the range pH 4 – 8. The sensor was constructed from a low cost optical fibre and optoelectronic components including a blue light emitting diode and a photodiode. This sensing scheme relies on the measurement of the fluorescence intensity of the pH indicator relative to the intensity of the blue excitation light reflected by the sensing phase. The ratio between the two signals is proportional to pH but independent of excitation light intensity. The applicability of this sensor has been tested for its performance in pH analysis in tap and bottled mineral water [167].

Ion sensing often employs similar methodology to pH sensors; an example of such an evanescent wave direct spectroscopic sensor for chromate anions was reported by Tao [168]. This used a flexible fused silica light guiding capillary as a sensor. The capillary had a cladding layer to guide light and a protective polymer coating on the outer surface to increase mechanical strength. Like similar sensors described before, the sensor was based on the intrinsic evanescent wave absorption by chromate ions in a water sample inside the capillary, with a 30 m long capillary capable of detecting as little as 31 ppm of chromate.

4.4.3 Sensors for organic chemicals

Much like biosensors, chemical sensors utilise specific recognition through binding to the target molecule. Mohr *et al* [169] give an example of such, where they describe fluoro-reactands for the determination of saccharides, based on hemicyanine dyes containing a boronic acid receptor. These receptors are capable of forming a covalent bond between their boronic acid moiety and the diol moiety of saccharide with a resultant increase in fluorescence. The probe can be photoexcited at ~460 nm and emits a peak at 600 nm, and can be used at near neutral pH.

Dissolved organic compounds in water samples can be sensed with a nanoporous zeolite thin film-based fibre sensor [170]. A Fabry-Perot interferometric system was developed containing a thin layer of nanoporous zeolite synthesised on the cleaved end face of a single mode fibre. The sensor was operated by monitoring changes in the thickness of the thin film caused by the adsorption of organic molecules by white light interferometry, allowing for the detection of methanol, isopropanol, and toluene with high sensitivity. Furthermore, a fibre optic chemical sensor for toluene in water was described by Consales *et al* [171] which utilised the reflectivity changes when single-walled carbon nanotubes are introduced to toluene. These systems feature good stability of the steady-state signal, sensitivity, and rapid response.

4.4.4 Advantages and disadvantages of fibre optic sensors

In the simplest case, optical fibre allows for the miniaturisation of conventional spectroscopy techniques, allowing for more compact devices that can be used in new environments and on a much smaller scale. Etching the cladding generates an evanescent field that can be used to probe locally these environments and through

functionalisation introduce specificity. Furthermore the use of novel fibre structures, such as micro-capillaries allows for the merger of fibre optics with a microfluidic system, producing compact, multifunction sensors.

While these methods are all effective, they mostly use the optical fibre as an optical probe; coating an etched fibre with a metal can form a SPR fibre sensor that combine the strengths of both these techniques and allows for *in situ* interrogation of a sensor site. This approach is discussed further in the context of fibre Bragg grating sensors in the following section (4.5.2).

The main drawback of these techniques is that they still require many of the components found within a conventional spectrometer, including a source and a detector. While the miniaturisation of fibre components, such as lasers, is rapidly improving, these systems are still some distance from forming truly integrated lab-on-a-chip devices.

4.5 Grating Couplers

In contrast to SPR sensors, grating couplers make use of dielectric waveguides in which there are no metallic elements and in which the modal properties are dominated by the real part of the refractive index of the waveguide and of the measurand. The most familiar format for such a device is an optical fibre sensor.

Grating couplers can be classified as long-period gratings (LPGs) or short-period gratings (Bragg gratings). As with Bragg gratings, LPGs have proven to be effective refractive index sensors [51, 172, 173]. The shorter physical length of a Bragg grating (typically 1 mm) is 10-100 times smaller than that for a long-period grating, giving Bragg gratings an advantage in near point sensing applications.

Gratings can be written into many different substrate geometries, the most common of which is into the core of an optical fibre but they can also be fabricated into two-dimensional and three-dimensional systems using such techniques as direct UV grating writing or femtosecond writing.

4.5.1 Optical fibre Bragg grating sensors [110]

Although the formation of fibre gratings had been reported in 1978 [68, 69], the intensive study of fibre gratings began after a controllable and effective method for

their fabrication was devised in 1989 [72]. From add/drop filters and dispersion compensators to fibre lasers, optical fibre gratings have been used in a wide range of components for optical communications [174]. Extensive studies have also been performed on fibre grating sensors with some reaching commercialisation.

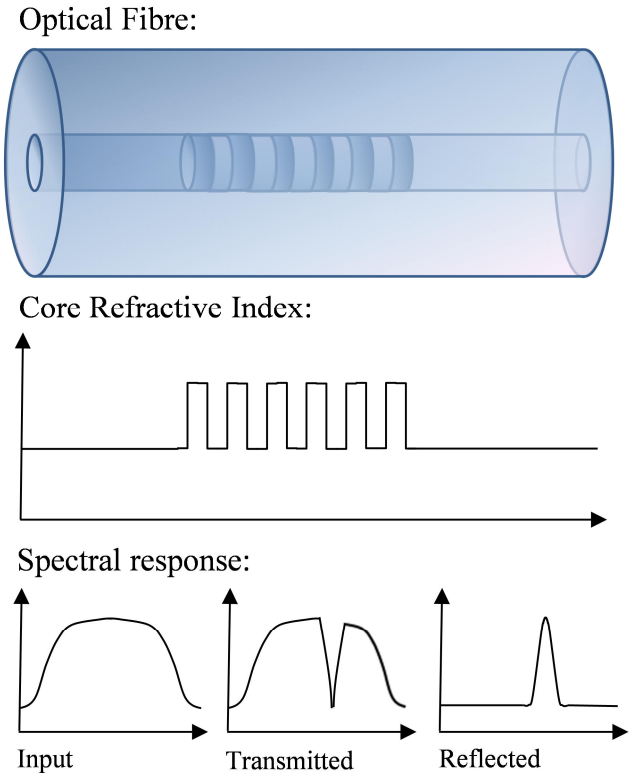

Fig. 4.4 A long-period fibre Bragg Grating structure with the associated refractive index profile and spectral response.

In these systems, a periodic refractive index structure is induced into the core of a waveguide; typically through exposing a germanium-doped optical fibre to UV light through a mask. Many different grating structures can be written into optical fibre; a long-period fibre grating can couple the forward propagating core mode to one or more forward propagating cladding modes, while a chirped fibre grating has a wider reflection spectrum through reflecting each wavelength component at different positions. A tilted fibre grating can couple the forward propagating core mode to the backward propagating core mode and a backward propagating cladding mode. All these have been applied to optical sensors but it is the fibre Bragg grating that is most commonly used.

As discussed in Chapter 2, Bragg gratings respond to both strain and temperature. To study or exclude these properties from the measurand response a reference

grating is often used [175]. Another fibre Bragg grating (the reference grating), which is isolated from the analysis parameter is placed near the sensor Bragg grating. Another method is to use two fibre Bragg gratings with significantly different Bragg wavelengths which respond similarly to physical effects but show different responses to the same measurand [176]. This concept can be applied to chemical sensing by applying the unique dispersion properties of a given analyte to detect it within the optical sensor [37].

From fibre optic gyroscopes [177] to sensors for current [178] or pressure [10], many physical properties can be measured by optical fibre sensors. The fibre Bragg grating can also be used for chemical sensing based on the fact that the central wavelength of an exposed Bragg grating varies with refractive index change, through an evanescent field interaction. An approach based on a fibre Bragg grating written onto an etched D-fibre has been demonstrated [179] and more recently, a modified version based on a side-polished fibre configuration has been reported as a refractive index sensor, allowing fast on-line measurements of chemicals, such as carbon hydrides for the petrol industry [180].

Because of the constraint of current interrogation techniques, with a typical sub-picometre resolution for static wavelength-shift measurement, the sensitivity obtained for fibre Bragg gratings is lower ($\Delta n \approx 10^{-5}$) than for other fibre optic techniques. Long-period gratings have been found to be more sensitive to the refractive index change than fibre Bragg gratings, overcoming this limitation [181]. As LPGs couple light from the forward-propagating mode into several forward-propagating cladding modes, any variation on the refractive index of the material around the cladding modifies the transmission spectrum properties to generate loss peaks. A sensitivity of up to 10^{-7} is possible with further improvement of the interrogation resolution [53]. The concentration of a number of organic chemicals, including ethanol, hexanol, methylcyclohexane, hexadecane [182], and inorganic chemicals; calcium chloride and sodium chloride [183], have been tested with LPGs.

4.5.2 Integrated optical Bragg grating sensors

Compared to optical fibre Bragg sensors, a relatively small number of Bragg grating sensors have been considered and implemented in a planar form factor. The approaches demonstrated cover a wide variety of techniques and material platforms,

including: polymers [184-187], sol-gel systems [188], silicon-on-insulator [15, 189], lithium niobate [190], and silica-on-silicon [191, 192].

The wave-guiding and Bragg grating structures in these optical sensors have been fabricated by a number of different approaches leading to sensing elements with ridge waveguides [193], UV written waveguides and gratings [191, 192], etched corrugated gratings [11, 194] and even Bragg gratings through selective precipitation of nanoparticles [195].

Such planar Bragg grating devices are appealing for sensing applications for several reasons [196]:

- Multiple wavelengths may be used, offering the possibility for analyte identification through optical dispersion measurements.
- A range of evanescent field penetration depths can be employed which may provide additional information on the structure near to the surface; this can be applied to determine such properties as the dimensions of biological entities.
- Multiple separate sensing regions may be incorporated onto a single sensor chip. This can be an advantage particularly in immunoassay based bio-detection where it is advantageous to test for multiple different targets simultaneously without the need for duplication of equipment or time delays.
- A monolithic silicon chip-based design is robust, requires no electrical signal and is resistant to a wide range of chemicals making these devices suitable for deployment in a wide range of environments.

Integrated optical Bragg grating sensors have much in common with fibre Bragg grating sensors, utilising the same underlying physics and thus affording all the same benefits. Just as for the majority of optical fibre based sensors these devices have the principal attraction of high sensitivity with real-time and on-site measurement. However there are several key differences that set the two approaches apart, the most significant being the ability to produce complex sensor networks within a single device. The planar geometry allows compatibility between a diverse range of technologies from optical fibre sensors to micromachining and microfluidics. This allows for the development of these sensors into highly compact lab-on-a-chip

devices that aim to achieve multiple functions in a single device, such as the one pictured below.

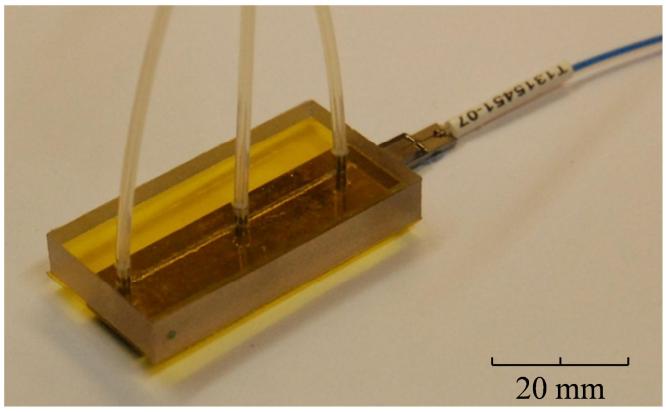

Fig. 4.5 A planar Bragg grating sensor incorporated into a microfluidic flow cell, with an optical fibre pigtail for optical interrogation.

As discussed in the previous chapter, the planar Bragg sensors developed in this work were fabricated by direct UV writing into a silica-on-silicon platform and a detailed discussion of these techniques can be found there. These sensors have been shown [31] to be able to detect changes in refractive index down to 10^{-6}.

4.5.3 Advantages and disadvantages of integrated Bragg grating sensors

Despite the lower absolute sensitivity ($\Delta n \approx 10^{-6}$ versus 10^{-8} for MZI sensors), the ability to measure the absolute Bragg wavelength and thus the absolute refractive index of the analyte is a major advantage over Mach-Zehnder interferometer based sensors. In this way the interrogation setup can both continuously measure a single sensor (that can still contain multiple Bragg gratings), sample at set times or even sequentially interrogate multiple independent sensor devices. This would be much more challenging with a Mach-Zehnder based system, where even integrating multiple sensors within a single integrated device is more complex.

While the underlying physics is markedly different, integrated Bragg grating sensors are in many ways similar to waveguide SPR sensors. Both refractometer systems have similar sensitivities to refractive index change ($\Delta n \approx 10^{-6}$), they can integrate multiple sensors into an array and can be readily chemically functionalised for binding at the sensor surface. However some advantages exist for an integrated Bragg grating sensor over its SPR counterpart. Firstly, temperature referencing is much simpler to achieve with a Bragg grating sensor, with approaches including the

use of reference gratings and comparison of orthogonal modes (Chapter 7), all of which can be integrated into the same waveguide with no additional fabrication steps. Secondly, fabricating an integrated Bragg grating sensor (particularly by direct UV grating writing) is more straightforward with less fabrication steps and clean-room processing, even for complex waveguide networks. In contrast, most waveguide SPR sensors are developed upon the optical fibre platform.

SPR requires a metallic surface to support the plasmon mode, typically gold. Deposition of this thin gold film to a suitable standard of uniformity, thickness and coverage is not trivial, particularly as gold will not robustly bind to silica directly. While both gold and silica can be readily chemically functionalised with a thiol or silane respectively, gold is more chemically inert. This has the advantages of biological compatibility and minimising secondary interactions that may interfere with the intended binding events.

The gold layer is typically attached through an organic mercaptoalkylsilane linker, as discussed in Chapter 9, where a silyl group at one end of the linker can bind to a silica surface while a thiol at the other end tethers to a gold surface. Silica is sparingly soluble in aqueous solutions, with its solubility reported as 113 mg/L in distilled water and 85 mg/L in seawater, with the initial rate of dissolution much greater in seawater [197]. In long-term sensor applications, particularly in the harsh environments found in oceanographic sensing, silica sensors will slowly dissolve. For a Bragg grating sensor this will have little effect, other than to subtly increase the sensitivity over time. In contrast, this erosion in a SPR sensor can remove the silica that is attached to the organic linker, necessary for the adhesion of the gold film. This ultimately can lead to degradation of the gold surface, causing the sensor to fail.

There may be some applications where the deeper penetration of the evanescent field of the Bragg grating sensor over that seen for SPR has an advantage, particularly when the bulk analyte is of interest in addition to surface binding. The converse will also be true of SPR however, where the shallower interrogation depth will be beneficial in localised studies of interactions at the surface.

4.6 Cross-responsive and array-based optical sensors

While the discussion of optical sensors up to this point has focused upon integrated optical sensors; as previously mentioned optical fibre can also be used as a medium to transport an optical signal from an interrogation site to the analysis system. Such a system has been demonstrated by Walt [198], whereby the individual fibres within an optical fibre bundle were selectively coated with a fluorescent dye, encapsulated within a series of different polymer environments. The fluorescent dye within each polymer environment was shown to respond differently to a range of analytes; based upon changes in polarity, hydrophobicity, pore size, flexibility and swelling tendency. By investigating the outputs of this array of fluorescent probes, a fingerprint could be developed for an individual organic vapour without the need for the presence of a specific receptor (Figure 4.6). This process acts as a simple model of the vertebrate olfactory system, whereby a large number of smells can be identified despite a relatively small number of receptors.

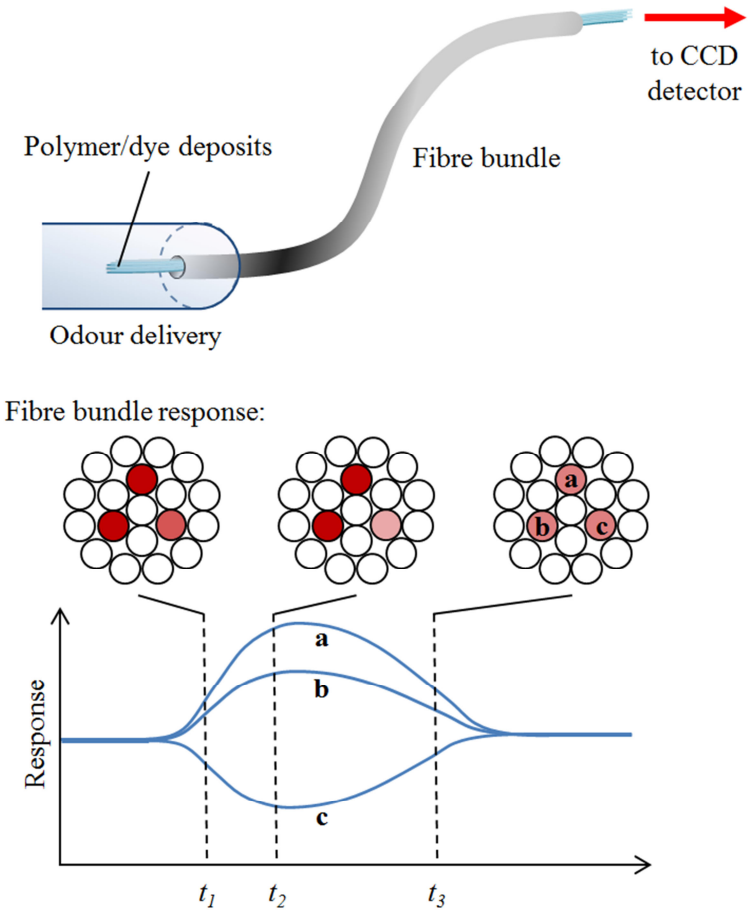

Fig. 4.6 A schematic illustrating the fibre bundle employed by Walt [198] for array-based optical sensing. Not only the presence of fluorescence, but the fluorescence lifetime of the individual coated fibres was used in identification of an analyte

By not only using the presence and intensity of the fluorescence emitted by each polymer, but also its temporal response, the neural networks presented by Walt were able to identify compounds with a high degree of certainty. They demonstrated that the system was able to differentiate individual components in mixtures and identify analytes based on their chemical characteristics; including the presence of functional groups and relative molecular weight.

The main drawback of such a sensor system targeting a broad range of analytes is that the ability to quantify the presence of an individual analyte is reduced. While Walt demonstrated that the system could identify analytes at both a saturated vapour and in a 50% vapour/air mixture with high certainty, it was not possible to give the detected concentration or a calibration graph. Much like the biological nose the system aims to mimic, this sensor can also be overcome by strong vapours that could mask the response of others in lower concentrations or prevent quantitative analysis.

An alternative array-based optical sensor system has been developed by Suslick [199]; this again aimed to mimic the mammalian olfactory by producing composite responses unique to each odorant. The use of the chemically selective response of a library of immobilised vapour-sensing metalloporphyrin dyes permitted the visual identification of a wide range of ligating (alcohols, amines, ethers, phosphines, phosphites, thioethers and thiols) and even weakly ligating (arenes, halocarbons and ketones) vapours. Where this approach differs from the work of Walt [198], above, was that selective and specific interactions between the analytes and the metalloporphyrin library is employed rather than the use of a single indicating fluorophore doped in a variety of matrices, where weak matrix–analyte interactions are required to provide selectivity.

While the metalloporphyrins were originally dispersed upon reverse phase silica because of its hydrophobic ability to mitigate the presence of water (a major advantage over mass-sensing techniques) it was subsequently found that a Teflon support allowed for miniaturisation of the metalloporphyrin targets to spots of just 500 µm, with much faster response times for vapour concentrations below 1 ppm.

Through use of a wide range of colours, both specific quantification of a single analyte and the identification of a mixture of vapours were achieved. This process

allowed for the determination of the composition of an unknown blend of trimethylphosphite and 2-methylpyridine.

It should be noted that while this system is an example of a multiplex optical sensor, it is not an integrated optical device, for example in terms of form-factor or integratability with microfluidics, and as such is not directly comparable to the examples discussed in the previous sections. However, the concept of a colorimetric array of receptors used by Suslick [199] to identify and quantify a wide range of analytes is directly applicable to those integrated optical refractometers, offering a clear direction for future developments in the field of integrated optical sensors.

A further example of an optical array-based sensor was demonstrated by Anslyn [200], however this device differed in that it aimed to "taste flavours" rather than "smell odours".

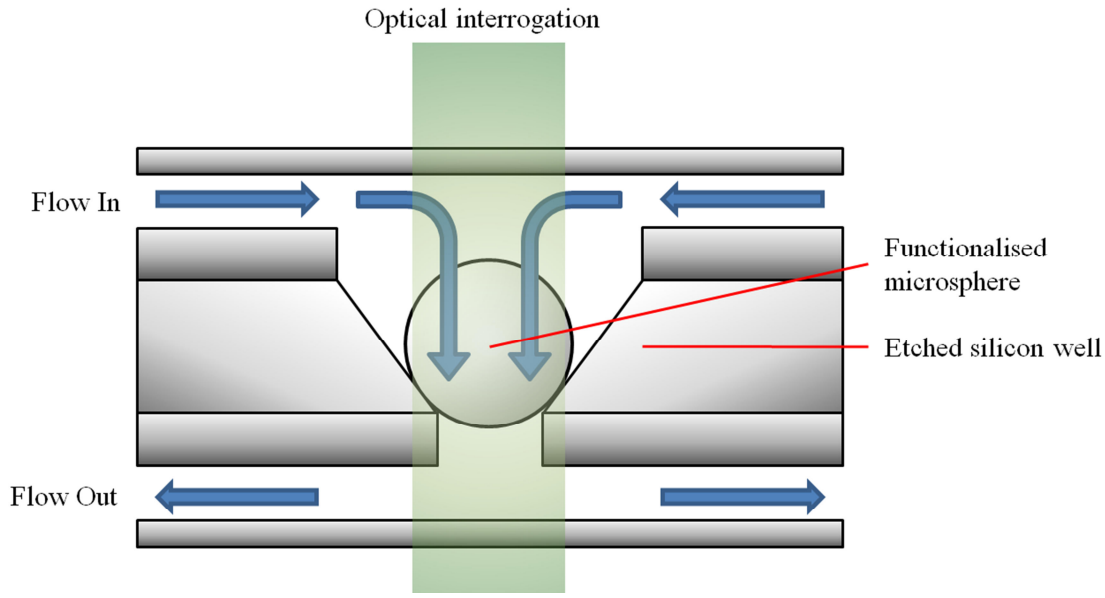

Fig. 4.7 A cross-section schematic showing of the fluid delivery method and bead confinement strategy. Fluid samples containing the various analyte species are introduced from the top side of the chip, pass through the analysis chamber, and exit out the bottom region of the assembly. The small size of the hole at the bottom of the well prevents the loss of the microsphere.

As illustrated above in Figure 4.7, polystyrene/poly(ethylene glycol) co-polymer microspheres were selectively arranged in micromachined cavities localised on a silicon wafer. Each microcavity can act as either a microreactor or analysis chamber, with the derivatised microsphere within acting as a probe. The sensor array chips are sealed within a customised flow cell composed of two siloxane polymer layers held together by a two-piece aluminum casing. Solutions are then

introduced to the flow cell using a liquid chromatography system. The flow cell sits atop the base of an optical/fluorescence microscope with the array observed and analysed through the microscope optics using a CCD. The immobilised beads function as micro-cuvettes, through which analyte−receptor interactions can be observed optically with both fluorometric and colourimetric procedures used to quantify analyte concentration.

Through use of a wide range of receptors, Anslyn [200]was able to successfully demonstrate the near-simultaneous collection of absorbance or fluorescence signals at multiple sites with the detection of pH over a wide range of concentrations with agreement to within ± 0.02 pH unit of that acquired at glass electrodes. A typical sensor equilibration time of two minutes was observed with uniform flow characteristics and little noticeable motion of the microspheres detected. Incorporation of receptors/signalling agents suitable for the analysis of acids, bases, numerous metal cations, enzymatic substrates, proteins, and antibodies, allowed for the acquisition in near-real-time of data that can be used to interpret the chemical/biochemical content of complex fluids.

This system differs from the previous examples it that it demonstrates a high-throughput approach to array-based sensing. The advantage of flowing the analyte solution through the porous microsphere is that it increases the interaction volume over that observed with functionalised planar surface, dramatically improving the equilibration time. The modular approach applied here to assembling the device allows for the system to be tailored through appropriate choice of functionalised beads making it suitable for a wide range of applications. However, the system makes use of bulk optical components and is thus not naturally well suited to operation outside the lab.

4.7 Summary

There are many different technologies that utilise light to sense changes in the surrounding environment actively under development, of which several key approaches have been described. While the methods of interrogating the environment, device fabrication and underlying physics differ wildly, they can all be applied to physical, chemical and biological sensing. For analysis systems based upon a refractometer, the sensitivity limit is typically 10^{-5} to 10^{-7}, with interferometer

systems demonstrating the highest sensitivity. There is no clear answer as to which is the best optical sensor system, but rather the best solution is specific to the desired application. For highly parallel systems, an integrated solution may be more appropriate than a fibre-based one, while the ease of direct incorporation into fibre networks over large areas can make a fibre solution more appropriate in others.

While great success in chemical identification has been demonstrated in array-based optical sensors, these systems all rely on large laboratory systems to interrogate the sensor chip. By learning from the strengths of these approaches in terms of high parallelisation and throughput and combining them with the miniaturisation and sophistication of integrated optical sensors, low-cost sensitive and specific optical sensors should be possible.

The work described in the subsequent chapters discusses Bragg grating sensors incorporated into compact planar integrated optical devices. The work focuses upon enhancing and quantifying the sensitivity of such sensors, incorporating them into a microfluidic system and developing surface functionalisation to induce chemical specificity. These approaches will investigate if the chemical sensor proposed here is able to compete with current developments in optical sensing.

5. Bragg Grating Sensor Development

5.1 Introduction

The previous chapters have introduced the theory of optical waveguides and Bragg gratings UV written into a silica-on-silicon substrate and described the current fabrication techniques used by the author to transform the commercially produced wafer into a Bragg grating refractometer. These optical devices were placed in context and compared to competing integrated optical sensors in the literature, with a focus upon surface plasmon resonance, optical fibre and Mach-Zehnder interferometer-based systems. The following chapters will discuss the developments made by the author to develop these simple proof-of-concept Bragg grating refractometers into optofluidic chemical sensors.

For practical sensor devices, the fabrication processes must be robust and reproducible. While this is true for the FHD wafer fabrication (an industrial technique) and the direct UV grating writing method (well established within the University of Southampton and the associated spin-out company, Stratophase [201]) the methodologies used to transform these optical circuits into practical chemical sensors had not been developed in any way at the start of this work. This chapter discusses the developments made by the author to develop the fabrication process and enhance the sensitivity of these integrated Bragg grating sensors.

This chapter will introduce a study made to optimise the etch medium towards the optimum etch rate, while still maintaining surface quality. Furthermore, it will be shown that a post-etch polishing step allows for the sensor surface to be restored to near-optical quality. This was confirmed via atomic force microscopy (AFM), where the surface roughness after polishing was comparable to that of the unetched surface.

The design of the lightwave circuit has been optimised to allow a broader range of applications, with integrated temperature referencing and multiple Bragg gratings in different sensor regions.

Finally in this chapter, it is shown that the sensitivity of these sensors can be dramatically improved through the inclusion of a high-index overlayer, such as tantalum pentoxide. Within a vacuum system, this device was able to detect sub-nanometre thickness changes of a silica layer deposited onto the surface.

5.2 Surface Etching

As discussed in Chapters 3 and 4; direct UV grating writing can be used fabricate integrated optical devices containing Bragg gratings. The reflectance spectrum in the infrared region of these gratings can be analysed remotely by commercial telecoms test and measurement equipment via a fibre pigtail, providing sub-picometre precision of the measured Bragg wavelength.

Such Bragg gratings are inherently sensitive to temperature and strain. However, to convert the buried grating into a refractive index sensor the Bragg grating must be exposed to its environment, as shown in Figure 5.1. By etching away a portion of the upper cladding, the mode within the grating region can be exposed to an analyte [192].

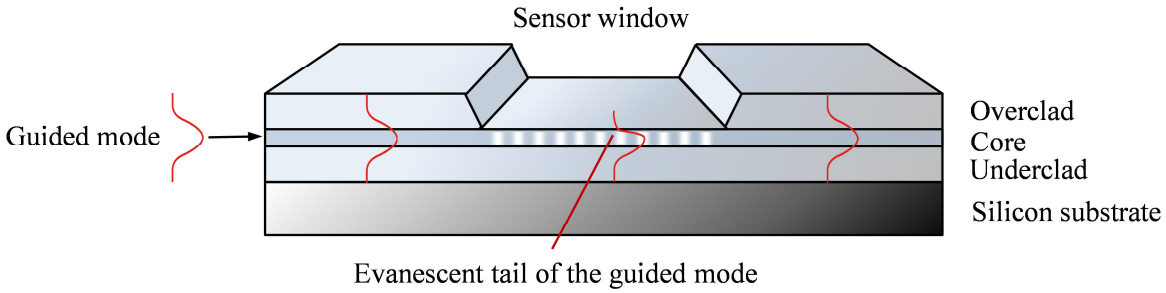

Fig. 5.1 A symmetric mode travelling along a waveguide with a Bragg grating exposed within an etched well, showing the evanescent tail of the mode within the cladding and into the etched region.

5.2.1 Masking

To etch the overclad selectively a mask must be employed. For wet-etched samples this can be achieved by coating the surface with a negative mask that only exposes the regions to be etched to the etchant solution.

Early work used a silicone mask to conceal the region to be etched, before coating the remaining surface and end facets with acid resistant UV-curing glue. When the silicone mask was subsequently removed, the glue formed a negative mask over the surface. While this method worked well, it was less practical for more complex etch designs. For this reason, it was decided to switch to using a polyimide adhesive tape for all further work. The polyimide tape uses a silicone-based adhesive that is acid resistant but easily removed without leaving a residue. The tape can be easily applied to the surface before cutting out any desired regions to be etched. After etching, the tape is simply removed. The precision of this method can be further enhanced by using the high-precision air bearing stages used for the UV writing process. By translating the taped device under a focussed 100 mW 1064 nm laser beam precisely located windows can be cut into the tape to any design that can be programmed in G-code. A schematic of the system is shown in Figure 5.2.

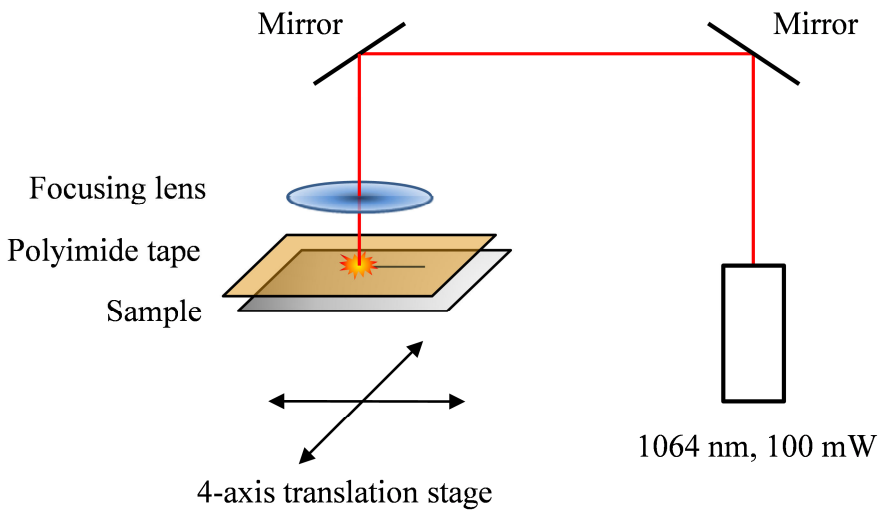

Fig. 5.2 A schematic of the system used for the laser cutting of polyimide tape for precision negative masks used in wet etching.

5.2.2 Wet etching

Silica glass is a commonly used substrate material in micromachining and microfluidics. Glass offers high chemical and heat resistance, high electrical isolation, large optical transmission range and low optical absorption, making it ideal for a wide range of applications from laboratory glassware through to window glass. While silica is resistant to most acids, it is highly susceptible to hydrofluoric acid, HF and its less aggressive analogue ammonium fluoride, NH_4F. Commercial glass etchants typically contain a buffered blend of dilute hydrofluoric acid and

ammonium fluoride. The low concentrations found in such solutions result in a slow etch rate, with an 18 µm overclad layer taking about three hours to etch.

As the overclad is slowly etched away, the proportion of evanescent tail of the guided mode exposed to the etchant increases. The lower refractive index of this aqueous etchant, compared to the removed silica overclad, reduces the effective index of the waveguide; this is detected as a negative shift in the Bragg wavelength. As the etch depth increases, the proportion of the mode exposed increases exponentially, increasing the rate of the Bragg wavelength shift. This is shown in Figure 5.3(a), where a pigtailed Bragg device was immersed in an etchant with real-time monitoring of the Bragg wavelength (and amplitude).

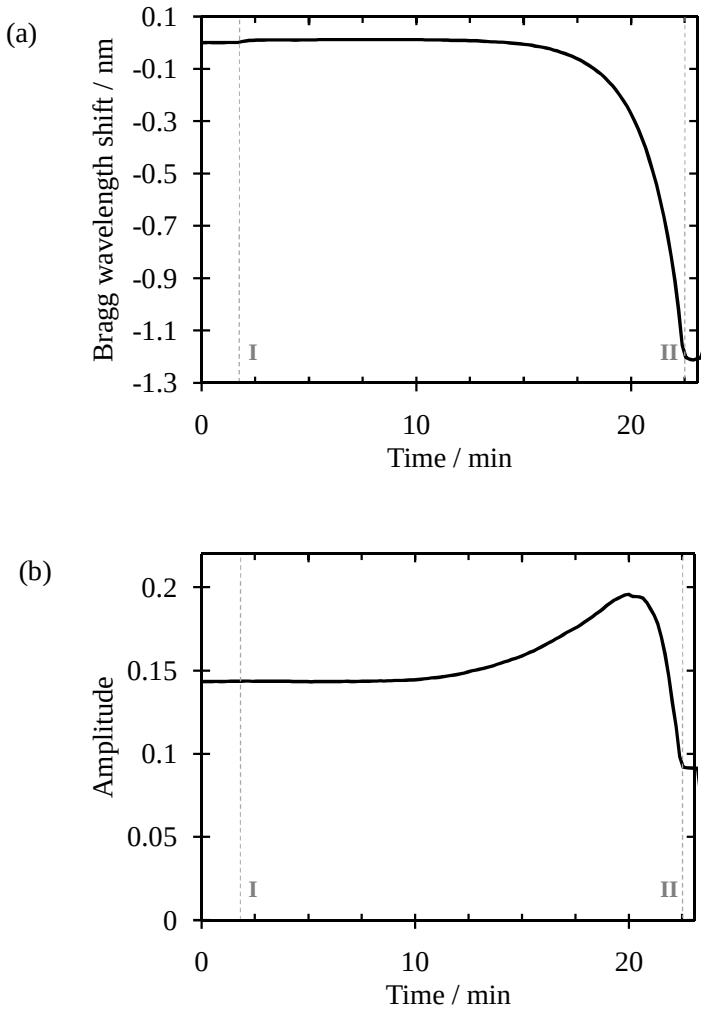

Fig. 5.3 The Bragg wavelength shift (a) and change in Bragg peak amplitude (b) upon etching, demonstrating the negative shift in wavelength and decrease in amplitude. The device was immersed in the etchant at point I and transferred to deionised water at point II.

Initially the amplitude increases (Figure 5.3(b)); this has been attributed to preferential etching of the Bragg grating, giving rise to a 'relief grating'-like periodic

structure on the surface, that enhances the refractive index contrast of the grating, increasing the strength of the spectral Bragg response. This effect was first observed by Snow [202] where, as shown in Figure 5.4, detectable grooves were found to be preferentially etched into a surface, matching the location of the waveguides within the silica. This localised increase in etch rate has been attributed to the increased density of defects within the photosensitised silica.

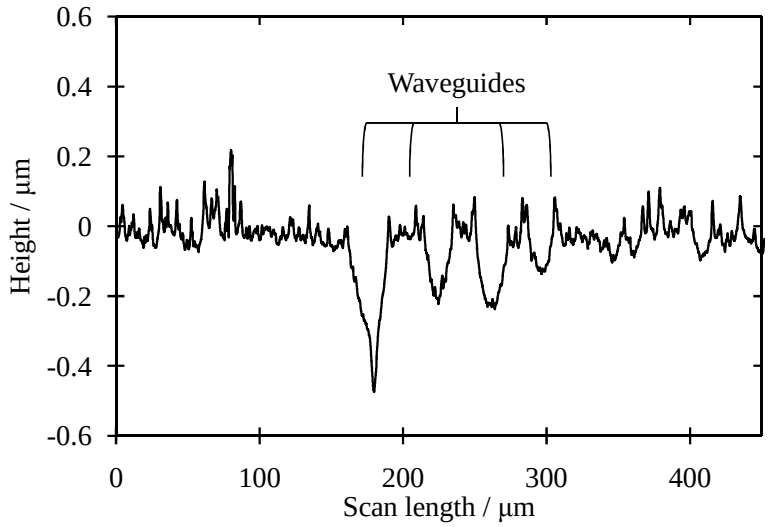

Fig. 5.4 A transverse surface profile to show the preferential etching of four UV written waveguides (data courtesy of B. Snow [202]).

As the etch depth approaches the core layer, the amplitude of the reflected Bragg peak reduces, until eventually the peak is lost and no Bragg response is detected. This effect is two-fold. As the etch depth increases, propagation losses at the boundary between the silica overclad and the etched region will increase, reducing the power in the waveguide. Finally, as the core itself is etched, the strength of the periodic index modulation is reduced, further weakening the grating, until ultimately the core is fully etched and the waveguide is lost.

Clearly this etching process needs to be controlled; the optimisation is a compromise between the sensitivity of the etched device and the strength of the Bragg response. Monitoring this etching process *in situ* through the Bragg response allows for the etch depth to be accurately and reproducibly controlled. It was empirically found that etching until a Bragg wavelength shift of 1.1 nm was detected gave the best sensor devices.

Two main factors have been identified as being important during the etching process; the etch rate and the surface roughness. It is attractive that the etch rate should be able to be increased dramatically without a large increase in the surface roughness. Low surface roughness is important to prevent loss through scattering at the interface with the analyte, reducing the amplitude of the reflected signal. As such, a target etch rate of ~1 µm/min was set, in order to achieve as smooth a surface as possible.

For pragmatic reasons of preparing the etching solution *in situ* on the acid bench in the clean room, concentrations were considered in parts neat acid (commercial concentrated hydrofluoric acid is 48 %) to parts water. Initially the etch rate for a range of concentrations of HF was investigated, as shown in Figure 5.5; the etch rate was calculated by measurement of the step etch depth of a masked FHD sample by surface profiler, after immersion in the etchant for two minutes. The surface profiler was able to calculate one-dimensional surface roughness from this same cross section.

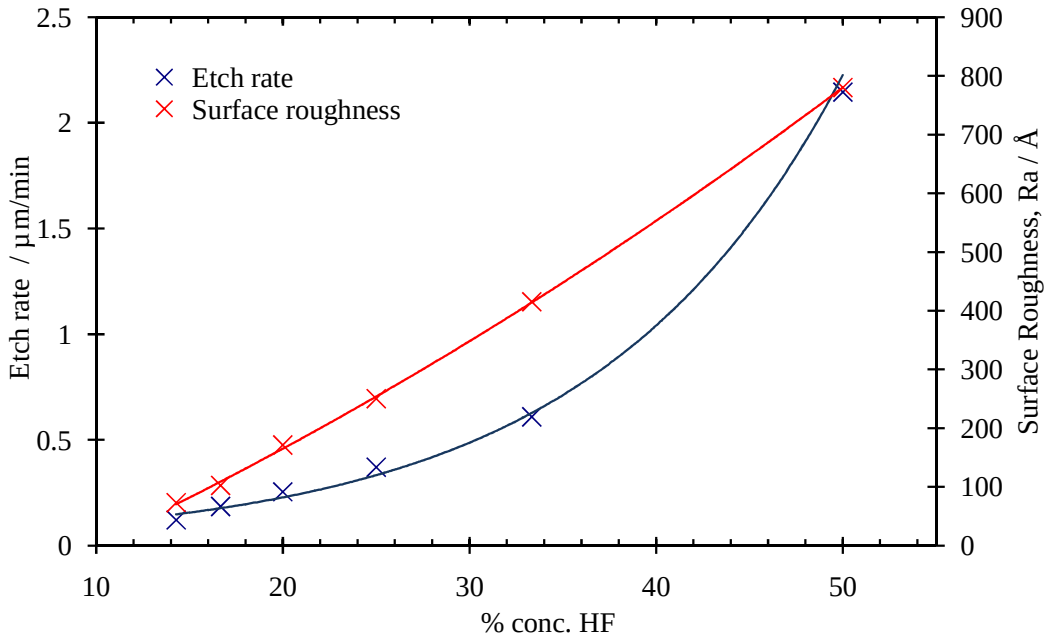

Fig. 5.5 The etch rate and one-dimensional surface roughness of a FHD silica-on-silicon wafer as a function of percentage concentration of concentrated hydrofluoric acid, HF to water.

Clearly, as the ratio of concentrated hydrofluoric acid to water increases both the rate at which the surface is etched and the surface roughness (as defined by R_a, the arithmetic average roughness of absolute deviations from the mean surface level) increase. However this shows that the relationship between the rate and

concentration is not linear. Further, to achieve removal of 1 µm of silica per minute only ~30 % concentrated hydrofluoric acid in water is required.

While the trend above indicates that the surface roughness increases with HF concentration, it is unclear whether this is due to the more aggressive etch or simply a function of etch depth (the surface may continue to increase in roughness as material is removed, irrespective of the rate of removal). As such the time required for an etch depth of 10 µm was predicted for solutions of 17, 25 and 50 % concentrated hydrofluoric acid in water. The surface roughness was additionally quantified in two dimensions by an atomic force microscope (AFM) in addition to the one-dimensional analysis by a step profiler, used above.

Conc. HF / %	Etch duration / min	Etch depth / µm	R_a [1-D] / Å	R_a [2-D] / Å
17	23:00	7.637	1376.8	168.0
25	14:46	8.872	805.3	102.2
50	4:40	9.997	982.4	124.2

Table 5.1 Surface roughness of a FHD silica-on-silicon wafer for different hydrofluoric acid concentrations when etched to a predicted depth of 10 µm.

While the one-dimensional values of surface roughness are much higher than those from the two-dimensional AFM data, the trend is the same. The roughest surface is seen for the slowest but shallowest etch, indicating that this is not simply a function of depth. Further AFM analysis for equivalent etches at 20 µm showed similar surface roughness data, reinforcing this conclusion. The lowest roughness is seen for the intermediate strength solution (25 %) and as such, the surface roughness appears to be dependent on more factors than concentration alone.

5.2.3 Hydrofluoric acid/hydrochloric acid etchant solutions

The defects generated after deep wet etching can be explained by the glass composition. Some oxides, give insoluble products in HF solution. For example, typical oxides found in common glasses include: CaO, MgO or Al_2O_3, all of which form insoluble fluorides on etching [203], although it must be noted that these specific examples are not expected to be present in the FHD silica fabricated for this work.

These insoluble products are deposited on the generated surfaces and act as masking layers. As a result, after etching the surface becomes rough, with much non-uniformity. By adding hydrochloric acid, HCl to the etchant mixture the insoluble

fluorides will be transformed to chlorides, improving the quality of the etching process. Furthermore, increasing the acidity of the etch solution with hydrochloric acid increases the acidity of the etchant solution, further acting to increase the etch rate.

A series of etches were undertaken with both the percentage of concentrated hydrofluoric acid (20, 33 and 50 %) and concentrated hydrochloric acid (0 – 50 %) being varied:

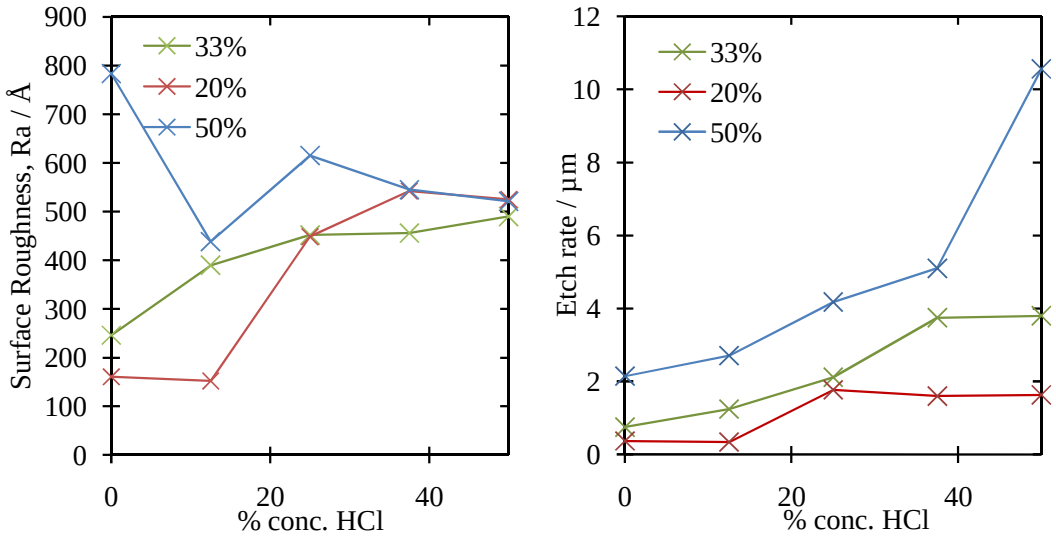

Fig. 5.6 The etch rate and surface roughness of a FHD silica-on-silicon wafer as a function of percentage concentration of hydrochloric acid, HCl for 20, 33 and 50 % hydrofluoric acid solutions.

Figure 5.6 shows that the etch rate can be dramatically increased with the addition of hydrochloric acid, but this effect will saturate when the HCl concentration is greater than that of the HF. While the etch rate is increased, the surface roughness is not significantly affected by the presence of HCl. Increasing the volume of the etch solution used over the 4 mL needed to fill the smallest PTFE beaker into which the sample would fit was shown to have little influence on the etch rate. From these preliminary experiments it was believed that an etching solution of volumetric ratio conc.HF/conc.HCl/H_2O of 4/3/9 would give the best compromise of surface quality and etch rate.

5.2.4 Etch rate as a function of immersion depth

The limitation of using *in situ* monitoring of the Bragg response during etching is that it must be linked to the characterisation set-up by a fibre pigtail. While, the glues used to attach the pigtail to the wafer are generally acid resistant, the optical

fibre needs to be protected. This introduces the requirement that the sample must be mounted vertically on etching. For small samples, or with only a single, small etch region this does not cause a problem. However, for larger or multi-etch samples, any gradient in etch rate will introduce discrepancies in the process. To investigate whether such gradients exist, the etch depth of a FHD silica-on-silicon wafer was measured after exposure to the above etchant solution for a typical etch duration of 18 minutes, comparing both stirred and unstirred systems.

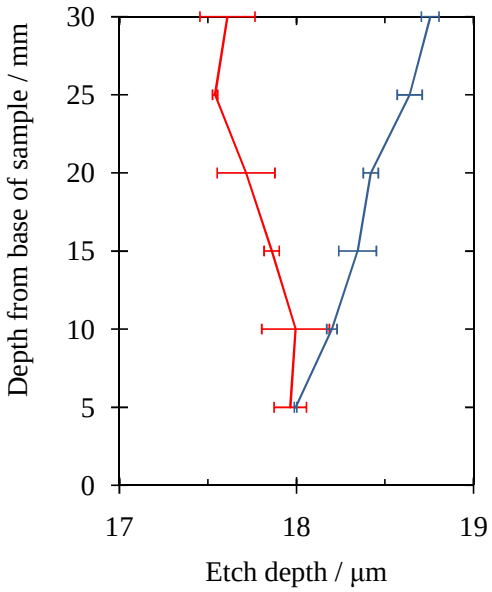

Fig. 5.7 The etch depth of a silica sample on immersion into a hydrofluoric acid etching solution for 18 minutes as a function of immersion depth, with (blue) and without stirring (red). Error bars represent the standard deviation of a series of measzurements.

Figure 5.7 shows that the etch depth of both systems varies with the depth of immersion. While stirring the etchant solution improved the etching gradient it was still not uniform. This is a problem for any system where multiple regions need to be etched equally. This could be resolved using a commercial glass etching cream, allowing the device to be laid horizontally allowing uniform etching. Alternatively a 'topless' wafer can be used, as detailed in Section 5.6.2.

5.3 Surface Roughness and Polishing

The volumetric ratio of HF:HCl:H_2O was investigated and it was found that the optimum etch rate to surface roughness was achieved with a ratio of 4:3:9 respectively. While the etch rate was ~1 µm/min as expected, the surface roughness increased dramatically (R_a(2-d) = 165.8 Å) from predictions and was still 15 – 20 times greater than that of an un-etched sample. A further test confirmed that the

orientation of the sample does affect the surface roughness. To overcome this, the concept of a fast etch with a subsequent polishing stage to restore the surface was considered.

This was achieved through mechanical erosion of the surface with a felt-ended handheld commercial polisher (Dremel 400 series digital rotary tool) with an alkali, colloidal silica solution (Logitech SF1). While these are designed for use in glass polishing they had not been used as a method for polishing an FHD wafer or for restoring an optical surface. Profile data collected indicated that the polished surface was near to the quality of the original silica (R_a (1-D) = 17 Å), as illustrated in Figure 5.8:

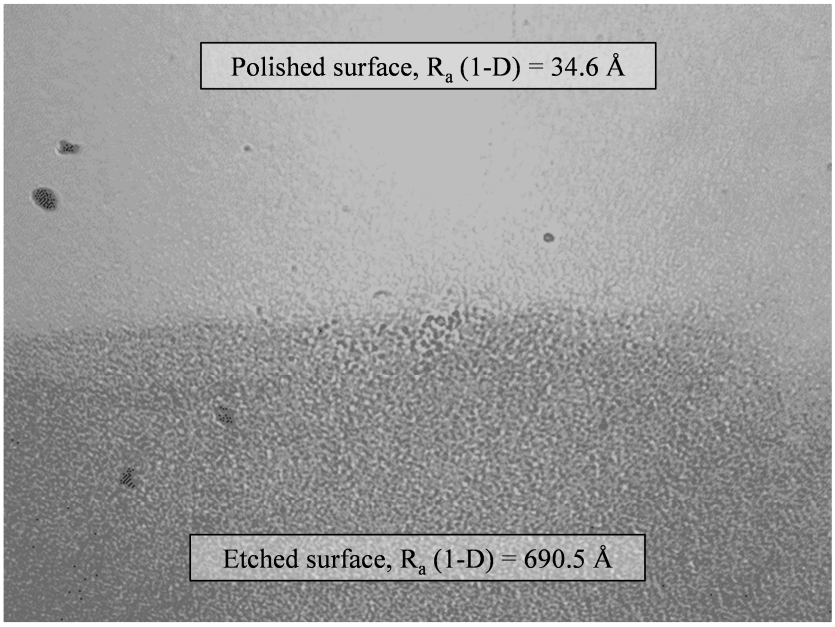

Fig. 5.8 An optical microscope image showing the near optical quality of the polished surface compared to the etched surfaces, one-dimensional surface roughness values are inset.

A polish of one minute increased the measured etch depth by no more than 400 nm. In contrast, polishing by hand removed less bulk material, but it only reduced the surface one-dimensional roughness from 836.5 to 780.9 Å.

As the following AFM images show (Figure 5.9), the two-dimensional surface roughness was dramatically reduced from 165.8 Å to 10.5 Å without loss of the Bragg gratings. As noted previously, the two-dimensional AFM measurements of R_a are much lower than those measured by the surface profiler but show the same trend. Furthermore the polished surface roughness is believed to be limited by feedback

errors within the AFM, and is likely to be more comparable with bare silica ~ 3 Å. The quality of the surface was good enough to see the waveguides within the core layer. The presence of two holes on the polished surface indicated that only a thin layer of bulk material had been removed. If these two features are excluded, the R_a for the remaining surface is 8.3 Å. The lines of small particulates are silica particles from the polishing solution that have become bound to the surface during polishing.

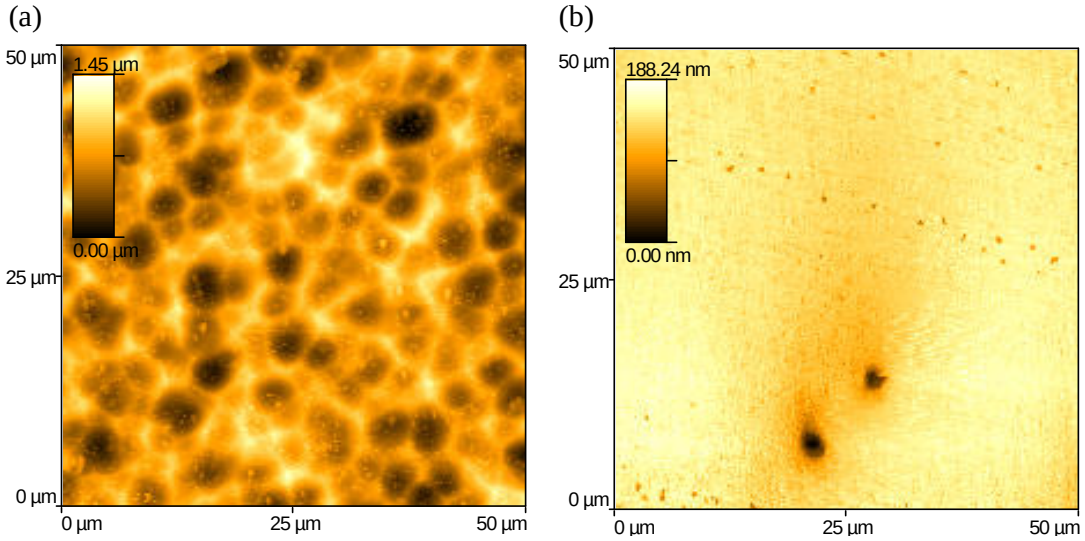

Fig. 5.9 AFM images of the surface of the etched well (a) before [R_a (2-D) = 165.8 Å] and (b) after polishing [R_a (2-D) = 10.5Å]. The lines of particulates on the left image are silica residue from the polishing step.

5.4 Waveguide Design

As mentioned previously, Bragg gratings are inherently sensitive to temperature, and strain. These effects can interfere or mask any wavelength shifts caused by refractive index change making *in situ* referencing necessary. In order to compensate for thermal errors, an additional local Bragg grating of different Bragg wavelength was written near to the etched region. This was left un-etched, and as such was insensitive to analyte but remained sensitive to changes in temperature and strain. In this way the Bragg response to changes in analyte refractive index within the etched region could be separated from other physical effects by a simple first order approximation.

The simplest design involves a linear channel waveguide containing two Bragg gratings, one to act as a buried reference and the other to act as the exposed sensor. While this system works sufficiently, it was decided to develop a device to include a "Y-splitter" junction after the buried reference. This allowed the design to include

two exposed gratings 100 µm apart. Including multiple gratings in parallel within the etched region afforded several advantages: firstly it increased the success rate of device fabrication, with wafer defects or etching anomalies less likely to interfere with the sensor grating; secondly by increasing the number of sensor gratings, the average response can be derived, reducing the standard deviation in the measurement. If these sensor gratings are written at markedly different wavelengths, the 'dispersion fingerprint' of the analyte can be measured, with analytes of similar index at 1550 nm often having different dispersion profiles leading to different responses at other wavelengths [37].

Figure 5.10, shows the typical dimensions of a device containing three waveguides, each containing a reference grating, r followed by a Y-splitter to two sensor gratings, $s_{1\text{-}2}$. The disadvantage of using a Y-splitter is the 6 dB loss incurred at the splitter, however as the Bragg gratings written are typically 20-30 dB above the noise floor, this loss does not significantly affect the precision of the Gaussian fit used to ascertain the Bragg wavelength.

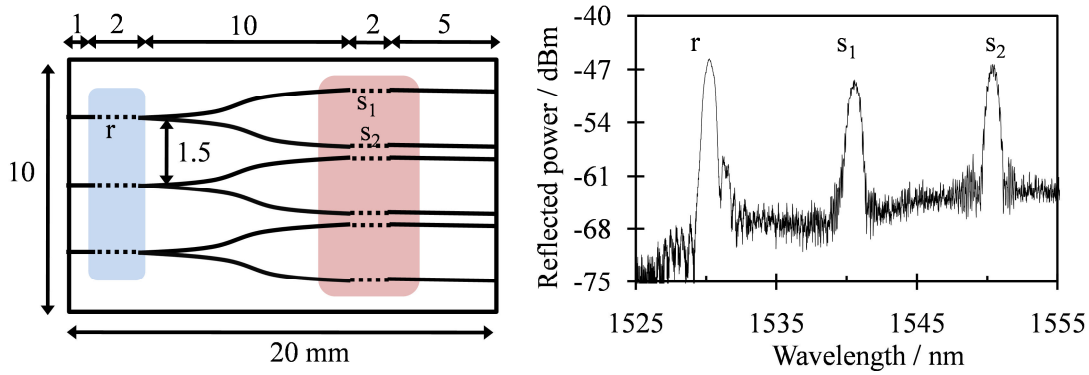

Fig. 5.10 A schematic of the UV written "y-splitter" optical device incorporating an etched well (pink); λ_r=1530 nm, λ_{s2}=1540 nm, λ_{s3}=1550 nm and the corresponding reflectance spectrum showing the Bragg responses.

5.5 High-Index Overlayers[31]

The sensitivity of the device to refractive index is strongly dependent on the fraction of the evanescent modal field that penetrates into the analyte. In air, the lower refractive index above the waveguide results in asymmetry in the guided mode. This shifts the mode further away from the surface, reducing sensitivity. This effect may be countered by the addition of a thin layer of a high-index material such as titanium dioxide or tantalum pentoxide ($n \approx$ 1.90-2.56 [204] and 2.08 [205] respectively), which increases the sensitivity by pulling the guided mode up into the analyte. This has

been previously been shown to enhance the surface sensitivity on Mach Zehnder interferometer-based sensors [154].

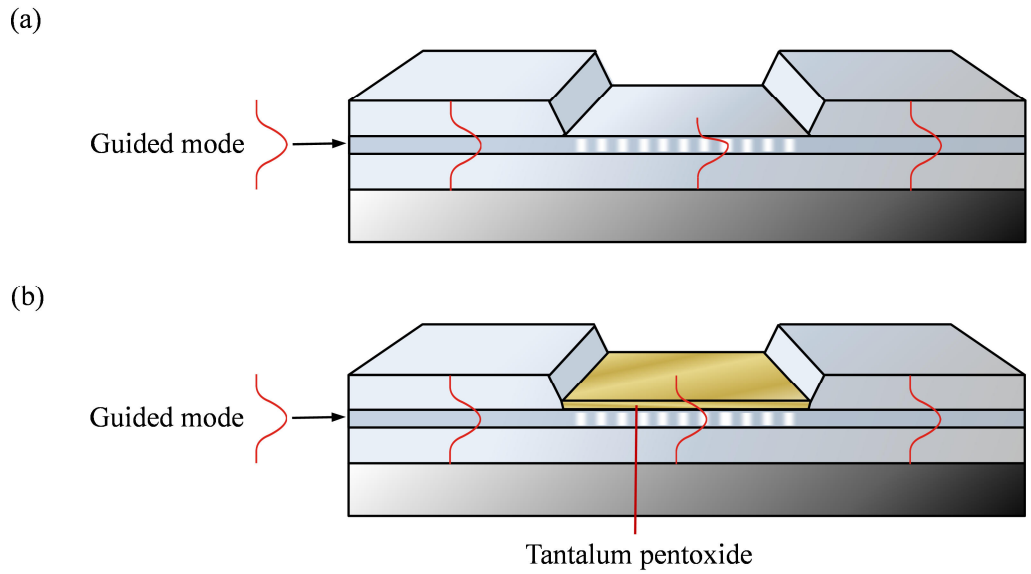

Fig. 5.11 The enhanced symmetry of the guided mode travelling along an exposed waveguide with an overlayer of tantalum pentoxide (b) compared to without (a).

5.5.1 Tantalum pentoxide – a high-index overlayer

For this work it was decided to investigate the deposition of tantalum pentoxide, a material that is well suited for sensor surface applications [206], onto the sensor surface. Tantalum pentoxide has a similar morphology to silica and thus not only produces good adhesion between the layers but allows for the direct application of surface techniques and chemistry developed around silica surfaces to be applied [207]. Tantalum pentoxide also has the advantages of being simple to deposit reproducibly by sputtering; a physical vapour deposition (PVD) technique of depositing thin films by ejecting a material from a target with argon plasma, which then deposits onto a substrate (Figure 5.12).

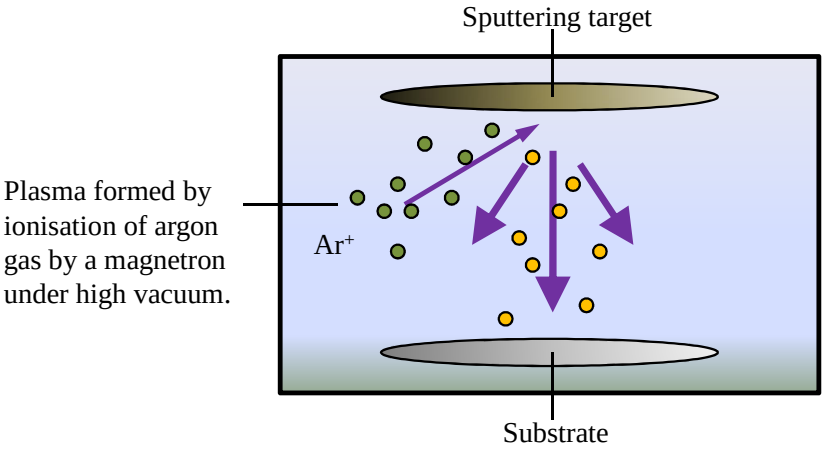

Fig. 5.12 A schematic of magnetron sputter deposition.

The thickness of the tantalum pentoxide overlayer was empirically determined by several calibration samples and modelling the waveguide with Fimmwave to give the optimum sensitivity without loss of guidance, a factor that depends on the index of the analyte being studied. Room temperature sputter deposition of 80.9 nm of tantalum pentoxide under ultra-high vacuum by an "Oxford Instruments Plasmalab 400 plus" directly onto the sensor surface was found to increase the sensitivity to changes in refractive index. This sensitivity increase was shown through comparison of the Bragg response to a series of "Cargille refractive index liquids" (Series AA and AAA) with index from 1.30 to 1.44, both before and after deposition of tantalum pentoxide (Figure 5.13). The sensitivity was found to have increased by over an order of magnitude relative to the bare surface, without altering the reflected Bragg spectrum. This is shown by the gradient, ($^{d\lambda}/_{dn}$) where for a typical analyte of index 1.38 this is found to be 73.0 nm with the high-index layer of tantalum pentoxide, while only 1.63 nm without.

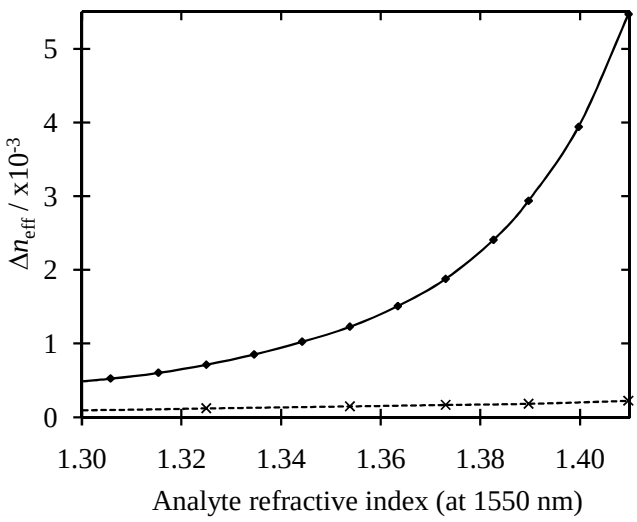

Fig. 5.13 The measured change in effective refractive index of the Bragg grating, for the transverse electric (TE) mode, when exposed to a series of analytes before (dashed) and after deposition of tantalum pentoxide (solid). Error bars are too small to show.

5.5.2 The sensitivity limit of Bragg grating sensors

As discussed in the previous chapter, to form a chemically selective optical sensor an active surface monolayer is often be employed. While this refractometer has been shown to be very sensitive to changes in refractive index in bulk analytes, having the ability to detect changes in index down to 10^{-6}, detection of a surface monolayer is a significantly harder challenge. A molecular monolayer typically consists of discrete molecules bound to a surface, forming a layer less than 1.5 nm in thickness. To monitor the deposition of, and changes in, such a subtle layer requires a very high sensitivity to index change within a tiny fraction of the evanescent regime.

At these high sensitivities it becomes increasingly difficult to make quantitative measurement of the absolute sensitivity limit in a laboratory environment. The challenge comes from the interference of minute surface effects and water adsorption that dominate at the limits of detection [208, 209]. Consequently to provide experimental verification of the sensitivity limit of the sensor, albeit in an idealised environment, the response of the Bragg wavelength to the deposition of ultra-thin layers of silica *in vacuo* was investigated. In this way, the sensitivity limit of the Bragg sensor was defined by the thickness limit of the silica layer detectable by the system. Silica was chosen as it has a comparable refractive index ($n \approx 1.44$) with that of a typical organic monolayer and can be deposited reliably and consistently.

The silica was sputtered onto the surface, allowing precise deposition of silica in 11.5 nm steps (Figure 5.14). An optical fibre feed-through allowed the Bragg grating to be interrogated during the deposition and cooling phases without removal from the sputterer. By measuring within the vacuum system it was possible to avoid surface contamination that would otherwise lead to further thickness changes.

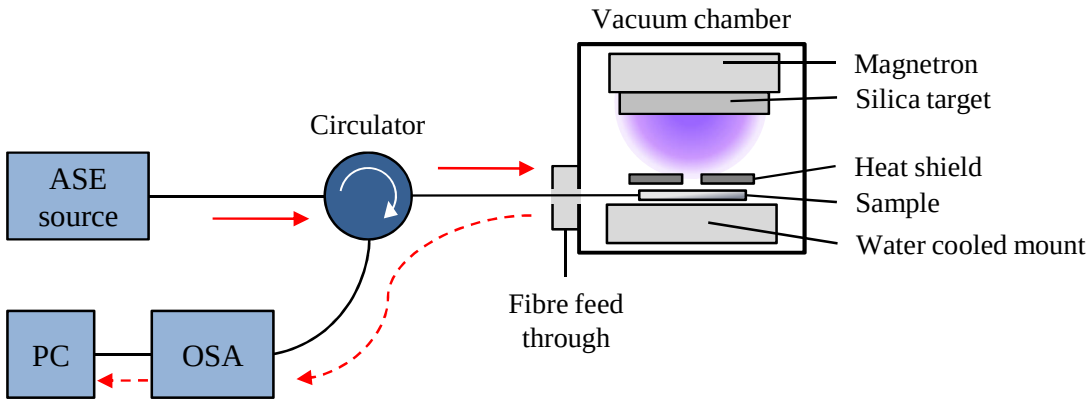

Fig. 5.14 A schematic of the *in vacuo* measurement apparatus used to monitor silica deposition.

As the Bragg gratings respond linearly with changes in temperature, (~10 pm / °C), it was necessary to use *in situ* temperature referencing. In order to compensate for thermal errors, an additional local Bragg grating of different Bragg wavelength was written near to the etched region. In this way the Bragg response to changes in analyte refractive index within the etched region could be separated from thermal effects by a simple first order approximation, a simpler configuration than that of current SPR technology [210].

Silica was deposited in steps of 11.5 nm up to a thickness of 103.5 nm, the sample being allowed to cool between each deposition (Figure 5.15). Region **I** in Figure 5.15(a) corresponds to the deposition of silica, giving rise to a shift in Bragg wavelength. However there is also a temperature component in this response, caused by heating of the surface by the argon plasma during sputtering. Region **II** shows the subsequent cooling of the sensor by ~15 ºC that gave rise to a reverse shift of ~150 pm. A first order compensation was applied to determine the deposition response separately from the thermal effects, transforming the raw data into a series of stepped plateaus (Figure 5.15(b)). Despite disregarding the relatively small tantalum pentoxide temperature coefficient ($^{dn}/_{dT}$) and the changing fraction of the mode exposed to the vacuum, this first order approximation gave a standard deviation on the plateau of 1.0×10^{-6}.

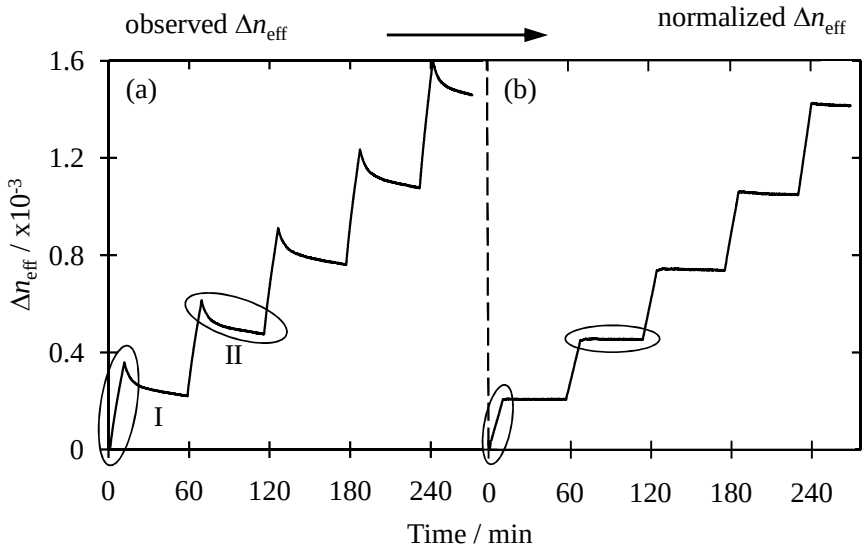

Fig. 5.15 The observed shift in effective refractive index on depositing silica onto the surface in steps of 11.5 nm (a) and after a first order compensation by the temperature reference Bragg grating (b).

Taking the average of each data series on each plateau between depositions allowed the change in the effective index of the Bragg sensor as a function of silica deposition thickness to be derived (Figure 5.16).

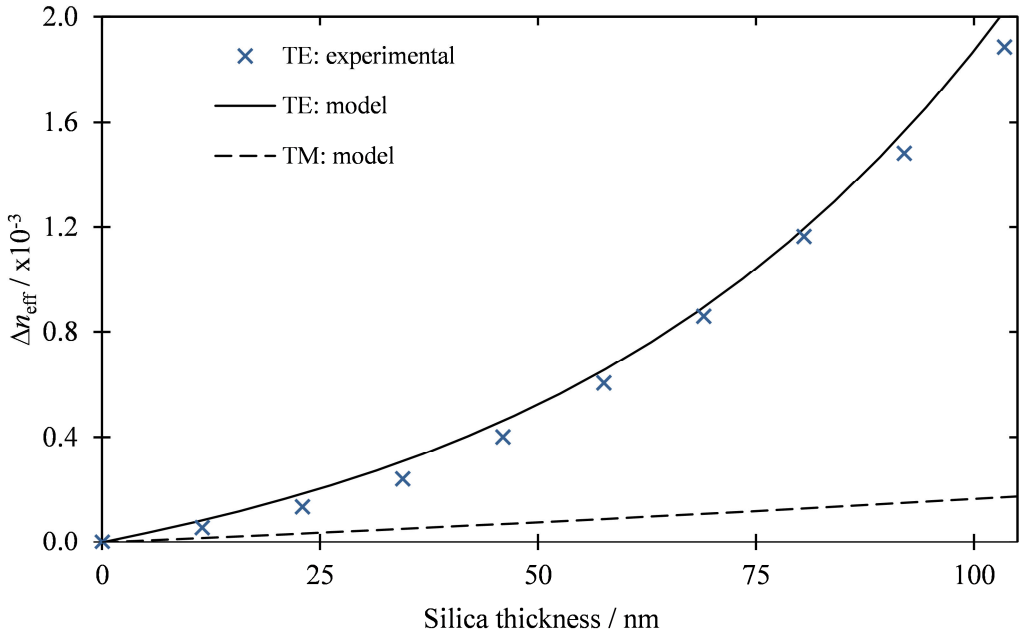

Fig. 5.16 The effective refractive index increase observed upon deposition of silica onto the Bragg sensor surface, compared to the modelled system. Error bars are too small to show.

The modal sensitivity to silica deposition was modelled using Fimmwave (Figure 5.17). This model was validated against the bulk sensitivity measurements taken before and after deposition of tantalum pentoxide, as shown previously in Figure

5.13. These gradient maps illustrate the intensity of the mode across a cross-section of the waveguide for both the bare sensor and with 100 nm of silica deposited. The change in effective index for the transverse electric (TE) mode was found to be consistent with that observed during the *in vacuo* studies. In contrast to the TE mode, the transverse magnetic (TM) mode was found to be relatively insensitive to silica deposition on the surface.

Investigation into the modal overlap of the TE and TM modes with the tantalum pentoxide overlayer revealed birefringence between the modes. The TE mode penetrates much further out of the surface than the TM mode, resulting in high sensitivity (Figure 5.17(a)). In contrast, as shown in Figure 5.17(b) the perpendicular TM mode is suppressed from the surface with little enhancement from the tantalum pentoxide overlayer. The insensitivity of the TM mode can be used for *in situ* temperature referencing through differential studies of the two modes, as discussed further in Chapter 7 [30, 211].

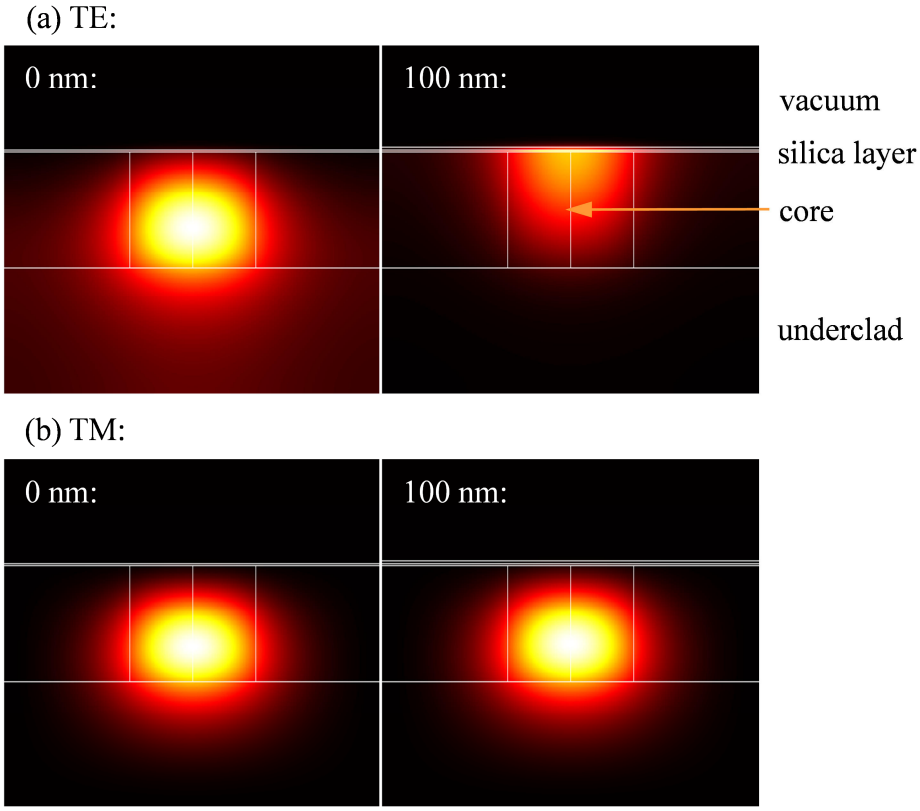

Fig. 5.17 On deposition of a 100 nm silica layer onto the surface of the waveguide, the modelled TE mode (a) is pulled up much further into the tantalum pentoxide overlayer than the TM mode (b), resulting in higher sensitivity to surface changes.

Investigation of the uncertainty in the experimental wavelength measurement for each silica deposition indicated an overall Bragg wavelength shift standard deviation of 1.18 pm, where this was obtained from the standard deviation of the Bragg wavelength measurements for each of the plateaux in Figure 5.15. From the Bragg condition, this wavelength variation of 1.18 pm corresponds to an effective index change of 1.1 x 10^{-6}. This uncertainty in wavelength can be used to infer the minimum detectable increase in silica film thickness upon the sensor surface.

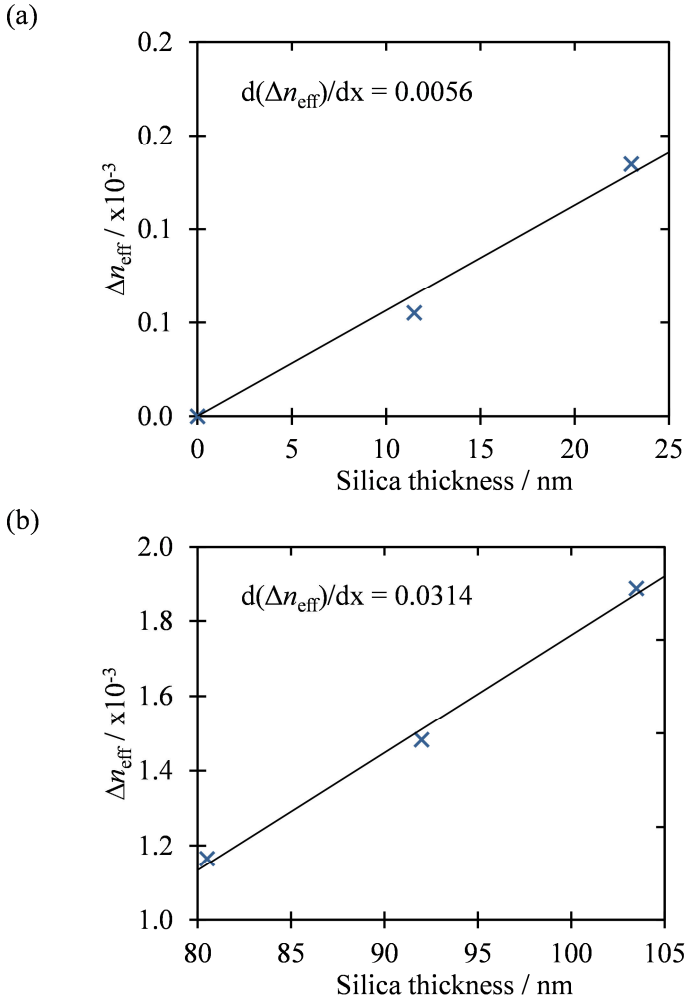

Fig. 5.18 Plots to show the increase in effective index with deposition of silica at both (a) small and (b) large silica film thicknesses. A simple linear trend line has been included to illustrate the sensitivity to deposition in these two regimes. Error bars are too small to show.

In the thin silica film regime as illustrated in Figure 5.18(a), the effective index response of the Bragg sensor to increasing film thickness, $d(\Delta n_{eff})/dx$, is given by the gradient of the linear trend line. Using this gradient of 0.0056 and the uncertainty in the effective index allows for the smallest detectable change in silica thickness to be inferred as 0.20 nm. This corresponds to the smallest increase in silica film

thickness that would be detectable above the random noise in wavelength measurement.

Similarly the thick film regime can be considered (Figure 5.18(b)); here the gradient, $d(\Delta n_{eff})/dx$, is much greater allowing for much smaller increases in film thickness to be detected. By applying the same approach, the inferred silica film thickness detection limit would be 0.035 nm. This increase in sensitivity occurs because the optical mode of the waveguide is pulled up as the vacuum is replaced by the higher refractive index silica layer.

As previously discussed, the growth of a thin film of silica acts as a suitable model for the deposition of an organic molecular monolayer upon the sensor surface, with typical monolayer thicknesses of 0.7–1.2 nm expected in the context of this work (this is discussed further in Chapter 9). The simple analysis above of the gradient in the two thickness regimes combined with the uncertainty in the Bragg grating wavelength measurement indicates that these Bragg sensors should be able to detect increases in silica thickness of ~ 0.2 nm in a vacuum. This thickness threshold is below that expected for an organic monolayer and as such it should be possible to detect the presence of an organic molecular monolayer upon a tantalum pentoxide enhanced Bragg grating sensor. It should be noted that these measurements were carried *in vacuo*, introducing the Bragg grating to the environment will increase the uncertainty in the Bragg wavelength, as physical and chemical variables can no longer be restrained. However, much like the thick film regime above, the higher refractive index of a solvent will act to pull the optical mode further out from the waveguide increasing sensitivity such that it may counter the increased uncertainty in the measurement. Chapter 8 will further discuss the successful attachment and detection of such a molecular monolayer upon a Bragg grating surface.

These results have led to a publication in the journal "Applied Physics Letters" [31]

5.6 Alternative Bragg Grating Sensor Geometries

In addition to the etched sensor geometry, several other methods of fabricating a refractive index sensor exist. Fundamentally all methods focus on exposing the evanescent tail of the guided mode over the Bragg grating; however the approach to achieving this varies. While this work focuses primarily on the 'etched' geometry,

both ‘groove’ and ‘topless’ geometries have been investigated and have been included here for completeness.

5.6.1 ‘Groove’ sensor

Most sensor geometries focus on accessing the evanescent field of the waveguide from the top; however side access is just as effective. To attain side access of the evanescent field, grooves were fabricated into the silica-on-silicon wafer using a dicing saw, with a 50 µm thick saw blade (fabricated by the Centre for Integrated Photonics). As the direct UV writing system’s translation stages are of higher absolute accuracy (<10 nm) than the saw blade’s translation stage (~ µm), the devices were fabricated by first cutting grooves into the substrate and then subsequently direct UV writing.

When cutting a groove into a silica-on-silicon wafer, the quality of the surface roughness is an important parameter to quantify, just as with wet-etched devices. Surface quality of the side walls is dependent upon the cutting conditions including feed-rate, depth of cut, coolant used and coolant flow rate. It was recorded that typical grooves [37], as illustrated in Figure 5.19, have a R_a value of 141.3 nm and a summit density of 13 $Å^{-2}$.

An advantage of the groove geometry is that it is an inherent platform for microfluidic operations. The side access geometry also has the benefit of utilising a combination of S-bends and gratings, such that gratings can be placed at different distances from the edge of the groove. If the different gratings are located at different distances from the edge, their modes will have different penetration depths into the analyte. This information could be used to interrogate refractive index gradients on the surface of the groove walls.

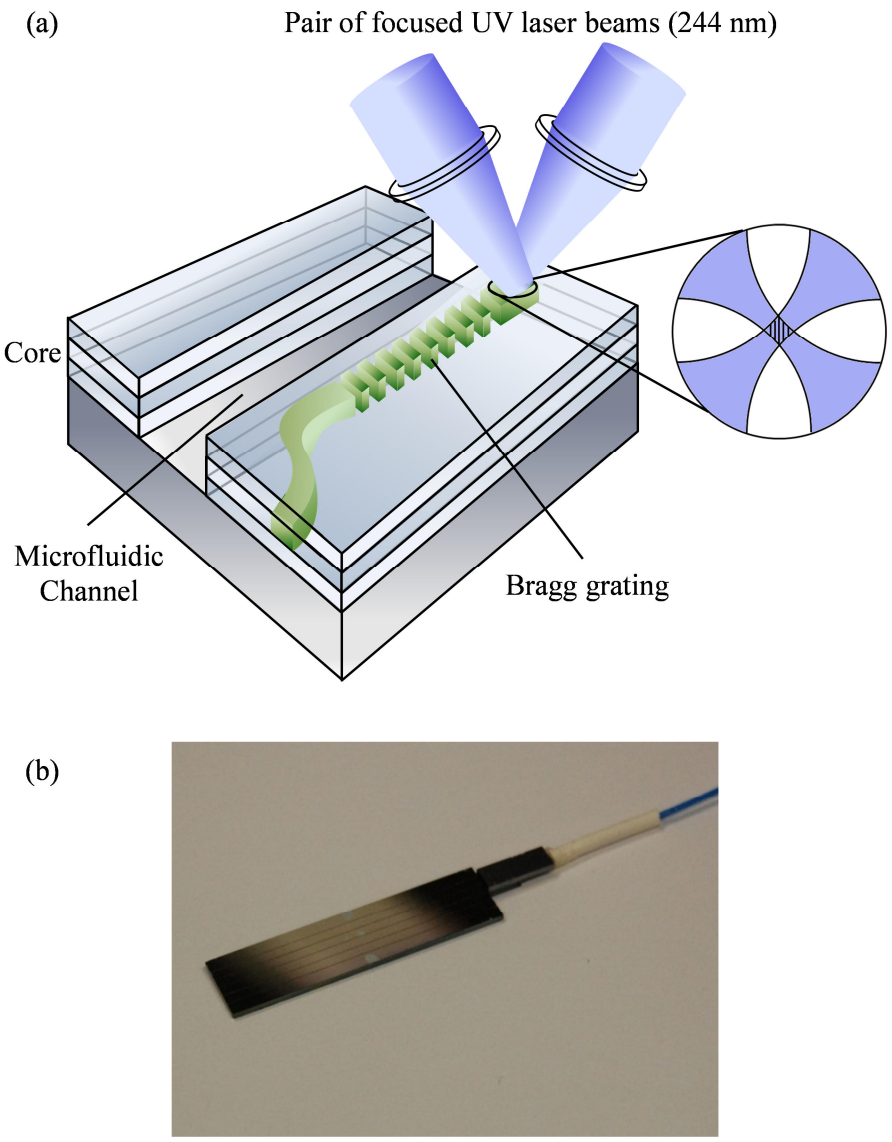

Fig. 5.19(a) A schematic of direct UV grating writing a Bragg grating into a groove substrate using a S-bend waveguide to approach the groove. (b) A photograph of such a tantalum pentoxide coated groove sensor.

Furthermore, the high-index overlayer used to enhance the etch geometry can be applied to groove sensors as well. By mounting the device at 45 ° in the sputterer, with the sensor face exposed, tantalum pentoxide can be sputtered onto the side wall of the groove. Figure 5.20, shows the sensitivity enhancement and induced birefringence for the orthogonal TE and TM modes on deposition of ~100 nm of tantalum pentoxide into the groove. With the etch sensor, the TE mode is seen to be the more sensitive, when switching to the side geometry, this geometrical factor is reversed with the orthogonal TM mode the more sensitive mode.

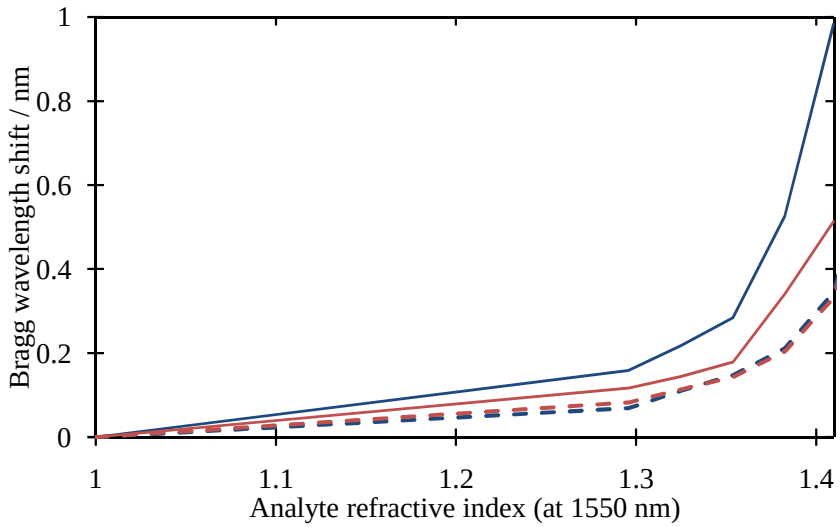

Fig. 5.20 The change in Bragg wavelength for the transverse electric (red) and transverse magnetic (blue) modes of a Bragg grating groove sensor, before (solid) and after (dashed) deposition of tantalum pentoxide. Error bars are too small to show.

5.6.2 'Topless' sensor

The etched devices discussed up to now are UV written prior to etching into a three-layer silica-on-silicon substrate. If during the FHD process, the top cladding layer is not deposited a two-layer structure is formed, where the core layer is exposed. Such a 'topless' geometry instead uses the air as the upper cladding layer. Waveguides and gratings can then be written into the wafer following the same procedure (Figure 5.21). The advantage of this approach is that the evanescent tail of any waveguide written will be exposed without the need for etching or a subsequent polishing step to remove surface defects. This process greatly simplifies the fabrication process for refractive index sensors. Furthermore a high-index overlayer can still be used analogously to the etched geometry to enhance the sensitivity.

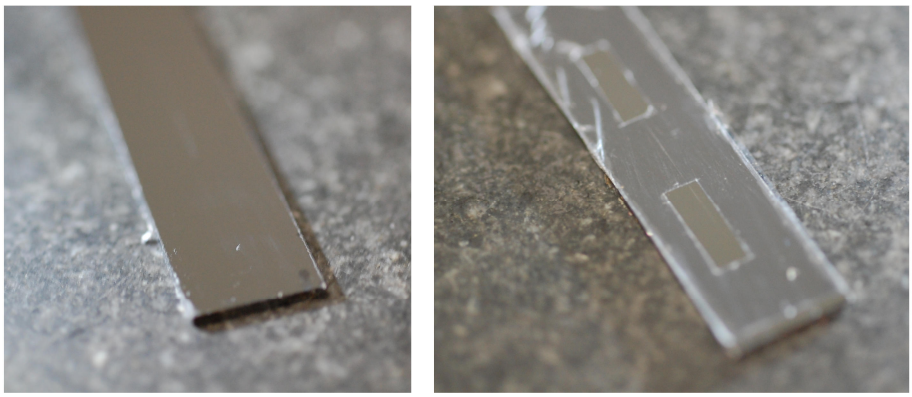

Fig. 5.21 A 'topless' tantalum pentoxide coated refractive index sensor with (right) and without (left) an FEP overlayer, containing two sensor windows.

When a ‘topless’ geometry is employed the entire length of the waveguide is exposed to the environment. This has several implications; firstly it is no longer possible to use a chemically insensitive reference grating to monitor physical changes and secondly any material of high-index (or loss) anywhere along the waveguide length will result in propagation loss, making packaging the device significantly more challenging. For a tantalum pentoxide-coated etched sample the birefringence of the TE and TM modes is only strong in the etched region, with the remainder of the waveguide still buried under the cladding layer. For a ‘topless’ sample this birefringence is present along the entire length of the waveguide, resulting in a different vertical alignment of the input optical fibre for each polarisation state. Due to this misalignment, attempts to simultaneously monitor both modes in such a system result in one mode being markedly weaker than the other.

Many of the drawbacks of using a ‘topless’ over an ‘etched’ device can be resolved by attaching a cladding layer over the non-sensor regions post UV writing. While this could be achieved through deposition of a material such as silica through techniques such as sputtering, the high cost and cleanroom requirements defeat the advantages of using this approach over an etched geometry. However a low cost approach has been developed. Fluorinated ethylene propylene (FEP) is very similar in composition to the fluoropolymer PTFE (polytetrafluoroethylene) sharing in it’s useful properties of low friction, non-reactivity and low refractive index ($n \approx 1.3380$ [212]) but is more easily formable with a low melting point of 260 °C, high transparency and resistance to sunlight.

By heating the UV written ‘topless’ device to 300 °C, a layer of 25 µm FEP sheet can be melted onto the surface. In this layer sensor windows can be cut and peeled away to produce a device much in appearance to the etched geometry (Figure 5.21). This results in a device very much like the etched sensors discussed previously. This regains the ability to use buried references and multiple sensor regions on a single device. However, with an etched sample, the core is etched into, increasing the proportion of the mode penetrating into the analyte that enhances the ultimate sensitivity limit over the FEP coated topless analogue.

On a more practical note, the adhesive used to attach the optical fibre pigtails (Dymax Ultra Light-Weld High T_g Optical Adhesive: OP-4-20632, n = 1.55) is sufficient to pull the guided mode out of the waveguide if any spills over the joint onto the top face of a topless device – a problem that is not normally encountered with etched samples. This can be overcome by frugal application of the adhesive but this leaves a much less robust joint. The FEP overlayer prevents any adhesive contacting the sensor surface, not only making such couplings more straightforward to fabricate but restoring the robustness.

If a good level of adhesion is achieved between the FEP and the silica surface such a device is suitable for use in a microfluidic system, such as discussed in Chapter 8.

5.7 Summary

In summary, direct grating writing can be used to fabricate planar Bragg grating sensors. Fabrication of these etched sensors has been optimised by using a mixed hydrochloric and hydrofluoric acid etchant solution, with a post-etch polishing step being introduced to restore the surface.

The sensitivity of these sensors can be dramatically improved through the inclusion of a high-index overlayer of tantalum pentoxide. It has been shown that, within a vacuum system, the device can detect sub-nanometre thickness changes of a silica layer. This demonstrates that detection of an organic monolayer on the surface is within its capabilities. Although, it must be noted that within a real environment effects such as stress, small-scale temperature fluctuations and contaminants could well increase this sensitivity limit. These results have led to a publication in "Applied Physics Letters" [31].

While the majority of the devices presented in this work are etched, alternative geometries have been proposed, which for specific applications, offer advantages over the etch geometry. Topless devices have been applied to the fabrication of a reconfigurable Bragg grating in Chapter 6 and combined with the groove geometry, these have been used to develop prototype microfluidic sensors in Chapter 8.

6. Reconfigurable Optical Bragg Gratings

6.1 Introduction

The optical telecommunication industry is currently in a state of growth, which is driven by several factors including an increase in demand for high-definition multimedia over the internet and a change of global dynamics. The vast capacity of optical telecommunication transmission is achieved through the use of silica-based optical fibre; an overview of which can be found in the introductory chapter.

To allow for high capacity, optical telecommunication networks require the routing of signals between Wavelength Division Multiplexing (WDM) channels. This can be achieved using various optical filtering techniques including arrayed waveguide gratings, diffraction gratings, thin film filters, Bragg gratings, micro-resonators, photonic crystals or liquid crystals and further description of these methods can be found in a review by Eldada [213]. For control over network routing these filters require tuning, which can be achieved through thermo-optical, electro-optical or mechanical-optical means, achieved using optical fibre components or integrated optical circuits. The elegance of using integrated optics is that many components can be compactly fitted onto a single device.

6.1.1 Reconfigurable optical Bragg gratings

Reconfigurable optical devices are of great interest for telecoms applications; including dispersion compensation and tuneable add-drop multiplexers. Bragg grating filters, with the advantages of potential narrow bandwidth and low crosstalk, are potentially important elements in such systems. For these applications, optical Bragg grating structures need to be reconfigurable with both fine control and wide

tuneability of the Bragg wavelength desired. Previous approaches to this problem were to incorporate a degree of reconfigurability into existing Bragg devices through tuning of the refractive index by temperature [214], piezoelectric [215], magnetostrictive [216], or mechanically induced strain [217]. With some exceptions, these all require a continual supply of electrical power to maintain the altered wavelength.

6.1.2 Photorefractive organic materials

Organic polymers have found many applications in electronic and optical devices. They offer process compatibility, flexibility in design, and the ability for integration of electronic and optoelectronic functions. Numerous polymer systems have been developed for optical applications, the key requirement imposed for such materials being transparency. Much interest has focussed on acrylic polymers because of their well-known optical properties and good film-forming capability [218]. Furthermore, azobenzene-based polymers can act as photosensitive, nonlinear optical, or photorefractive materials with ever increasing fields of application, including: programmable optical interconnects; electro-optic modulation; coherent image amplification; and holographic storage [219].

Barley [220] has reported an example of a siloxane-based polymer functionalised with a photoresponsive azobenzene derivative. This had a refractive index compatible with that of telecommunication grade devices (~1.46), usefully lower than that seen in other active materials such as liquid crystals. The polymer contained only 5 % azobenzene units but still exhibited a change in refractive index of 3.5×10^{-3}. Incorporation of such a polymer into an integrated Bragg grating device would allow a latched reconfiguration of the Bragg wavelength without the need for continual electrical input by photo-switching between isomeric states.

Examples of such a reconfigurable Bragg grating device exist within the fibre regime [221]. These differ from the approaches presented here in that the grating is written directly into the photoresponsive polymer. Through using the induced index change to modulate the polymer index and use of a wide range of different period masks, a wide range of Bragg wavelengths can be achieved, with a simple heating step necessary to erase the grating. While the tuneability of the Bragg wavelength is orders of magnitude higher than those presented within this chapter, there are several compromises that make this proof-of-concept impractical. The largest constraint is

the weak reflectivity of the induced grating structure that would need to be much longer than the gratings used here to achieve practical levels. In addition such grating lengths would have too small a bandwidth for real world applications. By coupling a prewritten integrated Bragg grating device with a photoresponsive polymer, this chapter shows that a suitable tuning for practical applications is achievable while still maintaining a good quality grating response.

6.2 Azobenzene

The simple azobenzene motif can undergo reversible photoisomerisation allowing the photoactive units to be optically pumped almost exclusively from the *trans* to the *cis* isomeric state upon exposure to ultraviolet light.

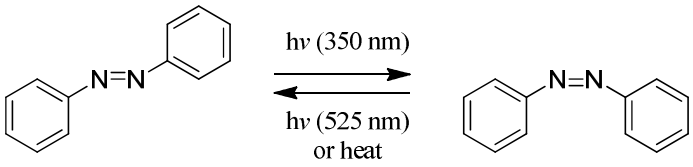

Fig. 6.1 *Trans* to *cis* photoisomerisation of the azobenzene unit.

Upon isomerisation there is a change in the polarisability of the azobenzene molecule, resulting in a change in refractive index. It has been reported [222] that the *trans*-isomer is thermodynamically more stable by 50 kJ mol^{-1}, while the barrier to photoisomerisation is approximately 200 kJ mol^{-1}. The *cis*-isomer will slowly relax thermally back to the *trans*-isomer in the absence of light, but the activation barrier for this process is 96 kJ mol^{-1} in solution or 130 kJ mol^{-1} in the solid state. The corresponding half-life of the *cis*-isomer is of the order of a day at room temperature.

6.2.1 The effect of para substituents on the azobenzene absorption spectrum

The absorption spectrum of the azobenzene unit contains an intense peak corresponding to the π-π* electronic transition of the trans-isomer and a weak peak that originates from the weak n–π* electronic transition of the *cis*-isomer [223]. The change in absorption upon photoisomerisation is directly related to the change in refractive-index. This is defined by the Kramers–Kronig relationship (Chapter 2), whereby a larger change in absorption or an adsorption closer to the wavelength of interest implies a greater change in refractive-index. This allows the change in refractive-index to be predicted from the magnitude of the change in the absorbance spectrum. To investigate the change in refractive-index upon photoisomerisation, a

family of para-substituted 4-phenylazophenoxyacetic acid derivatives were synthesised, as shown in Figure 6.2. Further details of the synthesis and characterisation of all compounds discussed in this work can be found in the synthesis section of Chapter 12.

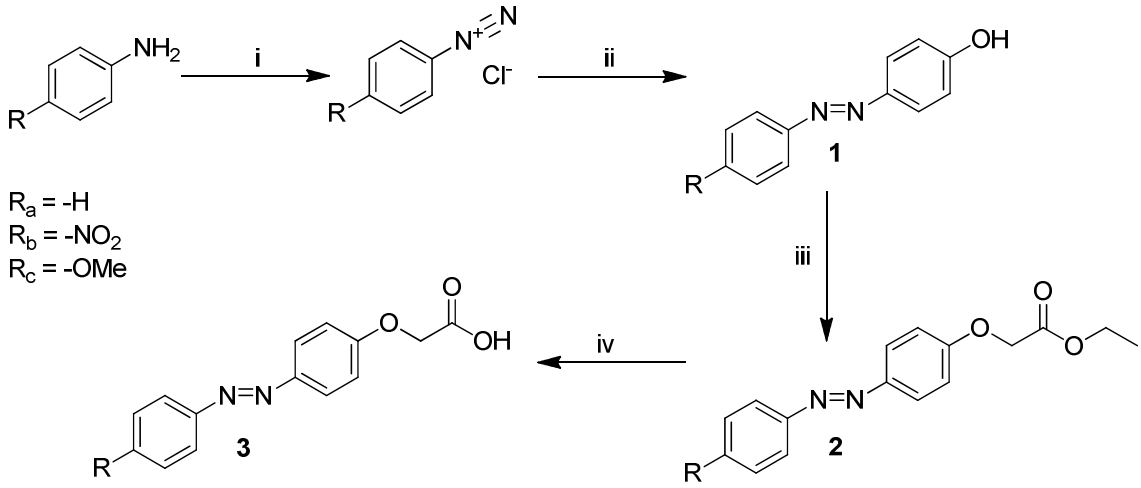

Fig. 6.2 The synthetic pathway towards a family of para substituted azobenzene derivatives; i) $NaNO_3$, HCl, <5 ºC, ii) phenol, <5 ºC, iii) ethyl bromoacetate, K_2CO_3, NaI acetone, iv) NaOH, ethanol.

The relative absorbance of the two isomers is dependent on the electron density within the conjugated azobenzene motif. Upon photoisomerisation, the azobenzene passes from the planar *trans*-isomer to the twisted *cis*-isomer in which the phenyl rings are rotated out of alignment to avoid steric interference. This results in reduced conjugation in the *cis*-isomer. Increasing electron density within the conjugated system exaggerates this difference in orbital alignment between the fully conjugated and partially conjugated states. This results in significant differences between the UV-visible spectrum of the electron rich *p*-methoxy derivative, **3c**, and the electron deficient *p*-nitro derivative, **3b**.

The solution phase UV-visible absorption spectra for compounds **3a**, **3b** and **3c** are shown in Figure 6.3, for a concentration of 2.5 x 10^{-5} $moldm^{-3}$ in methanol with a path length of 1.0 cm. For all three compounds, exposing the *trans*-isomer to ultraviolet light, at 365 nm, induces photoisomerisation to the *cis*-isomer with a reduction of the peak at 340-370 nm. For **3c**, the strong peak at 356 nm undergoes complete loss while simultaneously a second peak, corresponding to the *cis*-isomer, is observed to form at 444 nm. A similar transition is observed for **3a**, albeit to a lesser extent, with only a decrease in the absorption peak at 342 nm. In contrast, the

p-nitro-functionalised derivative **3b** shows a much less marked spectral change, with the formation of the new peak at higher wavelength not being observed.

While **3b** is the most polar of the three compounds, it has the lowest electron density within the conjugated system and this is seen with the smallest transition in the absorption spectrum upon photoisomerisation. In contrast **3c** has two electron-donating groups on the periphery of the azobenzene core and this correlates to the most marked change in the UV-visible absorption spectrum.

The reverse isomerism back to the *trans*-isomer can be achieved thermally, but for absorption studies this was achieved through exposure of the azobenzene derivative to laboratory fluorescent ceiling lighting. This broadband white light source was able to stimulate the absorption band of the *cis*-isomer at 450 nm, leading to reconversion to the *trans*-isomer in a comparable timescale. Using an optical power meter calibrated to 450 nm in combination with both a '400 nm long-pass' filter and '500 nm short-pass' filter, the intensity of the fluorescent ceiling lighting at 450 nm was estimated to be 19.6 µW upon the bench-top (corrected for the transmissivity of the pair of filters, measured as 72.8 % at 450 nm by a UV-vis spectrometer). Without use of the notch-filter, the optical power of the white light source was measured to be 180.6 µW.

It should be noted here, that the Bragg grating photoswitching studies discussed in Sections 6.4 and 6.5 used an alternative stimulation at 254 nm to achieve reconversion using a UV light source.

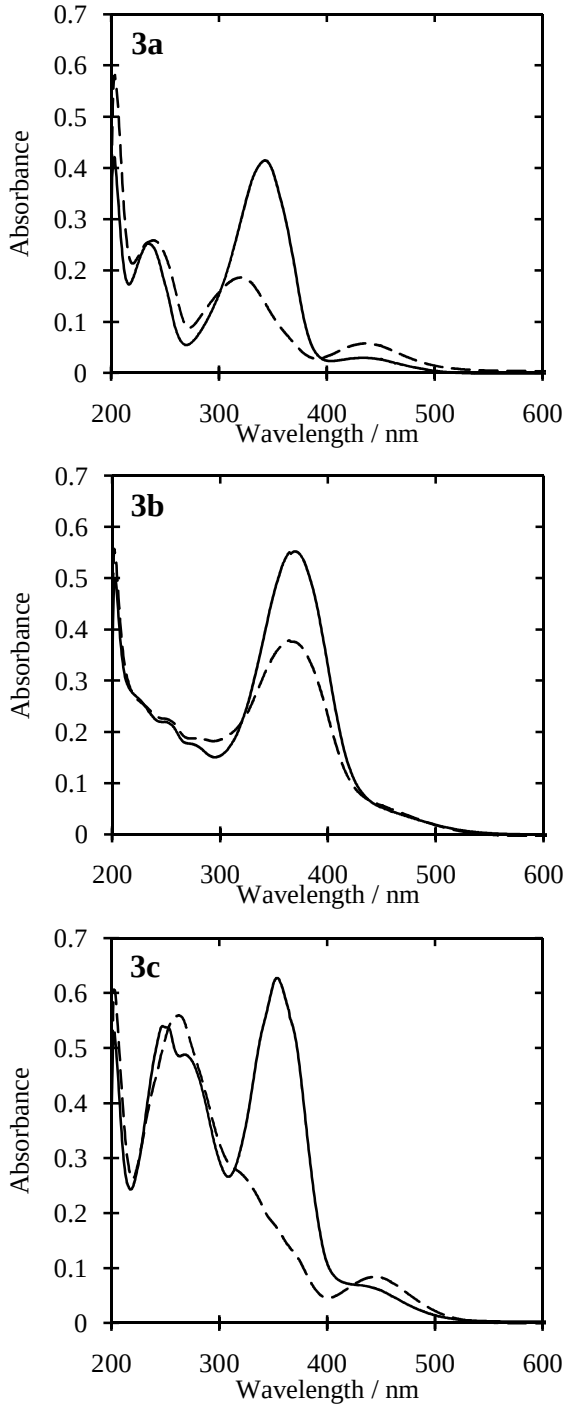

Fig. 6.3 The absorption spectra for para substituted azobenzene derivatives 3a-c in methanol, illustrating the difference between the *trans* ground state (solid) and the photostationary state (dashed): *cis*-3a (λ_{max} = 320.5, 450.5 nm) and *trans*-3a (λ_{max} = 342.0 nm), *cis*-3b (λ_{max} = 367.5 nm) and *trans*-3b (λ_{max} = 370.0 nm), *cis*-3c (λ_{max} = 444.0 nm) and *trans*-3c (λ_{max} = 356.0 nm).

The relative populations of the photostationary states for **3a-c** (defined here as the point at which further irradiation with UV light at 365 nm does not result in further spectral changes) were investigated by NMR spectroscopy. As reported by Wazzan [224], the chemical shift of the aromatic protons of an azobenzene dye can differ by as much as 1 ppm between the two isomers, with this separation sufficient to

distinguish between these isomeric states. Through use of the integrals the cis:trans ratio can be calculated. Figure 6.4 highlights the aromatic region of the NMR spectrum for **3a** at the photostationary state (a) and after thermal reconversion back to the initial state (b):

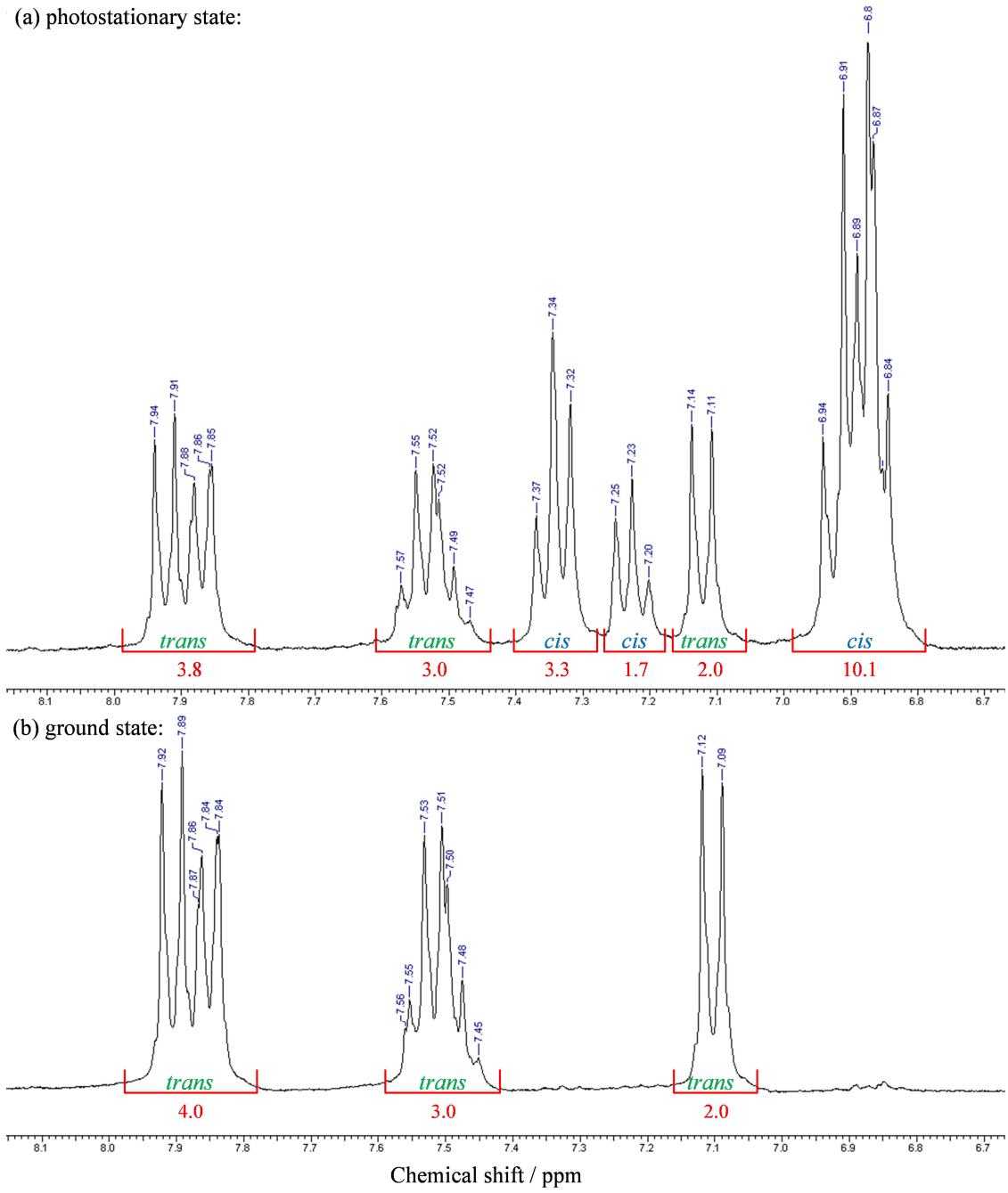

Fig. 6.4 The NMR spectra in deuterated methanol for 3a at the photostationary state (a) and after thermal reconversion back to the initial state (b), demonstrating photoisomerism to the *cis*-isomer. The *cis:trans* ratio is calculated to be 63:37 at the photostationary state.

NMR spectra were collected for the initial state, at the photostationary state and again at the ground state after thermal reconversion – demonstrating the reversibility

of any observed changes, with the initial and reconverted spectra observed to be identical. It was found that unlike the dilute solutions used in the absorption studies, the more concentrated solutions required for NMR analysis resulted in much slower photoswitching (2-4 h). To ensure that the photostationary state was achieved, samples were taken, diluted with methanol and the absorption spectrum compared to those in Figure 6.3, when no further change was observed the solution was transferred to a NMR tube in the dark and the spectrum collected.

Compound	*tran:cis* ratio	
	ground state	photostationary state
3a	100 : 0	3 : 63
3b	100 : 0	66 : 34
3c	100 : 0	33 : 66

Table 6.1 The relative populations of the photostationary state for compounds 3a-c.

While compounds **3a** and **3c** show a significant proportion have isomerised to the *cis*-isomer, **3b** demonstrates a much smaller conversion, with the *trans*-isomer still dominant. This is consistent with the much smaller change in the absorption upon irradiation (as shown in Figure 6.3). While the ratio of conversion to the *cis*-isomer is much lower than would be expected, with near complete conversion reported in polymer systems [225], this may be due to a combination of the high concentration of solution and the low power of the UV light source used.

6.3 An Azobenzene Functionalized Methacrylate Co-polymer.

Methyl methacrylate-derived co-polymers, such as poly(methyl methacrylate / 2-hydroxyethyl methacrylate), P(MMA)(HEMA), have suitable refractive-indices for use in waveguide systems (refractive-index of P(MMA)(HEMA) = 1.497 – 1.516, depending on the MMA:HEMA composition [223]), with the pendant hydroxyl groups in the latter component allowing for further functionalisation. The present work describes the radical copolymerization of methyl methacrylate and 2-hydroxyethyl methacrylate to form a 51:49 P(MMA)(HEMA), **5**, co-polymer, into which 4.8% para-methoxy azobenzene molecular units, **4**, were incorporated along the polymer backbone, **6** (Figure 6.5). The resulting MMA/HEMA ratio was determined by comparison of the integrals of the peaks in the ^{1}H NMR spectrum [223]. This

technique was further applied to calculate the molar ratio of azobenzene units present along the polymer backbone as a ratio of functionalised monomer units present.

The weight average molecular weight (M_w, expressed as 'PMMA equivalent' molecular weight) of **5** was determined to be ~190,500 by GPC (gel permeation chromatography), increasing to ~301,500 after attachment of the pendant azobenzene arms, **6**. A similar trend was observed for number average molecular weight, M_N, which increased from ~65,200 to ~90,850, resulting in the polydispersity increasing from 2.9 to 3.3.

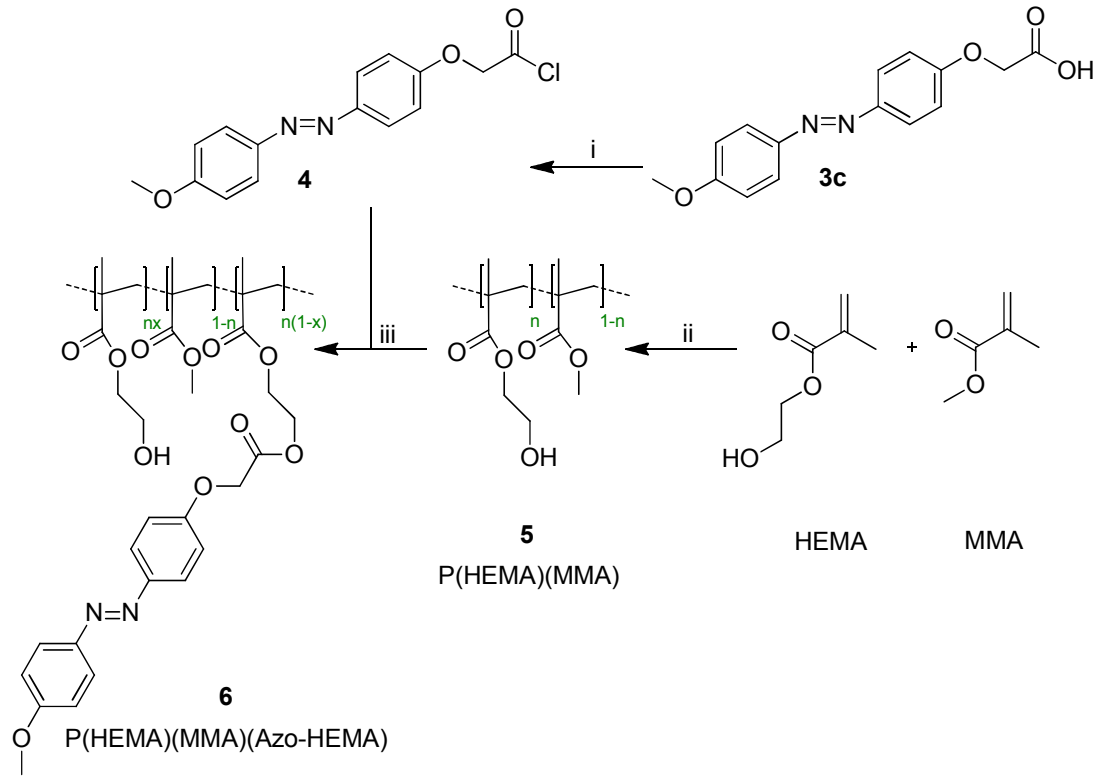

Fig. 6.5 The synthetic pathway towards an azobenzene functionalised methracylate co-polymer; i) thionyl chloride, reflux, ii) AIBN, methanol, iii) triethylamine, 2-butanone.

The UV-visible absorption spectrum for the co-polymer film, **6**, spun onto a silica substrate, shows that there is an intense absorption peak at 361 nm (Figure 6.6) corresponding to the *trans*-isomer and a weak peak at 451 nm which originates from the *cis*-isomer. When the film is irradiated by ultraviolet light at 365 nm, the azobenzene units within the co-polymer undergo *trans-cis* isomerisation; indicated by the decline of the strong *trans* and increase of the weak *cis* absorption band. After twelve minutes, no further change was detected in the absorption spectrum,

while the reverse isomerisation from *cis* to *trans* took fifteen minutes when illuminated by laboratory fluorescent ceiling lighting.

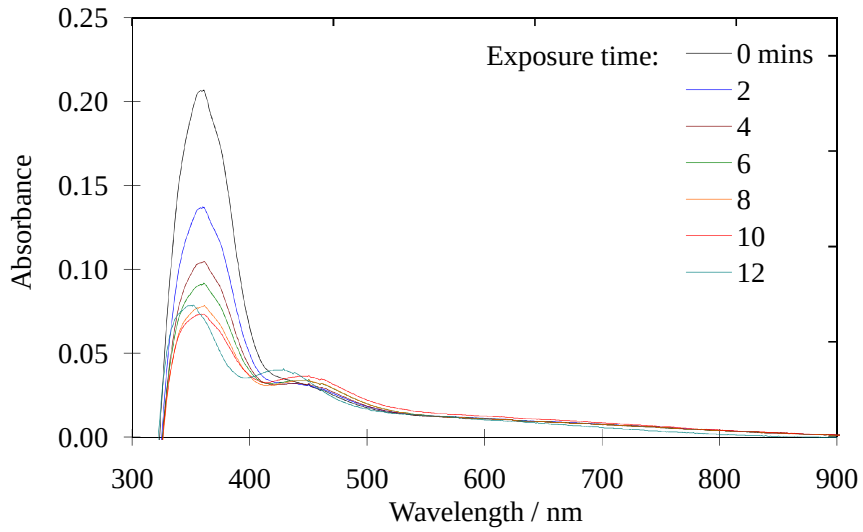

Fig. 6.6 Time-lapse UV-vis absorption spectra showing the *trans-cis* transition of a 191 nm thick *p*-methoxy azobenzene containing methacrylate co-polymer film, on exposure to ultraviolet light (354 nm) over 12 minutes.

6.4 A Reconfigurable Optical Bragg Grating.

As discussed in Chapters 3 and 5; a 'topless' silica-on-silicon sample was fabricated. On exposure to a pair of interferometric UV laser beams, four Bragg gratings of different periods were written simultaneously along the channel waveguide (Figure 6.7) that can be interrogated at both 1550 and 780 nm bands.

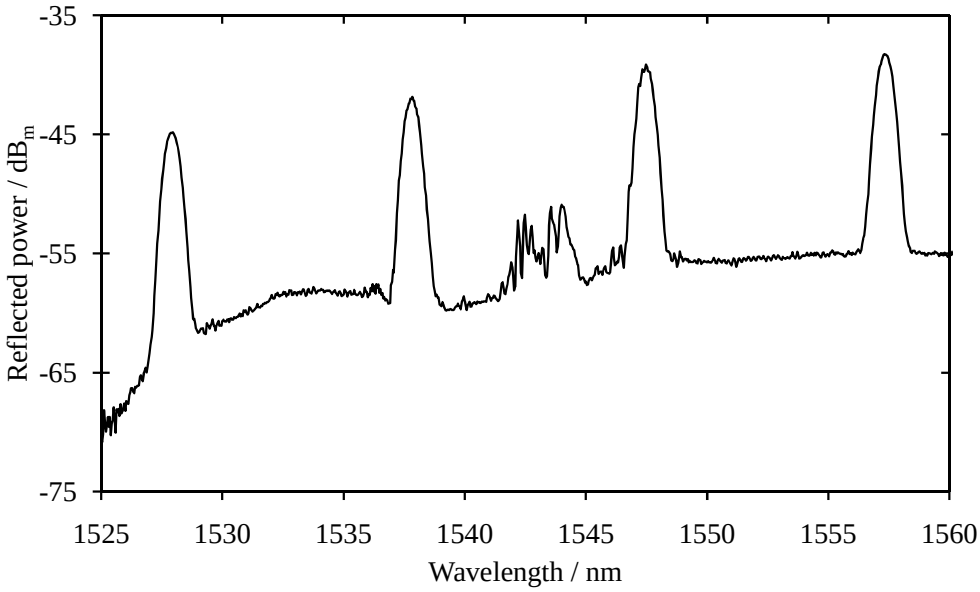

Fig. 6.7 Un-normalised reflected spectrum of the topless Bragg grating device (the response at ~1543 nm corresponds to a wafer defect crossing the waveguide).

The exposed evanescent field caused the optical mode to be sensitive to the refractive-index of its surroundings and the corresponding shift in peak wavelength of the Bragg spectrum was used to interrogate changes in this environment. Onto this surface a 413 ± 27 nm thick film of the azobenzene-functionalised co-polymer, **6**, was spun (Figure 6.8). The presence of the film and its ability to undergo photoisomerisation was confirmed by diffuse-reflectance UV-visible spectroscopy.

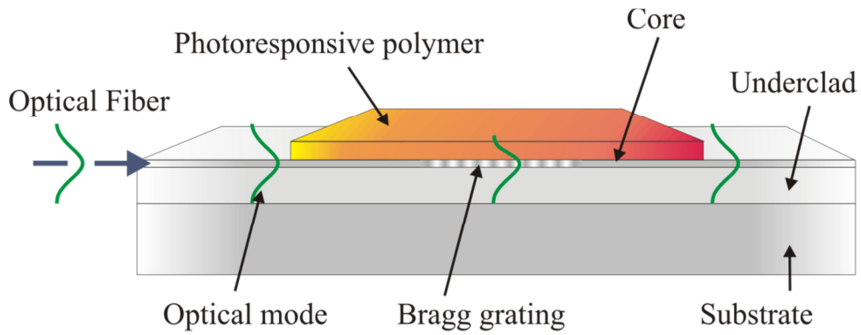

Fig. 6.8 A schematic of the evanescent field of the optical waveguide penetrating into the photo-responsive azobenzene co-polymer film.

6.4.1 Interrogation of the Bragg response at 780 nm wavelength

Analysis initially focussed on the interrogation of the Bragg responses around 780 nm, spectrally near to the absorption feature and hence a large refractive index change should be seen (Chapter 2: Kramers-Kronig relationship). At this wavelength, the co-polymer induced high optical loss into the waveguide device, with almost total loss of the optical mode after travelling only 20 mm along the polymer-coated waveguide (~1 dB/mm). Despite this loss, it was possible to interrogate the reflectance spectrum of two Bragg gratings within the waveguide. The sample was alternately exposed to ultraviolet light at 365 and 254 nm, with thermal changes being monitored by a thermocouple in thermal contact with the optical device. The Bragg response demonstrated reproducible wavelength tuning between the two isomeric states, separated by 30 pm – a well-resolved transition that corresponds to 17 GHz of spectral tuning at 780 nm (Figure 6.9).

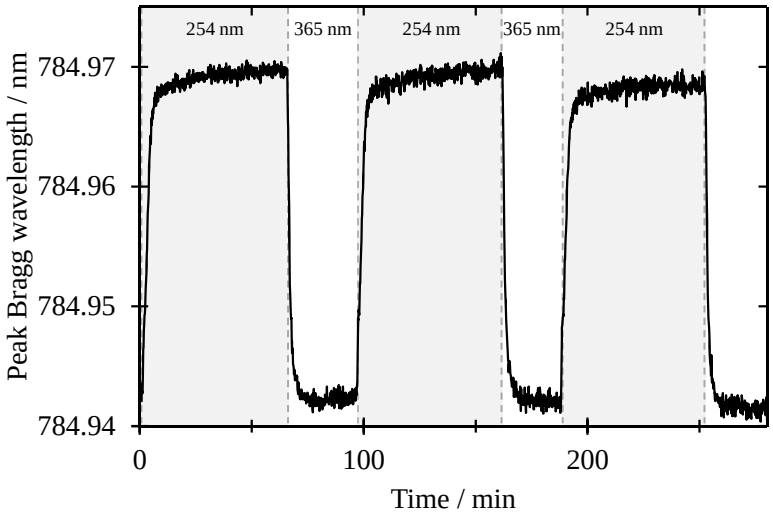

Fig. 6.9 Reversible photo-switching between the two isomeric statesof 6 results in a detectable optical Bragg shift of 30 nm when interrogated at ~780 nm. Photoisomerisation was achieved through alternate exposure to 365 nm and 254 nm UV light.

It is well known that planar waveguides exhibit birefingence as a result of the geometry of the waveguide and these are defined as the orthogonal transverse electric (TE) and transverse magnetic (TM) modes. The different mode profiles of these modes results in the TE mode penetrating further from the surface than the TM mode. Individual modes were interrogated by polarising the input light to be parallel or perpendicular to the sensor surface, coupling into the TE and TM modes respectively. Purely due to this geometry, the TE mode is more affected by changes in the azobenzene-functionalised co-polymer overlayer than the TM mode. This manifests itself as a greater range of tuning for the TE mode than that of the TM mode (Figure 6.10). It should be noted that the birefingence of the waveguide was consistent with the modelled system previously reported [31] and further, that no evidence for optical anisotropy in the co-polymer film was observed.

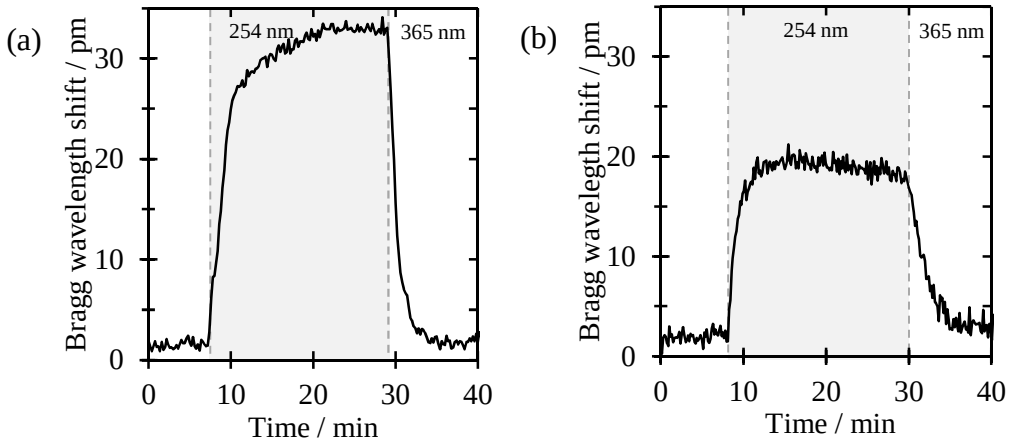

Fig. 6.10 The transverse electric (TE) mode (a) shows a much larger response to the refractive-index change upon photoisomerisation of 6 than the transverse magnetic (TM) mode (b). Photoisomerisation was achieved through alternate exposure to 365 nm and 254 nm UV light.

6.4.2 Interrogation of the Bragg response at 1550 nm wavelength

Switching the interrogation to telecomm wavelengths (C band, 1530-1565 nm) resulted in a reduced transition upon isomerisation – consistent with being much further from the absorption feature. However at this wavelength the co-polymer demonstrated greater transparency to the evanescent mode resulting in full guidance along the waveguide with little optical loss (~0.3 dB / mm). The higher transmitted power along the waveguide resulted in the reflected peak intensity of the Bragg gratings increasing from 6 dB to 22 dB above the noise floor, improving the signal-to-noise ratio.

The lower loss at ~1550 nm allowed for the deposition of a thicker film (719 ± 23 nm), resulting in a greater evanescent interaction between the waveguide and **6**, increasing the Bragg shift upon photoisomerisation by over an order of magnitude to 486 pm (Figure 6.11). The maximum Bragg shift corresponds to 63 GHz tuning at telecomm wavelengths, sufficiently broad for practical optical tuning within a telecomm channel.

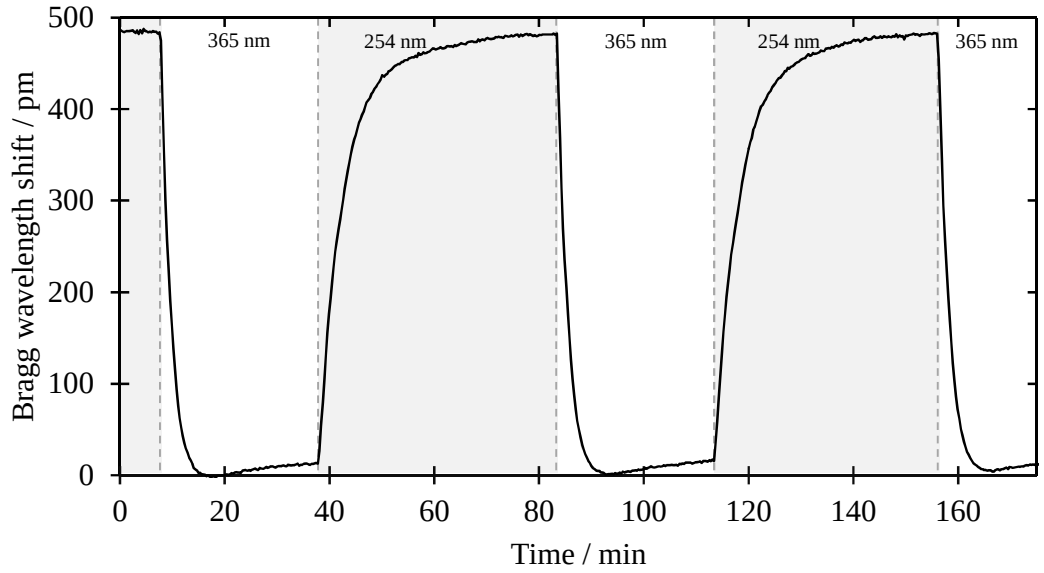

Fig. 6.11 Reversible photo-switching between the two isomeric states of 6 results in a detectable optical Bragg shift of 486 pm when interrogated at ~1550 nm. Photoisomerisation was achieved through alternate exposure to 365 nm and 254 nm UV light.

By limiting the duration of the UV exposure, the *cis:trans* ratio within the co-polymer can be regulated, allowing fine control of the Bragg wavelength to any value within this half nanometre tuning band. The index change showed the *trans*-

cis transition is faster than the reverse process, consistent with observations in the time-lapse UV-visible absorption measurements (Figure 6.6).

There has been no evidence of degradation of the index change response upon repeated switching of the device during evaluation. However, whilst the *cis*-isomer has long-term thermal instability at room temperature, with Barley [220] reporting ~20 h for a 50 % reconversion, the methacrylate polymer reported here shows a significantly slower linear reconversion over 5 days in the dark, with a 50% reconversion taking ~60 h at 21 °C in the dark.

As expected from the 780 nm data; the TE mode penetrates further from the surface than the TM mode, resulting in a greater sensitivity to changes in the refractive index of the co-polymer upon photoisomerism (Figure 6.12). The relative insensitivity of the TM mode could be used for *in situ* temperature referencing through differential studies of the two modes allowing for the fabrication of an athermal optical device [30].

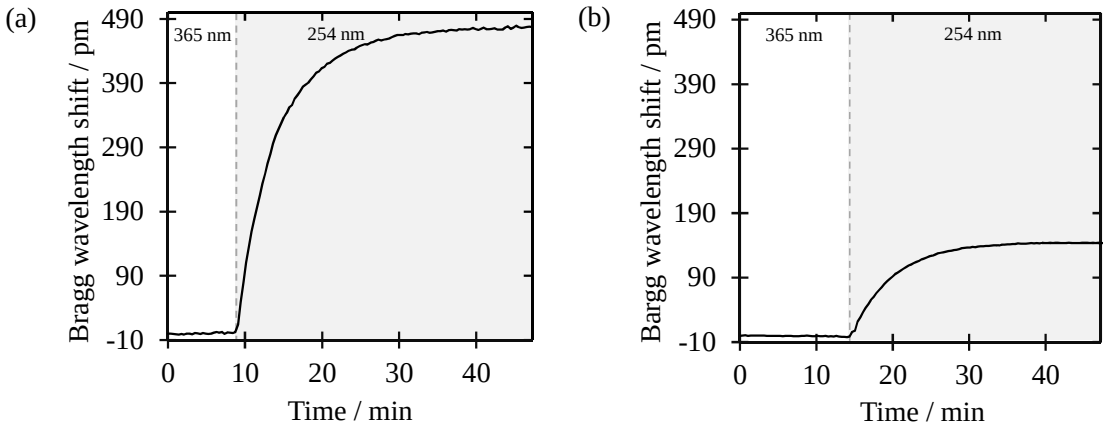

Fig. 6.12 The TE mode (a) shows a much larger response to the refractive-index change upon photoisomerisation of 6 than for the TM mode (b). Photoisomerisation was achieved through alternate exposure to 365 nm and 254 nm UV light.

6.5 An Azobenzene Functionalised Siloxane Co-polymer

The magnitude of the photoisomerism response of the Bragg grating is dependent on the thickness of the co-polymer film to which it is exposed. For the methacrylate co-polymer discussed above, the thickness was below the maximum penetration depth of the evanescent field of the waveguide; however a thicker film resulted in loss of guidance as the high index of the polymer pulled the mode out of the waveguide. While increasing the density of azobenzene units along the polymer backbone would

increase the co-polymer's refractive index further, reducing the optimum film thickness and negating any benefit.

Switching to a polymer backbone of a lower refractive index would overcome this problem, allowing for the mode to sense a much thicker layer. The knock-on effect of this would be that a greater number of azobenzene units would be within the evanescent tail, enhancing the change in effective index upon photoisomerism. Non-uniform film deposition, much like the unpolished etched sensors discussed previously, can cause scattering loss and Bragg peak broadening. By using a thicker film these effects are much reduced as the layer thickness can now be considered infinite to the mode and the surface will no longer interact with the mode.

6.5.1 Silicone co-polymers

Siloxanes such as polydimethylsiloxane (PDMS) belong to a group of polymeric organosilicone compounds consisting of an alternating silicon-oxygen chain with groups tethered to the remaining silicon sites. PDMS is the most widely used silicon-based organic polymer, and is particularly known for its unusual flow properties. Its applications range from contact lenses and medical devices to elastomers; it is also present in shampoos, caulking, lubricating oils, and heat-resistant tiles. PDMS is optically clear, and, in general, is considered to be inert, non-toxic and non-flammable. It is commonly used as a stamp resin in the procedure of soft lithography, making it one of the most common materials used for flow delivery in microfluidics chips. The process of soft lithography consists of creating an elastic stamp, which enables the transfer of patterns of only a few nanometres in size onto glass, silicon or polymer surfaces.

The similarity of such siloxane-based polymers to amorphous silica results in typically low refractive indices which, coupled with the ease of processing, ideally lends themselves to this application. To this end, (4-(4-methoxyphenyl)azo)phenoxyacetyl chloride, **4**, was peptide-linked to the commercial poly[dimethylsiloxane-co(3-aminopropyl)methylsiloxane] (50:50, $n_{20/D}$ = 1.4055), a PDMS analogue with pendant amine groups (Figure 6.13). This resulted in 10.4 % of the amine sites being functionalised, giving an overall coverage of 4.9 % of the monomer units – comparable to the methacrylate polymer discussed previously.

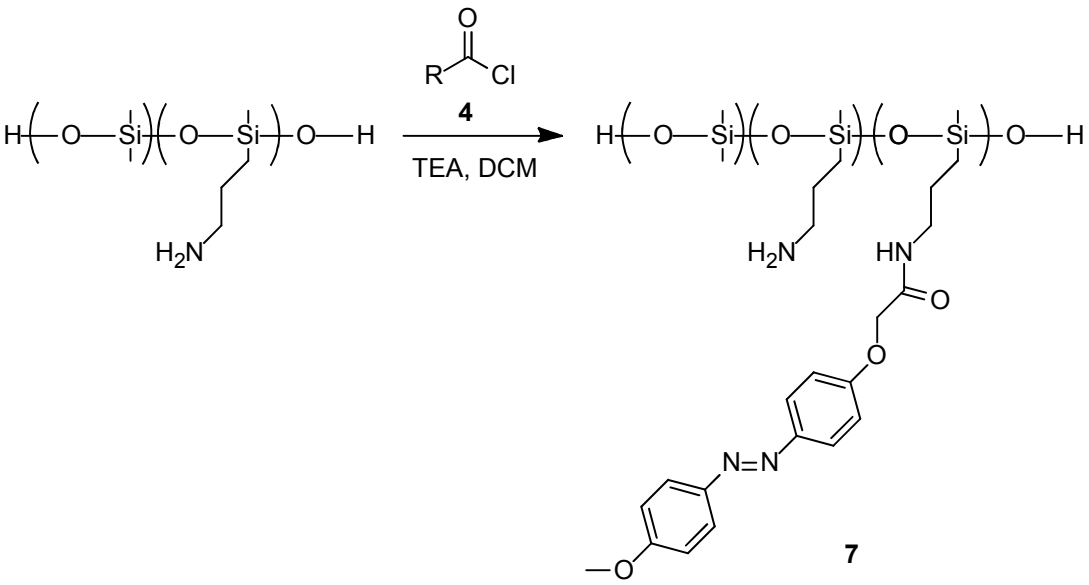

Fig. 6.13 Synthetic pathway to an azobenzene functionalised siloxane co-polymer.

Much like the methacrylate analogue, the silicone co-polymer **7** demonstrated reversible switching in methanol (5.5 mg/L), as detected by UV-visible spectroscopy (Figure 6.14).

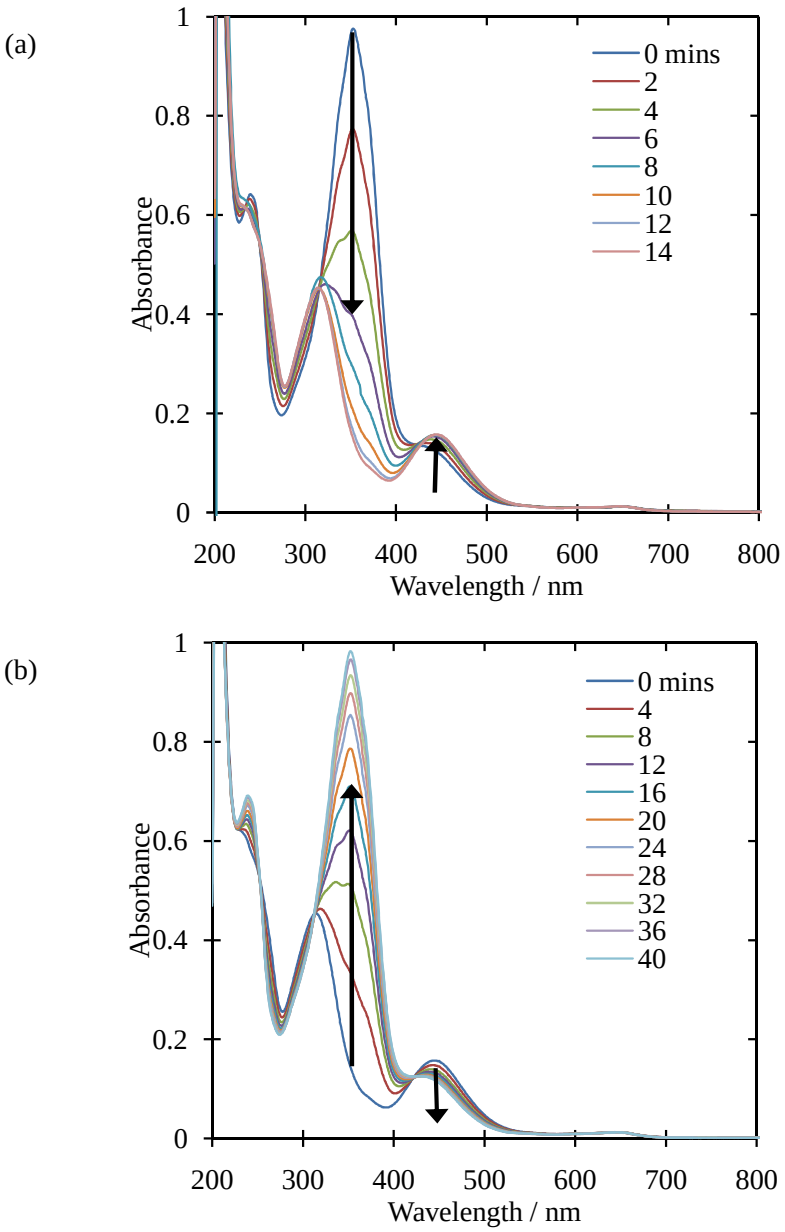

Fig. 6.14 Time-lapse UV-vis absorption spectra showing (a) the *trans-cis* transition of a *p*-methoxy azobenzene containing silicone co-polymer in methanol, on exposure to ultraviolet light (354 nm) over 14 minutes and (b) the reverse *cis-trans* transition on exposure to laboratory fluorescent ceiling lighting over 40 minutes.

6.5.2 Spray coating – an alternative deposition technique

If the refractive index of the co-polymer is low enough (less than the waveguide core of $n = 1.445$), deposition of a film on the surface will be unable to pull the mode out of the waveguide, irrespective of the film thickness. By removing the need for carefully controlled film thicknesses, fabrication of such devices can be simplified without the need for clean-room processing or spin-coating.

Spray-coating was proposed as a low-cost alternative to spin-coating. The technique uses a jet of compressed gas to aerosol the polymer onto the target surface through an atomiser nozzle. This allows for uniform films of controlled thickness to be easily deposited. To aerosolise the co-polymer it was necessary to first dissolve it into a volatile solvent, in this case acetone. This was then sprayed onto the same device as used above – to allow direct comparison of the two polymer systems.

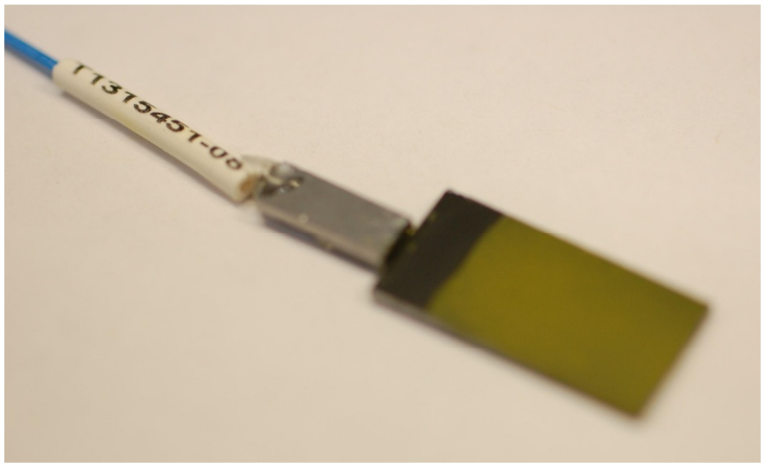

Fig. 6.15 The Bragg device spray-coated with a thick film of the azobenzene functionalised silicone polymer, 7. The first 4 mm were left uncovered to leave a reference Bragg grating.

6.5.3 Interrogation of the Bragg response at 1550 nm wavelength

First, a thick film was deposited to test if the polymer was below the refractive index threshold and that it was possible to fill the evanescent sensing region with the co-polymer without loss of guidance. It was found that with a thick film of 3.0 µm the Bragg peaks were all clearly visible with a reduction in amplitude of just 5-10 dB for a Bragg wavelength shift of 0.40 nm. It should be noted here that the soft nature of the silicone film made precise film thickness measurements by surface profiler less accurate than that of the methacrylate co-polymers.

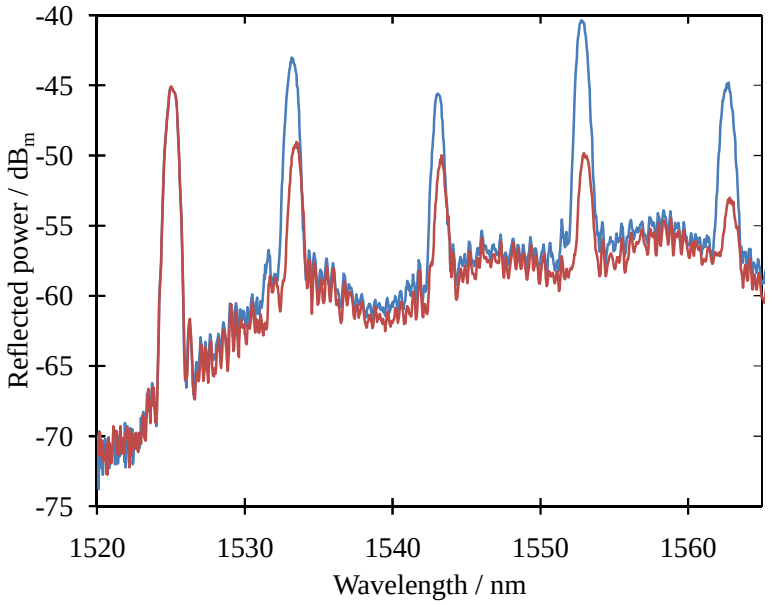

Fig. 6.16 The un-normalised reflected Bragg spectrum of a linear waveguide containing 5 Bragg gratings, before (blue) and after (red) deposition of a thick film of the azobenzene functionalised polymer 7, relative to reference grating at 1525 nm. Optical loss estimated at 0.4 dB / mm

However it was found that there was no Bragg response to any induced photoisomerisation of this layer. This was due to the upper part of the polymer film absorbing the incident UV light, preventing the azobenzene units near to the waveguide undergoing photoisomerisation to give a change in the effective index of the grating. To resolve this, a second, thinner film was investigated. By using a similar approach to the feedback technique used in wet etching (Chapter 5); the polymer was spray-coated until no further change in Bragg wavelength was observed (Figure 6.17). This allowed for the maximum effective film thickness (1.0 µm) to be deposited.

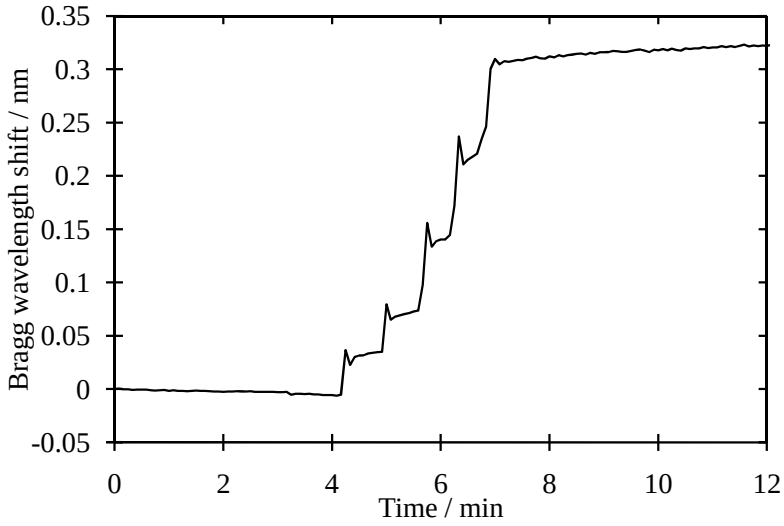

Fig. 6.17 The step-wise increase in Bragg wavelength with each subsequent spray-coat, after 5 coats no further shift was observed. The sharp drop after each coat is due to residual acetone solvent evaporating.

Optical microscopy of the sprayed polymer surface demonstrated a rough surface with a clear droplet pattern (Figure 6.18), however the underlying bulk material should be homogeneous, resulting in the low scattering losses observed.

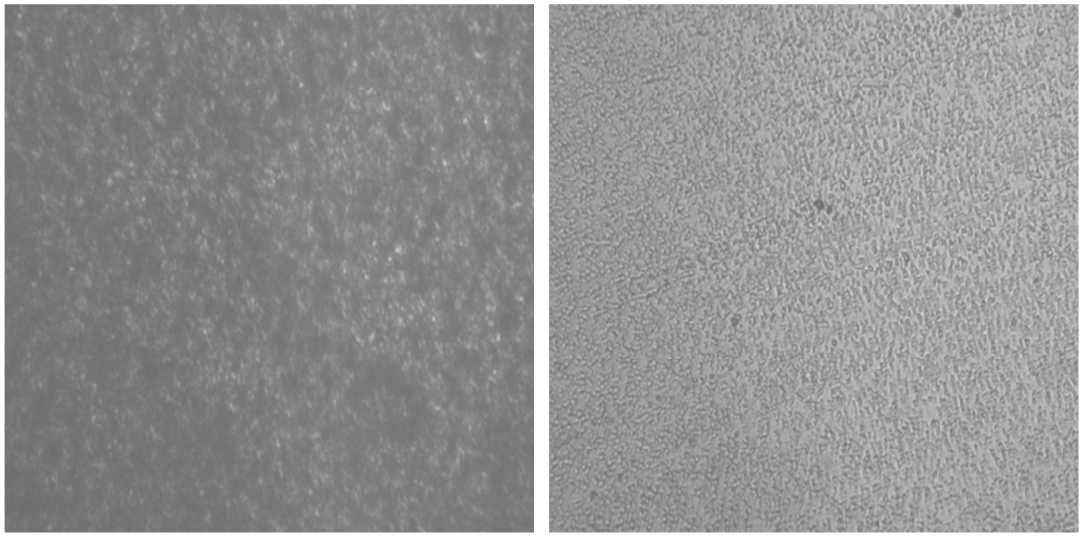

Fig. 6.18 Optical microscope images of a 1 mm by 1mm square of the surface of a thick film (left) and thin film (right) of the functionalised siloxane 7, showing the rough, droplet-like surface.

The sample was alternately exposed to ultraviolet light at 365 and 254 nm, thermal changes being monitored by a thermocouple in thermal contact with the optical device. The Bragg response demonstrated reproducible wavelength tuning between the two isomeric states, separated by 45 pm for the TE mode and 25 pm for the TM mode (Figure 6.19).

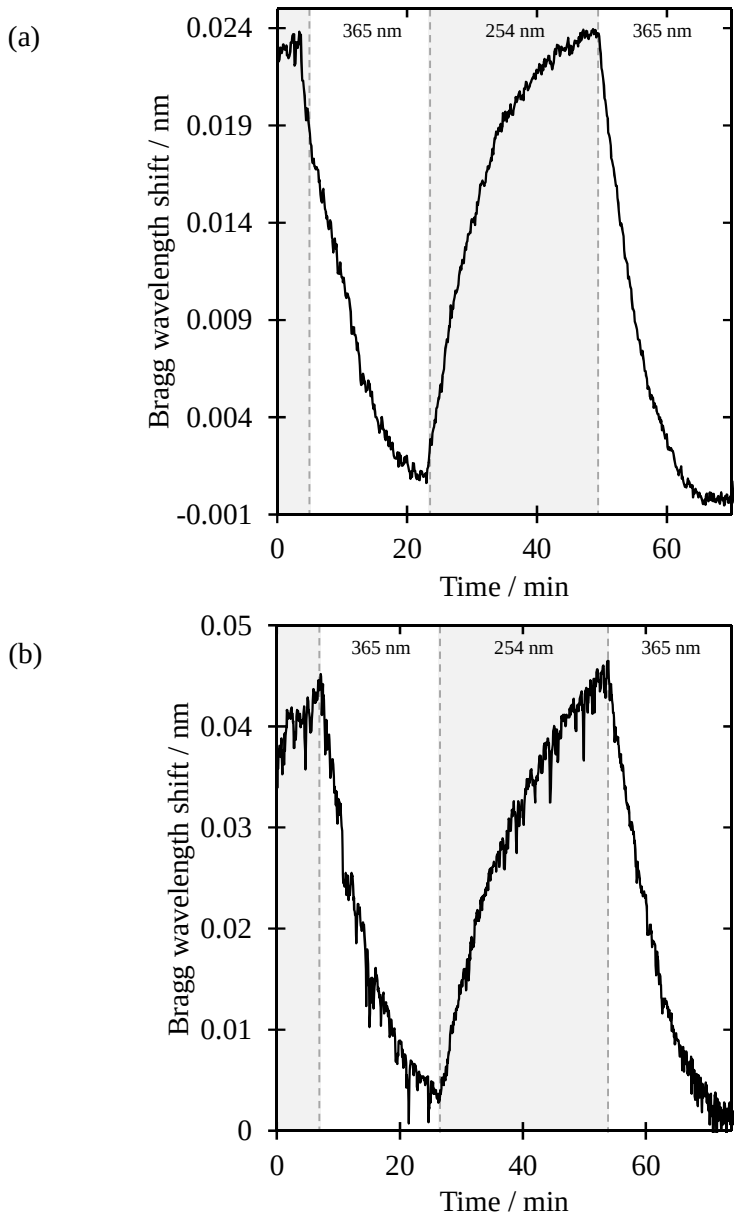

Fig. 6.19 The transverse magnetic mode (a) shows a smaller response to the refractive-index change upon photoisomerisation than the transverse electric mode (b). Photoisomerisation was achieved through alternate exposure to 365 nm and 254 nm UV light.

While the thinner film exhibits optical switching, the magnitude of the wavelength change is much smaller than for the methacrylate polymer, despite containing a comparable density of azobenzene units within the chain. With both polymers, the change in refractive index is solely due to the photoisomerisation of the azobenzene motif and will thus be similar in magnitude, resulting in similar changes in effective index. However the absolute effective index is much lower for the silicone variant. As discussed in Chapter 4, the wavelength response to changes in effective index increases exponentially with increasing index, such that the same magnitude of refractive index change centred at 1.40 will be an order of magnitude smaller than at

1.44. Furthermore any changes in the film thickness upon isomerism would enhance the magnitude of the refractive index change, though such effects would be more apparent within the thinner methacrylate film where the mode still penetrates all the way through the layer.

All of these explanations assume that the illuminated light is fully penetrating through the azobenzene film allowing switching throughout. As the evanescent tail decays exponentially out from the sensor surface, the closer to the surface the larger will be the induced change in effective index observed upon photoisomerisation. If the incident UV light is not fully penetrating through in the thicker silicone film, then the effective index response will be much reduced.

To overcome these drawbacks, several approaches could be made. Firstly a tantalum pentoxide overlayer could be deployed; this would increase the sensitivity of the device to refractive index, increasing the response to photoisomerisation centred at lower indices. However the thickness of such a film would need to be carefully calculated, were as it to be too thick, the same complications discovered with the methacrylate film would again arise. An alternative approach would be to slightly raise the index of the silicone polymer to ~1.45; this would increase the magnitude of the response to photoisomerisation but would still remain low enough to allow spray-coating. This could be achieved in two ways, firstly residual amine sites could be capped off by a subsequent reaction with acetyl chloride, or secondly the degree of azobenzene units could be increased, both increasing the bulk index and the magnitude of the index response to photoisomerisation. However as Barley [220] reported [220], there is an optimum azobenzene concentration and exceeding this can lead to a reduced index response.

6.6. Summary

A family of azobenzene derivatives have been synthesised and their optical properties have been studied. From these findings a *p*-methoxy azobenzene-functionalised methacrylate co-polymer has been synthesised that has been shown to undergo reversible photoisomerisation when exposed to UV light, producing a corresponding change in refractive index. This co-polymer demonstrated high thermal stability to isomerisation, giving rise to applications in passively latched devices. When deposited upon an optical surface, a reconfigurable Bragg grating

was formed that has the potential for a range of optical applications. In this prototype device the maximum observed tuning was 489 pm, corresponding to 63 GHz at telecomm wavelengths. This level of tuning is sufficient for future devices that could find application for wavelength trimming of lasers or for reconfigurable dispersion compensation.

A second system has been investigated using an alternative silicone co-polymer. This polymer has been shown to undergo a similar *cis-trans* photoisomerisation with a corresponding change in refractive index. The silicone co-polymer has been shown to have a lower bulk refractive index, below that of the waveguide core, allowing for easier deposition by the spray-coating technique. While this method removes the need for clean-room processing, reducing the cost and complexity of fabrication, further optimisation is needed to improve the response to that observed for the methacrylate system.

Further work on these systems would focus on the investigation of non-uniform exposure patterns. For example, using a gradient neutral density filter it would be possible to induce a gradient refractive index profile that would introduce a degree of chirp into the grating, while using a periodic mask could introduce additional spectral features.

These results have led to a publication in "Journal of Materials Chemistry" [33].

7. Temperature Compensation

7.1 Introduction

As discussed previously, the evanescent tail of an exposed Bragg grating can be used to form a highly sensitive refractive index sensor, where sub-picometre changes in the Bragg wavelength can be used to provide information about the refractive index of the analyte. However, as these Bragg gratings intrinsically respond linearly with changes in temperature, (~11 pm $°C^{-1}$), fluctuations in the ambient temperature is a significant problem when making precise measurements of the refractive index. In practical sensor applications, thermal control of the ambient environment is not a viable solution, making temperature referencing a necessity.

To overcome this problem several approaches to temperature referencing have been employed in this work. The simplest of these involves using a second Bragg grating that is not exposed to the environment. This grating, if placed locally on the device to the sensor grating will experience similar responses to physical stimuli such as temperature, allowing for a first order deduction of these fluctuations. This technique was demonstrated to work to great effect in the *in vacuo* sensitivity studies discussed in Chapter 5. However, this technique is less applicable when the sensor is coated with a thin layer of a high-index material, such as tantalum pentoxide. The physical environments of these two gratings are no longer comparable, with a much larger component of the sensor grating exposed to the environment and thus dictated by the thermal properties of the analyte. This effect is particularly well demonstrated for solution phase sensing, where the properties of liquids and solids differ substantially. In this situation the strong birefringence of the device can be used to its advantage by carrying out differential studies of the orthogonal TE and TM modes [30].

Developing from this approach is the concept of an athermal Bragg grating device [32], whereby the modal penetration into each medium is adjusted so that the thermal components act against each other giving no overall temperature response over the desired operational range.

This chapter will discuss the development of each of these techniques, highlighting their strengths and weakness and the relevant practical applications of each.

7.2 The Thermo-optic Coefficient

The refractive index of a material is not constant; it both varies with the properties of the light interacting with it (dispersion) and the physical environment. The refractive index response of a material to changes in temperature is known as the thermo-optic coefficient of the refractive index, d*n*/dT and is a fundamental property of a material, with many studies in the literature to quantify these constants for common materials. Theoretically, the refractive index is a function of density and the mean polarisability of the medium [226], which varies with pressure and temperature. The effects of pressure, temperature, and wavelength of the incident light on the refractive index were investigated [227-229] by noting that the mean polarisability depends on the density of the medium. The change in refractive index with temperature is closely associated with the phase transitions in transparent dielectrics [230].

Under typical laboratory conditions, the index of refraction of most organic liquids decreases by approximately 0.00045 ± 0.0001 for every 1 °C increase in temperature, as shown in Figure 7.1. This reduction is primarily associated with the decrease in density upon heating a liquid. The index of refraction of water is much less dependent on temperature than most organic liquids, decreasing by about 0.0001 for every 1 °C increase in temperature. Liquid temperature coefficients are usually so much higher than for solids that the temperature of a liquid must be known to predict its refractive index.

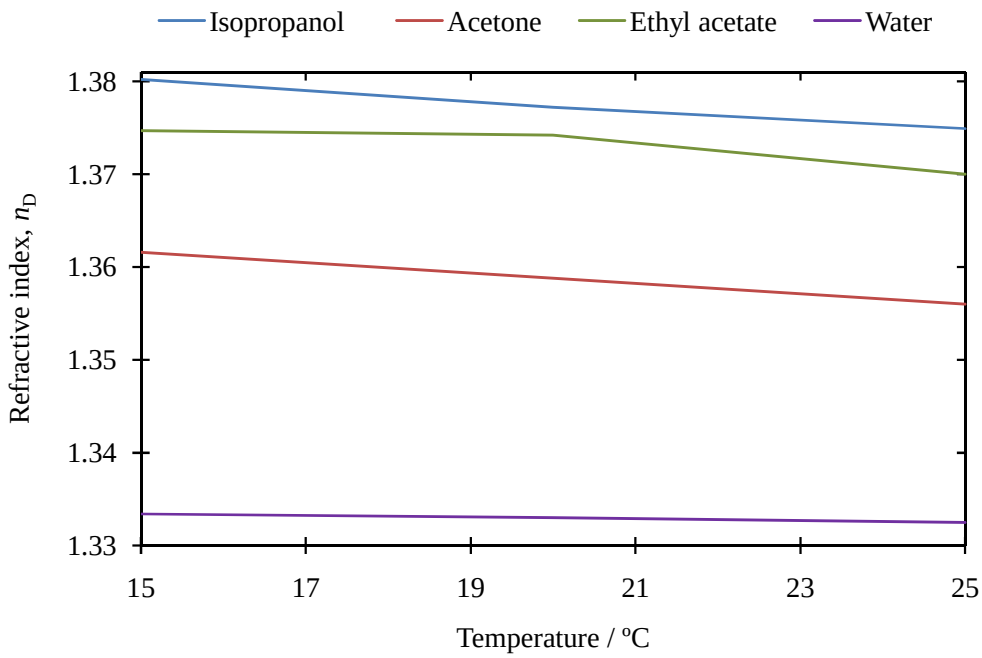

Fig. 7.1 The reported temperature dependence of the refractive index of common solvents at n_D (589.9 nm).

With solids, temperature is less critical. However it is important in optical design, where investigation of the temperature dependence of the refractive index in different frequency regions is important for understanding effects such as thermal lensing [231] and light scattering [232] processes in glasses. The thermal coefficient of the refractive index, d*n*/dT of silica glass is found to be strongly dependent on the temperature and the wavelength of the incident light. As a whole, the value of d*n*/dT increases with increasing temperature for a given wavelength of the incident light.

As discussed by Tan [227]; to describe the temperature dependence of refractive index of glasses it is necessary to consider two counteracting factors, the thermal expansion and the electronic polarisability. The electronic polarisability being the relative tendency of a charge distribution, such as the electron cloud of an atom or molecule, to be distorted from its normal shape by an external electric field. For silica glass, due to its very low thermal expansion coefficient [233], variations of the density with temperature are small. However, at a given wavelength, the change in refractive index with temperature is much larger than that associated purely from this change in the glass's density, indicating that the temperature dependence of the refractive index of silica glass is mainly associated with the change of the mean polarisability. The temperature coefficient of the electronic polarisation and thus the

mean polarisability increases with increasing temperature, resulting in an increase in the thermo-optic coefficient.

7.3 A Reference Bragg Grating for Temperature Compensation

The simplest solution to compensate for thermal drift, utilises an additional local Bragg grating of different Bragg wavelength written near to the etched region, a technique that works equally well within both fibre [234, 235] and planar Bragg grating sensors [31]. If this is left un-etched, it remains insensitive to changes in analyte but is still sensitive to changes in temperature and strain. In this way, the Bragg response to changes in analyte refractive index within the etched region can be separated from thermal effects by a simple first order approximation.

There are two disadvantages with this approach that become more apparent as the sensitivity of the system increases. Firstly, while the reference Bragg grating is located close to the sensor grating, temperature gradients can exist between the two locations even on the same device. In fast changing or microfluidic systems this lag in temperature referencing reduces the effectiveness of the thermal compensation. Secondly the mode structure and composition at the two Bragg gratings is markedly different; each grating will sense different thermo-optic properties. This results in a difference in dn_{eff}/dT between the reference and sensor gratings. While this temperature referencing technique is sufficient for simple systems; for the detection of the subtle changes in refractive index needed for practical chemical sensors, precise *in situ* temperature referencing is required.

In this chapter it will be shown that by using the orthogonal polarisation mode responses of the transverse electric and transverse magnetic modes, we can provide a more accurate compensation that addresses both of the limitations discussed above.

7.4 Using Orthogonal Polarisation Modes for *in situ* Temperature Compensation

When an exposed waveguide is coated with a high-index material, the mode is pulled into the high-index material (Figure 7.2) resulting in a greater proportion of the mode exposed to the environment (Chapter 5). This effect is experienced differently by the two polarisations modes, TE and TM, resulting in the physical environment of the two modes no longer similar. The TE mode is more influenced by the high-index

overlayer, resulting in a much larger component exposed to the environment. This results in the thermal-optic coefficient of the TE mode being principally dictated by the thermal properties of the analyte. This effect is particularly well demonstrated for solution phase sensing where the properties of liquids and solids differ substantially. In this situation the strong birefringence of the device can be used to its advantage by carrying out differential studies of the orthogonal TE and TM modes.

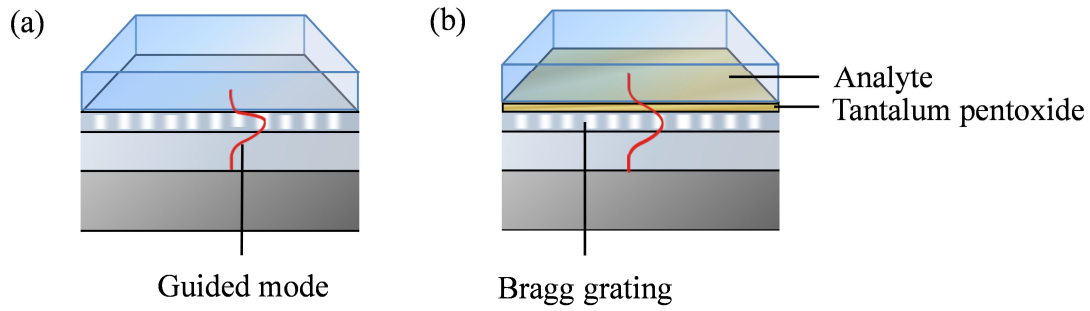

Fig. 7.2 A schematic of the Bragg grating sensor (a), showing the effect of a high-index overlayer on the guided mode (b).

The Bragg gratings fabricated for this study were 2.0 mm long with a period between 525 and 542 nm, satisfying the Bragg condition to reflect wavelengths between 1520 and 1570 nm. All the modelling presented in this chapter was performed using the commercial mode solver "Fimmwave". The waveguide was modelled as a 0.005 step index increase for a square cross-section, within the 5.0 μm core layer of index 1.4465. The index of the underclad was modelled to be 1.444, while the 72.5 nm thick tantalum pentoxide overlayer was found to be 2.05. The indices and thicknesses of the planar silica layers used in the modelling were determined using a Metricon prism coupler as part of the fabrication process, while the tantalum pentoxide thickness was measured using a surface profiler. Although the real refractive index profile of both the planar core layer vertically and the channel laterally exhibit Gaussian-like profiles, the precise refractive index profile of the waveguide is unknown. It has been previously shown that, for weak index guidance, a step refractive index profile for the modelled waveguide gives good agreement [38]. The model was corrected to compensate for the stress-induced birefringence inherent within the waveguide of the silica-on-silicon device, formed as a result of the flame hydrolysis deposition fabrication process.

7.4.1 Birefringence

The effective refractive index, n_{eff}, of the Bragg grating response represents the overall refractive index to which the guided mode is exposed to within the Bragg region. As such this is a combination of the refractive indices of the silica waveguide, the high-index overlayer and any analyte present. In this work, this is presented as a shift relative to an initial value rather than as an absolute index measurement. The shift in effective refractive index (Δn_{eff}) is simply calculated from the shift in Bragg wavelength ($\Delta\lambda_B$), according to Equation 7.1:

$$\Delta n_{eff} = \Delta\lambda_B / 2\Lambda \qquad (7.1)$$

where Λ is the period of the Bragg grating and is explicitly defined during the UV writing process.

For the un-etched Bragg grating, the fundamental mode is largely symmetric. However, etching introduces strong birefringence, B, within the waveguide, greatly modifying the transverse magnetic (TM) and transverse electric (TE) mode profiles of the Bragg grating waveguide. It is found that the TE mode is much more sensitive to changes in the overclad than the TM mode. The change in birefringence of the Bragg grating (ΔB_{eff}) can be expressed as the difference in the shift in the effective index of the TE and TM modes as temperature or analyte are changed (Equation 7.2):

$$\Delta B_{eff} = \Delta n_{eff}^{TE} - \Delta n_{eff}^{TM} \qquad (7.2)$$

ΔB_{eff}, is defined as zero at the initial conditions of analyte and temperature for the Bragg grating.

Sputtering the sensor region with tantalum pentoxide (72.5 nm, n = 2.05) pulls the evanescent field of the TE mode further out of the surface, not only increasing sensitivity but also further increasing the birefringence of the modes. This effect is illustrated in Figure 7.3, where the TM mode remains within the core of the waveguide while the TE mode is pulled into the high-index overlayer.

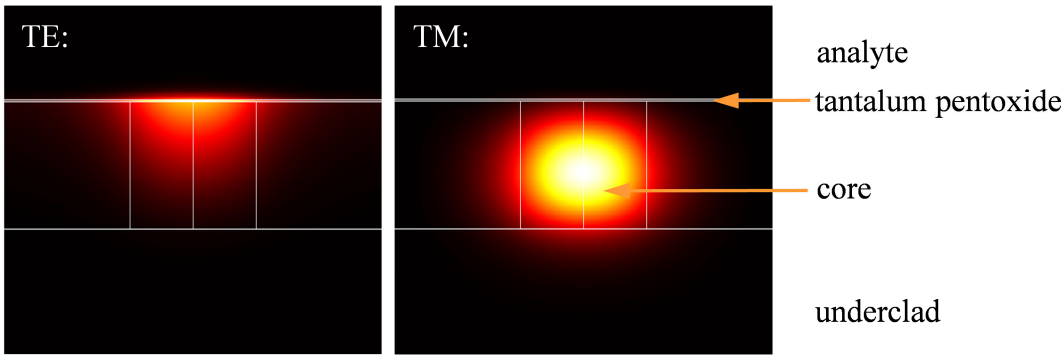

Fig. 7.3 The modelled intensity shows that the TE mode is pulled up into the tantalum pentoxide overlayer, resulting in a greater modal overlap with the analyte. In contrast, the evanescent field of the TM mode penetrates less out of the surface, resulting in much lower sensitivity to surface changes.

This increase in the birefringence of the two polarisation modes is sufficient to spectrally separate the two Bragg reflections, allowing simultaneous acquisition, as shown below in Figure 7.4:

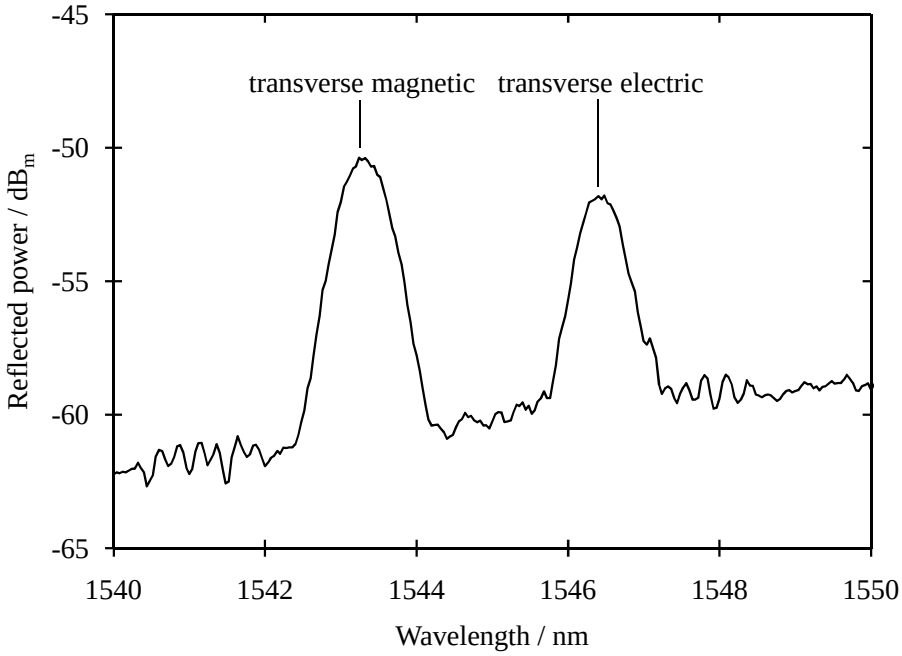

Fig. 7.4 The reflectance spectrum of a highly birefingent Bragg grating sensor in water, illustrating the spectral separation of the orthogonal polarisation modes; TE and TM.

Figure 7.5 shows the response of the Bragg grating with a central wavelength of ~1540 nm, to a series of Cargille refractive index liquids (Series AA and AAA) illustrating the increased sensitivity and birefringence of the two modes to changes in the analyte refractive index.

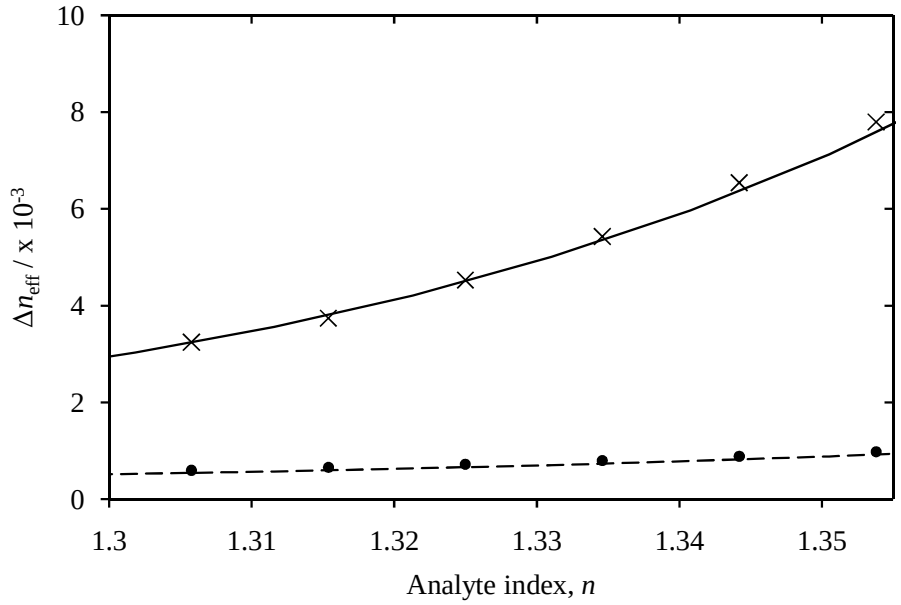

Fig. 7.5 Experimental data showing that an overlayer of tantalum pentoxide pulls the TE mode (cross) of the Bragg grating further into the analyte, enhancing the sensitivity to changes in refractive index of the analyte. The TM mode is also shown (circle) with little sensitivity. Both modes are consistent with modelling of the system (line). Error bars are too small to show.

7.4.2 Thermo-optic effects upon the birefringence of a waveguide

While the TE and TM modes have dramatically differing sensitivities to changes in the refractive index of the analyte, the TE and TM response to temperature fluctuations are much more closely matched. Dai *et al* [211] has shown that these properties can be used to decouple temperature fluctuations from changes in the analyte under interrogation. This method of temperature referencing allows for *in-situ* monitoring, an improvement over using a second reference Bragg grating as previously discussed.

However at the high sensitivities and broad range of analytes necessary for functional chemical sensors, these assumptions start to break down. Dai's method [211] relies on two assumptions. Firstly that only one mode is sensitive to changes in the refractive index (i.e. $d(n_{eff}^{TM})/dn \approx 0$) and secondly, that the thermal responses for both polarisation modes are comparable ($d(n_{eff}^{TM})/dT \approx d(n_{eff}^{TE})/dT$); combining these two assumptions into Equation 7.2, gives Equation 7.3.

$$\Delta B_{eff} = \Delta n_{eff}^{TE}(n,T) - \Delta n_{eff}^{TM}(n,T) \approx \Delta n_{eff}^{TE}(n) \qquad (7.3)$$

This shows that the expression approximates to $\Delta n_{eff}^{TE}(n)$, i.e. the change in birefringence of the Bragg response is solely dependent on the TE response to an analyte.

Figure 7.5 has shown that for small changes in the analyte the assumption that TM is chemically insensitive holds up well. Even when changing between two pure solvents, such as water (n = 1.315 at λ = 1550 nm) and ethanol (n = 1.354) [236], the shift in the peak Bragg wavelength of the TM mode is still small (Δn_{eff}^{TM} = 0.0003), and is an order of magnitude smaller than that for TE (Δn_{eff}^{TE} = 0.0034).

For the un-etched Bragg grating, the assumption that both fundamental modes have the same thermal response is reasonable (Figure 7.6(a)); both modes are exposed to similar silica environments and thus similar thermo-optic properties (dn/dT). The thermo-optic constant can be measured for the buried Bragg grating to be 10.49 x 10^{-6} °C^{-1} at a wavelength of 1550 nm, consistent with typical values for bulk silica [237]. Etching and sputtering the surface with tantalum pentoxide, as described previously, increases the birefringence of the modes, but at low analyte indices the assumption still holds true. For example, in air the low refractive index pushes the two modes back within the silica waveguide and underclad which, combined with the lack of a thermo-optic component for air (dn/dT = 0), again results in similar thermal properties between the two modes.

While this assumption has been shown to hold well in air [211], for the solvents required for chemical and biosensors the system becomes more complicated. The higher index of common solvents pulls the evanescent field from the waveguide into the solvent. The Bragg grating no longer senses just the silica, but a mixture of the silica, the tantalum pentoxide and the surrounding fluid, and hence their associated thermo-optic components. If the TE and TM modes were equally affected by the presence of the solvent, the gradient of Figure 7.6(a) would be altered to reflect the amalgamation of the various dn/dT values, but the modes would respond equally.

However, as shown in Figure 7.3, the penetration of the evanescent field into the analyte differs considerably for the two modes. The effect of this is that the dn_{eff}/dT of the TE mode is dominated by the dn/dT of the analyte, opposing that of the TM mode, which is still dominated by the intrinsic coefficient of the silica waveguide. This is demonstrated in Figure 7.6(b); where immersing the sensor in deionised water results in little change in the dn_{eff}/dT of the TM mode, which contrasts with the suppressed response observed for the TE mode. The suppression of the dn_{eff}/dT of the TE mode is a result of the negative dn/dT of water. This is further

complicated by the temperature dependence of the thermo-optic coefficient of water increasing the degree of suppression with temperature. For real world applications a simple subtraction between the modes as previously proposed by Dai is not only insufficient, but would enhance the thermal component rather than negate it.

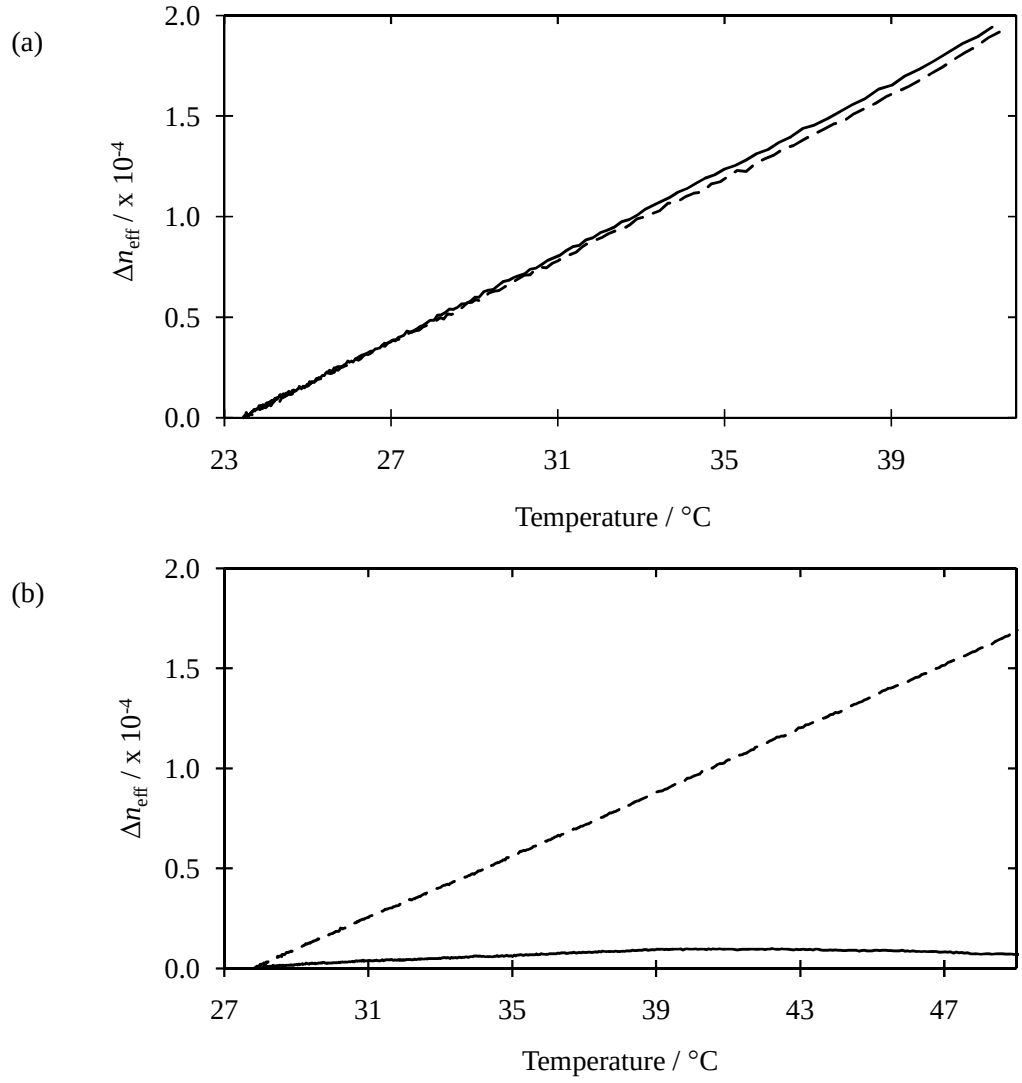

Fig. 7.6(a) The thermal response of Δn_{eff} for TE (solid) and TM (dashed) modes within an un-etched Bragg grating. 7.6(b) The thermal response of Δn_{eff} for TE (solid) and TM (dashed) modes with a Bragg grating exposed to water.

Although the two modes are different, an understanding of the system allows the temperature dependence to be compensated. For many sensing applications the solvent used is consistent or at least known in advance. For example, many bio-sensing devices are run in water or a saline solution. For the TM mode to be used for temperature referencing to produce temperature-insensitive Bragg grating sensors, a scaling factor can be employed. Modelling the system for the desired analyte or solvent allows the thermal properties of the two modes to be calculated.

In addition this model can be used to determine a scaling factor, *K*, between the modes. Equation 7.3 can thus be modified to incorporate *K*, to give Equation 7.4:

$$\Delta B_{eff} = \Delta n_{eff}^{TE}(n,T) - K.\Delta n_{eff}^{TM}(n,T) \qquad (7.4)$$

7.4.3 Application of birefringence temperature compensation to a real system

For most solvents this approach works well, providing accurate thermal referencing. With a suitable database of d*n*/dT for commonly used solvents, at the interrogation wavelength, this method can be fully incorporated into the grating analysis software. Figure 7.7 shows the measured response of a Cargille refractive index liquid (Series AAA, "1.3000") to changes in temperature and the fitted response of the model of the system from Figure 7.3. This model was verified against the analyte data shown in Figure 7.5 and can be used to find the value of *K* to allow temperature referencing for this fluid (*K* = -1.21, in this example).

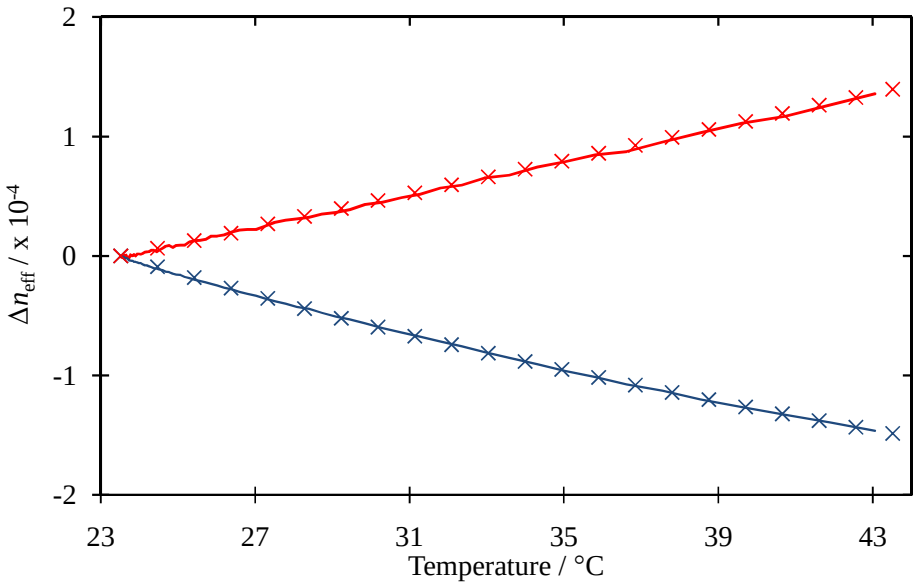

Fig. 7.7 The thermal response of Δn_{eff} for TE (blue line) and TM (red line) modes with a Bragg grating exposed to a Cargille refractive index liquid of index 1.296 at 1550 nm, compared to the modelled system (points).

To test this approach, the Bragg grating sensor was slowly cooled from 40 to 22 °C with the same Cargille refractive index liquid on the sensor window while the temperature was monitored with a thermocouple. As shown in Figure 7.8, the TM mode and TE mode demonstrated very different behaviours during this cooling curve experiment; however applying the scaled TE-TM normalisation removed the thermal component, and in the absence of any refractive index changes in the analyte, gave

the flat line (red line). In contrast, applying the simple subtraction of the two modes without the scaling factor, *K*, was shown to increase the thermal component of the TE mode rather than remove it (blue line). This shows that by monitoring the TM mode a temperature-insensitive Bragg grating sensor can be produced that can compensate for analytes with very different properties from those of the silica waveguide.

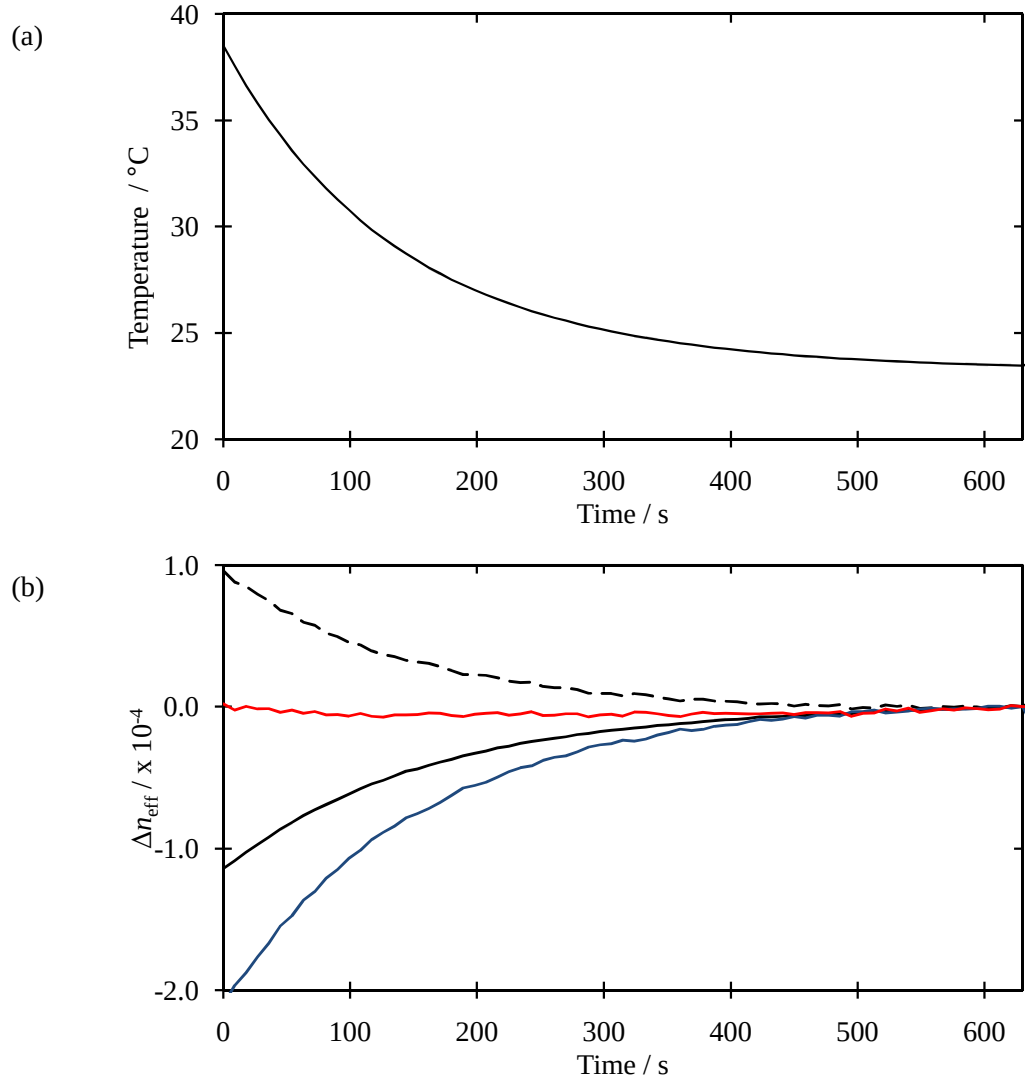

Fig. 7.8(a) The cooling curve recorded by the thermocouple. 7.8(b) Applying the scaling factor, *K* to the TM (dashed line) and subtracting from the TE mode (solid line) makes the Bragg response insensitive to temperature changes (red line). Without scaling TM by *K*, the thermal response of the TE mode is increased (blue line).

For more complex solvents, such as water, where the gradient, d*n*/dT is highly temperature dependent (Figure 7.9), *K* is no longer a constant but becomes a function of temperature, *K*(T), giving the relation:

$$\Delta B_{eff} = \Delta n_{eff}^{TE}(n,T) - K(T).\Delta n_{eff}^{TM}(n,T) \qquad (7.5)$$

This would imply that the temperature must be known in advance to be able to apply this approach. However, over small changes in temperature (i.e. < 5 °C) *K* can be approximated to a constant and only an initial estimate of the ambient temperature or a temperature range is needed to apply this method to remove thermal fluctuations from the system. An un-etched reference grating can be used to provide this initial information.

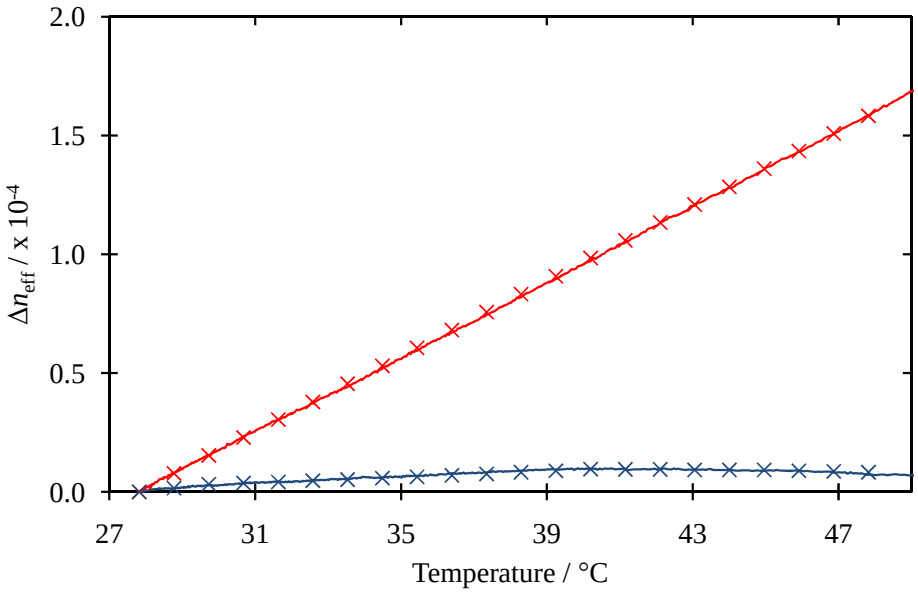

Fig. 7.9 The thermal response of Δn_{eff} for TE (blue line) and TM (red line) modes for a Bragg grating exposed to water, compared to the modelled system (points).

Not only does this approach simplify the system, as no additional components are necessary such as a second Bragg grating or thermocouple, but it makes use of the previously redundant TM mode of the Bragg response. The high resolution of this method of temperature compensation combined with the high sensitivity of a planar Bragg grating makes this system ideal for detection of the subtle changes in chemical and bio-sensing applications.

These findings have been published in the journal "Sensors and Actuators B: Chemical" [30].

7.4.4 Hybrid local reference Bragg gratings

While the method described above works successfully and allows both sensor measurements and temperature compensation to be achieved in a single Bragg grating, it is reliant on a highly birefringent waveguide. While it has been shown that the thicker the high-index overlayer, the greater the sensitivity enhancement, this

comes at a cost. As the layer increases in thickness it pulls the guided mode further out of the waveguide and into the analyte, lowering the maximum analyte refractive index possible before the mode is no longer efficiently reflected by the Bragg grating.

To maintain guidance at these higher indices a much thinner film is employed, often resulting in incomplete resolution of the two modes as distinct peaks in the reflectance spectrum. In these instances modal referencing is not possible, limiting the system to using a reference grating, yet as discussed previously a buried reference is not sufficient for precise sensing of subtle interactions. If the medium the analyte is dissolved in is constant (e.g. a known aqueous buffer solution is often used in bio-sensing), a second etched Bragg grating can be employed that has a sealed aliquot of this medium over the surface. In this way the modal penetration of the two Bragg gratings into the different materials will be similar, leading to similar effective thermo-optic components, as shown schematically below (Figure 7.10):

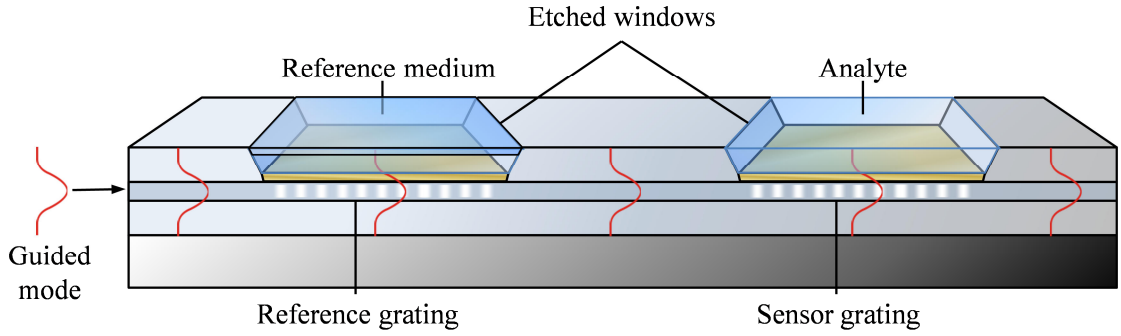

Fig. 7.10 A schematic of a Bragg grating sensor with a localised etched reference grating covered with a sealed aliquot of a reference medium.

7.5 Athermal Planar Bragg Grating Devices for Integrated Photonic Networks

Complex, narrow band optical components, such as filters, can be an important part of multiple-wavelength telecommunications systems. There are already many forms of optical filters in use, often utilising the Bragg effect for effective wavelength filtering. One difficulty in the use of these gratings is the inherent sensitivity of the Bragg wavelength (λ_B) to variations in temperature (and strain). This is observed as the shift of the central Bragg wavelength of the grating with changes in the local temperature. The thermo-optic response ($d\lambda_B/dT$) for a UV written planar Bragg grating is measured to be 11.1 pm/°C at a wavelength of 1550 nm [238].

7.5.1 Athermal Bragg gratings

A method of making an athermal Bragg grating is to control the temperature of the grating with an active stabilisation system, however this is both costly to implement and requires electrical power. A second approach, used in fibre, involves creating a negative expansion via a hybrid mounting arrangement in which materials with dissimilar positive expansion coefficients create a reduction in the length of the Bragg grating as temperature increases [239]. Such devices have several undesirable properties, these include the fabrication of a reliable union with the fibre and the fabrication costs associated with the mechanical assembly and adjustment of such devices. Such systems have also been found to show hysteresis [240], degrading the performance under repeated thermal cycling. Furthermore the requirement that the grating be suspended within such a device can make it incompatible to applications requiring tolerance to mechanical shock and vibration. Instead of creating a hybrid mounting it is possible to use composite materials to achieve an athermal response [241]. A fourth method of incorporating negative expansion is to provide a substrate for mounting the Bragg grating that is fabricated from a material with an intrinsic negative coefficient of expansion. An example of such a material is the beta-eucryptite solid solution of cerammed lithium aluminosilicate [242]. However such an approach is less well suited to integrated photonics due to difficulties in overcoming the substrate expansion.

7.5.2 Using the negative thermo-optic constant of a fluid

In general fluids have a negative thermo-optic coefficient that can counter the thermo-optic coefficient of the silica waveguide, reducing the thermal sensitivity of the Bragg grating (as shown previously in Figure 7.9). The evanescent field of the TE mode penetrates further into the analyte resulting in the suppression of the effective thermo-optic response ($d\lambda_B/dT$) of the TE mode compared to the un-etched-like response of the TM mode [30]. However, to produce an athermal grating, the modal overlap with the analyte needs to be fine-tuned. While switching to a fluid of higher or lower refractive index would allow the degree of overlap to be controlled, changing the fluid used changes many other properties, including the thermo-optic coefficient. As such it is useful to be able to tune the index independently from other properties.

While water is not an ideal fluid for telecoms applications, due to absorption losses with the TE loss modelled at -3.8 dB cm^{-1}, its large thermo-optic coefficient of -8 x 10^{-5} /°C at 1550 nm [243, 244] is particularly effective at reducing the thermal response of a Bragg grating. A practical alternative to water would be the use of deuterium oxide, shifting the inherent absorption losses towards the mid-infrared.

7.5.3 Tuning the thermal response

The refractive index of a solvent can be tuned by dissolving a solute, such as the addition of glucose into deionised water. Small concentrations of glucose significantly alter the refractive index of the fluid, but by retaining the same solvent, other properties remain relatively unaltered. Figure 7.11 shows the effect on increasing glucose concentration on the Bragg response for both TE and TM modes, demonstrating the induced birefringence. By changing the refractive index of the glucose solution, the balance between the different thermo-optic coefficients sensed by the mode of the waveguide can be altered, allowing for the temperature range of the athermal region to be tuned for the desired application.

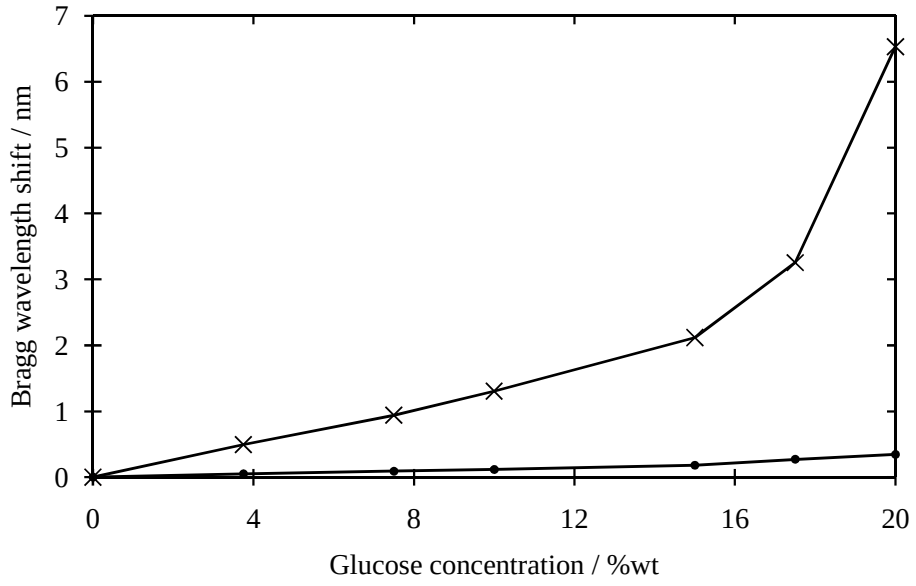

Fig. 7.11 The response of the two orthogonal modes, TE (cross) and TM (dot), to increasing the concentration of an aqueous solution of glucose. Error bars are too small to show.

Over typical operating temperatures of 20 to 50 °C a concentration of 1 – 8 wt% was found to compensate well for temperature. Over these concentrations the maximum of the curve (caused by the temperature dependence of the thermo-optic coefficient of water) shifted with glucose concentration, providing a tuneable athermal response.

At higher concentrations the negative thermo-optic coefficient of the solution dominates, resulting in a negative thermal response.

By choosing the correct concentration for the desired temperature range of the Bragg response, devices can be fabricated to cover a wide range of temperatures. For a concentration of 2.0 wt% of glucose, the Bragg response was found to vary by only 3.7 pm with a standard deviation of 1.1 pm over the 10 °C range from 37 to 47 °C, showing reproducible athermal behaviour. This is shown in Figure 7.12, where the TE mode is unaffected by changes in temperature while the TM mode is still comparable to that of an un-etched Bragg grating. This is an improvement of nearly two orders of magnitude over the un-etched Bragg grating.

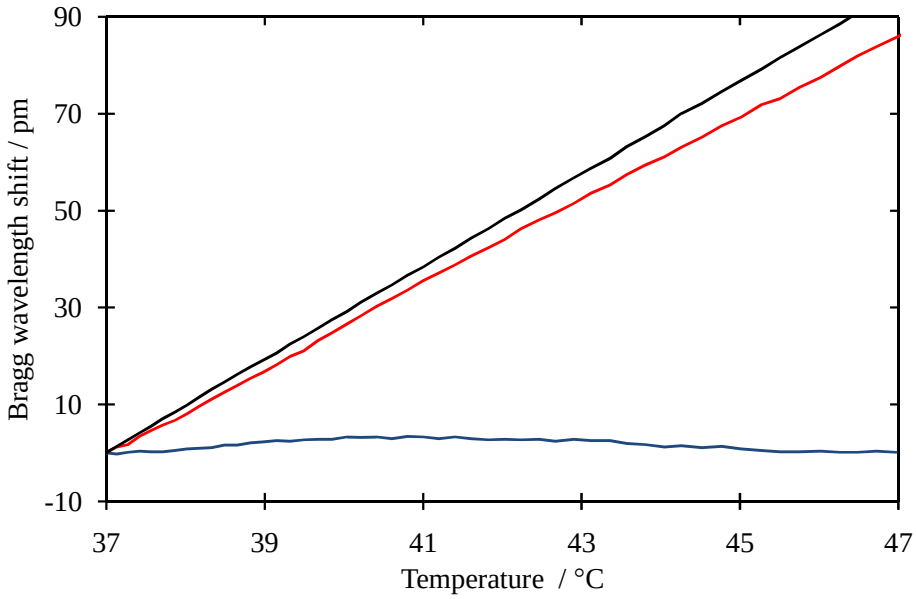

Fig. 7.12 The thermal response of the TE (blue line) and TM (red line) modes of a Bragg grating from 37 to 47 °C when exposed to a 2.0 wt% solution of glucose, compared to an un-etched grating (black line).

In this way, tuning the proportion of the mode exposed to the negative thermo-optic coefficient of a fluid by altering its refractive index has been shown to improve the temperature independence of an etched Bragg grating. These devices are resistant to mechanical shock, vibrations and strain. Combined with the low cost of fabrication compared to traditional athermal Bragg devices makes them ideal for incorporation within integrated photonic networks. While the use of liquids is not currently favoured in telecoms, packaging such devices could use techniques employed in the fabrication of liquid crystal displays.

This proof-of-concept device was reported in the journal "Electronics Letters" [32].

7.6 Summary

Temperature referencing has been shown to be necessary for a Bragg grating sensor to demonstrate sufficient sensitivity to be suitable for common sensing applications. Fortunately this can be achieved in several simple and robust ways without significantly modifying the existing fabrication techniques.

While it has been shown that simply using a reference grating is sufficient in simple systems or specific examples, for precise compensation of temperature, a modal comparison is a much more accurate.

It has been previously reported in the literature that the birefringence of the mode in an evanescent sensor can be used to compensate for temperature fluctuations [211]. Here we have shown that the assumption that $d(n_{eff}^{TM})/dT \approx d(n_{eff}^{TE})/dT$ is not well suited for a liquid environment. By using the TM mode to monitor temperature fluctuations and, in conjunction with the thermo-optic constants for the solvents of the system, a temperature-insensitive Bragg grating sensor can be fabricated. It has been shown that for a real system this approach can successfully remove the thermal component from the Bragg response while the simple approximation fails. Not only does this approach simplify the system, as no additional components are necessary (e.g. a second Bragg grating or thermocouple), it makes use of the previously redundant TM mode of the Bragg response. The high resolution of this method of temperature compensation combined with the high sensitivity of a planar Bragg grating makes this system ideal for detection of the subtle changes in chemical and bio-sensing applications. These findings have been published in the journal "Sensors and Actuators B: Chemical" [30].

Furthermore, the use of the negative thermo-optic coefficient of a fluid has been shown to improve the temperature independence of an etched Bragg grating. This can be enhanced further through use of a solute to modify the refractive index of the solvent, allowing this response to be tuned to the desired operating temperature range. This has been demonstrated with an aqueous glucose solution, where over a 10 °C range the Bragg response was found to vary by only 3.7 pm. This is an improvement of nearly two orders of magnitude over the un-etched Bragg grating.

The low cost and resistance to mechanical shock, vibrations and strain makes these devices ideal for incorporation within integrated photonic networks. This proof-of-concept device was reported in the journal “Electronics Letters” [32].

The following chapters will focus on using the high thermal stability that the systems discussed here offer to produce chemical sensors capable of looking at the subtle responses from chemical binding.

8. Optofluidic Sensors

8.1 Introduction

The previous chapters discussed the design and fabrication of a highly sensitive Bragg grating refractometer. While several applications have been alluded to, the primary aim of the project was to use the integrated optical devices fabricated here as chemical sensors. Similar sensors have been demonstrated previously by applying an analyte to the sensor window [238]. This sampling method was shown to be effective at identifying an analyte from a series of known compounds through accurate measurement of the refractive index and a comparison with known calibration curves.

The logical extension to this approach is to incorporate the sensor directly into a flow system which would have the potential to monitor continually either fluids or gases autonomously. This has several advantages over the previous method: dynamic changes in the system can be monitored in real time in more detail; and the system does not require manual loading or cleaning of the sensor surface, allowing for it to be incorporated directly into many industrial processes for in-line monitoring. The increased stability of the optical system allows for higher sensitivity with fewer anomalies through the reduction in surface contamination, a problem with bench-top and dip sampling methods.

To achieve this, a microfluidic system was developed that allowed the sensor to monitor a flow of liquid passing over the surface continuously and in an automated fashion for multiple days at a time. Automation of a series of valves allowed for control of the fluids through the system, enabling the study of the transitions at solvent interfaces, chemical reactions and ultimately chemical interactions upon the sensor surface.

The following chapter will focus upon the development of the microfluidic system and the unexpected refractive index profiles observed when common solvents were flowed through this system.

8.2 Microfluidics

The behaviour of fluids at the micro-scale (10^{-9} – 10^{-18} litres) can differ from the macrofluidic, with factors such as surface tension, energy dissipation, and fluidic resistance becoming much more dominant in the system. The field of microfluidics deals with the behaviour, control and manipulation of such fluids constrained geometrically to the micrometre scale.

Microfluidics has the potential to influence diverse areas, from chemical synthesis and biological analysis to optics and information technology. While the field is still in an early stage of development, it has been utilised in a wide range of applications from analytics and high throughput screening through to heterogeneous catalysis and chemical reactors. A comprehensive review of the state of the field of microfluidics was written by Whitesides in 1996 [245], covering the history and development of the field from early work on micro-analytical methods and molecular biology through to commercial products.

Continuous-flow microfluidic networks are based on the manipulation of the continuous flow of liquid through micro-fabricated channels under the actuation of mechanical pumps. This approach is easy to implement and is typically insensitive to fouling problems. Typical channel diameters of ~100 nm to 100's µm are used and at these small scales some interesting and sometimes non-intuitive properties appear.

At these dimensions the nature of the flow of the fluid becomes significant, with two distinct flow regimes; laminar and turbulent. Laminar flow can be considered "smooth" flow while turbulent flow is often described as "rough". Laminar flow occurs when a fluid flows in parallel layers, with no disruption (or mixing) between the layers. The fluid particles move in definite and observable paths (streamlines). In fluid dynamics, laminar flow is a flow regime characterised by high momentum diffusion and low momentum convection. Turbulent flow is the opposite of laminar flow and is characterised by the irregular movement of the particles of the fluid, with

no observable pattern and no definite layers. The flow regime influences the amount of fluid friction, which in turn determines the amount of energy required to maintain the desired flow. Laminar and turbulent flow are shown schematically in Figure 8.1, indicating the characteristic bullet profile of laminar flow. This is caused by the higher friction at the side walls producing a velocity gradient across the channel.

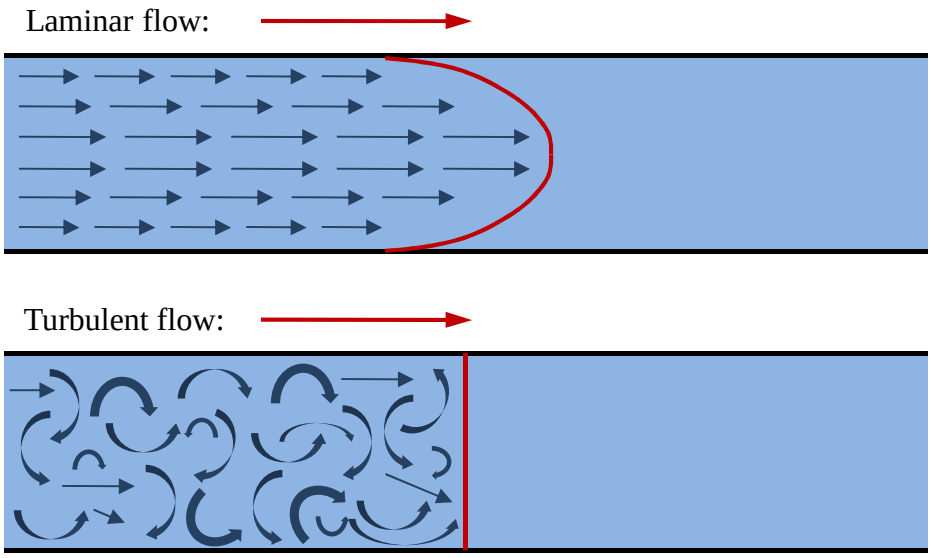

Fig. 8.1 A schematic of laminar and turbulent flow, showing the velocity profile.

The Reynolds number, R_e compares the effect of momentum of a fluid to the effect of viscosity. It is a dimensionless quantity that gives a measure of the ratio of inertial forces to viscous forces and consequently quantifies the relative importance of these two types of forces for given flow conditions.

$$R_e = \frac{QL}{vA} \tag{8.1}$$

where Q is the volumetric flow rate (m^3/s), L is a length of the object that the flow is going through or around (m), v is the kinematic viscosity (the ratio of the dynamic viscosity of the fluid to the density, $v = \mu / \rho$, m^2/s) and A is the pipe cross-sectional area (m^2). However, for flow in a circular pipe, the Reynolds number is generally defined as:

$$R_e = \frac{QD}{vA} \tag{8.2}$$

where D is the diameter of the pipe. Full development of the flow occurs as the flow enters the pipe, where the boundary layer thickens and then stabilises after several diameters distance into the pipe. Experimental observations show that for 'fully developed' flow, laminar flow occurs when $Re < 2{,}300$ and turbulent flow occurs when $Re > 4{,}000$ [246]. In the interval between 2300 and 4000, laminar and turbulent flows are possible ('transition' flows), depending on other factors, such as the pipe roughness and flow uniformity.

In microfluidic systems the Reynolds number can become very low. A key consequence of this is that fluids, when side-by-side, do not necessarily mix in the traditional sense and molecular transport between them must often be through diffusion alone. These effects become more apparent in Chapter 10, where binding to the surface of the microfluidic channel is investigated.

8.3 An Optofluidic Sensor

Microfluidic networks allow for the precise control of the chemical and physical properties of the system, such as the concentrations, pH, temperature and shear force. This results in more uniform reaction conditions and higher grade products in single and multi-step microfluidic reactors.

Optofluidics [247] is a relatively new field, integrating aspects of chemistry, microfluidics and integrated optics. However, combined with traditional “lab-on-a-chip” devices it has attracted much interest with journals such as “Sensors and Actuators B” containing a section dedicated to “Micro Total Analysis Systems” and with the journal “Lab on a Chip” focusing on these integrated systems. The following sections will discuss the incorporation of a Bragg grating sensor into a microfluidic flow cell to fabricate an optofluidic sensor.

8.3.1 Sensor design

For practical measurements it is desirable to incorporate the device into a microfluidic system as this offers increased reproducibility and control over that of an open system. To this end, a simple continuous-flow microfluidic system was engineered. The typical system comprised of several key components linked by 400 µm internal diameter PTFE pipe, as shown in Figure 8.2:

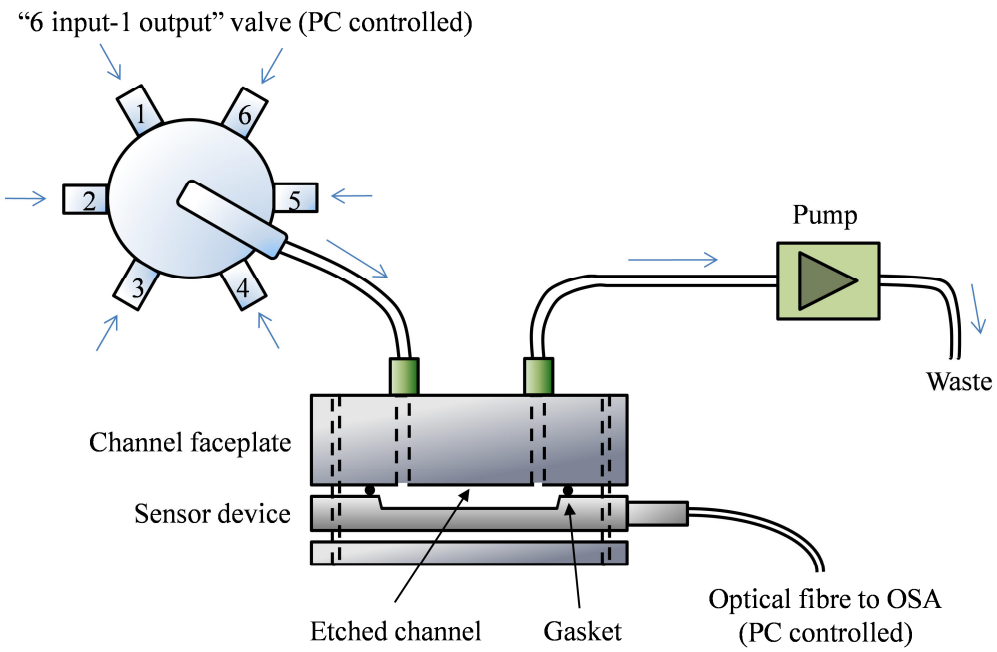

Fig. 8.2 A schematic of the microfluidic flow system.

The input can be selected from one of six reservoirs, controlled by a solenoid valve under the control of Labview [248], allowing automation to be introduced. The output of the valve is pulled through the system and flowed over the sensor surface (typically an etched region of dimensions 3 mm x 8 mm x 18 μm), before passing through a diaphragm pump to waste. The pump period is also controlled by Labview providing control of the flow rate of the system. The planar optical sensor was sandwiched between a faceplate, with the etched well aligned with the input and output ports. To ensure a good seal a gasket was used, typically an O-ring. As discussed in Chapter 3, the sensor can be remotely interrogated by an OSA via optical fibre. This is further controlled through Labview code, allowing the system to be controlled and interrogated by the same computer workstation.

An advantage of this system is that all components were constructed from PTFE and were immune to most chemical erosion, including chemicals that are unsuitable for the common polydimethylsiloxane (PDMS) microfluidic systems. This allows the system to be easily modified to undertake reactions on the surface without modification, i.e. each reservoir can hold a different reagent or solvent allowing sequential steps to be automated. Alternatively it allows full automation via Labview when analysing a series of different analyte flows.

While this system does not represent a lab-on-a-chip in the truest sense, the potential for miniaturisation into a single device is readily available. Examples of integrated pumps, valves and switches have been reported, such as in the work of Unger [249], where all three components have been demonstrated through soft lithography processes in a single device. Furthermore through the use of a tuneable laser the characterisation circuit can be compacted from one orientated towards laboratory prototyping to a commercial system as demonstrated by Stratophase [201] with their portable Bragg grating-based biosensors. Such small-scale Bragg grating interrogators are commercially available, with the "Smartscan" by Smart Fibres Limited [250] a notable example. This device combines the entire interrogation system within a single, small 14 by 11 cm case. Using only 7.5 W of power it can interrogate up to 16 sensors to sub-picometre resolution with a sampling frequency of 25 kHz, outputting the data over Ethernet. Such a device would allow for the miniaturisation of the lab-top sensor into a portable system-in-a-box, no larger than a suitcase.

8.3.2 Considerations on the faceplate

The faceplate was designed to cap the etched well of the Bragg sensor making a sealed microfluidic channel, allowing for the flow of fluids through the evanescent field penetrating from the sensor surface. To allow this flow, a port was installed at either end that was compatible with the 400 μm core pipe used to link to other components. The seal between the faceplate and the silica sample was achieved by sandwiching the device between a top and bottom plate under compression with a gasket to ensure a good fit.

The gasket was initially constructed from PTFE thread sealant tape which while inert, suffered from low compressibility which led to air leaks and the formation of micro-bubbles after several hours of use. As these bubbles passed over the sensor, generating "spikes" within the data as the effective index of the grating jumped from that of the fluid (1.30 – 1.44) to that of air (1.00), increasing the inherent uncertainty of the system. To overcome this issue, a refined faceplate using a "Kalrez" O-ring was fabricated. Kalrez is a fluorinated elastomer produced by DuPont [251] that combines the high chemical stability of PTFE with the compressibility and malleability of latex components. It is known to have a high resistance to

temperatures of up 327 °C and has been shown to be compatible with over 1800 chemicals to date.

The first iteration of the faceplate was fabricated from aluminium, because of the ease of milling and its reasonable chemical resistance. This faceplate was found to be sufficient for most microfluidic applications, with no observed degradation upon exposure to a wide range of common solvents. However the main shortcoming of this device was its high susceptibility to strong bases, which were required to prepare the surface for functionalisation (as discussed in the following chapter). Over time the aluminium was etched away by base producing a black precipitate that could block the flow system and also bubbles of hydrogen gas that interfered with the readings of the refractometer. While this did not prevent the intended chemistry from proceeding and though bubble formation would cease upon changing to the next reagent solution, these effects were undesirable.

To overcome this problem, a second generation of faceplate was commissioned from stainless steel, grade 303. This was inert to base, solving the previous issue but was now susceptible to acid treatment; with hydrochloric acid found to be corrosive at all concentrations. Grade 303 stainless steel is doped with sulphur to improve its machinability, however upon contact with acids it will rapidly etch and discolour as the acid reacts with the sulphates and sulphides present. To prevent this it is necessary to passivate the surface before use, this strips any sulphur from near the surface and thickens the oxide layer, protecting from future attack or discolouration. Passivation was achieved by sequential washing for thirty minutes each in:

i. 5 % sodium hydroxide solution at 70 °C
ii. 10 % citric acid at 60 °C
iii. 5 % sodium hydroxide solution at 70 °C

It was found that after passivation visible etching of the steel by acids no longer occurred.

It was considered that in order to analyse fluidic interactions and chemical reactions, multiple sensors sites would be of use. One such potential use would be to measure the sensitivity enhancement of a functionalised surface. To this end a double well sensor was proposed. This could be incorporated within the microfluidic network either in series or in parallel, such that each well would simultaneously be exposed to

the analyte solution. If one well were functionalised while the other was left unfunctionalised, any difference in sensitivities would be due to the surface binding. A schematic of the double well faceplate is shown in Figure 8.3. The Faceplate consists of the two oval grooves on the lower face, for the Kalrez O-rings to housed, marking the two flow regions. Each region comprises of an inlet and outlet channel that links through to ports on the top face, milled to be compatible with commercial PTFE ferrels. The Baseplate contains a vacuum chuck that is used to assist in aligning and securing the optical device. By sandwiching the etched sensor between these two plates a secure, water-tight seal can be formed, completing the microfluidic flow cell.

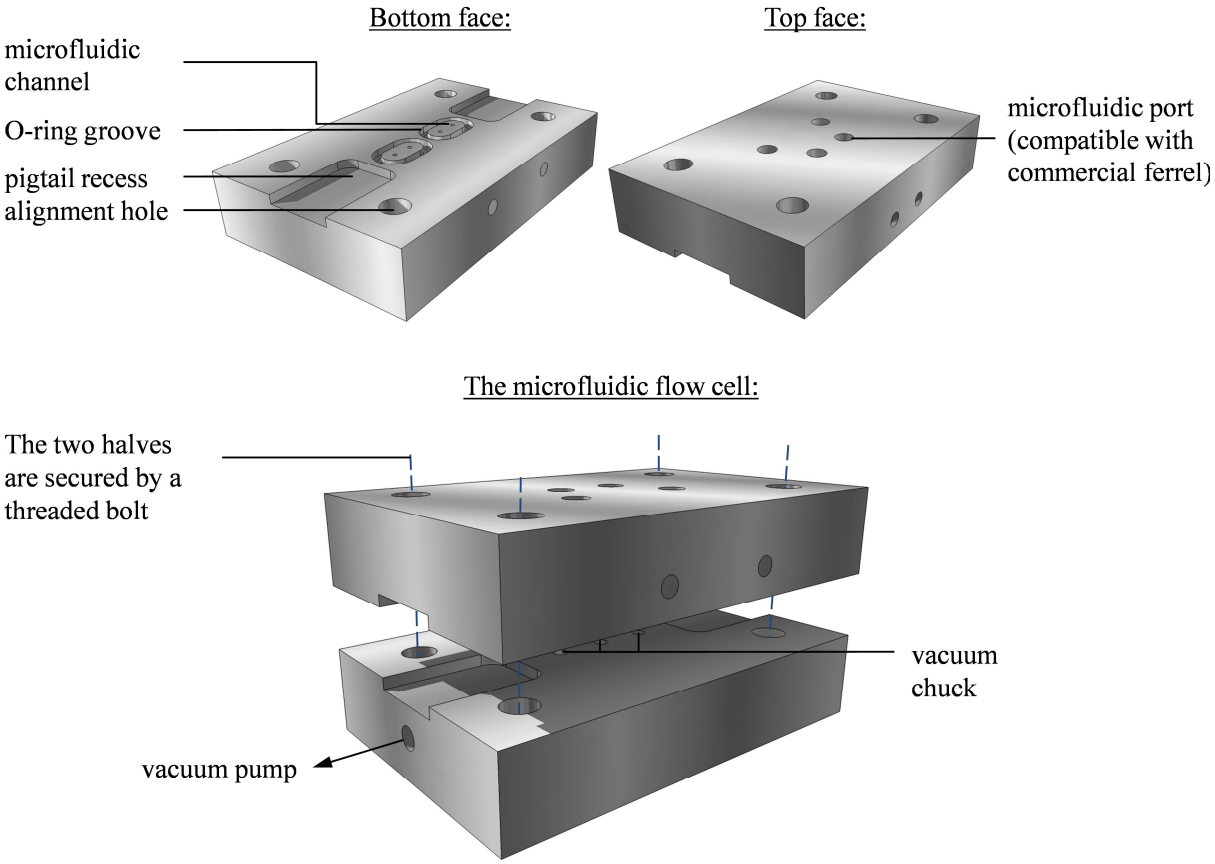

Fig. 8.3 Schematics of the double-well microfluidic flow cell. The Faceplate (top) comprises of two oval chambers on the lower face, linked to two input and two output ports on the top face. The pigtailed device is then sandwiched between the Faceplate and the Baseplate (bottom)

In practice it was found that because of the etching profile illustrated in Figure 5.6, etching two wells of equal depth and thus equal sensitivity was not easy to achieve. This could be resolved using the FEP-coated topless geometry, as discussed in Section 5.6.2.

8.4 Solvent Transitions in a Flow Cell

Initial work focussed on flowing common solvents through the microfluidic system to check for chemical compatibility and flow properties. The system was found to be stable to a wide range of solvents, from volatile organics, such as dichloromethane and acetone, through to water and dimethylsulphoxide.

It was expected that for fast switching times in a laminar regime, little mixing would occur between the proceeding and receding solvent, leading to sharp solvent transitions that would be detectable as sharp changes in refractive index. For immiscible solvents this was found to be the case. Figure 8.4 below shows the refractive index profile for transitioning between water and ethyl acetate. As no stable mixed state can exist, there are no possible intermediate stable refractive indices and the sensor must switch smoothly from one value to the other. However the leading edge of each transition did not rise as vertically as expected. Further investigation with a faster refresh rate on the OSA showed that initially the Bragg sensor sees alternating "bubbles" of ethyl acetate and water resulting in the index jumping quickly between the two bulk indices - which were averaged over the scan to give the slope.

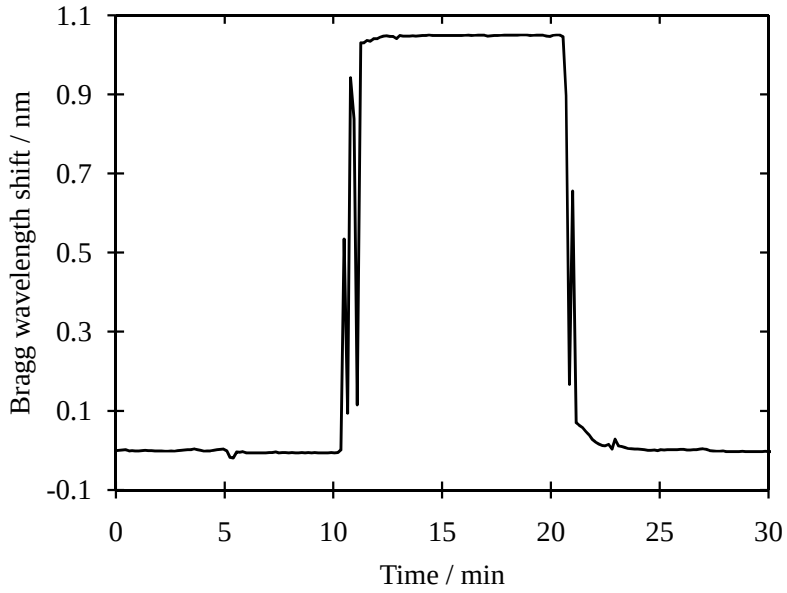

Fig. 8.4 Switching between water of index 1.33 and ethyl acetate of index 1.37 produced a sharp transition in refractive index; the "spikes" observed are due to pockets of the receding solvent forced through the system at the interface between solvents.

When miscible solvents were investigated, the refractive index profile upon solvent transition differed. Figure 8.5 shows that switching between methanol and

isopropanol within the microfluidic system resulted in a reproducible series of changes in the effective index of the grating, similar to those seen for water and ethyl acetate. However upon closer examination it is seen that it takes over five minutes for the refractive index to normalise to the index of the new solvent, as shown in the inset.

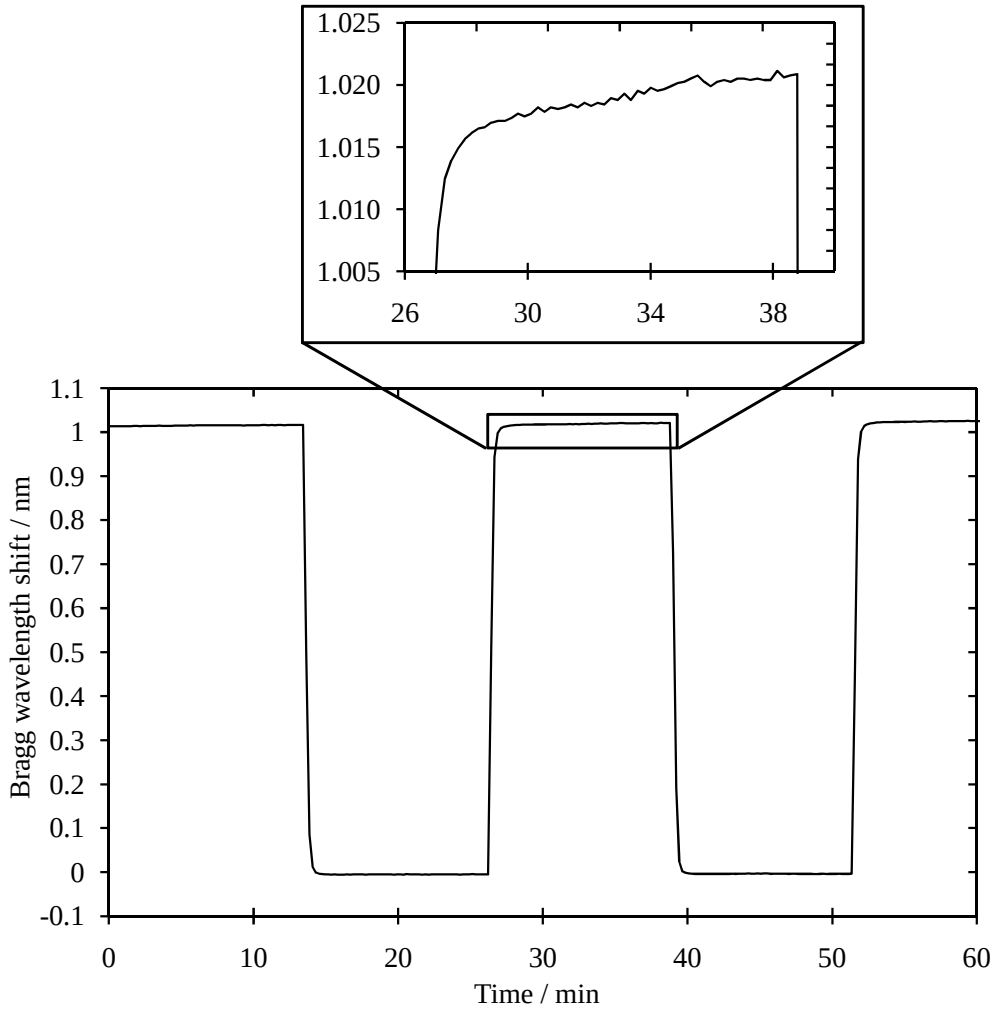

Fig. 8.5 The effective index response to transitions between isopropanol and methanol within the microfluidic system; the inset shows the slow transition to pure isopropanol.

Furthermore, on exploring the mixing of a range of different solvents, it was found that the shape of the transition was dependent on the nature of the previous solvent. This is shown in Figure 8.6 where all possible transitions between the common solvents isopropanol (n_D = 1.3772), acetone (1.3586), methanol (1.3284) and water (1.3330) are demonstrated. While for most transitions the same initial rise followed by a gradual transition curve was observed, for methanol-water and acetone-water transitions a large "spike" was observed at the transition. These were reproducible and not due to air bubbles in the system – something that could not cause an increase

in refractive index above that of the pure solvent. To understand the nature of these transitional structures and explain the nature of the long timescales observed it was chosen to focus on the methanol-water transitional "spikes".

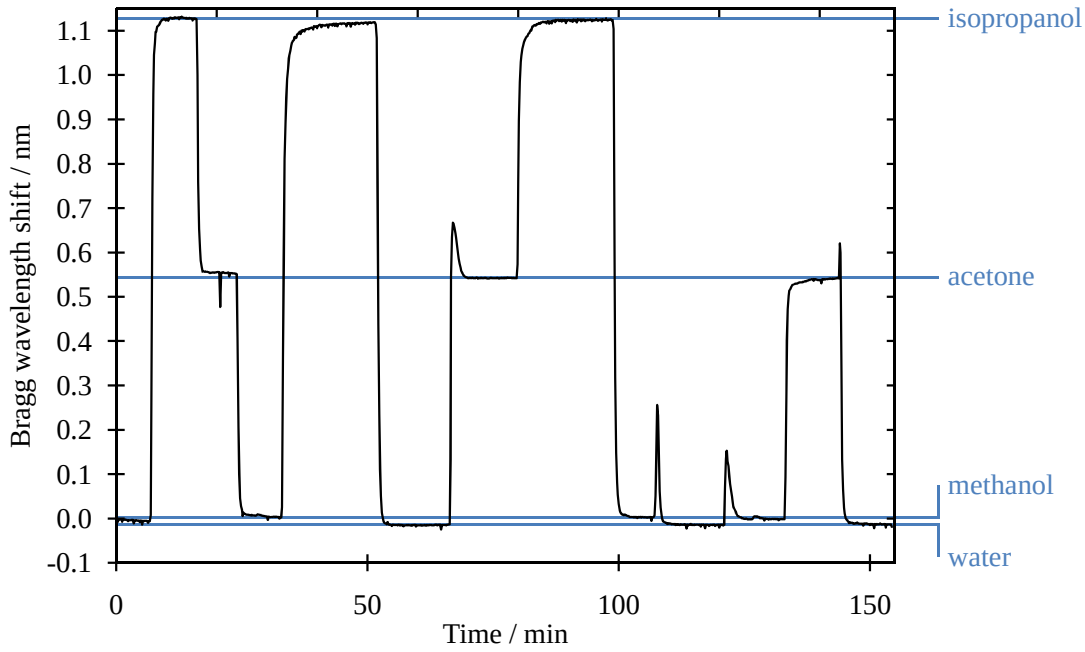

Fig. 8.6 The shift in peak wavelength observed upon switching between isopropanol, methanol, acetone and water within a microfluidic flow cell.

8.5 Methanol-Water Mixtures

On exploring the mixing of a range of solvents, it was found that the nature of the transition was dependent on the solvents being mixed. While isopropanol-water gave a square wave like response but with a small mixing transient (comparable to that for isopropanol-methanol, above in Figure 8.5), mixing water with other alcohols such as methanol or ethanol produced a "spike" in the refractive index during the transition. These "spikes" are particularly significant for the interchange between methanol and water, where the peak index change is over an order of magnitude larger than the difference in the bulk fluids.

8.5.1 Methanol-water "spikes"

Successive switching between the two solvents in the methanol-water binary system demonstrated that the "spikes" are both reproducible and consistent, as shown in Figure 8.7. On switching from methanol to water a narrower "spike" was observed, while the reverse transition produced a much broader "spike". The raw spectra were studied and it was found that the response of the Bragg grating remained Gaussian

across the "spike" transition. This confirmed that the profile was genuine and not an artefact of the fitting algorithm such as the result of bubbles passing over the surface or rapid changes in the reflection spectrum.

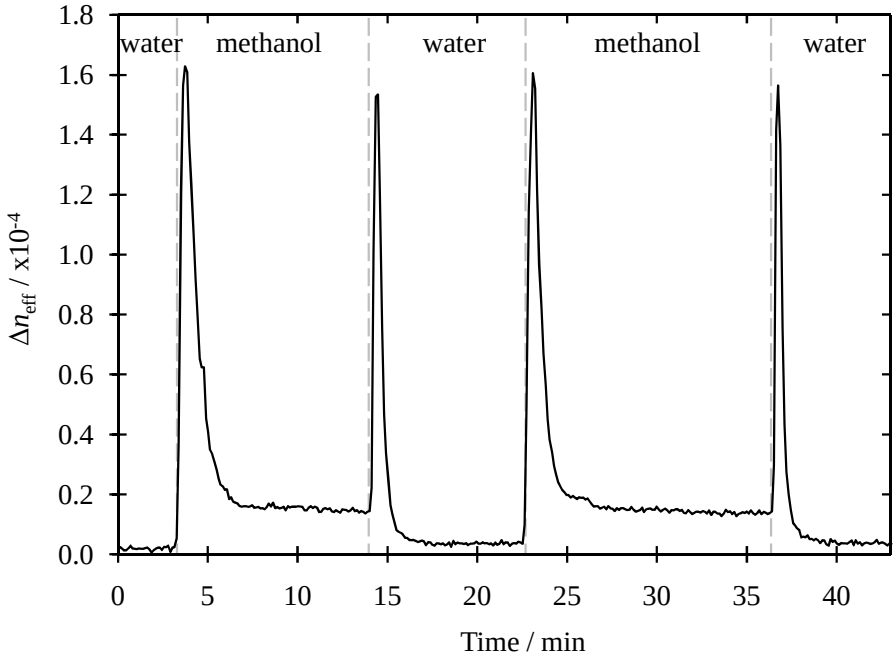

Fig. 8.7 The change in effective index upon cycling between methanol and water within a microfluidic flow cell, showing the "spikes" caused by transitional solvent mixing.

Comparison of these TE data with those for the relatively insensitive TM mode (Figure 8.8) shows that the ratio of the magnitude of the "spikes" to the bulk change is consistent for both – it is believed that if this were a thermal response (arising from the enthalpy of mixing), the two modes would sense this thermal change comparably and would give similar "spikes", but would have differing sensitivities to the bulk change. As such it was concluded that these "spikes" are the result of genuine increases in refractive index at the fluidic interface.

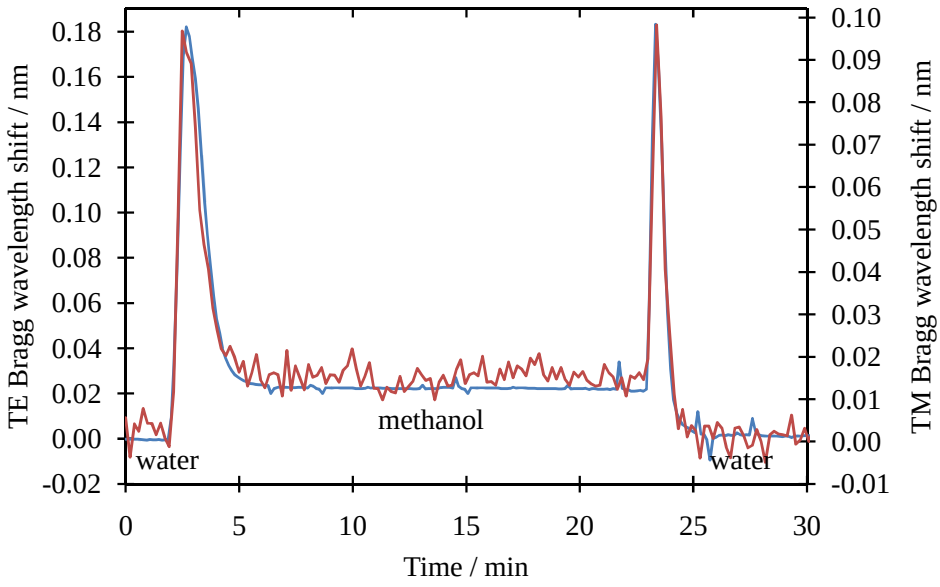

Fig. 8.8 A comparison of the "spike" transition profile for the TE (blue) and TM (red) modes.

8.5.2 Methanol-water, a binary liquid

Work by Katz [252] on methanol-water mixtures in liquid chromatography discussed the formation of a methanol-water associate phase upon mixing. This resulted in a ternary mixture of associated water, associated methanol, and water associated with methanol producing a significantly different structure. They showed that the bulk refractive index at n_D is dependent on the proportion of this methanol-water associate phase, producing a significantly humped curve when comparing refractive index against solvent composition.

To investigate if the "spikes" observed on solvent switching were genuinely the result of large changes in refractive index, a similar curve was recorded in the microfluidic system by switching between a series of premixed methanol-water solutions, as shown in Figure 8.10. As predicted by Katz[252], a much higher refractive index (corresponding to a larger wavelength shift) was observed for mixtures of methanol and water than for either solvent separately. The peak refractive index found in an aqueous solution containing 60% methanol is consistent with the amplitude of the "spike" in the flow system. This confirms that this is a genuine refractive index change and it was hypothesised that the "spikes" on the microfluidic data correspond to the change in effective index upon travelling across this curve – as the two solvents mix and exchange along the microfluidic channel.

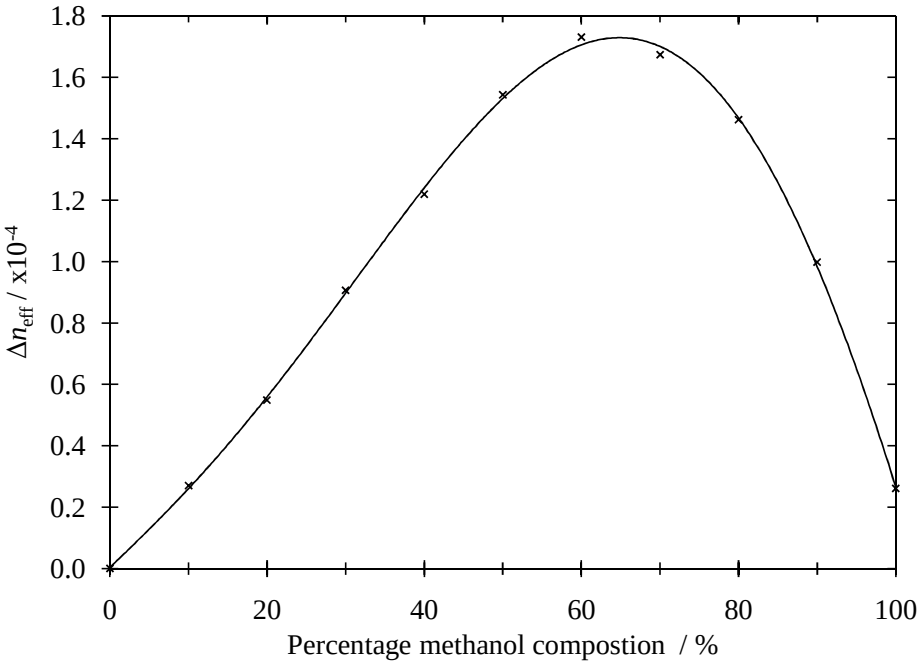

Fig. 8.9 The change in peak Bragg wavelength with the composition of the methanol-water binary mixture.

The curve shown in Figure 8.9 is asymmetric. This may explain why the peaks are broader when switching from water to methanol (traversing from left to right on the figure above) than for methanol to water (right to left). The isopropanol-methanol data seems to imply there is an initial rapid change in index followed by a slower transient; applying that rate to the case of methanol to water this would result in passing over the hump much more quickly when switching from methanol to water than for the reverse process.

With a central Bragg wavelength sensitivity of 1 pm, corresponding to a change in effective index, Δn_{eff} of 10^{-6}, it should be possible to determine composition down to 0.3 %, although the error increases near the peak of the curve where the curve levels out.

8.5.3 Investigation of the nature of these transitions

The laminar flow regime model predicts a gradient in flow velocity across the channel, with side wall friction slowing the fluid and producing the bullet velocity profile, illustrated in Figure 8.1. At the interface between two fluids, such a profile could lead to a concentration gradient at the walls from the proceeding to the receding solvent. With the TE and TM modes penetrating different distances into the fluid, it would be expected that, if these “spikes” were due to such a localised

concentration gradient at the surface, the modal response would differ, with the TE observing a more "bulk" like transition. As was shown in Figure 8.8, the profiles of the two modes are identical, implying the concentration gradient is effectively uniform across the evanescent length scale of the sensing region.

It was found that turning off the pump during the transition between methanol and water allowed these "spikes" to be frozen for up to several hours without change or degradation. Furthermore, on re-engaging the pump the spike profile would continue unperturbed (Figure 8.10). The long life span of these profiles further indicates that the concentration gradient detected upon transitioning between solvents is a bulk effect rather than a short-range concentration gradient perpendicular to the flow which would become lost by diffusion over the time scales observed.

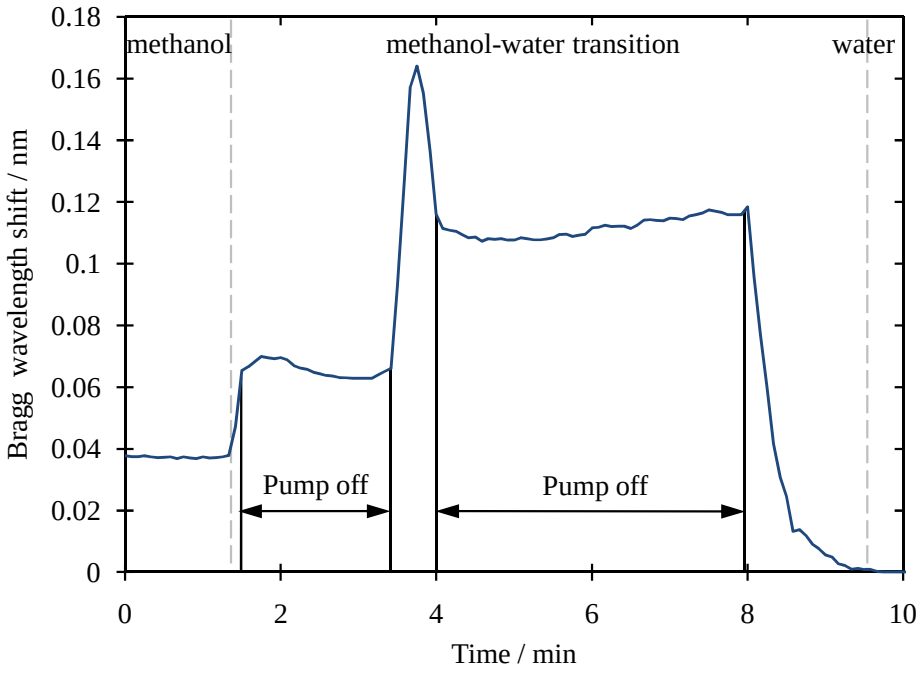

Fig. 8.10 The transition from methanol to water can be paused by switching off the pump and subsequently resumed to complete the "spike" spectral response.

The width of the "spikes" is not insignificant, with the effective index taking between two to five minutes to normalise to the bulk value. When put in context, the diaphragm pump pushes through up to thirty times the volume of the sensor channel with each pump and is pumped once every 1.5 s. On varying the pump period from 0.5 to 5.0 seconds, an order of magnitude increase, the duration of each of these spikes increased as expected. However, when re-plotted as a function of pump cycle

rather than time, comparison of the full width half maximum (FWHM) of these transitions showed that the spike duration was primarily dependent on the number of pump pulses – irrespective of the time left to stand between them (Figure 8.11). This indicates that the mixing occurring within the microfluidic channel is not dependent on diffusion occurring within the system, but by the perturbation of the pump.

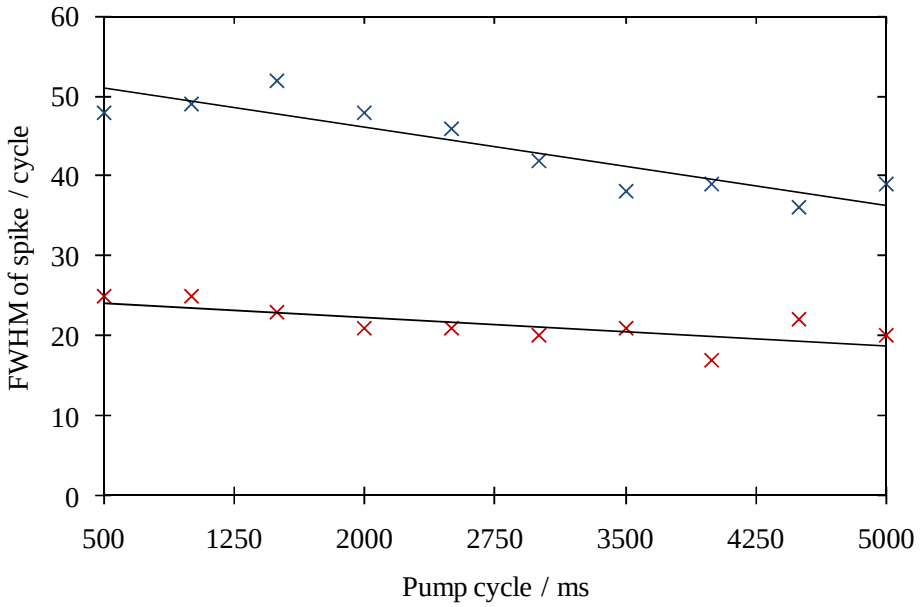

Fig. 8.11 Comparison of a range of transitions as a function of pump cycle indicates that the period of pumping has little effect on the spike duration; water-methanol transitions indicated in blue and methanol-water in red.

The diaphragm pump pushes 4.0 μL with each pulse. While this pulse lasts for 100 ms, the piston is much quicker and the majority of the displacement occurs in a much shorter time (~1 ms). The microfluidic setup uses a 400 μm diameter pipe, which when calculated with the peak velocity of the pump, gives a Reynolds number of ~9,600 indicating that, initially at least, the flow with each pump pulse is turbulent. This would result in any mixing at the fluidic interface being dominated by the pump, with diffusion a minor influence – consistent with the above conclusions.

8.5.4 Laminar versus turbulent flow

Ethyl acetate and water are immiscible, while methanol and water are fully miscible. As shown previously in Figure 8.4, ethyl acetate-water transitions give a sharp transition, giving rise to a square-wave like profile on repeated switching. However with methanol-water the transitional spikes are observed, as previously illustrated in Figure 8.7.

Introducing a water soluble blue dye, “Quink” pen ink, into the water phase allowed the solvent front to be visualised. With the miscible water-methanol transition a gradual change in bulk concentration occurred over several inches of the pipe until the clear solution had fully switched to the dye solution. However this could be visualised as both the initial front which moved quickly with pump rate and a tail of a dynamic mixed solution. In contrast the immiscible ethyl acetate-water transition produced a sharp solvent front.

While the ethyl acetate-water transition was sharp, the refractive index profile indicated that bubbles were present. But with two immiscible liquids why are there bubbles forming rather than a sharp solvent front? The answer again is linked with the high Reynolds number introduced by the pulsed nature of the diaphragm pump. After each pulse of the pump, visible drops of dye condensed out of suspension in the ethyl acetate giving rise to alternating water and ethyl acetate regions along the pipe. This effect explains why the transition is not as sharp as expected, despite the lack of a mixing region and gives further evidence for turbulent flow within the system introduced through the pulsed nature of the diaphragm pump.

Switching to a peristaltic pump allowed the flow rate to be both reduced and to be constant. The much lower Reynolds number of 9.4 should remove any turbulence from the system and any pressure effect that may be associated with the high velocity pulse. This was observed with a sharper transition profile in refractive index between ethyl acetate and water from the clear solvent front.

It was observed that the spikes on transition from methanol to water, and the reverse, were still present with the peristaltic pump (Figure 8.12). The spikes on switching between the two pure fluids lasted for several minutes, but typically had half the life-time of those of produced with the diaphragm pump. As the Reynolds number is far below the limit for turbulent flow, this indicates there must still be sufficient diffusion-controlled mixing within the laminar flow regime to produce the long concentration gradients observed.

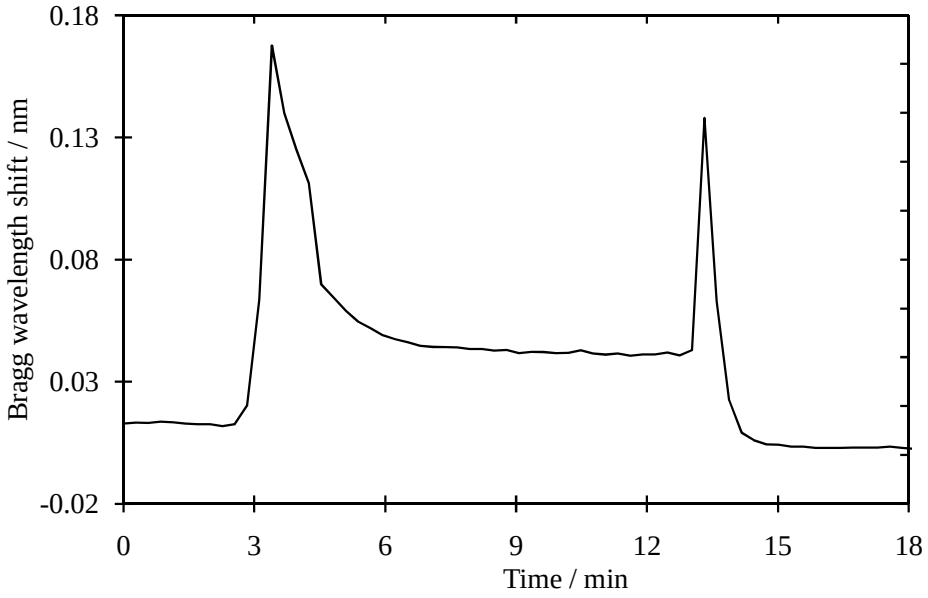

Fig. 8.12 The change in Bragg wavelength upon transitioning between methanol and water within a laminar flow microfluidic network, demonstrating the continued existence of "spikes".

Figure 8.9 showed that the relationship between concentration and refractive index for methanol-water mixtures is linear for low concentrations of methanol. By investigating this regime, the concentration profile can be easily be explored without confusion from the non-linear index relationship. Figure 8.13(a) shows the transition profile on switching between pure water and a 33 % methanol solution. The profile is similar to that previously observed for methanol-isopropanol, that of a sharp initial rise followed by a gradual tail over several minutes. As these concentrations avoid the spike in index, this profile can be considered to be representative of the change in concentration. Figure 8.13(b) plots the natural log of this transition. After the initial few points the plot shows a linear negative gradient, indicative of an exponential decay. This implies that there are two aspects to the concentration gradient as the solvent front mixes along the pipe. Firstly there is a rapid change in concentration which is followed by a secondary slow exponential tail as it normalises to that of the new bulk fluid.

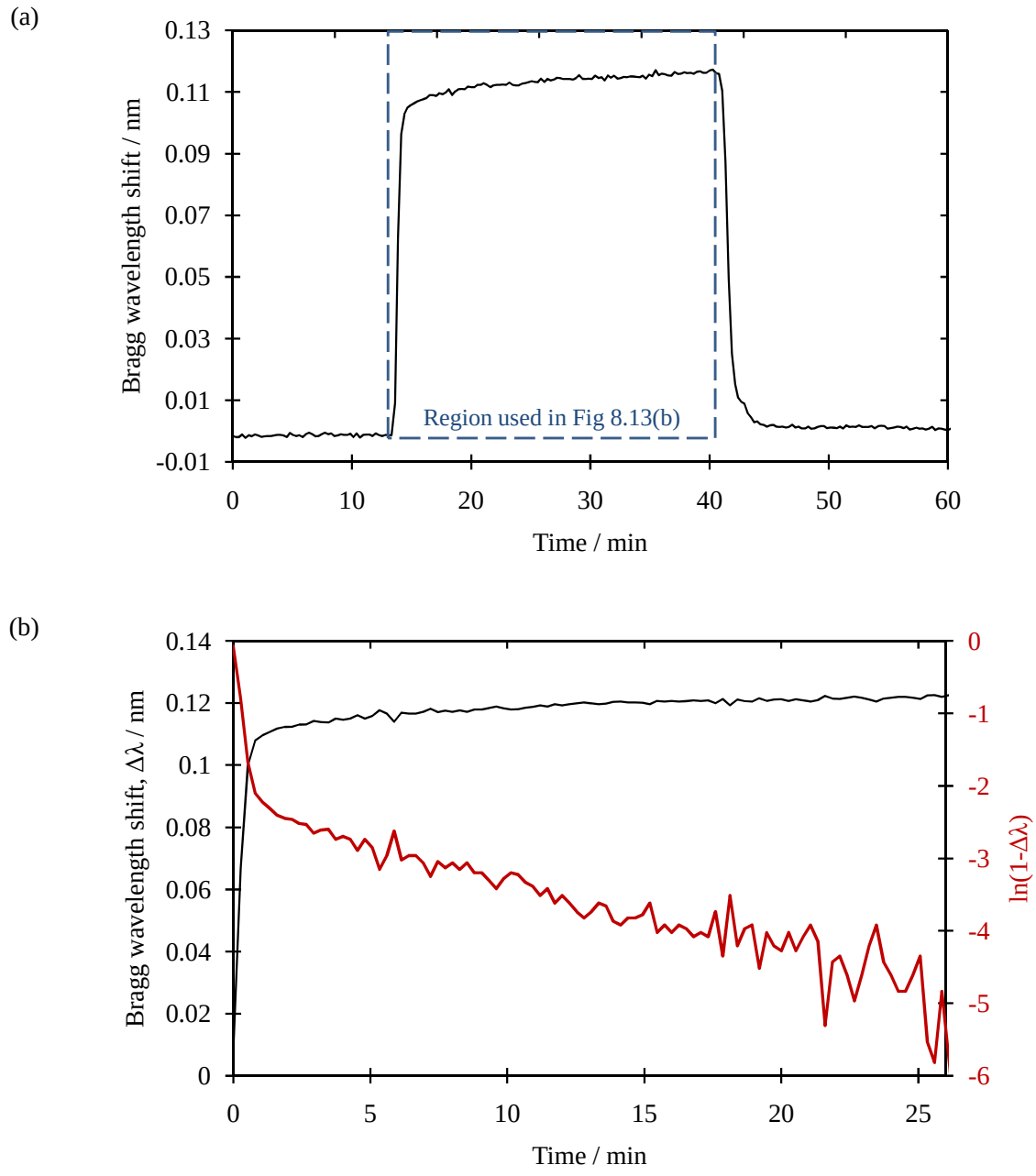

Fig. 8.13(a) The change in effective index upon cycling between water and a 33 % methanol-water solution within a microfluidic flow cell. Fig. 8.13(b) The log plot of this transition (red) showing the linear gradient, indicative of exponential decay.

Within a laminar flow regime the velocity along a circular pipe is greatest at the centre, while tending to zero at the walls. With the relatively high velocities of the peristaltic pump, lateral diffusion along the pipe is negligible resulting in a "solvent front" where the concentration jumps from that of the receding bulk solvent to that of the new solvent. This will give rise to an initial rapid change in concentration. However when mixing can occur, diffusion with the receding solvent moving slower at the side walls will be high. This will initially be greatest at the "solvent front"

where the concentration gradient is highest, and will continue but diminish down the pipe until the bulk approaching solvent is achieved. This will result in a long mixing regime that will exponentially tend towards the new bulk index (Figure 8.14). With the relatively large bore of the microfluidic pipe used (D = 400 μm) the time for diffusion will be of the order of a minute - consistent with the lifetimes observed for the spikes. As the "front" travels along the system, this diffusion will result in the profile switching from the Gaussian like distribution shown on the left to the bulk profile shown on the right. This long bulk concentration gradient is what is then detected at the Bragg grating sensor– the length of this region is much greater than anything lateral diffusion can broaden (in any real time scale) explaining why the spikes could be paused (Figure 8.10).

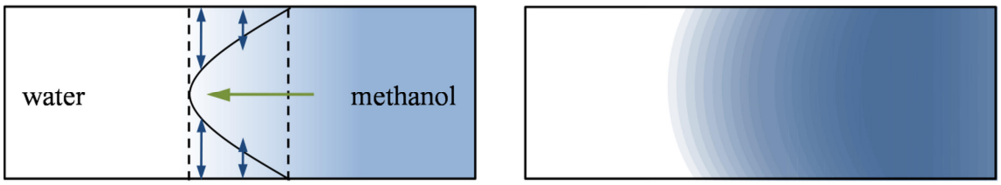

Fig. 8.14 A schematic of the laminar flow profile down the pipe indicating diffusion in from the side walls (left) and the resultant bulk concentration gradient seen as this broadens along the pipe to produce a plug of concentration gradient (right).

8.6 An Optofluidic Flow Sensor for Determining the Water Content in Alcohols

8.6.1 The fluid composition sensor concept

For continuous monitoring of a dynamic fluid system, such as within a chemical reactor, an understanding of these mixing effects is crucial to be able to extract conclusions from the observed changes in effective index. However, this property can also be exploited to produce a real-time sensor that has the capability to detect accurately the fluid composition of a dynamic mixture.

As demonstrated in Figure 8.15, it would be difficult to differentiate an aqueous solution containing 33% methanol from one containing 90% with a single measurement of refractive index, as indicated in blue. However if each of these solutions were diluted by half to 16 and 45 % methanol respectively, as indicated in red in Figure 8.15, the difference in the effective index is exaggerated greatly, corresponding to a well resolved ~0.1 nm difference in Bragg wavelength.

Furthermore the nature of the transition will change upon the dilution. Switching between 33 and 90 % will result in a solvent front with a concentration gradient that passes through all intermediate compositions that will produce the characteristic "spike" as discussed previously. In contrast switching between 16 and 45 % does not encompass the peak at ~ 60 % methanol, and will instead produce a rounded square-wave, similar to Figure 8.13(a). Comparison of the nature of these transitions would give further confirmation of the original concentration.

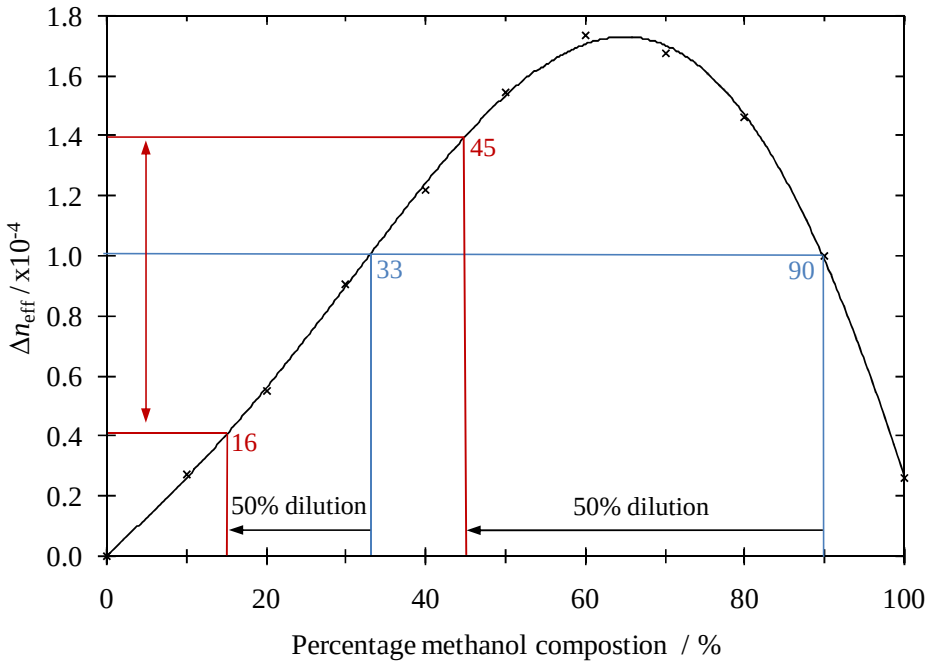

Fig. 8.15 A plot to illustrate that a dilution step can lead to better differentiation between solutions of different composition but similar refractive index.

A Bragg sensor concept was developed with two sensor regions along a microfluidic channel, as illustrated in Figure 8.16. The first sensor (A) measures the index of the aqueous methanol mixture, narrowing the composition down to two points on the parabolic index curve (Figure 8.15); the mixture is then subsequently diluted with water (or methanol) before a second sensor (B) measures the index again. For concentrations below 60% methanol the second reading will be lower than the first, while for concentrations over 60% the refractive index will have increased upon dilution.

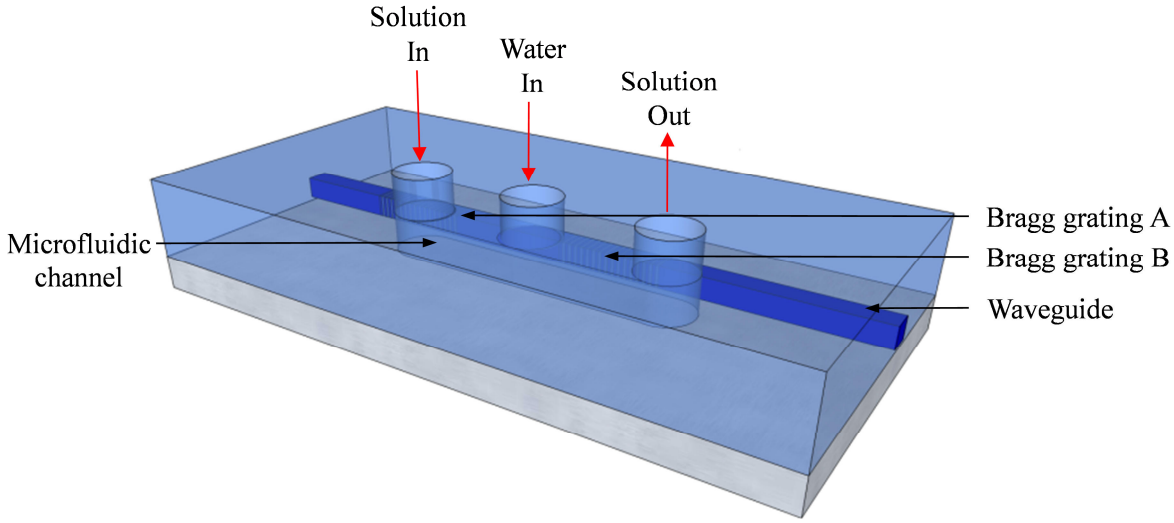

Fig. 8.16 A schematic of the integrated optofluidic Bragg grating device acting as an alcohol concentration sensor

This concept is demonstrated in the following sections where 30% and 90% methanol solutions are flowed alternately through the microfluidic cell. Without any mixing, there is little separation between the two solutions other than the "spikes" that are seen on jumping between such extremes, and whilst this can be used to determine that a large change in composition has occurred, this method only works for relative continual measurements. However, when the same flow is repeated with an intermediate dilution between the two sensor regions a marked change is observed in the shift of the second sensor, B, allowing for much greater differentiation between the two similar solutions, without the need to compare to a reference solution.

8.6.2 Development into a lab-on-a-chip device

This concept was first confirmed through the use of two etched sensors of comparable sensitivity, encased in two flow cells, each with its own independent optical characterisation system. The methanol-water analyte was passed through the first cell, giving rise to the primary refractive index measurement (sensor A), by comparison with the calibration curve (Figure 8.15) the composition could be narrowed down to two possible values. The fluid then is mixed with a separate flow of deionised water before entering the second cell (sensor B) and the refractive index is measured a second time, the nature of the shift on the calibration curve (i.e. to higher or lower wavelength) relative to the first measurement allows confirmation as to which side of the 60 % composition peak the original analyte composition was.

The calibration curve of the refractive index of aqueous solutions containing 0 – 100 % methanol was collected for both sensor A (pre mix) and sensor B (post mix), and is shown below (Figure 8.17). With only one side of the characteristic peak being observed by sensor B, the shape and magnitude confirms that a dilution of ~ 50 % with water is occurring between the two sensor regions, resulting in a change in the refractive index profile.

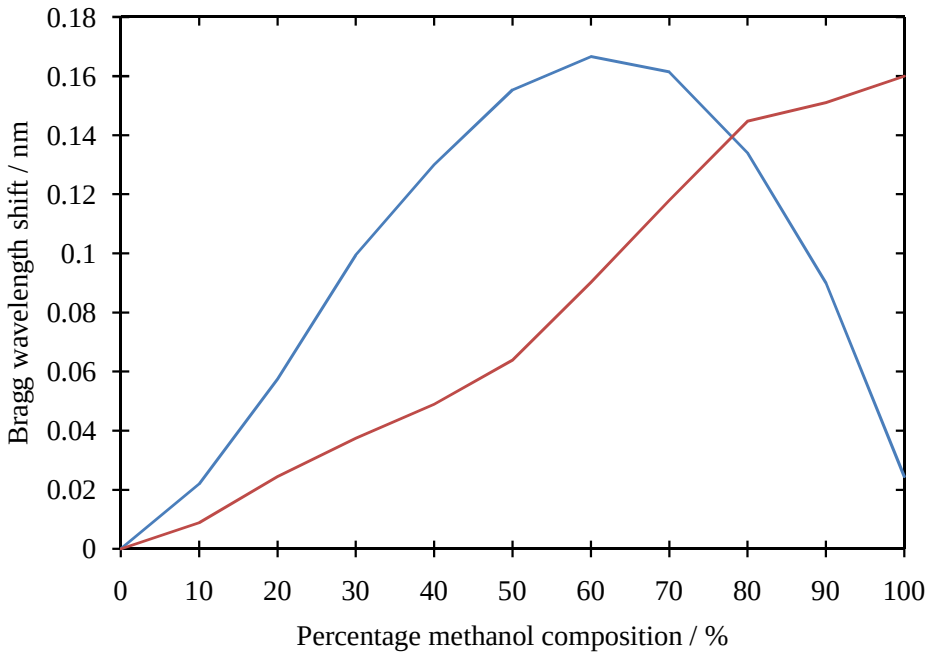

Fig. 8.17 The shift in peak wavelength with the composition of the methanol-water binary mixture, before (blue) and after (red) a dilution with water in the microfluidic flow cell

To demonstrate that the system can detect the difference between two similar index solutions of wildly differing concentrations; 30 % and 90 % methanol in water solutions were alternated through the system. As shown below in Figure 8.18(a), without mixing the indices of the bulk solutions are similar with only the “spikes” to indicate that a significant transition in solvent composition has occurred. After subsequent dilution the “spikes” are no longer observed but the difference in index has been greatly enhanced. As expected, the refractive index of the 90 % solution increases upon dilution while that of the 30% solution decreases upon dilution. The noise present in the post-dilution sensor trace is greater than that observed for the pre-dilution sensor; however, as demonstrated in Figure 8.18(b), for the undiluted equivalent system, this is not an inherent feature of the second sensor. The large fluctuations in Bragg wavelength are the result of genuine fluctuations in refractive index, caused by non-uniform mixing within the flow system. This is confirmed by

larger fluctuations observed for the diluted 90 % methanol solutions; where mixtures can vary from 90 % down to 45 % methanol, giving a potential peak-to-peak fluctuation of 0.07 nm with poorer miscibility due to the wildly varying solvent properties. In contrast the consistently high water content of a diluted 30 % methanol solution leads to smoother mixing.

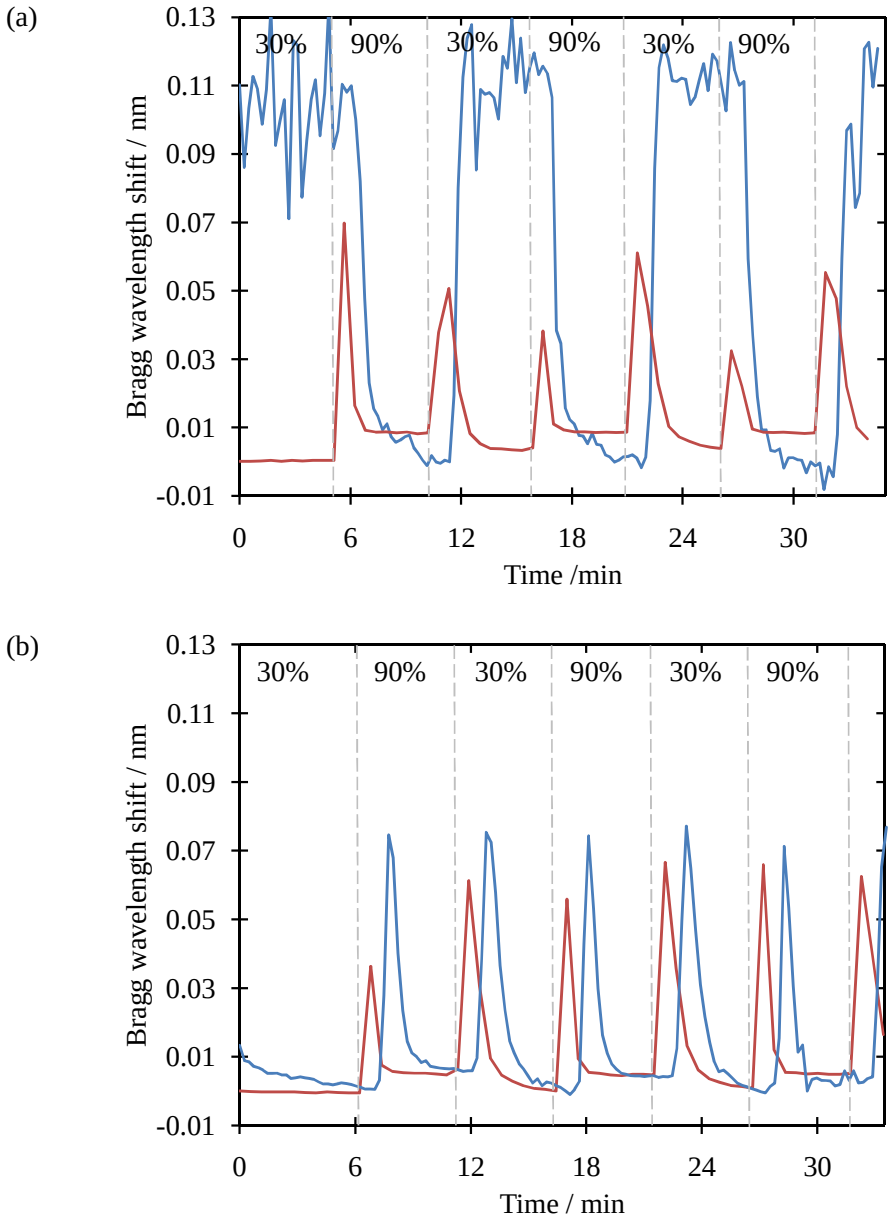

Fig. 8.18(a) The differing Bragg response for two sensor regions within a microfluidic cell to switching between 30% and 90% methanol in water solutions before (Sensor A, red) and after an intermediate dilution step(Sensor B, blue); this response contrasts with the Bragg responses for the unmixed system shown in Fig. 8.18(b).

It should be noted that the sampling rate of the pre-mix trace (red) is lower than that of the post-mix (blue) as a result of the need to use a second, less powerful PC for the second characterisation system. This reduced sampling rate, in conjunction with

the shorter "spike" lifetimes observed with the peristaltic pump (as illustrated previously in Figure 8.12), has resulted in lower resolution of these "spikes", leading to a reduction in the observed amplitude. As shown in Figure 8.18(b), when no dilution occurs the same spikes have a comparable lifetime but greater, more consistent amplitude when observed by the second sensor (B) that are consistent with the height expected from the amplitude of the curve upon passing from 30% to 60 % in Figure 8.17.

Secondly it is also apparent that there is a time lag between detection of the solvent front by sensor A and sensor B as a result of the length of microfluidic pipe between the two cells (~ 40 cm). Such lag is undesirable as it can lead to slower sampling rates or confused composition readings.

8.6.2.1 Using the groove geometry to fabricate the flow sensor

While the above system demonstrated the sensor concept successfully within a microfluidic system, it is not an elegant lab-on-a-chip integrated device. To further miniaturise the system into a single device, it was considered that the groove sensor geometry, introduced in Chapter 5, would allow for the mixing and sensing steps to be achieved along a single microfluidic channel. This should also remove the response lag seen between the two sensor regions seen previously.

A 50 x 50 µm groove was cut into the silica-on-silicon substrate using a dicing technique described previously in Chapter 3. A waveguiding circuit containing a "Y-splitter" was then UV written into the core layer, as illustrated schematically in Figure 8.19. Each arm of the splitter was brought into proximity of the groove through sequential "S-bends" and Bragg gratings were placed parallel to the groove to produce two sensor regions along the channel, separated by 8 mm. λ_1 acts as a reference grating, while $\lambda_{2\text{-}4}$ and $\lambda_{5\text{-}7}$ act as sensors, with increasing sensitivity as the mode penetrates further into the groove. This allows for the grating with the best sensitivity and dynamic range for the application to be chosen post fabrication – improving fabrication tolerances and thus yield. In this case, the relatively low index of methanol and water made the λ_4 and λ_6 gratings the best choice. To further enhance the sensitivity, a tantalum pentoxide overlayer was deposited into the groove.

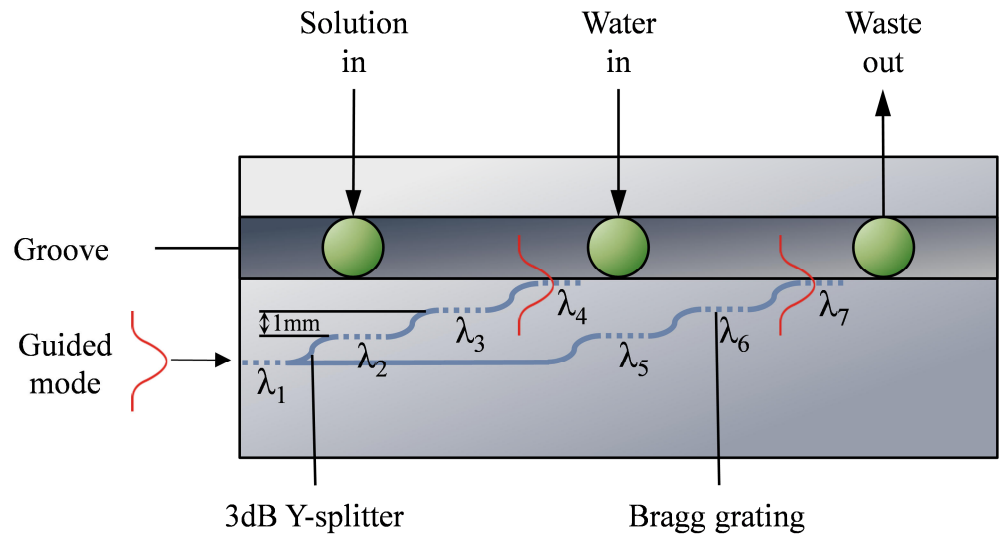

Fig. 8.19 Schematic of the integrated optical Bragg sensor device, viewed from above.

To package the groove sensor, a cap was constructed from Perspex. This had three ports allowing the flow of the analyte in, water in and waste out of the microfluidic channel. The two halves were aligned by eye and sealed through a layer of double-sided polyimide adhesive tape. The tape uses a silicone-based adhesive that did not lose adhesion upon exposure to alcohols or water. Finally, to seal the ends of the channel a small amount of silicone sealant was used that was viscous enough to prevent wicking along the channel that would inhibit sensitivity. The complete packaged microfluidic device is shown in Figure 8.20; it is robust enough to be moved around and used continuously for multiple hours at a time. A PM optical fibre is linked to the standard characterisation set-up, while the two inputs are linked via a peristaltic pump to reservoirs with the output piped to a waste receptacle.

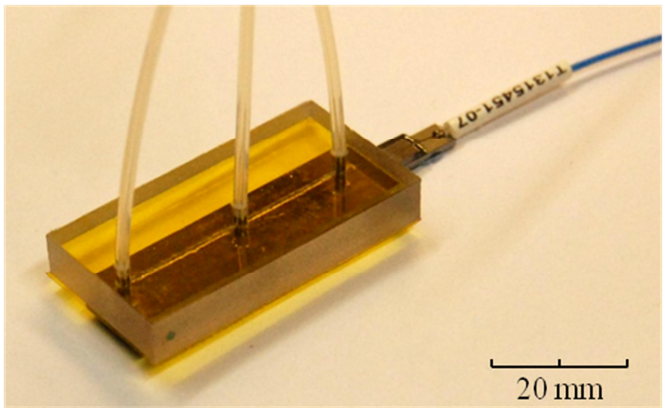

Fig. 8.20 The fabricated integrated optofluidic sensor device

Unfortunately it was found that the adhesive used on the polyimide tape would press into the groove upon assembling the device, inhibiting flow rate. To resolve this, a slot was cut in the tape and was aligned over the groove preventing the groove coming into contact with the tape directly. This had the effect of increasing the vertical dimension of the groove by ~ 100 µm.

Calibration indicated that a mixing ratio of 45 % water to analyte solution was occurring within the microfluidic system. The effect this had upon the input flow of alternating between thirty and ninety percent methanol solutions is shown below (Figure 8.21). As shown in blue, sensor A detected a small difference in refractive index between the two solutions, with the characteristic spike at the interface of each transition. In contrast sensor B showed a larger "square wave" response upon switching between solutions.

The diluted trace at sensor B appears to have more noise on the signal than observed for the original analyte at sensor A, with large fluctuations in refractive index, especially apparent when the 30 % methanol was present. This is not a reflection upon the quality of the Bragg grating, but a direct refractive index measurement of the fluid. The perpendicular geometry of the water inlet and the short mixing region before reaching sensor B did not result in homogenous mixing but in regions of highly diluted methanol followed by regions of lower dilution, resulting in the sensor detecting refractive index fluctuations between these two extremes. In contrast, the humped nature of the refractive index response to concentration leads to concentrations from 50 to 80 % having a much smaller range in refractive index than for 0 to 30 % methanol. This results in the suppression of the detection of these fluctuations when 90 % methanol is passed through the system. This is the converse effect to that seen in the linear network described in the previous section, and demonstrates the importance of the channel geometry upon the sensor operation.

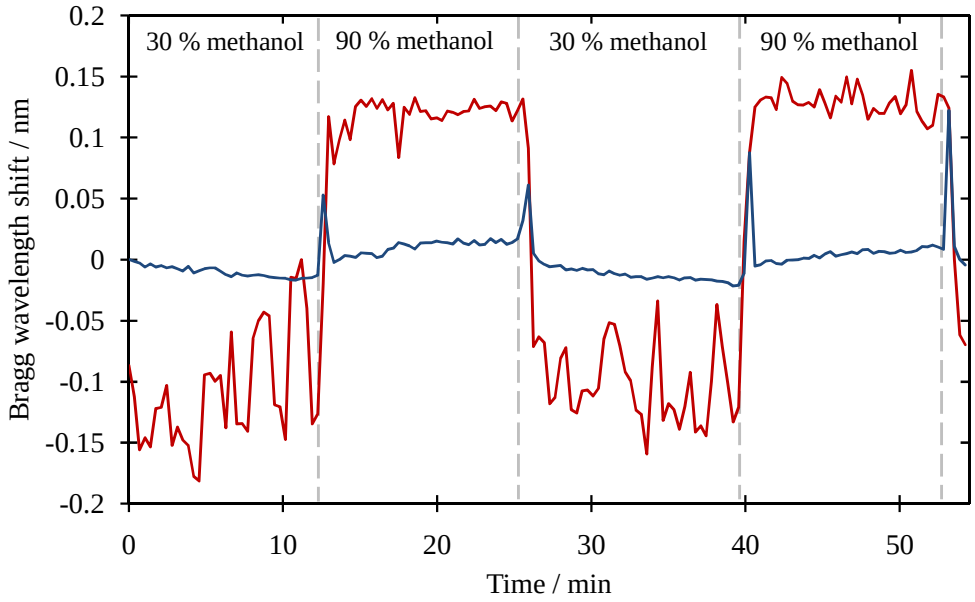

Fig. 8.21 The differential response upon switching between 30 and 90 % methanol in water solutions (blue), showing enhancement upon dilution (red).

While the magnitude of the refractive index enhancement shown in Figure 8.21 appears impressive at first glance, a comparison with the magnitude of the spikes observed for the initial concentrations indicates that something is awry. As discussed previously, the peak of the spike represents the highest refractive index achievable through mixing methanol-water, at around 60 % methanol. The spike between 30 and 90 % solutions (~ 0.15 nm from Figure 8.21) should be ~ 50 % of the amplitude of switching between pure solvents, which would imply the maximum refractive index range achievable is ~ 0.3 nm. Even assuming that the short lifetime of the spikes observed has resulted in the full amplitude not being observed, the diluted differentiation of the two analytes at sensor B is too large. This was found to be the result of differing sensitivities between the pair of sensor gratings, and can be caused by a number of issues, ranging from uneven deposition of the tantalum pentoxide overlayer or uneven side walls during milling during fabrication to the waveguide not being written perfectly parallel to the groove resulting in the second arm penetrating further into the analyte.

To simplify the system it was felt both sensor regions needed to have comparable sensitivity, which combined with the poor mixing and flow rate observed within the narrow groove, it was clear that an alternative approach was necessary.

8.6.2.2 Using the topless geometry to fabricate the flow sensor

To overcome the drawbacks to the 'groove' sensor geometry, a second approach was taken, built upon a FEP-coated, tantalum pentoxide-sputtered (44 nm), 'topless' Bragg grating sensor device.

Rather than machining a channel into the silica, a channel was built up around it, with the sensor lying along the bottom. This was achieved through cutting a thin window of dimensions 34.0 x 0.5 mm into the 25 µm FEP overlayer (as discussed in Chapter 3). This was then aligned with a similar slot cut into the double sided polyimide adhesive tape to produce a similarly design flow sensor to the one pictured in Figure 8.20. As the groove was now confined within the device, no sealant was needed.

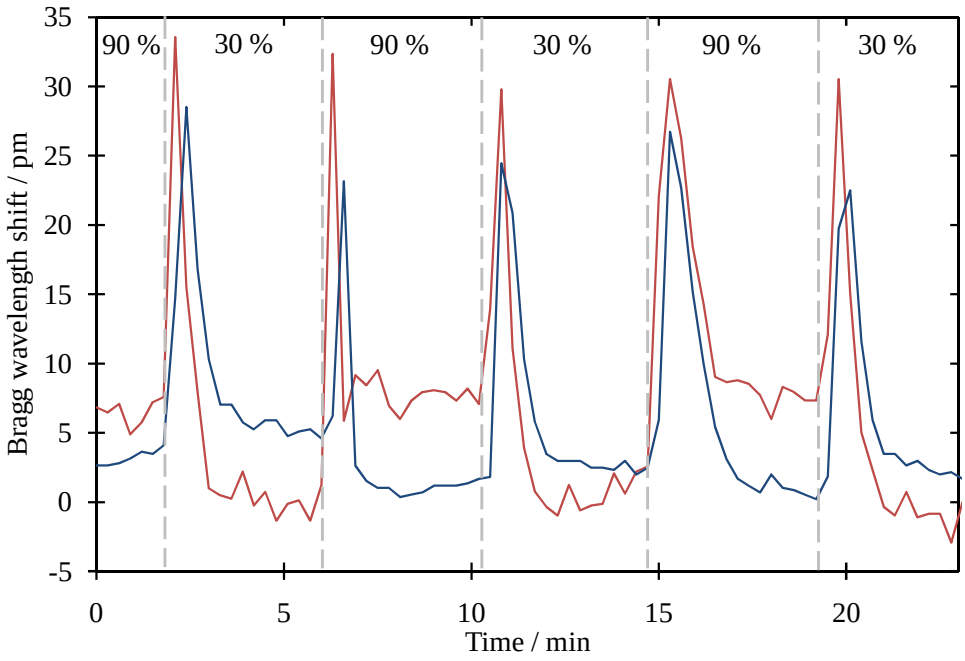

Fig. 8.22 The Bragg response to switching between 30% and 90% methanol in water solutions for Sensor A (red) and Sensor B (blue) within a microfluidic cell.

As shown in Figure 8.22, above, flowing alternating 30 % and 90 % methanol in water solutions through the flow cell without a dilution step produced similar responses at both sensor regions. Sensor B did not show as large a response to switching as observed for sensor A, leading to little differentiation between bulk solvents. The difference in sensitivity were not observed during calibration steps, but was introduced during the cell assembly. This could be caused by any contact

with the silicone adhesive leaving a residue on the sensor surface that would inhibit the proportion of the mode sensitive to the fluid passing over it.

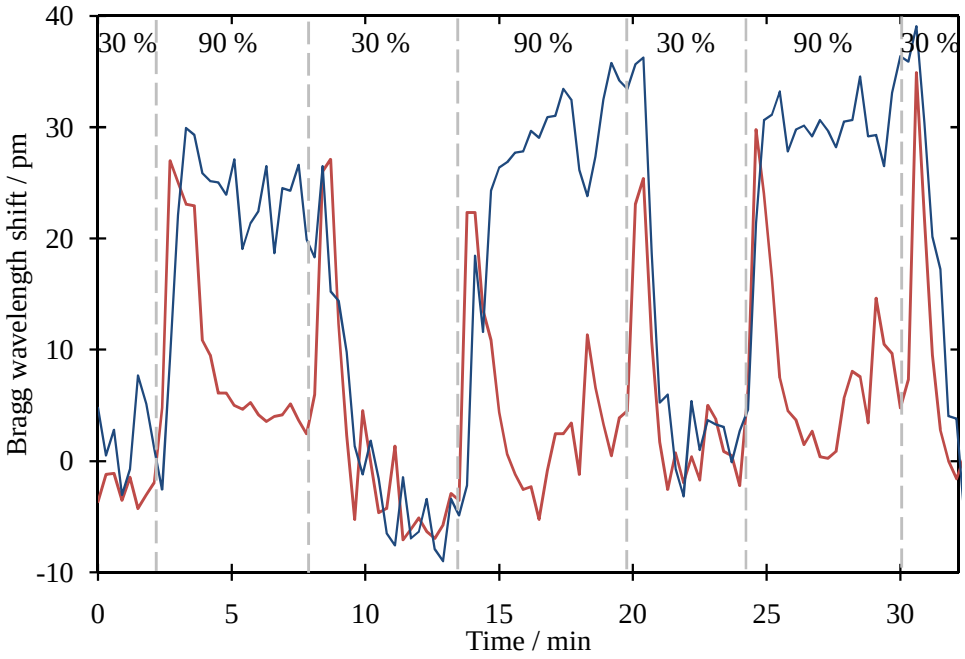

Fig. 8.23 The Bragg response to switching between 30% and 90% methanol in water solutions for two sensor regions within a microfluidic cell before (Sensor A, red) and after an intermediate dilution step (Sensor B, blue).

Upon introduction of a flow of water to dilute the analyte, the sensor traces became quite different (Figure 8.23). As before, sensor A still demonstrated little bulk difference in index, with clear spikes, while sensor B, adopted a larger "square wave" like response. As with the groove sensor the noise has increased dramatically for sensor grating B, as a result of non-uniform mixing, however this is not as severe as observed previously. Unexpectedly, this increase has also been seen for sensor A, implying that the proximity to the second inlet has lead to a degree of back-mixing or fluctuating flow along the channel.

This device has shown, as a proof of concept, that the methanol water "spike" phenomenon observed can be applied to a practical lab-on-a-chip sensor to solve a genuine difficulty in measuring the composition of an alcohol-water solution. To develop the sensor further, a longer mixing region or turbulent mixing chamber [253] would be needed, to reduce the fluctuations seen upon mixing. Furthermore, the sensitivity of the topless sensor, even with a comparable high-index overlayer, was found to be an order of magnitude less than an etched sensor. If the difficulty in

producing etched sensors of equal sensitivity can be overcome, this will allow for the signal to be improved, enhancing the resolution of the sensor.

8.6.2.3 Comparison of the three sensor geometries

Of the three approaches demonstrated here, each has strengths and weaknesses. The simple proof-of-concept device used two separate sensors to demonstrate the concept succinctly but suffered from a time-lag between observing an event at the first sensor and the second. Incomplete mixing with the introduced water was also observed, leading to fluctuations in the Bragg measurement as the inhomogeneous fluid passed over the sensor surface.

Use of a groove allowed for the microfluidic sensor to be miniaturised onto a single device, removing the apparent time-lag of the proof-of-concept device. However the small dimension of the channel further reduced homogeneous mixing in this highly laminar-flow regime. The high back pressure also led to signs of mixing occurring at sensor A, impeding the ability to measure concentration.

The use of the topless geometry allowed for a larger channel to be fabricated, this allowed for simpler fabrication and deposition of a better tantalum pentoxide overlayer. The larger channel improved mixing within the channel and reduced evidence of back-mixing further up the channel.

To optimise the design further, a combination of these approaches would be desired. The ability to isolate the sensors, shown in the first approach improves the quality of the data which when combined with the short channel lengths seen in the later examples gives a rapid and strong sensor response. To achieve this improvement homogeneous mixing is required with no back-flow. Using a more sophisticated microfluidic channel incorporating valves [254] and passive mixing structures [253], combined with an optical device comprising multiple etched Bragg sensors, such a device could be realised.

8.6.3 Applications

Bioethanol [255] is the principle fuel used as a petrol substitute for road transport vehicles and is mainly produced by the fermentation of sugars from renewable energy crops, such as maize, corn and grasses (although it can also be manufactured by the reaction of ethylene with steam).

Ethanol is a high octane fuel and has replaced lead as an octane enhancer in petrol. By blending ethanol with petrol, it is possible to oxygenate the fuel mixture so that it burns more completely and reduces polluting emissions. Ethanol fuel blends are widely sold in the United States, with the most common blend of 10% ethanol and 90% petrol (E10) requiring no vehicle engine modification. Further, "flexible fuel" vehicles can run on up to 85% ethanol (E85). Use of bioethanol in fuels is predicted to cut carbon dioxide emissions and to extend the current oil reserves without major changes to the transport infrastructure.

For ethanol to be usable as a fuel, water must be removed. Most of the water is removed by distillation, but the purity is limited to 95-96% because of the formation of a low-boiling water-ethanol azeotrope. The 96.5% v/v ethanol / 3.5% v/v water mixture may be used as a fuel alone, but unlike anhydrous ethanol, it is immiscible in gasoline, leading to the water fraction being removed in further treatment in order to burn in combination with gasoline. Further, to avoid phase separation, the water content must be kept below the tolerated limit, with fuel mileage declining with increasing water content.

This method described here to determine the water content applies equally to aqueous ethanol mixtures, where a similar refractive index profile is observed [256, 257], with the ethanol-water analogue to the methanol-water "spike" illustrated in Figure 8.24. With the increased interest in bio-ethanol as a future environmentally clean fuel, such monitoring of the wetness of methanol and ethanol solutions in a spark-free environment may become increasingly of interest. Further, it must be noted that such profiles are not unique to alcohol-water mixtures, as illustrated by acetone-water in Figure 8.6, and other applications may become apparent over time.

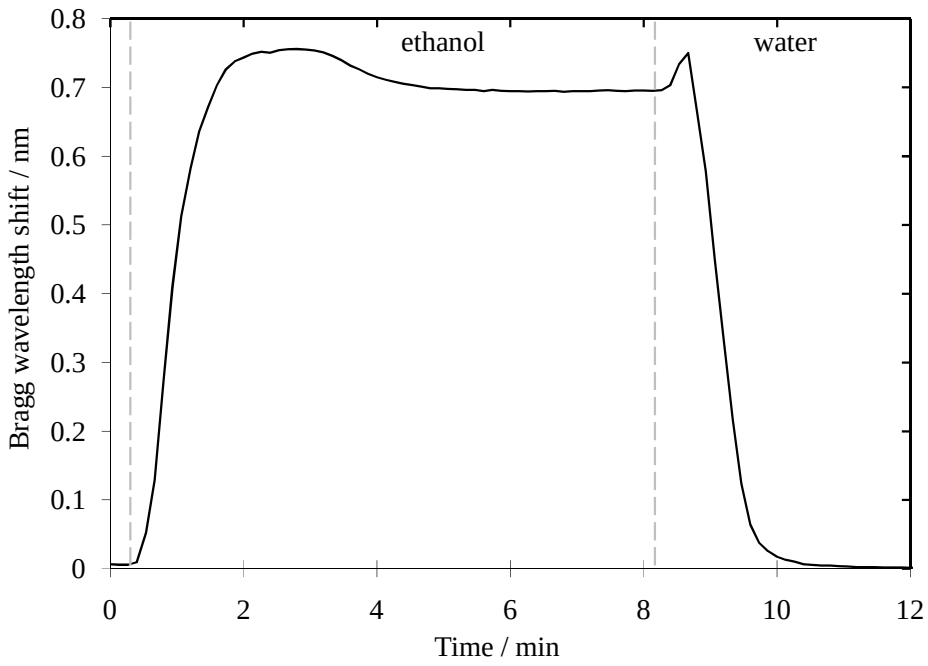

Fig. 8.24 The change in Bragg wavelength upon cycling between ethanol and water within a microfluidic flow cell, showing the "spikes" caused by transitional solvent mixing.

8.7 Summary

A microfluidic flow cell has been developed that allows the Bragg grating sensors to sample a continuous flow of fluid over the surface. The system is compatible with a wide range of chemicals and has been fully automated.

Transitioning between isopropanol and water within this microfluidic flow cell gave an expected square-wave like response in refractive index, but with a small mixing transient. In contrast, mixing water with other alcohols, such as methanol or ethanol, produced a "spike" in the refractive index during the transition. This spike was shown to be caused by the formation intermediate binary liquids of higher index to the constituent solvents.

This spike was shown to have a long life-time, with stability to interruptions in flow, suggesting a bulk concentration gradient along the system that formed independently of the pump rate of the system. Furthermore the length of the microfluidic channel was observed to be independent of the spike forming, with the increase from 0.3 m to 9.0 m having little effect on the spike duration or shape.

This unusual transitional flow property was applied to fabricate a proof-of-concept microfluidic flow sensor. This has been developed to demonstrate a method of

measuring the water content of an alcohol-water mix, overcoming the issues of the parabolic refractive index profile previously reported.

With the development of the microfluidic system and an understanding of the properties of bulk fluids flowing through the system, the following chapter will focus on functionalising the sensor surface with an organic monolayer within this microfluidic reactor. The formation of such a surface layer should be detectable by the highly sensitive Bragg grating refractometer, as postulated in Chapter 5.

9. Surface Functionalisation

9.1 Introduction

In the previous chapter the development of a planar Bragg grating sensor into an optofluidic sensor capable of detecting subtle changes in the refractive index of a fluid was discussed. Physical properties can be separated from chemical fluctuations through a combination of referencing and comparative mode techniques. However such a system cannot differentiate between different chemical analytes in a mixed system. For example the methanol-water composition sensor discussed previously can precisely measure the water content in a known system through comparison with a known calibration, but upon introduction of an additional component such as a solute (e.g. glucose) into the system, the sensor readings will become meaningless. To overcome this limitation it is necessary to separate the refractive index response of an individual chemical species from bulk changes.

As discussed in Chapter 4, many biosensors use antibodies, enzymes or peptides tethered to the surface to control specific binding events. If the desired analyte is present, the preferential binding will enhance the response over that of the bulk solvent. In this way, bio-specificity can be introduced into a sensor system.

A similar approach can be applied to chemical sensing and examples of surface functionalisation being applied to a range of optical sensors were discussed in Chapter 4. There has been much work in supramolecular chemistry investigating the nature of intermolecular associations and much progress has been made on designing specific receptors that can preferentially bind to an analyte in the presence of others. Bringing together the high sensitivity of optical sensors with the selectivity of supramolecular chemistry offers the potential to produce a highly sensitive chemically specific sensor.

To fabricate such systems it was first necessary to develop a robust method of introducing an active surface layer, confirm its presence and characterise the functionality. This chapter will focus on the development and characterisation of such a layer through organosilane chemistry and will demonstrate use of the microfluidic system as a microreactor for surface functionalisation, with real-time feedback.

9.2 An Organic Monolayer on a Surface

Functionalising the sensor surface with an active supramolecular layer should introduce a degree of chemical specificity into the system providing discrimination between different analytes, from pH and ion detection to the concentration of contaminants and pollutants. A straightforward method to generate modified surfaces is through synthesis of a self-assembled monolayer (SAM).

A SAM is an organized layer of amphiphilic molecules in which one end of the molecule, the "head group", shows a special affinity for a substrate. Incorporation of a functional "tail" at the terminus leads to active chemical surfaces. A SAM can be formed on a wide range of surfaces from nanoparticles to macroscopic sheets utilising a wide range of substrates.

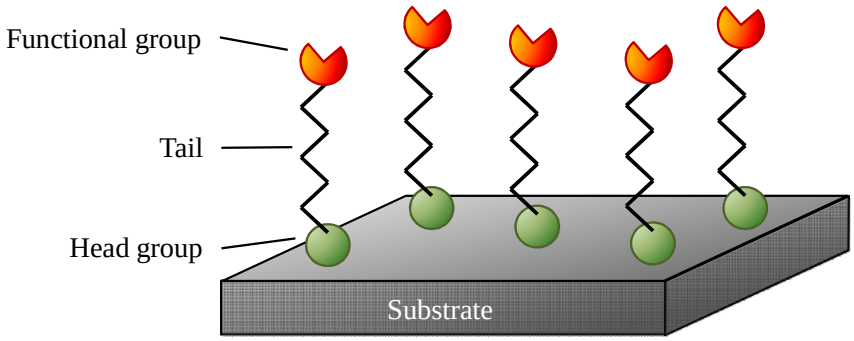

Fig. 9.1 A schematic of a self-assembled monolayer upon a surface.

To fabricate a SAM, it is necessary to clean and prepare the surface ready for reaction; this generally involves removing grease and dirt, stripping surface oxidation or other bound analytes. The deposition of a SAM is directly applicable to a microfluidic system, since the reagents can simply be flowed through the channels, in series to any cleaning and preparative steps, functionalising the surface *in situ* before recontamination can occur.

Sulphur-based thiol head groups are often used for binding organic molecules to a wide range of metals, including gold, platinum and copper [258]. With its many applications in SPR and SERS analytics, the gold surface is one of the more common surfaces encountered in the literature [258] and it is in conjunction with this that the use of thiols is most widely known. In contrast a thiol head group is of no use to bind to a silica surface, where a silane must be employed [259]. However if the substrate is switched from silica to silicon, silane chemistry is no longer applicable without first growing an oxide layer. In photovoltaic applications, where an oxide layer is not viable, direct silicon-carbon bonds are employed through a variety of techniques, including: surface halogenation-Grignard alkylation [260], hydrosilation mediated by metal complexes [261], thermal grafting of alkyl Grignard reagents [261-263] and photo-oxidisation of the surface and subsequent reaction with an alkene [261, 263]. This demonstrates that the chemistry used to fabricate a SAM is highly dependent upon the nature of the substrate. With the choice of substrate often limited by the application of the device, it is necessary to design the chemistry around this restriction. For further examples, Love [258] has included a comprehensive table on the combinations of head groups and substrates that are compatible in a review concerning thiolate self-assembled monolayers.

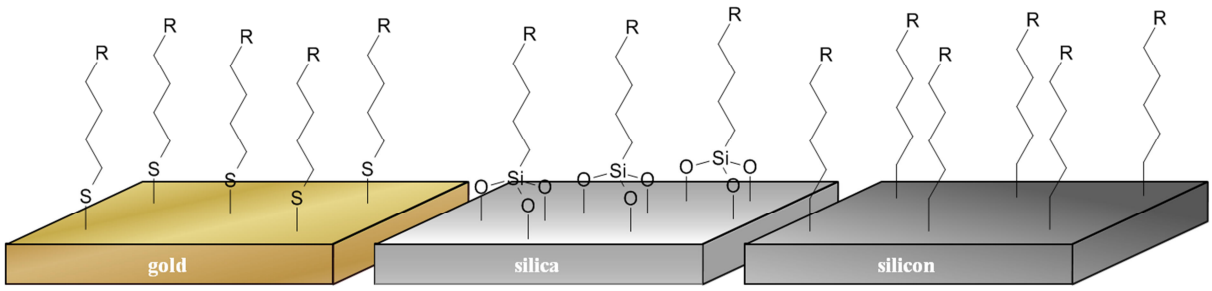

Fig. 9.2 Several common head groups used in surface functionalisation.

In the work presented here, silane chemistry has been employed to functionalise the silica sensor surfaces to form a robust organic monolayer. A functional head group was employed to allow for the potential of a diverse range of receptors to be subsequently incorporated onto the sensor surface.

9.3 Using Organosilane Chemistry to Functionalise a Silica Surface

In some circumstances, functionalising a silica surface is relatively straightforward, with many examples in the literature of organic molecules tethered to a surface via chemical deposition. Commonly this is focussed around silica nanoparticles [264, 265], but the same approach can be applied to planar silica surfaces. This is primarily achieved using a functionalised alkylsilane to produce a surface monolayer of the desired species. For example, Perruchot [266] has shown that glass can be coated with polypyrrole under relatively mild conditions using an alkylsilane linker. The alkylsilane can be added straightforwardly and, with the correct choice of linking group, can be linked to a range of functional molecules. This linker is robust, as shown by Macquarrie [267], who successfully carried out a series of Heck reactions on silica-immobilised compounds with no evidence of the linker interacting or decomposing. The ease of work up, by washing the surface with solvent without risk of removing the organic layer, is also useful when dealing with a microfluidic system.

A wide variety of organosilanes are commercially available allowing for a wide range of organic moieties to be introduced onto a silica surface. In basic aqueous conditions organosilanes will polymerise through nucleophilic attack on the silicon to form silicone polymers. For this reaction a labile leaving group is required on the silicon atom, with common examples including chlorosilane [268] or ethoxysilane [269] derivatives. The degree of cross-linking is dependent on the number of leaving groups bound to the silicon core, with tetraethoxysilane producing a highly cross-linked silicone, contrasting with the polymerisation of dimethyldichlorosilane that will lead to unlinked chains of polydimethylsilicone.

Fabrication of an organosilane surface monolayer relies on similar chemistry, with the S_N2 nucleophilic attack of the silanol groups on a clean silica substrate forming new oxygen-silicon bonds. Depending on the nature of the silane, further cross linking can then occur with a bound (triethoxy)organosilane represented as either a pyramid of three surface bonds, or as a layer with one surface bond and two cross-linked bonds. The issue of which process is correct is something that will depend upon the surface density of silane molecules and the conditions used, however the

low surface density of silanol groups (reported [270] as ~ 5 nm^2 for amorphous porous silica) will tend to favour the second pathway.

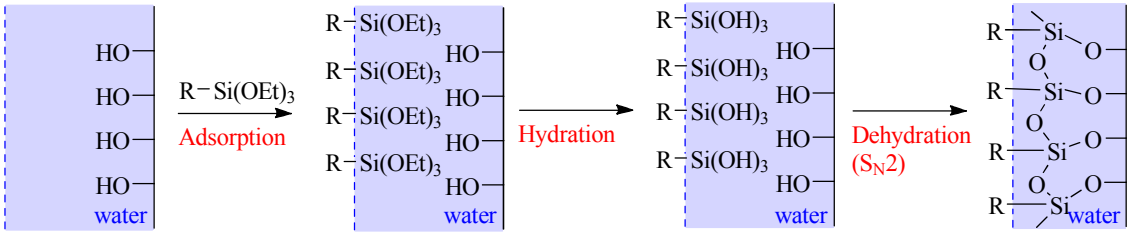

Fig. 9.3 The typical silanisation mechanism to form a silane monolayer [271, 272].

The exact mechanism of silanisation depends upon the reaction conditions present and multiple mechanisms have been reported in the literature, however it is generally accepted that the silanisation process is a three-step process in solution [271, 272]. First, the silane forms a silanetriol by hydrolysis in the presence of water on the surface or in the solvent (as has been observed by second harmonic generation [272]). These silanetriols are then physisorbed, via hydrogen bonding, onto the substrate surface where the silanol groups react with the free hydroxyl groups on the surface by an S_N2-like mechanism, resulting in dehydration. This is outlined in Figure 9.3, where hydrolysis occurs in the inherent water layer on the surface. It should be noted that while the physisorbed system is often presented [271] as a reciprocal hydrogen bonding network between the surface silanol and the silanetriol, it is not apparent how this structure promotes an S_N2-like dehydration mechanism without the interaction of neighbouring silanol groups.

The quality of the silane layer is highly sensitive to the cleanliness of the surface (the degree of free silanol groups at the surface), the presence of water and the nature of the leaving groups present. Too much water will lead to polymerisation and the formation of a polymeric film, while a low degree of free surface silanols will lead to patchy or poor surface coverage. Furthermore characterisation is severely limited over chemistry in the solution or solid phase, with common techniques such as nuclear magnetic resonance (NMR) spectroscopy or mass spectrometry rendered useless.

9.3.1 The typical methodology used for the formation of a silane surface

Preparation of a silane surface can be subdivided into two distinct stages; cleaning and functionalisation. While initial work focussed on developing this process *in situ*,

it was later adapted for application within the microfluidic cell (further details of these experimental methods can be found in Chapter 12).

To clean the surface it is necessary to both remove contaminants from the surface and to restore the chemistry of the surface to hydroxyl groups. This is achieved through successive washings in deionised water and acetone to remove both inorganic and organic impurities, followed by an extended exposure to a basic sodium hydroxide solution. The sodium hydroxide is necessary to restore the surface silanol groups, to ensure the reaction would occur. In some cases where a previous functionalisation or heavy contamination had occurred, an additional wash with "piranha" (3:1 concentrated sulphuric acid to hydrogen peroxide) was deemed necessary to activate the surface.

Immediately after cleaning, the surface would be functionalised by immersion in a 10 % solution of the silane in distilled ethanol or methanol. While the pathway described in Figure 9.3 requires water to activate the silane, this can also lead to polymerisation. Initial work using an aqueous ethanol solvent and a short reaction time (~5 min) yielded poor surface quality with evidence of polymerisation resulting in layers up to tens of nanometres thick. The presence of 3-APS was exemplified with the attachment of a fluorescent dansyl head group to a partially functionalised glass slide and as a result of which the functionalised region of the glass slide was visibly seen to fluoresce when illuminated by UV light.

This method of functionalisation was later refined to produce more consistent monolayers on the surface. The refinement involved two major steps: firstly a more rigorous basic cleaning procedure removed the surface layer, activating the silanol surface; and secondly, reaction with the silane in anhydrous conditions thereby limiting the amount of the catalytic water present and so preventing polymerisation.

An alternative solution was to bake the sample between several short exposures to the silane solution to crosslink the deposited silane, again preventing polymerisation.

9.3.2 Functionalising a tantalum pentoxide surface

As discussed in Chapter 5, the high refractive index of tantalum pentoxide can be used to increase the sensitivity of the Bragg sensor. The structure of tantalum pentoxide is not unlike that of silica, with individual tantalum atoms linked by

oxygen bridges to form either an amorphous or polycrystalline structure. A clean tantalum pentoxide surface will, again like silica, be covered in hydrophilic hydroxyl groups and it is this property that allows it to be functionalised analogously to silica [207].

The ability to functionalise tantalum pentoxide using standard silane chemistry was tested by tethering a layer of (3-mercaptopropyl)trimethoxysilane to the surface, before subsequently depositing a 50 nm film of gold on top [273] using a BOC Edwards E-beam crucible linked to a vacuum deposition system. As discussed above, gold is known to tether to thiols, but will not adhere strongly to silica or tantalum pentoxide surfaces, allowing for functionalised and unfunctionalised areas to be differentiated (Figure 9.4(a)).

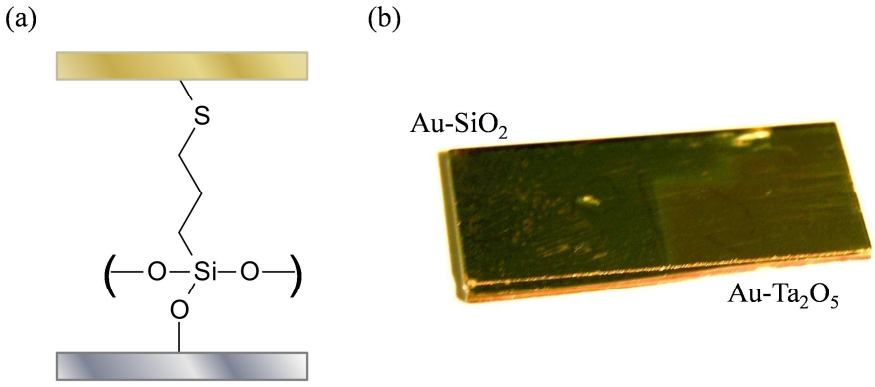

Fig. 9.4 (a) (3-Mercaptopropyl)trimethoxysilane can be used to bond gold to a silica surface. Fig. 9.4(b) Demonstration of the successful tethering of gold to both a silica and tantalum pentoxide surface via (3-mercaptopropyl)trimethoxysilane.

Adhesion tests demonstrated that untreated surfaces retained no gold, while both silica- and tantalum pentoxide-functionalised surfaces retained complete gold films, as illustrated in Figure 9.4(b) above. This test was conclusive that silane chemistry was compatible with tantalum pentoxide and as a result of the higher density of surface hydroxyl groups may even be superior in binding a monolayer.

9.3.3 Diverse surfaces from (3-aminopropyl)triethoxysilane

It was believed that to produce a wide range of functional surfaces, a diverse, robust linker was required. In this way the surface can be cleaned and functionalised by a routine method, to give a wide range of selectivity which can be introduced by the use of the correct receptor for the application. (3-Aminopropyl)triethoxysilane, often abbreviated to “3-APS” or “APTES”, is a common example of such a linker in the

literature [274]. The incorporation of the amino functional group allows for a wide range of functional moieties to be introduced onto the surface via peptide coupling [274]. Appropriate choice of the subsequent group to be attached allows for the properties of the surface to be controlled, from relative hydrophobicity or charge to potential receptor interactions. This principle is illustrated in Figure 9.5, below:

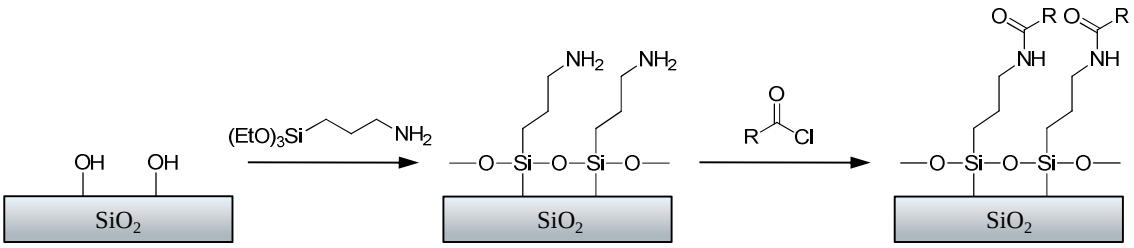

Fig. 9.5 A generic scheme for the synthesis of functionalised organic surfaces on planar silica using the functionalisable alkylsilane tether, 3-APS.

Initial work concerned with attaching (3-aminopropyl)triethoxysilane to silica was successful, with surface attachment being monitored by contact angle goniometry of a 1.0 µL water droplet (Table 9.1). An unactivated silica surface was found to have a contact angle of ~ 35 ° that corresponded to a mildly hydrophobic surface. On cleaning, the contact angle reduced to below the limit of the goniometer (<5 °) indicating a hydrophilic surface. This was visually apparent, with the surface no longer sustaining individual droplets, but with water spreading to the boundaries of the wafer. Upon functionalisation with 3-APS, the contact angle increased, consistent with literature [275]. This chemistry was shown to work equally well with the FHD silica samples used to make the optical chips, with the resultant organic layer proving to be resistant to abrasion and common solvents.

	Contact angle / °
Unactivated surface	30-35
Cleaned surface	<5
3-APS functionalised surface	53 ± 4 (lit [275]: 52 ± 2)

Table 9.1 Contact angle goniometry for a droplet of water (1 µL) on functionalised FHD silica

While this chemistry was compatible with tantalum pentoxide, it was found that an additional clean in concentrated “piranha” solution was required to restore the hydrophilicity of the surface before chemical functionalisation:

	Contact angle / °
Unactivated surface	75-90
Cleaned surface	<5
After 12 h in air	60-65

Table 9.2 Contact angle goniometry for a droplet water (1 µL) before and after surface preparation, showing subsequent rapid recontamination.

For silica and tantalum pentoxide surfaces recontamination was observed in air, with the hydrophobicity of a freshly cleaned sample seen to increase over the course of several minutes. This recontamination was more apparent for tantalum pentoxide, where after twelve hours the hydrophobicity had returned to near that of an unactivated surface (Table 9.2). These observations demonstrate the need to functionalise the surface immediately after cleaning; within an enclosed microfluidic system the risk of recontamination is lowered and such steps can be automated to immediately follow each other to ensure the best surface. Once the surface is coated with 3-APS it is much more resistant, with greater stability being observed, as demonstrated by consistent contact angle measurements being observed over several days.

9.4 Characterisation of Functionalised Silica Surfaces

Robust and reliable methods of independently interrogating the functionalisation of the silica surface need to be developed to prove whether any observed change in refractive index upon functionalisation of the optical device is genuine. There are many approaches to measuring the functionalisation of mesoporous silica particles, where the flexibility of analysing in suspension or the solid state and the high surface area give clear results. However, such measurements are significantly more challenging on a planar surface. While the presence of 3-APS upon mesoporous silica particles can be readily identified by conventional tests, such as ninhydrin, in the planar geometry alternative approaches must be found. The successful (and less successful) approaches used in this work are discussed in the following section.

9.4.1 Contact angle goniometry

The simplest technique discovered thus far used a contact angle goniometer to measure the tangent that a 1.0 µL droplet of deionised water makes with the surface. This gives an indication of the hydrophobicity of the bulk surface. The uncertainty in contact angle measurements was determined from the maximum range of a series

of measurements upon the surface, which was significantly larger than the uncertainty in fitting the tangent to the droplet. To explore the sensitivity of this technique for different surface functionalities, a family of organic compounds were synthesised, as shown in Figure 9.6.

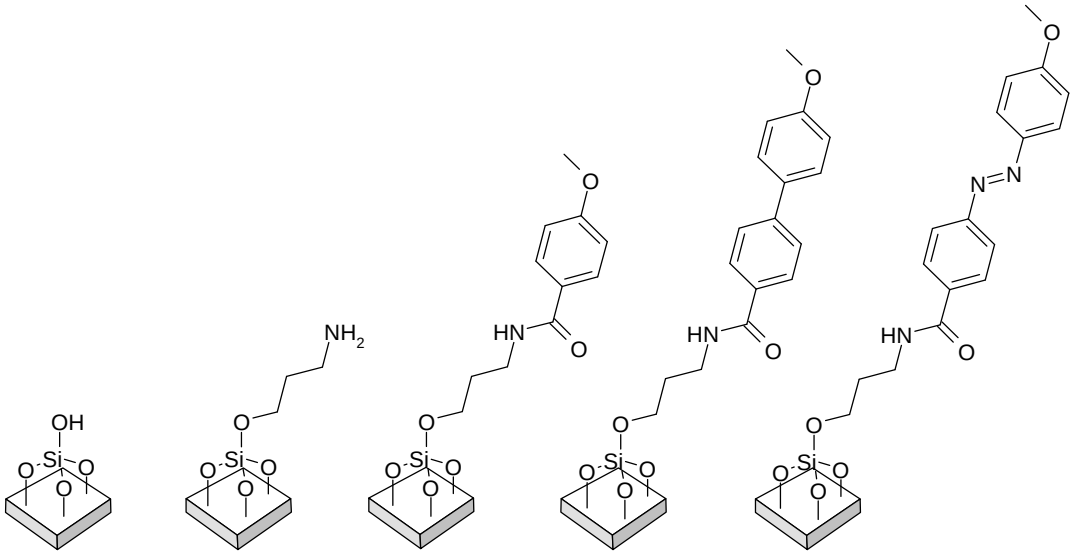

Fig. 9.6 A family of functionalised surfaces derived from coupling to a 3-APS linker on silica.

The contact angles, CA in Figure 9.7 show that each surface is distinguishable from each other within the family, even with subtle changes in the substructure. This indicates that the folding of the chains and packing must vary significantly between each species, which may also result in changes to the density of surface-functionalised sites.

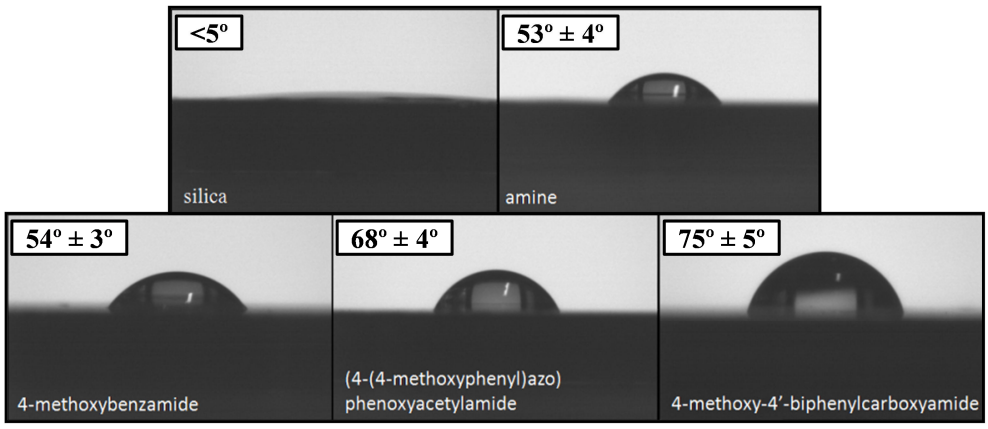

Fig. 9.7 Droplet shape and corresponding contact angle for the family of silane-SAM surfaces above (error determined by the range of 5 repeat measurements).

9.4.2 Fluorescence microscopy

Fluorescence microscopy can be a powerful technique for detecting subtle structural and surface motifs on a microscopic scale. As such it is often used in biochemistry for visualising cells and tracking the chemistry within. As reported by Mela [276], fluorescence microscopy is able to detect changes in fluorescence of a fluorescent tag bound to a surface monolayer. In this way it lends itself ideally to the 3-APS-coated surface as a means of at least checking that the surface chemistry is occurring as predicted. It can be used in conjunction with contact angle measurements to develop an understanding of the nature of the surface. Furthermore, as the fluorescence wavelength is specific to the fluorescent tag used, it is less susceptible to contamination or a misreading that goniometry can suffer from.

Fluorescein isothiocyanate (FITC) is a fluorophore commonly used in microscopy, as a dye laser and to probe biological systems. It fluoresces strongly at 521 nm, a property that allows it to be detected by fluorescence microscopy down to very low concentrations. FITC will readily react with any amine groups present within a molecule or protein making it an ideal tag for detection of an aminated surface.

FITC will not attach itself to the bare surface but will bind to the amine groups of the 3-APS monolayer. To this extent a scheme was proposed to produce a simple striped surface that allows for contrast between the regions of functionalised and bare silica (Figure 9.8). Under the fluorescence microscope, regions functionalised with FITC would fluoresce green while all other areas would remain dark.

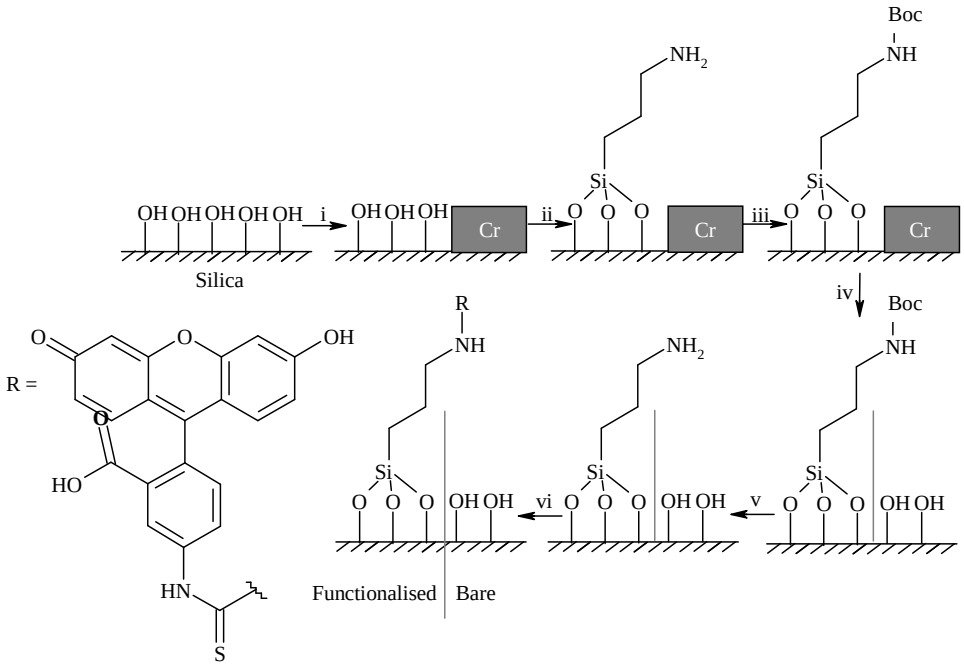

Fig. 9.8 Reaction scheme for striped functionalised silica surfaces; (i) evaporated chromium onto masked surface, (ii) cleaned with acetone/water, then piranha solution followed by 10% 3-APS in ethanol, (iii) Boc_2O DCM with TEA, (iv) "MS 8 chrome etchant" (acetic acid/ceric ammonium nitrate) for ~1 min, (v) 50% TFA in DCM, (vi) FITC in DMSO/DMF.

The chromium was evaporated onto the surface in stripes, using a tape mask. This produced a distinct boundary between the masked and unmasked regions for easier identification of the functionalised regions. The silane reacted only with the clean silica regions allowing for selective functionalisation of the surface. While the chromium can be removed easily, in mildly acidic conditions, it was believed that the ceric ammonium nitrate, a strong oxidising agent, present within the "MS 8 chrome etchant" solution may oxidise the amine group – as such a *tert*-butyloxycarbonyl (Boc) protecting group was applied before removal of the chromium. On removal, stripes of differing hydrophobicity were clearly seen – with the freshly exposed silica exhibiting a highly hydrophilic surface, while the amine-coated regions showed a much more hydrophobic surface.

Figure 9.9 shows the fluorescence microscope image of the boundary of a stripe. When illuminated under blue light, regions of green fluorescence, characteristic of fluorescein, were observed in sharp stripes across the surface, contrasting with the dark regions of bare silica. This surface was found to be more robust than expected, with the surface unchanged by sonication in a range of organic solvents and even surviving wiping with a cloth, with only mild damage visible by fluorescence imaging.

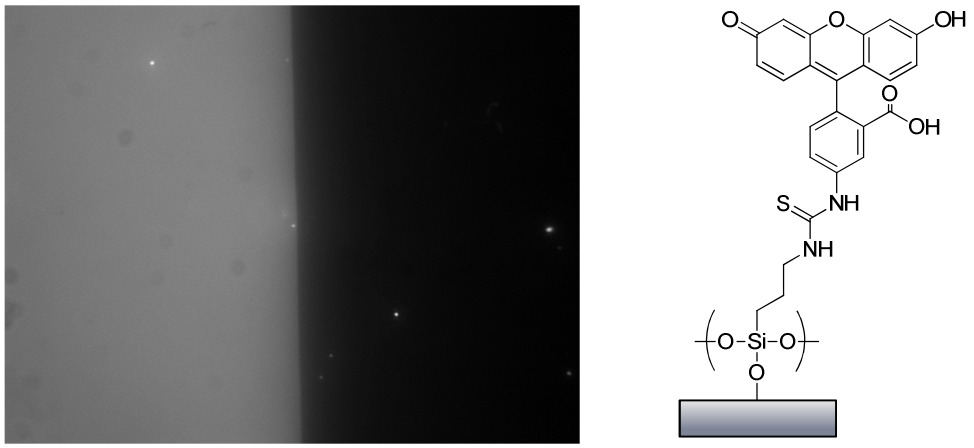

Fig. 9.9 Fluorescence microscopy image of a fluorinated surface; fluorescein-functionalised region (left) and unfunctionalised (right) shown with the structure of the fluorescein silane-SAM.

9.4.3 Ellipsometry and EDX, Raman, IR and UV reflectance spectroscopy's

Mela reported that such surfaces can be further characterised and their thickness can be quantified by ellipsometry [276]. Imaging null ellipsometry is a technique that can accurately measure the thickness of a surface layer, based on changes in refractive index [277]. The technique relies on minimising the transmission of polarised light in a region and looking for contrast with other regions. In this way, the change on moving from the bare to the coated region could potentially be quantified, and through modelling, the thickness can be estimated.

Initial work focussed on the striped fluorescein samples used for fluorescence microscopy. While it was clear from the image map that there was something on the surface, it was not possible to detect a measurable difference between the two bulk surfaces. This was a result of complications introduced by the planes of differing refractive index within the silica of the FHD samples. To overcome this problem samples were re-synthesised on an oxidised silicon wafer. The higher refractive index of the silicon was different enough from that of the organic layer to allow the two regions to be faintly distinguished on the image map, with this difference being quantifiable. However, the ellipsometer was unable to use this to calculate the thickness of this film. Further work with a wavelength scanning ellipsometer again confirmed the presence of a surface film but was not able to quantify the thickness because of difficulties in background deduction of the native thermal oxide and silicon signals.

Based on literature discussing the characterisation of mesoporous silica surfaces [278], reflectance UV-visible spectroscopy was identified as a viable characterisation technique. Three dyes were investigated: fluorescein, dansyl and anthracene, each being tethered to the surface via 3-APS. The solid state absorption spectra were compared with the solution phase. The spectrometer was shown to be easily able to detect thin films of each of the dyes evaporated onto the surface; however it was not possible to reproducibly detect any SAM present.

A similar result was found when using infrared and Raman spectroscopy to detect the presence of a monolayer. The IR spectrum was dominated by water peaks and the Raman spectrum, without the benefit of the enhancement layer employed in SERS, could only detect peaks corresponding to the silica substrate. As such, while these techniques have the potential to detect thin films, it was found that the surface layers (confirmed by contact angle goniometry) were below the sensitivity limits of the spectrometers available during the course of this project.

Energy dispersive X-ray spectroscopy (EDX) uses characteristic X-rays emitted from a surface undergoing scanning electron microscopy (SEM) to produce an elemental map of a region. While this technique will probe the top micron of material it was believed that it would have the sensitivity to detect an organic monolayer – if it contained a characteristic element. To this end attempts were made to tether ferrocene carbonyl chloride to the surface. This resulted in an iron-containing monolayer across the surface, an element that was not detected in background EDX scans. To give contrast, regions were coated with narrow stripes (~ 1-10 μm) of chromium metal. It was expected that the elemental maps for chromium and iron should be the inverse of each other – with ferrocene only found in the exposed silica regions. However, no significant iron trace was detected (Figure 9.10). Further, the 50 nm thick layer of chromium required continuous scanning for up to an hour to give a well-resolved image, demonstrating that the technique lacked the sensitivity to probe thin films, a conclusion compounded by the evidence of surface ablation by the electron beam, seen when comparing the SEM image before and after exposure.

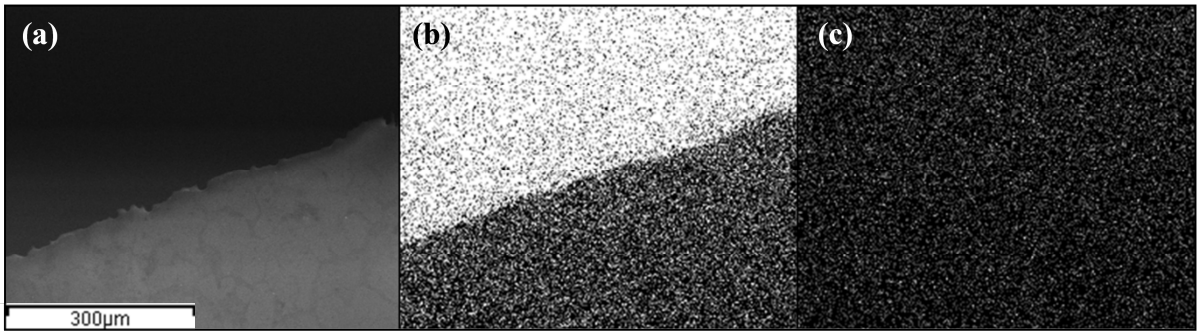

Fig. 9.10 EDX spectroscopy of a ferrocene functionalised surface; (a) SEM image of the chromium silica boundary, (b) chromium EDX map, (c) iron EDX map.

9.4.3 Summary of techniques

A broad range of analytical techniques have been applied to characterising the functionalised surfaces. The success of these techniques has ranged from fluorescence spectroscopy and contact angle goniometry that have successfully detected specific changes in the surface chemistry, through to infrared and UV-visible spectroscopy's which, while having the potential to detect these subtle surface layers, were not able to do so with the equipment available.

However, other than the partial result with ellipsometry, these techniques are not sufficiently quantitative to confirm the thickness of the "monolayer" upon the surface. To overcome this shortcoming, modelling of the waveguide will be employed in the subsequent section to corroborate the observed Bragg wavelength shift upon functionalisation.

9.5 A Microfluidic Reactor for Surface Functionalisation

The stepwise washing and functionalisation processes lend themselves ideally to application within a microfluidic system. By combination with the optical Bragg grating sensor, the surface can be probed in real-time during reaction, allowing for characterisation of the surface to occur *in situ*.

9.5.1 Fluorescein functionalised surfaces

Initial work focussed on functionalising the sensor surface with a FITC-derived SAM *in situ,* within the microfluidic cell (Figure 9.11). This microfluidic reactor allowed real time, automated monitoring of the changes at the surface by the evanescent field of the Bragg grating.

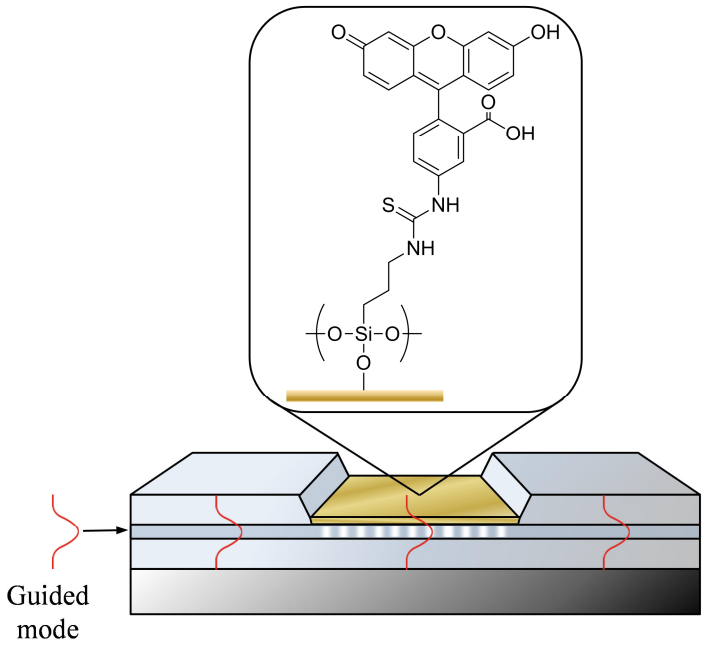

Fig. 9.11 A schematic of fluorescein functionalised onto the microfluidic Bragg grating sensor surface.

An etched Bragg grating sensor was fabricated with a 50 nm tantalum pentoxide overlayer and installed into the microfluidic flow system. The sensor surface was cleaned within the automated microfluidic system by a series of washes with water and acetone followed by potassium hydroxide to restore the silanol surface. The cleaned surface was then exposed to an ethanol solution containing 10 % (3-aminopropyl)triethoxysilane. After a second washing step, subsequent reaction with fluorescein isothiocyanate in dimethylsulphoxide was undertaken. The presence of the resultant fluorescent surface was confirmed by fluorescence microscopy and contact angle goniometry (Figure 9.12).

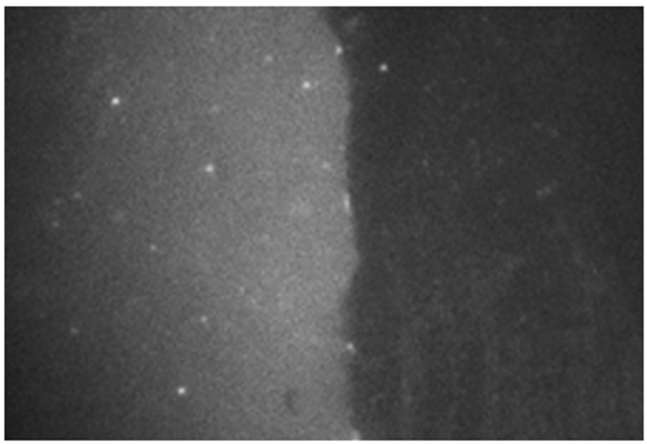

Fig. 9.12 Fluorescence microscopy image of a surface boundary between regions of fluoresein functionalised and unfunctionalised silica for the microfluidic Bragg grating sensor.

After cleaning the surface and after each subsequent functionalisation the shift in peak Bragg wavelength was compared in an ethanol reference solution. With temperature suitably normalised, any change observed should arise from displacement of ethanol at the surface with the higher index SAM substrate. It was observed that after functionalisation with 3-APS an average shift of 5 (±2) pm (Δn_{eff} = 4.7 x 10^{-6}) was observed, which increased to 56 (±4) pm (5.3 x 10^{-5}) with the subsequent attachment of fluorescein isothiocyanate.

9.5.2 Modelling of the interaction of the evanescent field with an organic self-assembled monolayer

The intensity distribution of the optical modes within the fluorescein-APS SAM sensor system were modelled using Fimmwave (Figure 9.13).

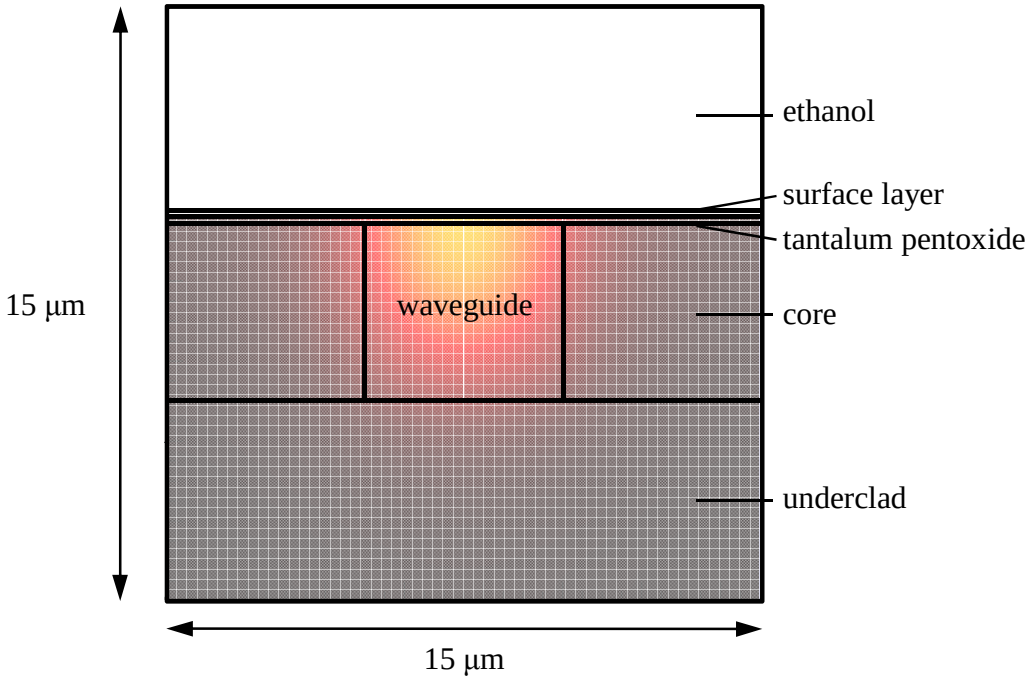

Fig. 9.13 The modelled cross-section of the waveguide for the TE mode, showing the high-index overlayer and organic layer on the waveguide surface, in ethanol.

The initial model was calibrated against bulk sensitivity measurements recorded for both the bare silica surface and after deposition of 50 nm of tantalum pentoxide, as shown in Figure 9.14. This allowed for factors such as the etch depth, the index step of the waveguide core and the tantalum thickness to be corroborated. This tantalum-coated system was then used to model the effect of depositing a film of index 1.44 (comparable to that of 3-APS SAM, Figure 9.15) and a film of index 1.74

(comparable to that of the fluorescein-APS SAM, Figure 9.16) with an effectively infinite layer of ethanol (1.35) above it.

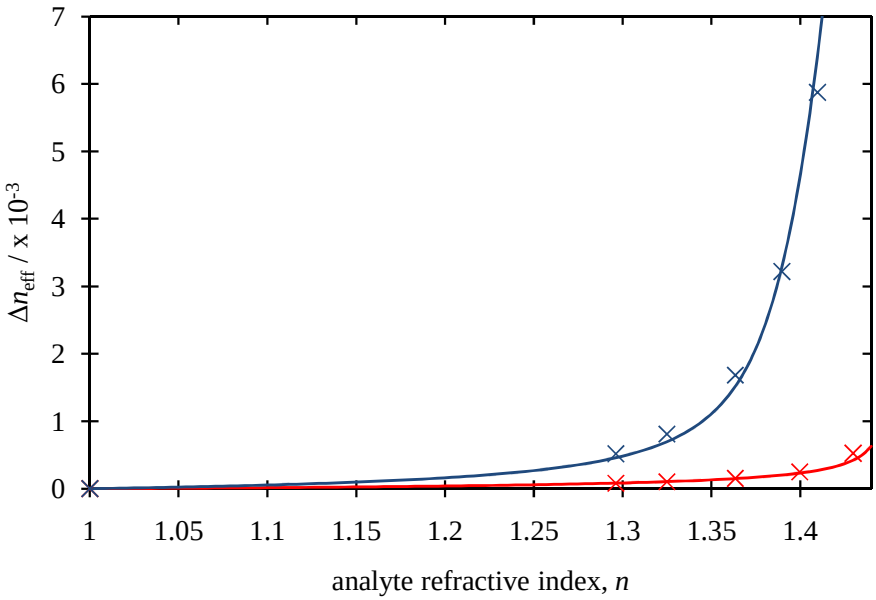

Fig. 9.14 A comparison of the modelled (line) and experimental (cross) effective index of the TE mode of the waveguide for increasing analyte index for both bare (red) and tantalum pentoxide (blue) coated sensors.

Figure 9.15 shows the effective index change of the waveguide as a function of the (3-aminopropyl)silane film thickness. The initial gradient predicts that for a thin film of index 1.44, a shift in peak Bragg wavelength of 10 pm for each nanometre deposited would be observed. A monolayer of 3-APS is approximately 0.7 nm thick [276] and therefore should yield a shift of 7 pm. The model assumes an amorphous region and not a discrete molecular film with a limit to packing density. The predicted shift is consistent with the experimental value of 5 (±2) pm allowing for the assumptions made.

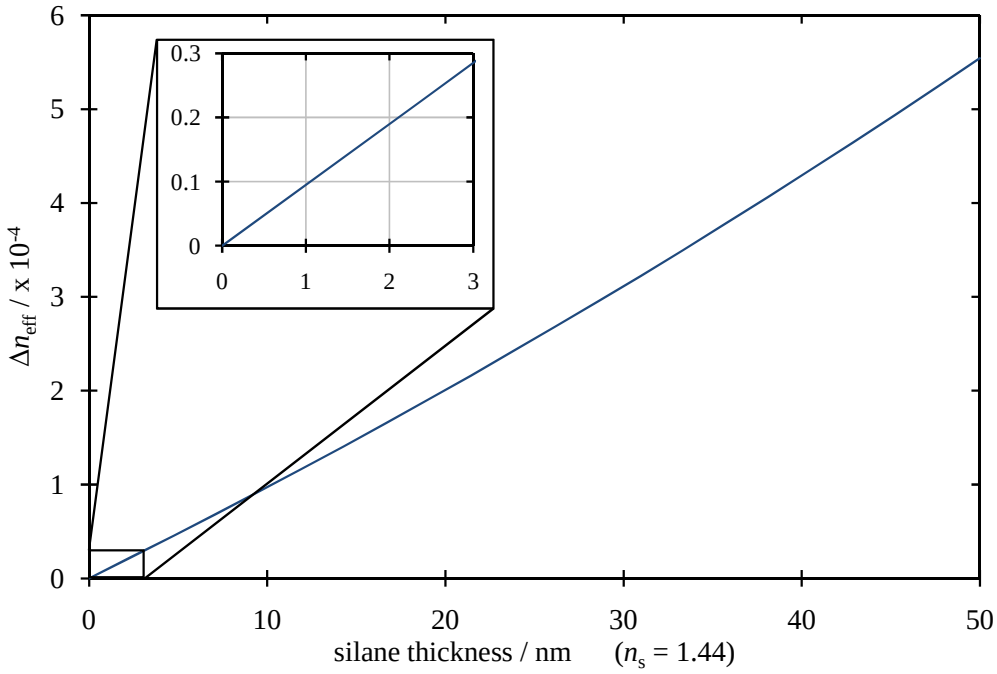

Fig. 9.15 The modelled change in effective index on increasing the thickness of a film of index 1.44, comparable to 3-APS.

Figure 9.16 shows the effective index change of the waveguide as a function of the fluorescein film thickness. It shows an order of magnitude increase in sensitivity compared to 3-APS as a result of the higher refractive index of fluorescein. The initial gradient predicts that for a thin film of index 1.74, a shift in peak Bragg wavelength of 51 pm per nm deposited will be observed. A monolayer of flourescein-APS is approximately 1.2 nm thick [276] and therefore should result in a shift of 60 pm. This is again consistent with the experimental value of 56 (±4) pm, allowing for the assumptions made in the model.

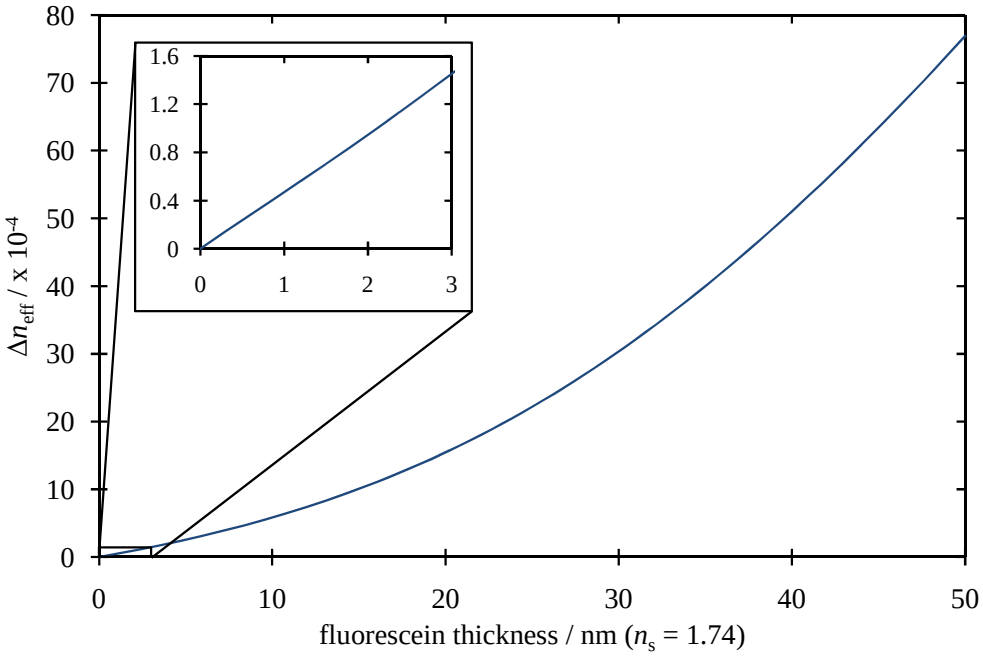

Fig. 9.16 The modelled change in effective index on increasing the thickness of a film of index 1.74, comparable to fluorescein-APS.

Overall both of these shifts are consistent with the modelled planar sensor system and are the best analytical evidence for the presence of a deposited organic monolayer on the surface.

9.5.3 Comparison with (3-aminopropyl)dimethylethoxysilane

To prove that the fluorescein layer is a discrete monolayer and not oligomeric, the deposition of the analogous (3-aminopropyl)dimethylethoxysilane (3-APDMS) was undertaken. As 3-APDMS contains only a single *ethoxy*- ligand, it is restricted to binding to the surface, preventing the potential cross-linking or polymerisation present with 3-APS. This limitation ensures only a single monolayer can form on the surface [279]. However the single bond to the surface results in the 3-APDMS layer much more labile than the 3-APS analogue [271], with a higher susceptibility to base, making it less robust for use in sensor applications. As demonstrated by Dagenais [279], the refractive index of 3-APS and 3-APDMS are comparable. It would be expected that, if 3-APS formed a single, discrete monolayer, the magnitude of the Bragg wavelength shift would be comparable with that of 3-APDMS.

A standard device comprising of a buried reference grating and four tantalum pentoxide coated sensor gratings, within the etched well, was functionalised with 3-APS by the standard method discussed previously (discussed further in Chapter 12).

This device consisted of a thicker tantalum pentoxide overlayer than the one previously compared to the modelled system (Section 9.5.2) and was thus expected to show a larger response to surface functionalisation. The surface was cleaned with a combination of conc. H_2SO_4/H_2O_2 followed by KOH and then functionalised analogously with 3-APDMS. Deposition of 3-APS onto this sensor was found to give an average shift in Bragg wavelength of 13.98 ± 0.81 pm for the four sensor gratings, while 3-APDMS was found to shift the average Bragg response by 11.06 ± 2.6 pm. Allowing for subtle differences in refractive index, the surface topography and the uncertainty of the Bragg sensitivity of the four sensor gratings, these shifts are comparable. This combined with the modelling and the fluorescence microscopy using FITC indicates that the assumption that this method produces a molecular monolayer is reasonable.

9.6 Summary

A method for functionalising the silica surface of a Bragg grating has been described using a self-assembling monolayer of an organosilane. This chemistry has been shown to be applicable to the tantalum pentoxide surfaces present within the higher sensitivity Bragg grating sensors discussed within this work. Through use of an organosilane linker, such as 3-APS, a diverse range of surface functionalities can be introduced to dictate the physical properties and chemical interactions at the surface.

Through gold adhesion tests, these films have been shown to be robust to both chemical attack and physical abrasion, an observation further confirmed by the fluorescein-silane surfaces.

While many conventional characterisation techniques did not have the resolution needed to characterise these surfaces, successful characterisation by contact angle goniometry and fluorescence microscopy allowed subtle changes in surface chemistry to be detected. However, these techniques could not confirm that the surface was only a single monolayer and not oligomeric. Furthermore, the ability to monitor and detect such films forming *in situ* within the microfluidic Bragg sensor cell bypasses the need to independently characterise every surface produced once the initial chemistry has been proved.

A fluorescein-silane surface has been formed within this microfluidic cell, using the two step approach. Both the attachment of 3-APS and fluorescein yielded well-resolved Bragg wavelength shifts, consistent with the modelled response. Comparison with the analogous 3-APDMS experiments showed that the magnitudes of these shifts were indeed comparable, further confirming that by functionalising in anhydrous conditions, only a molecular monolayer is formed upon the surface.

The following chapter will discuss how such surfaces can be used to introduce chemical specificity into the Bragg sensor system, with two distinct examples being explored.

10. Optofluidic Chemical Sensors

10.1 Introduction

It has been shown in the previous chapters that a planar Bragg grating sensor can be developed into an optofluidic sensor capable of detecting subtle changes in the refractive index of a fluid. The surface of such a sensor can be functionalised *in situ*, with the presence of the resultant surface monolayer being confirmed by the Bragg sensor itself. Through careful selection of the nature of the surface layer, the chemical interactions at the surface can be controlled, allowing chemical selectivity to be introduced to the optofluidic sensor.

There has been much work in supramolecular chemistry investigating the nature of intermolecular associations and much progress has been made on designing specific receptors that can preferentially bind to a particular analyte in the presence of others. Bringing together the high sensitivity of optical sensors with the selectivity of supramolecular chemistry will introduce chemical specificity to a sensor otherwise incapable of distinguishing between different analytes with the same refractive index response.

While the scope of supramolecular receptors presented within the literature is near limitless with many examples available for selective binding of anions [280, 281], cations [281, 282] and small molecules [281, 282] in a broad range of solvent systems, it was chosen here to present simple examples where the receptor properties were well known and beyond question. This allows for the success of the sensor system to be restricted to that of the optofluidic sensor and not to be dependent upon the receptor system. If these simple systems are proven to be successful, it is not unreasonable to presume that many of these other receptor systems would also be applicable.

This chapter will focus on how such surfaces can be used to introduce chemical specificity into the Bragg sensor system and will explore two distinct examples for detecting cations. The first investigates the use of a simple amine surface to coordinate copper (II) cations from aqueous solution, while the second develops this surface to include a crown ether motif – a size-selective cation receptor that demonstrates selectivity towards sodium cations in methanol.

10.2 An Optofluidic Sensor for Copper (II) Nitrate

10.2.1 Copper in the environment [283-285]

The detection and measurement of heavy metal ions present in aquatic streams is of great importance in assessing environmental damage and possible strategies for remediation. Copper can be released into the environment by both natural sources (wind-blown dust, decaying vegetation, forest fires and sea spray) and human sources (mining, metal production, wood production and phosphate fertilisers) leading to widespread environmental exposure.

Most copper compounds will settle and be bound to either water sediment or soil particles. When copper ends up in soil it strongly attaches to organic matter and minerals. As a result it does not travel far after release and it hardly ever enters groundwater. In surface water, copper can travel great distances, either suspended on sludge particles or as free ions. Water soluble copper compounds occur in the environment after release through application in agriculture and it is these compounds that form the largest threat to human health.

Immediate effects from drinking water which contains elevated levels of copper include: vomiting, diarrhoea, stomach cramps and nausea. However the seriousness of these effects will increase with increased copper levels or length of exposure. Children under one year of age are more sensitive to copper than adults, with long-term exposure to over 1 mg/L of copper in drinking water found to cause kidney and liver damage. People with liver damage or Wilson's disease are also highly susceptible to copper toxicity.

10.2.2 Selective copper (II) coordination

(3-Aminopropyl)triethoxysilane (3-APS) functionalised surfaces have been shown to extract copper from solution[286]. This has been used for a range of applications; from

copper selective electrochemical sensors [287] through to the removal of copper from aqueous solutions [288].

As reported by Kang *et al* [289], an aminated surface can be used to selectively bind copper (II) cations in aqueous media. This surface can then be recycled through subsequent washings with an acid to un-coordinate the copper ions, followed by a base wash to prime the surface for the next binding event. While the previously reported work used 2-aminoethanethiol to functionalise a gold surface for Surface Plasmon Resonance spectroscopy [289], the silane analogue using 3-APS should work equally well, as illustrated in Figure 10.1.

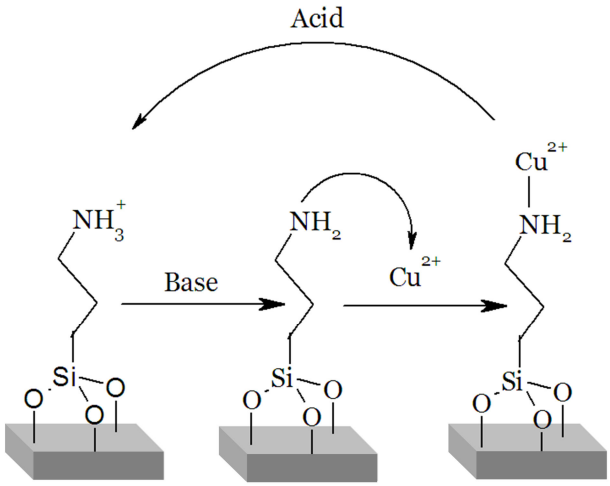

Fig. 10.1 The binding of copper (II) cations to an amine functionalised surface can be controlled through pH.

Surface Plasmon Resonance studies by Kang [289] of the resultant change upon copper binding demonstrated sensitivity down to 0.1 μM, below the 1.3 ppm (0.02 mM) threshold permitted by the US Environmental Protection Agency (EPA). As SPR is the main competing sensor technique to the integrated optical Bragg grating sensors presented here, it is important to compare the sensitivities and dynamic ranges of the two systems.

10.2.3 An optofluidic sensor with selective binding of copper

As discussed previously, the deposition of a fluorescein SAM was found to be detectable by a Bragg grating sensor. Furthermore the Bragg shift was found to be reproducible and consistent with the modelled system. This sensitivity was believed to be sufficient to observe monolayer binding to the waveguide surface, allowing for the development of highly sensitive chemical specific sensors.

A standard sensor device comprising of a buried reference grating and four sensor gratings was fabricated by UV writing. The sensor region was etched, polished and sputtered with 72.5 nm of tantalum pentoxide, before encapsulating it within the microfluidic flow cell. The high sensitivity of this sensor (as a result of the thickness of the high-index overlayer) reduced the dynamic refractive index range to 1.00 – 1.35; this was sufficient for the study of aqueous copper solutions, but was too low for ethanol solutions. As such it was necessary to switch to the lower index methanol as a solvent to allow real time monitoring of the functionalisation of the surface with 3-APS (Figure 10.2).

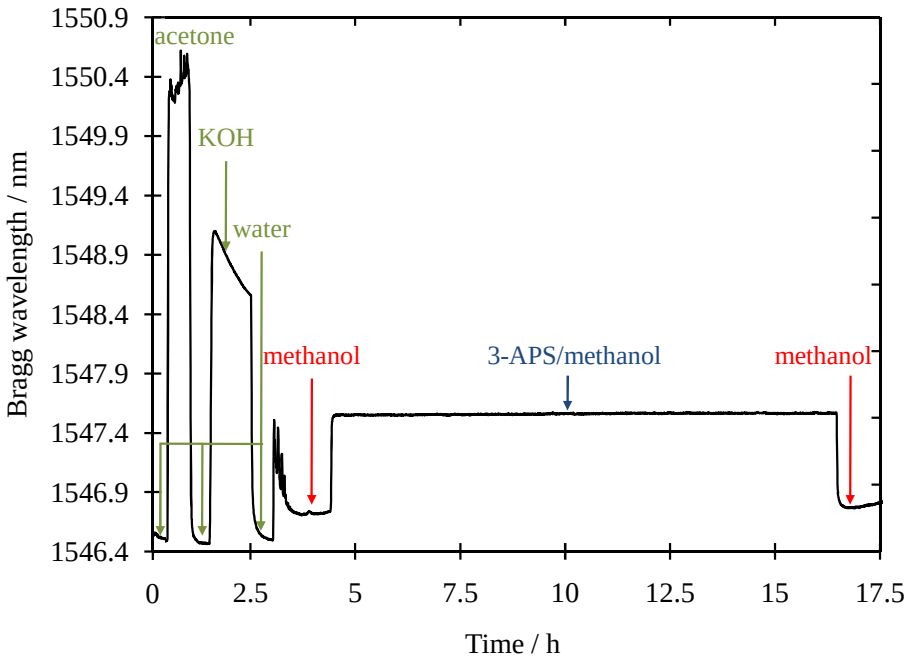

Fig. 10.2 The Bragg wavelength response to a series of sequential washing and functionalisation steps: water, acetone, water, aqueous potassium hydroxide, water, methanol, 10 % 3-APS in methanol, methanol.

It was observed that the Bragg response to methanol after surface functionalisation was shifted to higher wavelength by 54 pm and this corresponds to a monolayer of 3-APS on the surface of the sensor. This is also comparable to the 38 pm increase in Bragg wavelength over the period of the 3-APS/methanol wash. The high refractive index of acetone was at the upper limit of the dynamic range of the sensor, leading to the increased noise observed for the weak Bragg reflection. It is interesting to note the presence of a methanol-water "spike" for the first methanol wash, a spectral artefact that would have caused confusion without the preliminary microfluidic studies discussed in Chapter 8.

To investigate the potential applications of the functionalised surface as a copper sensor, a series of copper (II) nitrate solutions from 0.1 μM to 1.0 mM were prepared in a pH 5.5 buffered aqueous solution of 2-(*N*-morpholino)ethanesulphonic acid (MES) /sodium hydroxide, by serial dilution. The slightly acidic pH was deemed necessary to prevent any precipitation of copper nitrate that can occur in basic conditions [289]. MES was selected as a buffer because of its suitable buffering range and its inability to chelate copper (II) [290], an issue found with acetate, citrate and phosphate buffered systems.

On washing the protonated amine surface with a basic sodium hydroxide solution, Kang [289] observed a change in the SPR angle, attributed to the deprotonation of the ammonium salt back to the neutral amine. A similar result was observed for the amine-functionalised waveguide surface; the surface was first washed with citric acid (1.0M) for 10 minutes, followed by the pH 5.5 buffered aqueous MES/NaOH solution. Upon subsequent washing with a weak sodium hydroxide solution (pH 11) the Bragg wavelength upon returning to the buffered MES solution had reduced by 10.1 ± 3.7 pm on average (Figure 10.3). Compared to the previous work on the FITC surface and the shift seen upon forming the SAM, the magnitude of this shift is not unreasonable for the dissociation of citric acid bound to the amine surface

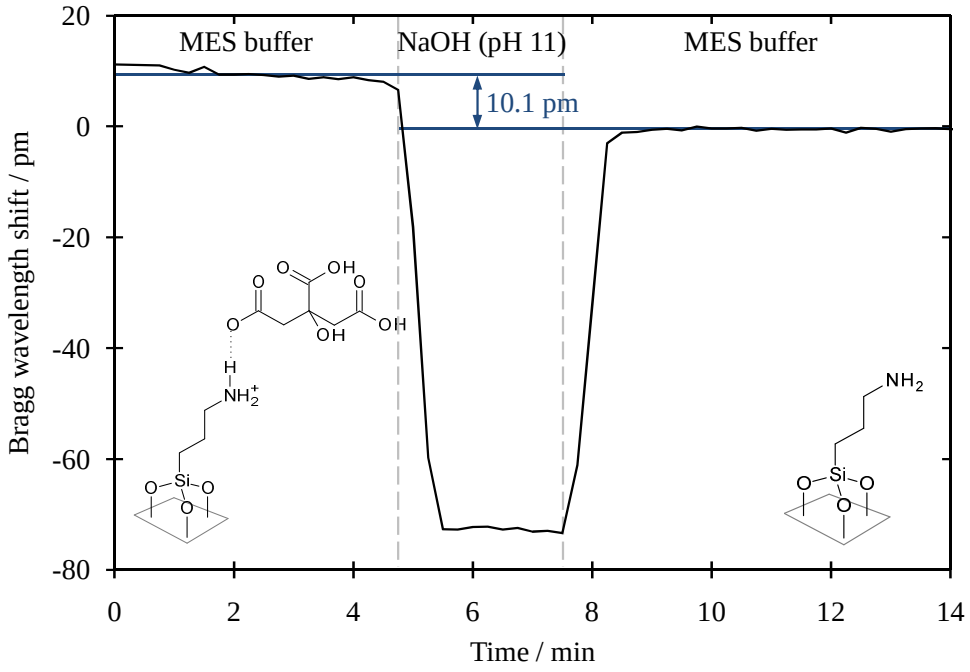

Fig. 10.3 The change in peak Bragg wavelength upon deprotonating the amine surface (average of 8 datasets).

The microfluidic, tantalum pentoxide-enhanced Bragg sensor was prepared by a series of washes consisting of citric acid to clean the surface of previous coordinated cations and a basic wash to restore the neutral amine, with intermediate washes with the MES-buffer to remove residual acid and base. This was followed by exposure to the various buffered copper nitrate solutions, repeating the acid/base washing steps between each solution. Figure 10.4 illustrates the change in Bragg wavelength upon transitioning from the aqueous MES buffer to a copper nitrate containing buffer solution. In all cases the Bragg sensor response is constant prior to the addition of copper to the surface. Upon switching to the copper containing solution, a sharp initial increase is observed followed by a subsequent gradual increase, with the magnitude of this initial increase increasing with copper concentration.

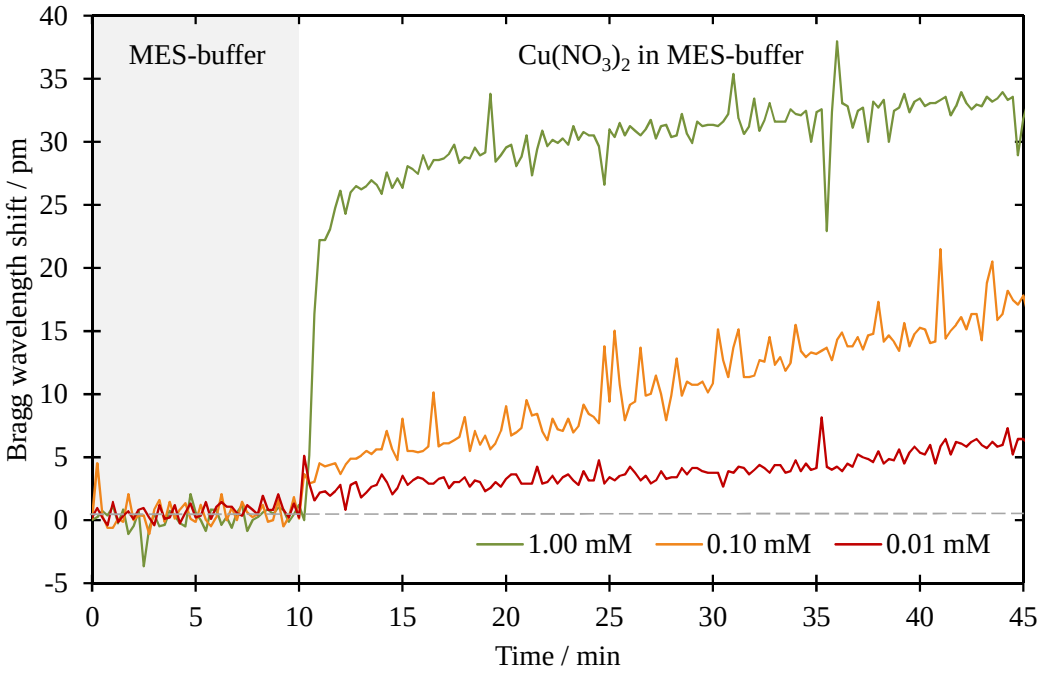

Fig. 10.4 The Bragg response upon switching from a pH 5.5 MES buffer to a MES buffered copper nitrate solution (0.01 – 1.00 mM), demonstrating the binding at the amine surface.

The Bragg sensor demonstrated a gradual increase upon exposure to the copper solution, levelling off over six hours. The raw data (uncorrected for temperature fluctuations) is shown in Figure 10.5, below:

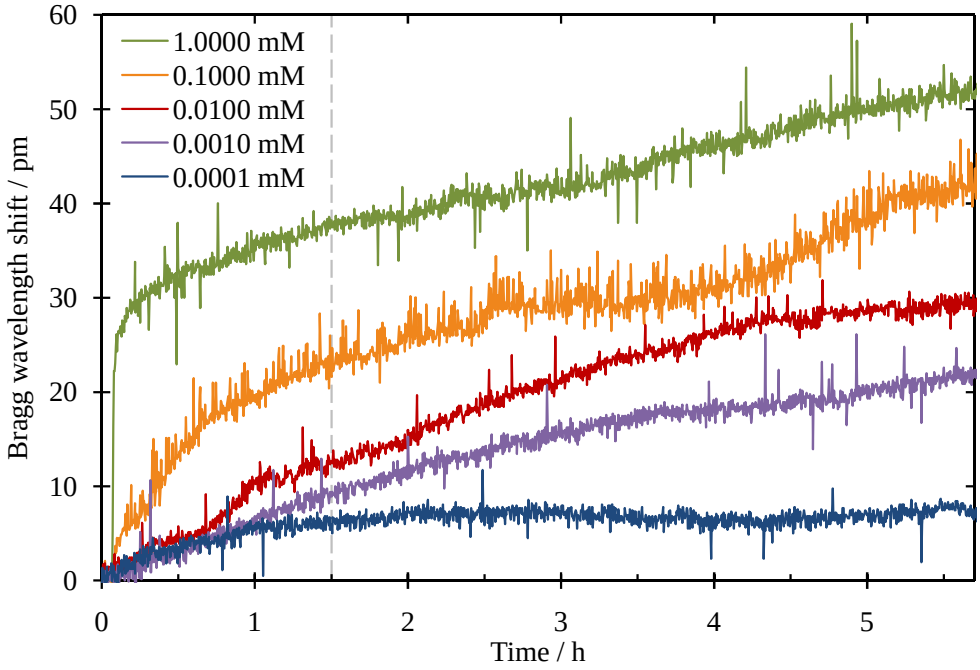

Fig. 10.5 The uncorrected Bragg response upon binding copper nitrate solutions (1mM to 0.1 µM) to the amine surface.

As seen in Figure 10.5, the Bragg grating is sensitive to the concentration of the copper nitrate, suggesting that an equilibrium forms with the surface, rather than just the rate at which a complete surface-bound layer is formed. This is again consistent with the observations of Kang [289]. While the Bragg wavelength shifts show that it takes up to six hours for equilibrium to form between the flowing copper nitrate solution and the Bragg surface, this is still significantly shorter that the 18-24 hour equilibrium time required in the unperturbed system used by Kang. While this sampling rate is not practical, it still is a marked improvement and demonstrates the advantage of the microfluidic flow cell over sampling techniques. Furthermore, after 1.5 hours a clear separation of the different concentrations has been achieved (as indicated on Figure 10.5), demonstrating the potential to increase the sampling rate of the sensor.

The exposure to each concentration was repeated three times sequentially, allowing for the reproducibility of the sensor to be assessed. The error bars indicated in the following figures represent the standard deviation from the average shift observed over these three repeat measurements, calculated individually for each concentration. It was found the range of values varied more greatly than would be expected simply from the uncertainty in the Bragg measurement (such as that demonstrated by the silica deposition experiment in Chapter 5) with a standard deviation of ~3 pm

common. This order of magnitude increase in noise is mostly due to the increased difficulties in temperature referencing this highly sensitive device over long time-scales within a dynamic fluid environment; however deviations in the chemical composition of the analyte solutions and physical phenomena such as bubbles and pressure changes are likely to have had an effect. These effects are likely to be similar in all the following sensor work, justified by the comparable standard deviation values recorded across both sensor systems.

The surface was cleaned with "piranha" to remove the amine SAM and the exposure to the buffered copper nitrate solutions was repeated. Exposing the unfunctionalised surface to the same copper solutions gave a more instantaneous square-like response, without the slow increase seen in Figure 10.5 – consistent with a reduction in a slow binding mechanism at the surface. As shown in Figure 10.6, the sensitivity to copper is much reduced, with concentrations below 10 μM undetectable. This shows that the sensor is highly sensitive to bulk measurements of low concentrations, but also that the sensitivity is enhanced by the presence of the amine surface.

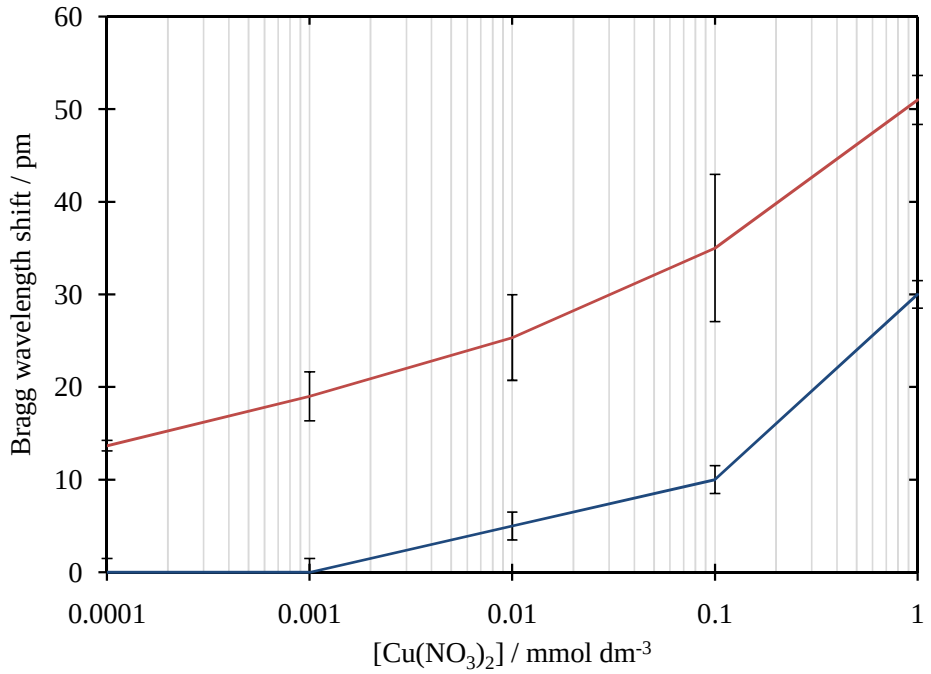

Fig. 10.6 The wavelength response to a series of copper nitrate solutions from 0.1 to 1000 μM for an amine functionalised Bragg grating sensor (red), compared to the unfunctionalised surface (blue). Error bars represent the standard deviation of a series of measurements.

Plotting the data for the amine functionalised surface as a log-log plot (Figure 10.7) generates a straight graph, again following the same trend as reported by Kang [289]. This suggests that the surface is working successfully as a copper sensor at very low

concentrations. The equivalent SPR plot demonstrates successful detection of copper in the range 1.0 mM to 0.1 µM and this is similarly demonstrated by the sensor presented here. For both the SPR and Bragg grating systems, the lowest detected concentration is well resolved above the baseline, implying that more dilute concentrations may be detectable.

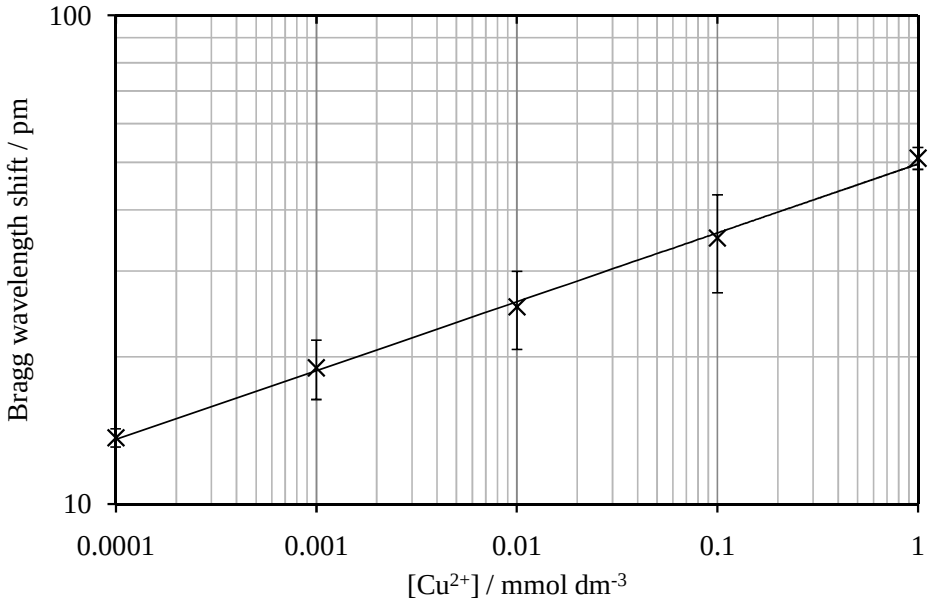

Fig. 10.7 The Bragg wavelength shift as a function of the copper nitrate concentration, plotted on logarithmic axes. Error bars represent the standard deviation of a series of measurements.

Further work was undertaken to show that this result is not dependent on the presence of the MES buffer. The surface was cleaned in piranha, refunctionalised and the microfluidic study was repeated with the MES buffered solution replaced by a weak nitric acid solution, made up to pH 5.5. As shown in Figure 10.8, the functionalised surface was found to still be sensitive to the presence of copper ions resulting in a Bragg wavelength shift that was not observed with an unfunctionalised surface. The shift upon binding is smaller than that previously observed in the presence of the MES buffer. This is likely to arise from the presence of MES raising the background refractive index of the aqueous solutions, thereby increasing the sensitivity of the Bragg grating and will thus lead to a larger wavelength shift for the same change in effective index.

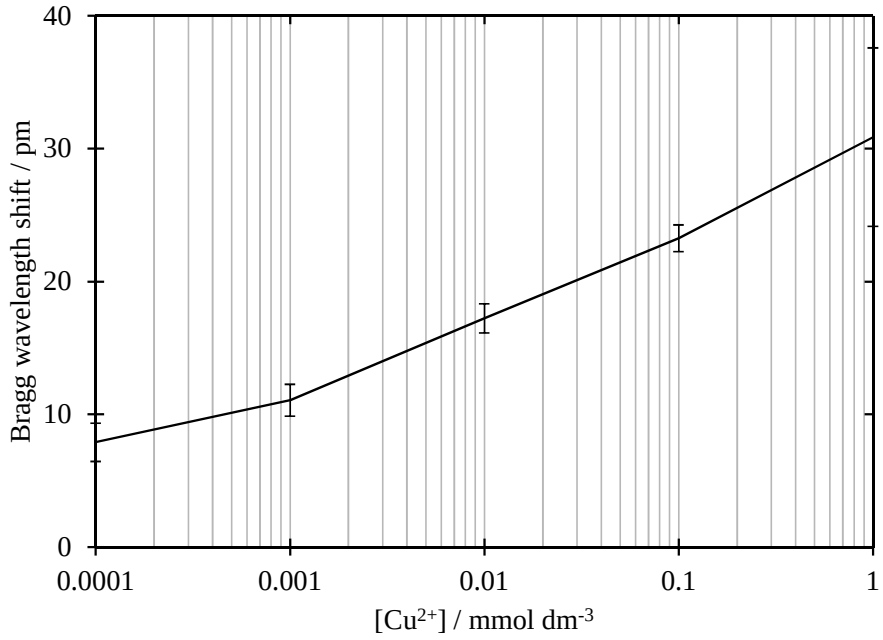

Fig. 10.8 The peak Bragg wavelength shift as a function of the concentration of copper nitrate flowed over the surface. Error bars represent the standard deviation of a series of measurements.

As discussed previously, in addition to enhancements in sensitivity, surface functionalisation should reduce possible interference from other metal ions in realistic samples. The sensitivity of copper was compared with that of nickel and zinc, reported as common competing metals for such sensor systems by Kang [289]. Nickel and zinc are both divalent cations with similar ionic radii to Cu^{2+}. Specifically, Ni^{2+} has a similar hydrodynamic radius, ionic mobility, and limiting ionic conductivity. It is known to interfere with Cu^{2+} detection as both ions form square planar *4N* complexes with a ‘‘nitrogen’’ containing functional group [291].

While there was little enhancement to the zinc and nickel response upon functionalisation, as shown in Figure 10.9, the copper response is amplified by six times – demonstrating that the functionalised Bragg grating is acting as a chemically specific sensor. Such increased sensitivity is attributed to increased binding at the surface; this is believed to be due to the increased bond strength of the copper complex over the nickel and zinc analogues [292].

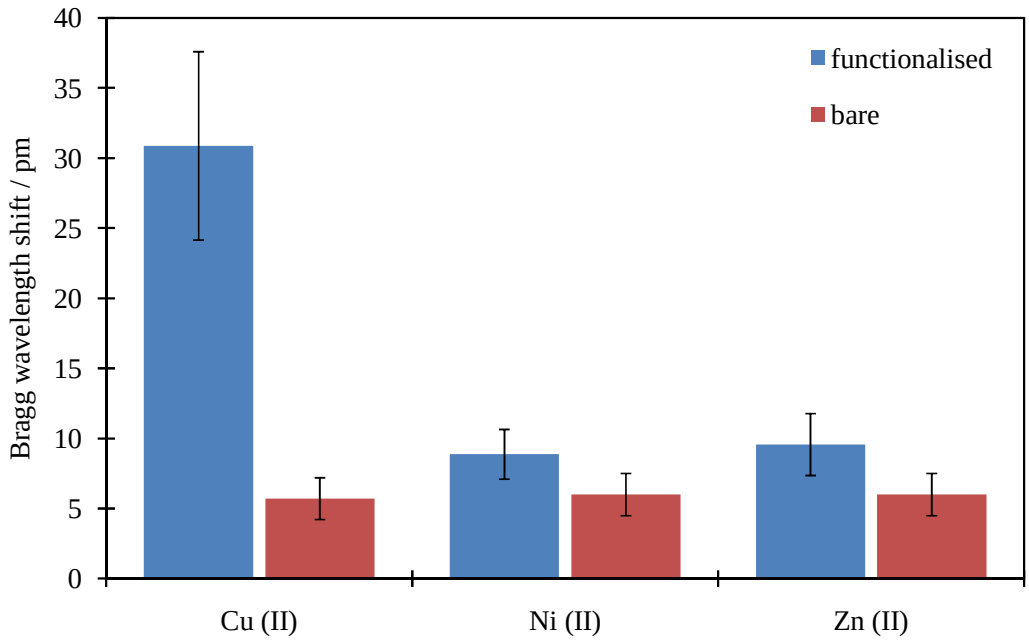

Fig. 10.9 A comparison of the Bragg response to 1.0 mM $M(NO_3)_2$ for amine functionalised and bare surfaces, where M = Cu, Ni, Zn. Error bars represent the standard deviation of a series of measurements.

In summary, the aminated surface shows high sensitivity to dilute copper nitrate solutions with good selectivity over common competing metals; nickel and zinc. The chelation of copper to the surface requires the surface to be restored with an acid/base wash between measurements. The observations were all found to be consistent with the analogous SPR system with comparable levels of selectivity and specificity, with the additional advantages introduced by the microfluidic flow cell of faster sampling rates automation and a protected sensor environment, increasing the SAM lifetime.

10.3 An Optofluidic Chemical Sensor for Sodium Chloride

Supramolecular chemistry is an area of chemistry that focuses on non-covalent bonding interactions; specifically the weaker and reversible non-covalent interactions between molecules [293]. These forces include hydrogen bonding, metal coordination, hydrophobic forces, van der Waals forces, π-π interactions and electrostatic effects.

A major field within supramolecular chemistry, is that of "host-guest" complexes, in which a host molecule recognises and selectively binds a certain guest. One of the earliest examples of a synthetic host-guest complex was that of the crown ethers, discovered in the 1960s by Pedersen [294]. Crown ethers are macrocyclic molecules

that consist of a ring containing several ether groups, and as such represent one of the simplest host-guest systems in supramolecular chemistry. The size of the cavity within the crown ether ring strongly determines which cation will bind most favourably and this property has been used to demonstrate selective binding to a specific cation from a mixture. Benzo-15-crown-5, as illustrated below in Figure 10.10, has a fifteen-member polyether ring containing five oxygen atoms.

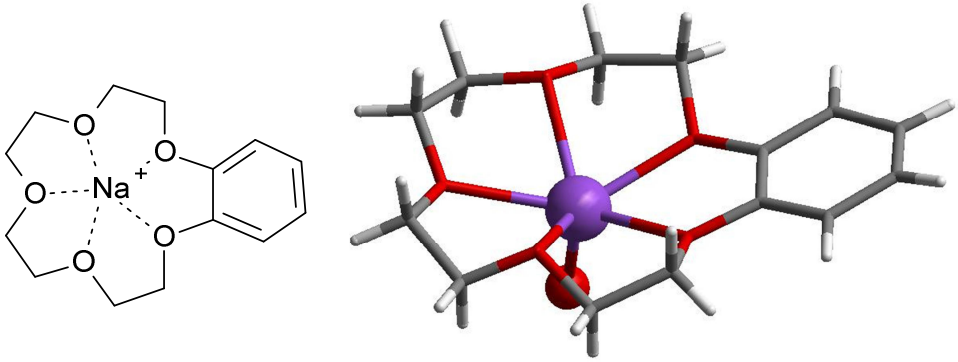

Fig. 10.10 The crystal structure for sodium bound within the benzo-15-crown-5 heterocycle (including coordinated water) [295].

As shown in Figure 10.11, benzo-15-crown-5 is known to preferentially bind to sodium over other Group I metals [296].

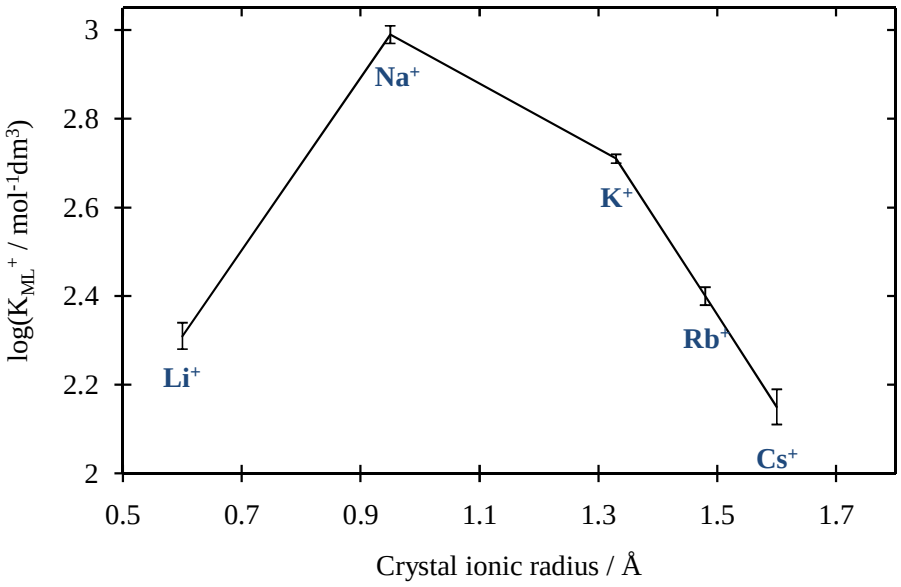

Fig. 10.11 The formation constant, K_{ML} for complexes of benzo-15-crown-5 with Group I alkali metals in methanol at 25 °C as a function of ionic radius (as reported by Takeda [296]), showing the selectivity for sodium.

For a host-guest system to form a good candidate for a sensor it must selectively bind the desired species from a series of similar species in a reasonable solvent.

However, for the sensor to be viable, this binding must be dynamic with a high turnover rate. If the host binds the guest too strongly or irreversibly the sensor will rapidly saturate. This concept has been shown in part by Nakajima [297], who demonstrated that crown ethers can be immobilised on a silica surface and the resulting complex has sufficient cation selectivity to be used in chromatography for separating mixed salts.

As discussed earlier, crown ethers will selectively bind cations of comparable radius within the pore. Tethering crown ether to the surface was seen as a good starting point to investigate whether specificity could be introduced to the bulk refractive index sensor, as it represents a simple and well-known interaction. 4'-(Chlorocarbonyl)benzo-15-crown-5 (**14**) was synthesised following literature procedures [298-301] from benzo-15-crown-5 in three steps, each in good yield (Figure 10.12, synthetic methods are detailed in Chapter 12):

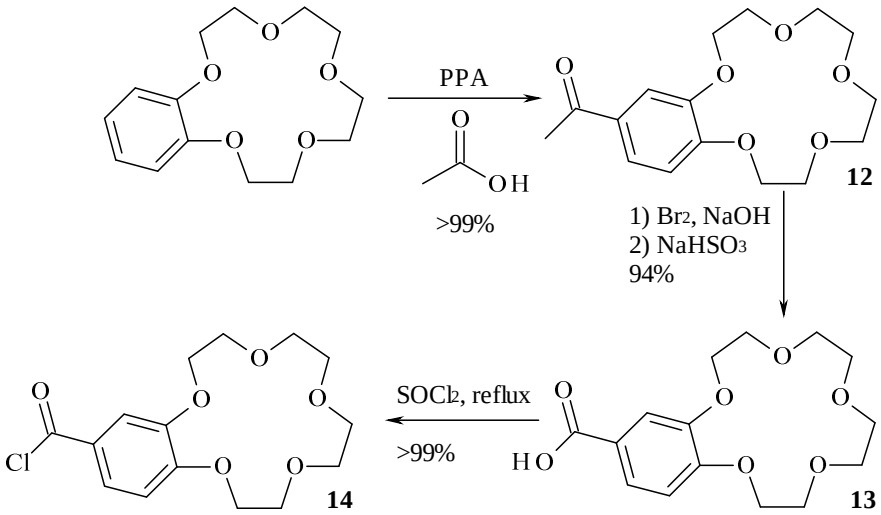

Fig. 10.12 The synthetic pathway towards 4'-(chlorocarbonyl)benzo-15-crown-5 (3).

To maximise the detectable wavelength response, the same highly sensitive sensor was used as in the copper work above. The crown ether was attached to the surface via a peptide bond to the amino head group of the pre-alkylated sensor surface (Figure 10.13). It was observed that the Bragg response to methanol after functionalisation with the crown was shifted to higher wavelength by 455 pm. This is comparable to the 464 pm increase in Bragg wavelength during flow of the crown ether solution over the surface. While this shift is much larger than that measured

for the fluorescein work presented previously, it is again the result of the higher sensitivity that this thicker tantalum pentoxide layer affords.

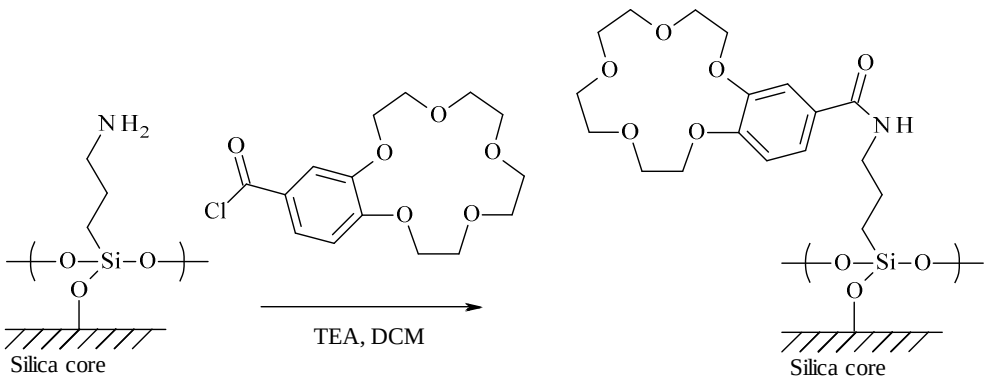

Fig. 10.13 The surface functionalisation of the Bragg sensor with 4'-(chlorocarbonyl)benzo-15-crown-5 within the microfluidic flow cell .

The crown ether-functionalised surface was exposed to a series of Group I metal halides, varying concentration from 10 mM down to 1 μM in HPLC methanol, as shown in Figure 10.14. Unlike the co-ordination of copper discussed above, the cations are more weakly bound to the crown ether surface resulting in an equilibrium forming with the solvent. The surface can thus be restored for the next measurement by simply flowing pure methanol over it. It was found that it took up to an hour for the surface to fully equilibrate with no further changes in Bragg wavelength (depending on the strength of the salt solution), with the reverse cleaning step taking a comparable time to restore the surface. These preliminary results showed that the sensor was selective to sodium, as expected for benzo-15-crown-5 (Figure 10.11), with the shift due to binding sodium twice that seen for other Group I cations.

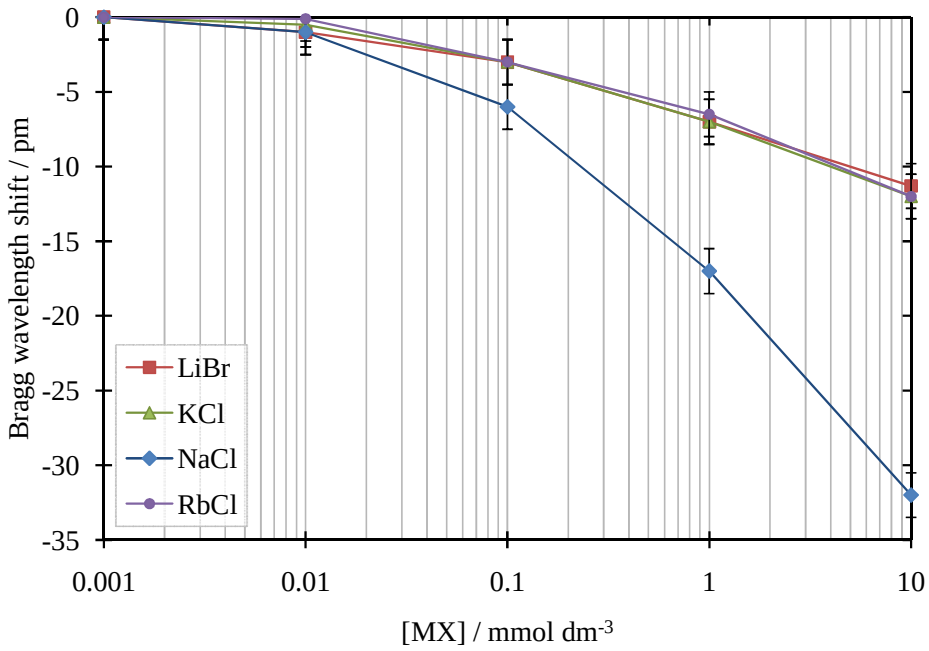

Fig. 10.14 The Bragg response of the benzo-15-crown-5 functionalised sensor to varying concentration of lithium, sodium, potassium and rubidium cations in methanol. Error bars represent the standard deviation of a series of measurements.

In contrast to the copper system, the shift upon binding was observed to result in a decrease in Bragg wavelength, and therefore refractive index. This is contrary to the effect observed in bulk sensing of salt solutions, where a positive shift is measured for increasing salt concentration. Looking at the raw data for the 10 mM solutions for both the bare and functionalised systems (Figure 10.15), it was observed that there are two components, a fast initial positive shift, that is equal in magnitude for both surfaces, which is then followed by a slow decrease in Bragg wavelength for the functionalised surface. For more dilute solutions the bulk is below the sensor threshold, and only the slow decrease is observed, whilst for higher concentrations the sharp bulk transition becomes dominant.

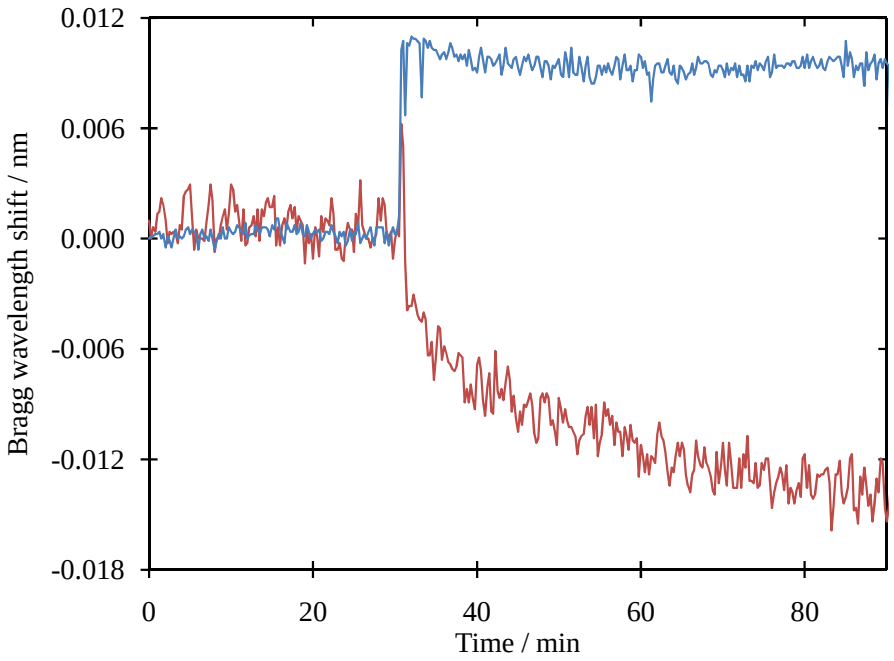

Fig. 10.15 Comparison of the Bragg response upon switching to a 1 mM sodium chloride solution for the bare (blue) and crown ether functionalised (red) sensor surfaces.

A reduction in refractive index could be the result of a variety of causes. Any rearrangements at the surface arising from binding with the crown can cause changes to the shape and packing of the SAM. This can reduce the density at the surface and thus may further influence the arrangement of solvent molecules near the surface – amplifying this effect. Alternatively it may be the result of electronic changes in the SAM upon binding the sodium to the crown ether, changing the polarisability of the nearby phenyl ring.

Weak binding is clearly occurring with lithium, potassium and rubidium. This is to be expected, with the size mismatch between these cations and the macrocycle not too great to prevent a weak association between lithium or potassium and the flexible crown ether [302] (as indicated by Figure 10.11). While potassium can form a sandwich complex [303] with benzo-15-crown-5 that rivals the binding of sodium [302], the lack of enhancement of potassium over lithium implies that the geometry of the surface is too confined for this to be occurring. This could be overcome through use of a more complex receptor, which can be tailored more to the size and shape of the analyte. In this case, use of a calix[4]arene [304, 305] may improve the selectivity of the surface towards sodium.

Further measurements of mixed solutions were intended to quantify the degree of selectivity and specificity displayed by the sensor. However a contamination of the crown ether surface occurred, identified by a permanent Bragg wavelength shift to higher wavelength with a corresponding reduction in amplitude. This required the surface to be refunctionalised.

Due to traces of hydrochloric acid from the synthesis of **14**, protonating the amine surface and inhibiting reaction, this refunctionalised surface had a lower density of crown ether receptors upon the surface than the previous example (as determined by the smaller Bragg shift upon functionalisation). This resulted in a reduced Bragg wavelength shift upon binding cations, compared to that seen in Figures 10.14 and 10.15.

Despite this reduction in sensitivity, an investigation into mixed analyte systems was briefly explored, with a mixed 50:50 solution of sodium chloride and potassium chloride flowed over the sensor surface. This was compared to the Bragg wavelength shift of separate solutions of 10 mM sodium chloride and 10 mM potassium chloride, as shown in Figure 10.16. It was observed that the resultant Bragg shift for the mixed solution (10 mM sodium chloride and 10 mM potassium chloride) was greater than that of the unmixed 10 mM sodium chloride solution. As a concentration of 10 mM is not sufficiently concentrated to saturate the crown ether surface, and weak binding to potassium has been shown to occur, it is likely that both sodium and potassium are simultaneously binding to the surface, with the resultant Bragg wavelength shift representing this cumulated effect. Indeed the combined shift for the individual sodium and potassium solutions is consistent, within error, with the mixed solution.

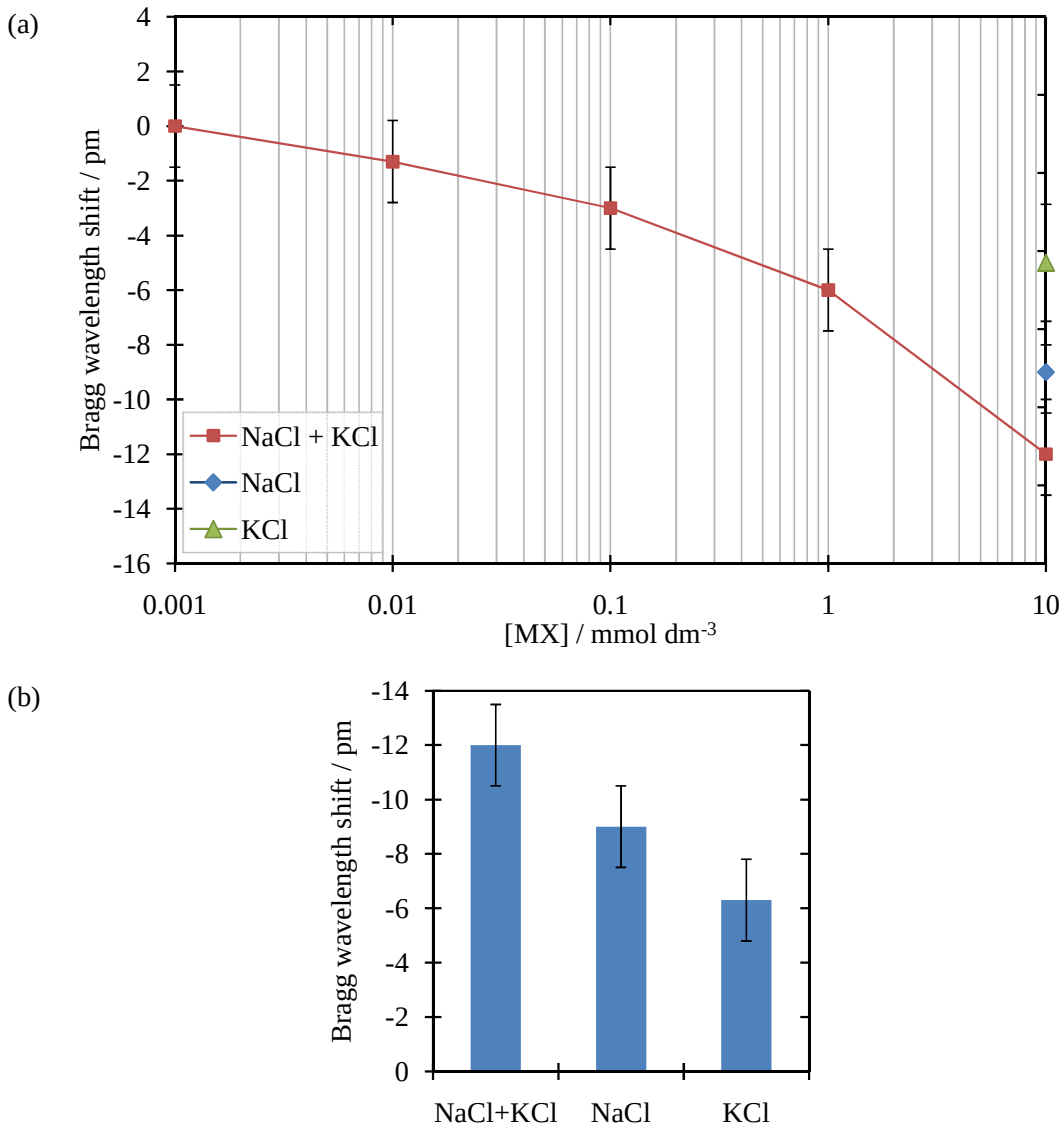

Fig. 10.16(a) The Bragg response of the benzo-15-crown-5 functionalised sensor to varying concentration of a mixed solution of sodium and potassium in methanol, compared to individual solutions sodium and potassium. Fig. 10.16(b) Comparison of 10mM NaCl and 10mM KCl to a mixed solution of 10mM NaCl and 10mM KCl (20mM combined concentration).

10.4 Summary

A simple copper-selective functionalised chemical sensor has been demonstrated. It has been shown to be sensitive down to concentrations of 0.1 µM, an improvement of two orders of magnitude over the unfunctionalised sensor. This has been shown to work in acidic solutions, without the presence of a buffer and demonstrates selective binding over the common contaminants, nickel and zinc. This system was found to be consistent with the analogous SPR system, with comparable levels of selectivity and specificity. The additional advantages introduced by the microfluidic

flow cell of faster sampling rates, increased automation and a protected sensor environment give this system an advantage over the one reported by Kang [289].

This has led to the development of a more sophisticated sensor that utilises the host-guest binding properties of benzo-15-crown-5 to selectively detect sodium cations over other Group I metal halides in methanol. This sensor was shown to be able to detect such ions down to 10 μM solutions of sodium chloride.

Both of these sensor systems demonstrate high sensitivity and a degree of chemical selectivity. The success of these simple proof-of-concept sensors proves that a modified surface can improve the practicality of the sensor over that of the simple microfluidic device. The wide range of receptors previously reported within the literature should allow these systems to be directed towards a wide range of different analytes with even greater sensitivity and through more sophisticated structures, greater selectivity should be achievable.

11. Conclusion

11.1 Conclusion

The technique of direct UV grating writing is based upon on the localised refractive index increase induced within a photosensitive planar glass layer through exposure to a tightly focussed UV beam. In this work, direct UV writing has been used to define optical waveguides and Bragg gratings simultaneously into a silica-on-silicon substrate. These Bragg gratings can be written with a Bragg wavelength from 1400 – 1700 nm by precise modulation of the inherent interference pattern produced by the overlap of two focussed coherent UV laser beams.

The reflectance spectrum of the gratings in the infrared region was analysed remotely by commercial telecoms test and measurement equipment via a fibre pigtail, allowing sub-picometre resolution of the peak Bragg wavelength.

Exposing the waveguide, through etching, allows these Bragg gratings to be used as highly sensitive refractometers. Fabrication of these etched sensors has been optimised by using a mixed hydrochloric and hydrofluoric acid etchant solution, followed by post-etch polishing to restore the quality of the surface.

The sensitivity of these refractometers can be dramatically improved through the inclusion of a high-index overlayer of tantalum pentoxide. It was shown that, within a vacuum system, the device can detect sub-nanometre thickness changes of an amorphous silica layer. While this is an idealised system, it demonstrates that detection of an organic monolayer on the sensor surface is within the capabilities of this sensor platform.

A family of azobenzene derivatives have been synthesised and their optical properties studied. From these findings a *p*-methoxy azobenzene-functionalised

methacrylate co-polymer was prepared that was shown to undergo reversible photoisomerisation when exposed to UV light, producing a corresponding change in refractive index. This co-polymer demonstrated high thermal stability to isomerisation, giving rise to applications in passively latched devices. When deposited upon an optical surface, a reconfigurable Bragg grating was formed that has the potential for a range of optical applications. This prototype device was tuneable by up to 489 pm, corresponding to 63 GHz at telecomm wavelengths. This type of reconfigurable device could find application in wavelength trimming of lasers or reconfigurable dispersion compensation.

A second system was investigated using a silicone co-polymer with a lower bulk refractive index. This was below that of the waveguide core, allowing for easier deposition by a spray-coating technique, removing the need for clean-room processing. While this technique reduces the cost and complexity of fabrication, further optimisation is needed to improve the optical response to that observed for the polymethacrylate system.

Further work on these systems should focus on the investigation of non-uniform exposure patterns to develop more sophisticated devices. For example, illumination with an intensity gradient would induce a gradient refractive index profile that would introduce a degree of “chirp” into the grating. Alternatively, use of a periodic mask would introduce additional spectral features.

Temperature referencing was shown to be necessary to achieve the sensitivity required for common sensing applications. While it has been shown that using a reference grating is sufficient, in simple systems or in specific examples, for precise compensation of temperature, a modal comparison is more accurate. By using the transverse magnetic mode of the Bragg grating to monitor and remove temperature fluctuations from the transverse electric mode, a temperature-insensitive Bragg grating sensor can be fabricated. It has been shown that for a real system this approach can successfully remove the thermal component from the Bragg response. Not only does this approach simplify the system, as no additional components are necessary, but it makes use of the previously redundant transverse magnetic mode. The high resolution of this method of temperature compensation combined with the

high sensitivity of a planar Bragg grating makes this system ideal for detection of the subtle changes in chemical and bio-sensing applications.

Furthermore, the use of the negative thermo-optic coefficient of a fluid has been shown to improve the temperature independence of an etched Bragg grating. This can be enhanced further through use of a solute to modify the refractive index of the solvent, allowing this response to be tuned to the desired operating temperature range. This has been demonstrated with an aqueous glucose solution, where over a 10 °C range the Bragg response was found to vary by only 3.7 pm. This is an improvement of nearly two orders of magnitude over the un-etched Bragg grating. The low cost and resistance to mechanical shock, vibration and strain makes these devices ideal for incorporation within integrated photonic networks as temperature-insensitive wavelength references.

A microfluidic flow cell was developed that allows the Bragg grating sensors to sample a continuous flow of fluid over the surface. The system is compatible with a wide range of chemicals and has been fully automated. Transitioning between isopropanol and water within this microfluidic flow cell gave an expected square wave-like response in refractive index, but with a small mixing transient. In contrast, mixing water with other alcohols, such as methanol or ethanol, produced a "spike" in the refractive index during the transition. This "spike" was shown to be caused by the formation of intermediate binary liquids with higher refractive index than the constituent solvents. The "spikes" were shown to have a long life-time, with stability to interruptions in flow suggesting a bulk concentration gradient along the system that formed independently of the pump rate of the system.

This unusual transitional flow property was harnessed to fabricate a proof-of-concept microfluidic flow sensor. This was developed to demonstrate a method of measuring the water content of an alcohol-water mixture, overcoming the issues of the parabolic refractive index profile of such systems.

With the development of the microfluidic system and an understanding of the properties of bulk fluids flowing through them, it was possible to functionalise the sensor surface with an organic monolayer *in situ*. An organosilane was used to form such a self-assembled monolayer on the silica surface of the Bragg grating and this chemistry was found to also be compatible with a tantalum pentoxide surface. Gold

adhesion tests and functionalisation with the organic dye fluorescein have shown that these monolayers were robust to both chemical attack and physical abrasion. While many conventional characterisation techniques did not have the resolution needed to characterise these surfaces, successful characterisation by contact angle goniometry and fluorescence microscopy allowed for subtle changes in surface chemistry to be detected.

Through use of (3-aminopropyl)triethoxysilane as a linker, a diverse range of surface functionalities can be introduced to dictate the physical properties and chemical interactions at the surface. The ability to monitor the formation of such films *in situ* within the microfluidic Bragg sensor cell was demonstrated, with both the attachment of 3-APS and fluorescein yielding well-resolved Bragg wavelength shifts, consistent with the modelled response.

The versatile amino head group of 3-APS allows for a wide range of chemistry to be introduced to the surface. A simple copper selective, 3-APS-functionalised chemical sensor was shown to be able to detect the concentration of a copper (II) solution to below 0.10 µM. This has been shown to work in acidic solutions, without the presence of a buffer and demonstrates selective binding over the common contaminants, nickel and zinc.

This simple surface led to the development of a more sophisticated sensor that utilises the host-guest binding properties of benzo-15-crown-5 to selectively detect the presence of sodium over other Group I metal halides in methanol. This sensor was shown to be sensitive down to 10 µM concentrations of sodium chloride in methanol.

The success of these simple proof-of-concept sensors demonstrates that a modified surface can improve the sensitivity and selectivity over that of the simple microfluidic device. The wide range of receptors previously reported within the literature should allow these systems to be directed towards a wide range of different analytes with even greater sensitivity and, through more sophisticated optical structures, greater selectivity should be achievable.

11.2 Further work

While the work presented here has demonstrated that a surface monolayer is sufficient to introduce chemical specificity to the sensitive Bragg grating refractometers developed in this work, a larger response is desirable for practical applications. To achieve this, either the density of binding sites within the sensing region or the magnitude of the refractive index response generated would need to be increased. There are several potential routes that could be used to achieve such a sensor enhancement and these are briefly discussed below.

11.2.1 Chromoionophores

The sensors presented within this work relied on directly detecting the change in refractive index upon binding an analyte. This effect could be further enhanced if the binding event stimulates a further change in the receptor compound. This could arise from a change in the packing at the surface (changing the bulk layer thickness or density) or a shift in the absorption peak of a chromophore.

A chromoionophore is compound that will selectively bind to a specific ion (ionophore) with an associated colour change (or shift in absorption). An example of such a receptor molecule was presented by Hayashita *et al* [306], where the binding of sodium by a supramolecular calix[4]crown macrocycle induces a tautomerism within an azobenzene dye (as illustrated in Figure 11.1, below).

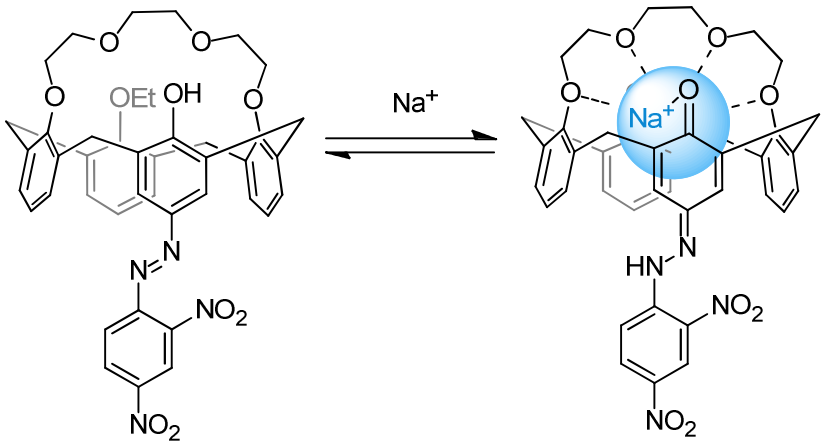

Fig. 11.1 Tautomerism from the phenylazophenol to the quinine phenylhydrazone form upon selective binding of sodium results in a detectable colour change [306].

Based upon the tautomerism of the chromophoric moiety from phenylazophenol to quinine phenylhydrazone, this calix[4]crown demonstrates a specific colourimetric response to sodium in acidic and homogeneous aqueous dioxane solution. This

bathochromic shift from 380 nm to 480 nm is not exhibited with lithium, potassium or tetramethylammonium chlorides. The selectivity for sodium over potassium is found to be 10^5, allowing for quantitative determination of the sodium concentration of a solution even in the presence of excess potassium ions. This, combined with small change in the extinction coefficient over the physiologically important pH range 7 – 9 suggests that such chromoionophores may be suitable for application in integrated optical sensors.

11.2.2 Silica nanoparticles

Increasing the surface area of the sensor increases the number of silation sites that should lead to an increase in the density of receptors upon the surface. It would be expected that such an increase would amplify the Bragg response over that of the smooth surface.

A potential approach would be to tether silica nanoparticles to the surface. These particles can then be further functionalised to produce the active sensor surface, as illustrated for a crown ether sensor in Figure 11.2.

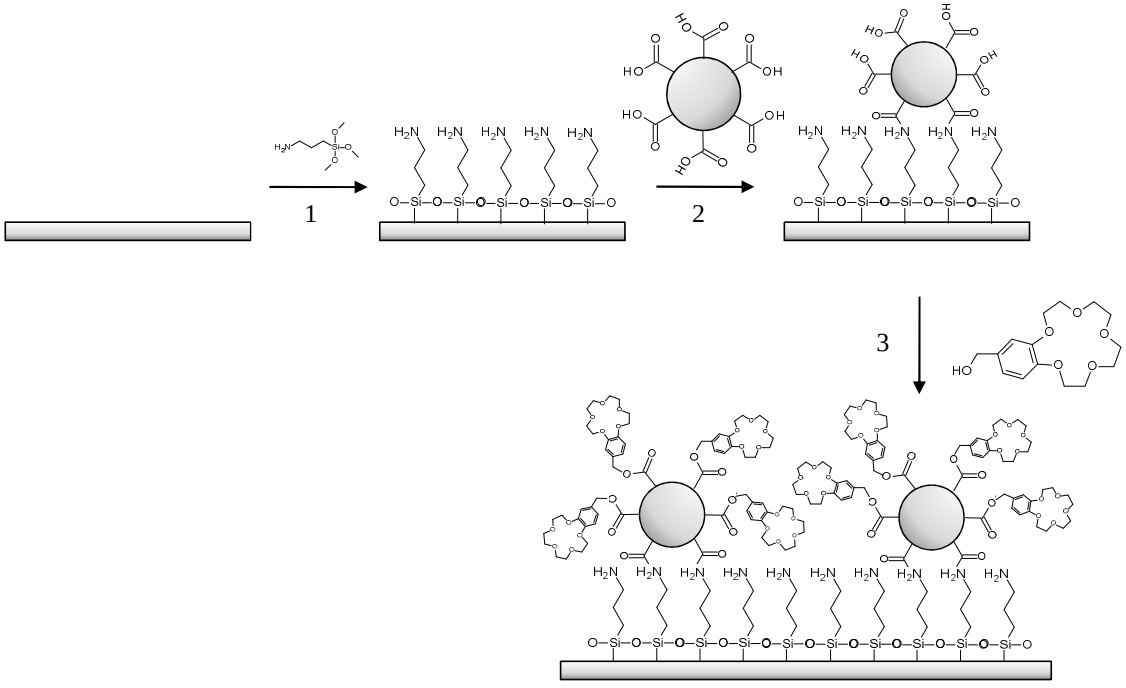

Fig. 11.2 A potential route to enhancing the surface density of binding sites through tethering silica nanoparticles to the surface. 1) functionalisation with 3-APS, 2) linking silica nanoparticles to the surface, 3) functionalisation of the surface with a chemical receptor.

For this approach to work two criteria would need to be met. The size of the particles needs to be large enough that the increase in the number of active surface

sites is consequential, but sufficiently small (below 150 nm) so as to avoid increasing optical loss via scattering. Secondly the refractive index of the particles needs to be low enough to avoid pulling the mode out of the grating. For this it is believed that tethering silica nanoparticles of ~ 50 nm to the surface should be sufficient.

While linking surfaces of different morphologies, such as gold nanoparticles to a silica surface (or vice-versa) is relatively straightforward through thiol and silane directing groups [307], controlled tethering of silica nanoparticles onto a silica surface without polymerisation is more challenging. Using a modified approach to that used for 3-APS, with the nanoparticle surface functionalised so that it is only labile to the functionalised sensor surface (e.g. acid functionalised) and not other particles, it should be possible to deposit a controlled film upon the surface.

11.2.3 Dendritic surfaces

The term dendrimer [308] is used to describe a family of large, repeatedly branched, roughly spherical polymeric molecules (Figure 11.3). They are fabricated by the attachment of successive layers (generations) onto a single core unit. The properties of dendrimers are typically dominated by the functional groups on the molecular surface, with the ability to attach a wide range of groups to the dendrimer surface.

Poly(amidoamine) often abbreviated to PAMAM is one of the most common dendrimer systems [309]. The core is typically ammonia or a diamine (commonly ethylenediamine), which is reacted with methyl acrylate, and then with excess ethylenediamine to make the generation zero PAMAM. Successive reactions can then be used to create higher generations. Lower generations tend to form flexible molecules with no appreciable inner regions, while medium sized PAMAMs (third or fourth generation) have internal space separated from the outer shell of the dendrimer. Large (seventh generation and above) dendrimers can be thought of as more like solid nanoparticles with very dense surfaces arising from the structure of their outer shell. The functional groups on the surface of PAMAM dendrimers can be compatible with click chemistry [310], which has given rise to a variety of functional surfaces for many potential applications.

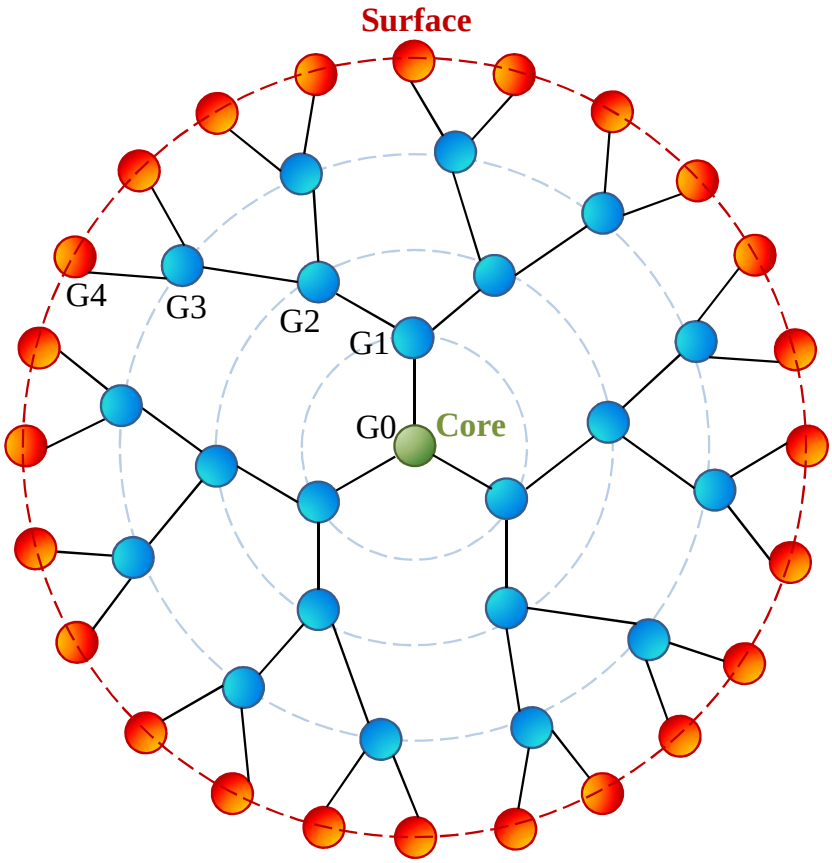

Fig. 11.3 A schematic of a fourth generation dendrimer.

Dendritic structures are not confined to single particles. Attachment of a suitably functionalised SAM upon the sensor surface would allow for such branched systems to be grown [311, 312]. If the outer shell of this dendritic surface was then functionalised with a suitable receptor then an analogous chemical sensor would be fabricated with a greatly increased density of active sites. The advantage of this approach over that of the silica nanoparticles is that the receptors are closer to the waveguide where, due to the exponential decay of the mode into the fluidic region, changes in refractive index have a greater effect upon the effective index of the Bragg grating.

11.2.4 Porous silica sol-gel

The final route would involve the deposition of a porous silica sol-gel onto the sensor surface. This porous structure would occupy a greater percentage of the evanescent tail of the guided mode than a surface monolayer. If the pore surfaces within this structure were functionalised, this would increase the number of active sites within the sensitive region, hopefully improving the Bragg response.

Porous silica sol-gels can be fabricated from the hydrolysis of tetraalkoxysilanes [313]. The properties of these pores can be directly controlled through the blend of alkylsilanes used; with the incorporation of 3-aminopropylsilane resulting in hydrophilic aminated pores, while *t*-butylsilane would result in hydrophobic pores. Alternatively, functionalisation could be carried out post fabrication upon the sol-gel layer in an analogous methodology to the planar system. Pore size can be controlled through structure directing agents such as surfactants, that can template the sol-gel formation before being washed away [314, 315]. In this way the surface functionalisation can be protected from surface abrasion within the pores, with only analytes of suitable size being able to enter the pores and interact with the surface – introducing further chemical (size) selectivity to the sensor.

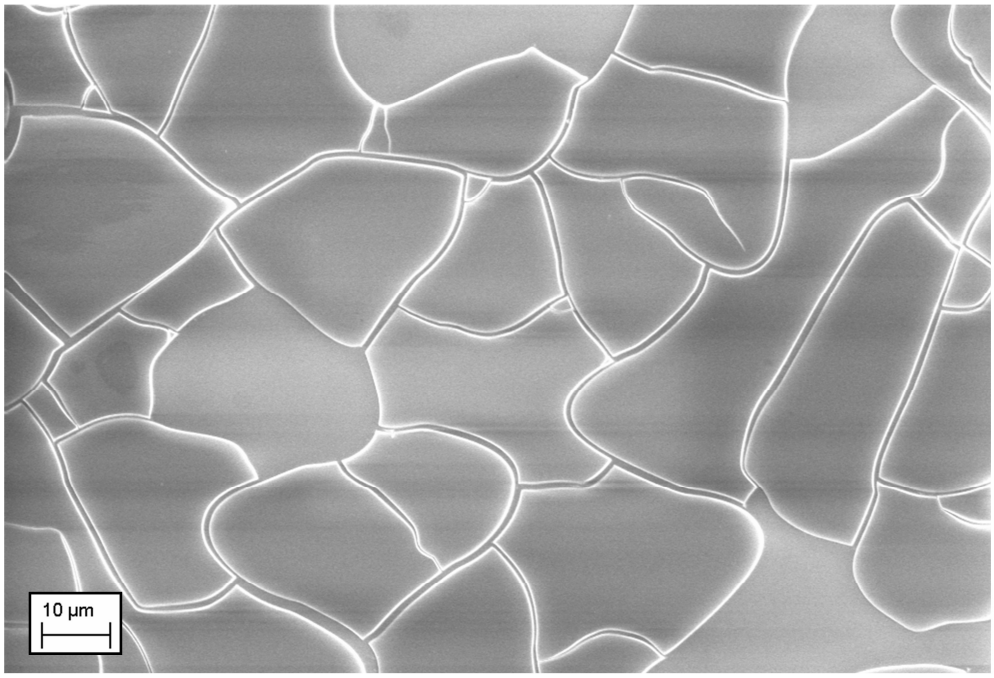

Fig. 11.4 A scanning electron microscope image of a silica sol-gel spun onto a Bragg grating sensor (courtesy of D. Wales [316])

11.3 Final Comments

The optofluidic sensors developed in this work have been shown to be competitive with other integrated optical approaches to chemical sensing, with specific focus upon SPR showing that the Bragg grating presented within this work are comparable in terms of absolute sensitivity and selectivity. While the sensitivity, response time and specificity of the sensors reported here cannot rival non-integrated optical systems, such as the cross-responsive fluorescent sensor arrays developed by Walt [198] or flow cell of Anslyn [200], these are all areas that can be improved. Through use a

series of functionalised sol-gels combined with multiple Bragg gratings an integrated network of Bragg sensors could be fabricated on a single chip that would form a similar sensor array to that described by Walt without any additional requirements or challenges to the characterisation of the device. Combined with a suitable series of chromatic receptors that would enhance the refractive index response upon binding, it is reasonable to presume that such a system could rival existing "optical noses".

When used as chemical sensors, the integrated Bragg grating devices have been shown to exhibit good selectivity that has potential for further advancements, building on the wealth of supramolecular receptors within the literature, such as the colourmetric metalloporphyrin arrays developed by Suslick [199]. Incorporated within a microfluidic network, they are robust and reusable, with high resistance to chemical attack. These properties demonstrate the potential of the prototype optofluidic sensors presented here for real world application in environmental and oceanographic sensors.

11.4 Dissemination of Research

11.4.1 The journal publications that have arisen from this work:

1. R. M. Parker, J. C. Gates, M. C. Grossel, P. G. R. Smith, "*In vacuo* measurement of the sensitivity limit of planar Bragg grating sensors for monolayer detection", *Appl. Phys. Lett.*, 2009, **95**, 173306, (3 pages). [31]

2. R. M. Parker, J. C. Gates, M. C. Grossel, P. G. R. Smith, "A temperature-insensitive Bragg grating sensor – using orthogonal polarisation modes for in-situ temperature compensation", *Sensors and Actuators B*, 2010, **145**, 428-432.[30]

3. R. M. Parker, J. C. Gates, M. C. Grossel, P. G. R. Smith, "Athermal planar Bragg grating device for integrated photonic networks", *Electron. Lett.*, 2010, **46**, 358-359. [32]

4. R. M. Parker, J. C. Gates, H. L. Rogers, P. G. R. Smith, M. C. Grossel, "Using the Photoinduced Reversible Refractive-index Change of an Azobenzene Co-polymer to Reconfigure an Optical Bragg Grating", *J. Mater. Chem.*, 2010, **20**, 9118-9125. [33]

11.4.2 The conference proceedings that have arisen from this work:

1. R. M. Parker, D. Wales, J. C. Gates, P. G. R. S. Smith, M. C. Grossel, "Optofluidic Bragg Grating Sensors for Chemical Detection", *Challenger 10*, Southampton, 10 September 2010.

2. R. M. Parker, J. C. Gates, M. C. Grossel, P. G. R. Smith, "An Integrated Optofluidic Bragg Grating Device to Measure the Dynamic Composition of a Fluid System", *CLEO/QELS 2010*, San Jose, 16-21 May 2010.

3. R. M. Parker, J. C. Gates, M. C. Grossel, P. G. R. Smith, "Integrated Temperature Compensated Bragg Grating Refractometer – Benefiting from Birefringence", *CLEO/QELS 2010*, San Jose, 16-21 May 2010.

4. R. M. Parker, J. C. Gates, P. G. R. Smith, M. C. Grossel, "A Reconfigurable Bragg grating using a photoresponsive polymer", *ECIO 2010*, Cambridge, 7-9 April 2010.

5. R. M. Parker, J. C. Gates, P. G. R. S. Smith, M. C. Grossel, "Optofluidic Sensors for Chemical Detection", *Set for Britain 2010*, Houses of Parliament, 8 March 2010.

6. R. M. Parker, J. C. Gates, M. C. Grossel, P. G. R. Smith, "A microfluidic Bragg grating sensor for monolayer detection at a surface", *MC9, embedded in the 42nd IUPAC Congress*, Glasgow, 2-7 August 2009.

7. R. M. Parker, J. C. Gates, N. P. Sessions, D. O. Kundys, C. B. E. Gawith, M. C. Grossel, P. G. R. Smith "*In vacuo* measurement of the sensitivity limit of planar Bragg sensors", *CLEO/Europe-EQEC 2009*, Munich, 14-19 June 2009.

8. R. M. Parker, J. C. Gates, P. G. R. Smith, M. C. Grossel, "A Bragg grating sensor for detection of monolayers at a surface", *CLEO/Europe-EQEC 2009*, Munich, 14-19 June 2009.

9. R. M. Parker, J. C. Gates, P. G. R. Smith, M. C. Grossel, "Optofluidic Bragg grating sensor for monolayer detection", *CLEO/IQEC 2009*, Baltimore, 31 May - 5 June 2009.

10. R. M. Parker, J. C. Gates, M. C. Grossel, P. G. R. Smith, "Supramolecular functionalised optical surfaces for remote sensing", *ISMSC 2008*, Las Vegas, 13-18 July 2008.

12. Experimental

12.1 Introduction

This chapter details the experimental procedures for the synthesis of the compounds prepared during this work and their subsequent characterisation. All compounds were synthesised from commercially available starting materials, and characterised by nuclear magnetic resonance spectroscopy, mass spectrometry, infrared spectroscopy and melting point determination where appropriate. Where relevant, additional characterisation was undertaken and compared with known literature data. Also outlined is the experimental methodology used to functionalise the optical surfaces presented within this work, with the corresponding analytical data used to confirm their presence.

The synthetic chemistry is followed by an overview of the optical device fabrication and interrogation systems, with focus upon the practical applications and methods used.

12.2 General Experimental

Commercially available compounds were obtained from Sigma Aldrich or Fisher and, unless specified, all reagents and solvents were reagent grade or better and were used as supplied without further purification.

Concentrated HCl refers to 37 % HCl, while concentrated HF refers to 48 % HF. “Piranha” solution was prepared at room temperature, dropwise addition of 30 % H_2O_2 to 95-97 % H_2SO_4 in the ratio of 1:3. Due to the hazards associated with highly corrosive “piranha” solution, it was always prepared on a small-scale in a fume-hood with acid resistant gauntlets and gown worn.

Melting points (MP) were measured using a Gallenkamp Electrothermal melting point apparatus and are uncorrected.

Electrospray (ES) mass spectra were recorded using a Micromass Platform II single quadrapole mass spectrometer.

Nuclear magnetic resonance (NMR) spectra were collected using either a Bruker AV300 spectrometer, or a Bruker DPX400 spectrometer; operating at 300 or 400 MHz respectively for ^{1}H NMR experiments and at 75 MHz or 100 MHz respectively for ^{13}C and Dept-135 NMR experiments. ^{13}C spectra were collected fully decoupled.

Infrared (IR) spectra were collected on a Nicolet 380 FT-IR spectrometer with a SmartOrbit Golden Gate Attenuated Total Reflection (ATR) attachment.

UV-visible spectra were collected using a Shimadzu UV-1601 UV-visible spectrophotometer running UVPC version 3.5. The presence of the polymer films and their ability to undergo photoisomerisation was confirmed by diffuse-reflectance UV-visible spectroscopy using a Varian Cary 500 Scan UV-VIS-NIR spectrophotometer fitted with an internal DRA 2500 integrating sphere.

Surface profile data (step height and R_a) was collected using either a KLA Tencor Alpha-step IQ surface profiler running KLA Alpha-step IQ v2.X or a KLA Tencor P.16 surface profiler running Profiler v7.21. Two-dimensional surface data was collected using a Veeco Thermomicroscopes Explorer non-contact AFM, running Veeco di SPMlabNT v6.02.

Contact angles were calculated for a drop size of 1 µL, with a Kruss DSA100 running Drop Shape Analysis (DSA) for windows v1.90.0.14.

Tantalum pentoxide was deposited using an OPT plasmalab 400 Sputter system, while gold and chromium were deposited using a BOC Edwards EB3 E-beam linked to a FL400 deposition system. Chromium was etched using “MS 8 chrome etchant”, a solution of acetic acid and ceric ammonium nitrate.

Photoisomerisation was stimulated with a UVP UVGL-25 dual wavelength UV-lamp (4 W, 254/365 nm). The reverse process was stimulated through irradiation by ambient fluorescent lighting.

Etch profile and polymer film thickness was measured using a KLA Tencor Alpha-step IQ surface profiler running KLA Alpha-step IQ v2.X.

Polymer molecular weights and polydispersities were determined by gel permeation chromatography with a polar solvent on a Polymer Laboratories PL-GPC 120 with a PL-AS-MT autosampler on behalf of the author by Dr S. Holding through the EPSRC Polymer Molecular Weight Service, in partnership with Smithers Rapra Technology Limited, UK.

Direct UV writing of waveguides was performed using a "Cambridge Laser Laboratories" Lexel 95 SHG UV laser combined with an Aerotech ABL9000 air-bearing stage.

Microfluidic pumping was achieved through either a peristaltic Masterflex C/L dual-channel variable speed tubing pump that could operate up to 6 rpm with a maximum pump rate of 1.3 mL/min through Viton tubing; or a Bio-Chem Fluidics Bio-Chem Valve solenoid operated micro-pump 130SP1210-1TP, with a 10 μL PTFE chamber, pumping up to 1.2 mL/min. Solvent switching was achieved with a Cole Parmer PTFE manifold mixing solenoid valve, with 6 inputs leading to 1 output, capable of transporting 14 L/min at 20 psi. These were linked with Cole Parmer Chemfluor ETFE tubing, with an internal diameter of 0.016" (400 μm) and external diameter of 1/16". Connections were made using Omnifit Omni-Lok Type P fittings, a chemically inert flangeless fitting with a permanently attached PTFE ferrule rated up to 1000 psi.

Interrogation of the Bragg grating at ~780 nm was carried out with a broadband source, generated from a frequency doubled 1550 nm femtosecond laser source. A 600 nm band pass filter was used to remove any third harmonic light at 515 nm that would interfere with photoisomerisation. For interrogation at ~1550 nm the waveguide was exposed to an Exfo IQ-2300 erbium fibre-based ASE source as part of an Exfo IQ-203 Optical Test system. The resultant signal was collected by an Ando AQ 6317B optical spectrum analyser (OSA) controlled via a PC running Labview 8.2.1. Labview is a graphical programming environment used to develop sophisticated measurement, test, and control systems using graphical icons and wires that resemble a flowchart. It is a product of National Instruments.

Fimmwave modelling software is a product of Photon Design and was used as a vectorial mode finder.

12.3 Synthesis of Organic Compounds

The syntheses of the compounds discussed within this work are detailed in the following section. The results of the associated characterisation techniques undertaken are included for each compound and where present, compared to published data.

12.3.1 4-Phenylazophenol (1a) [317, 318]

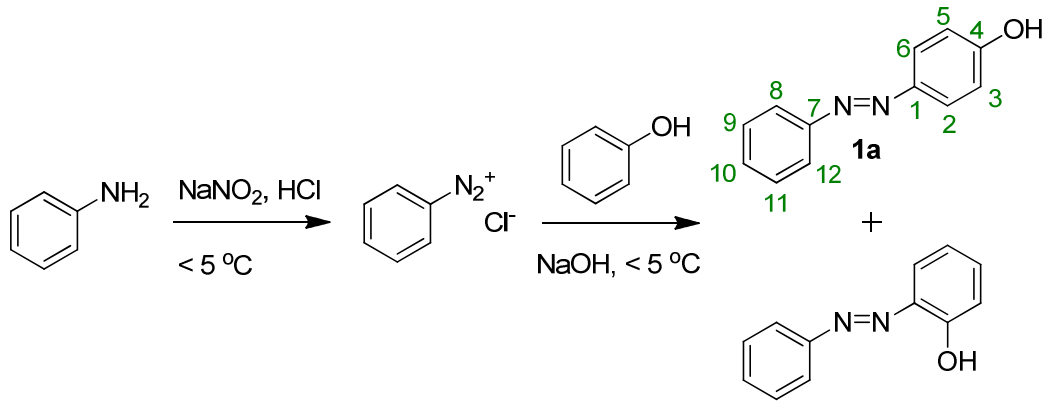

Freshly distilled aniline (0.50 mL, 5.37 mmol) was dissolved in a mixture of concentrated hydrochloric acid (0.50 mL, 16.4 mmol) and water (5.0 mL). This was cooled (<5 °C) before subsequent dropwise addition of a solution of sodium nitrite (0.40 g, 6.04 mmol) in water (5.0 mL) until an excess was present. This was stirred for 15 minutes, before subsequent addition of phenol (0.56 g, 5.49 mmol) in an aqueous solution of sodium hydroxide (1.0 M, 2.5 mL). This was stirred for 30 minutes, before filtering, washing with cold water and drying *in vacuo* to yield an orange solid (0.76 g, 71 %).

The *ortho*- and *para*- isomers were separated by column chromatography (50:50 diethyl ether : light petroleum (40-60)) that separated a red solid (2-phenylazophenol, 0.28 g, 26 %) from an orange solid (**1a**, 0.29 g, 27 %) from an orange oil.

Data for **1a**:

MP: decomposition at 80 ^{O}C (Lit [319]: 154 ^{O}C).

^{1}H NMR (MeOD, δ/ppm): 6.92 (d, *J*=8.8 Hz, 2H, $H_{1,5}$), 7.37 - 7.56 (m, 4H, H_{12-14}), 7.76 - 7.88 (m, J=8.8 Hz, 4H, $H_{2,6,8,12}$).

^{13}C NMR (MeOD, δ/ppm): 116.8 ($C_{3,5}$), 123.50 ($C_{8,12}$), 126.1 ($C_{2,6}$), 130.2 ($C_{9,11}$), 131.4 (C_{10}), 147.6 (C_{1}), 154.2 (C_{7}), 162.3 (C_{4}).

IR (ν/cm^{-1}): 3300-3100 (O-H), 3054 (C-H aromatic), 1602 (C=C aromatic), 1411 (N=N), 1139 (C-N), 1071 (C-O).

MS (ES^{+}, MeOH, m/z): 198.2 (100.0 %, $[M^{\cdot}]^{+}$), 199.1 (95.1 %, $[M+H]^{+}$), 221.1 (33.0 %, $[M+Na]^{+}$), 53.2 (18.7 %, $[M+Na+MeOH]^{+}$).

MS (ES^{-}, MeOH, m/z): 197.2 (100.0 %, $[M-H]^{-}$).

This is consistent with the reported data [317].

12.3.2 Ethyl (4-phenylazophenoxyacetate) (2a) [320]

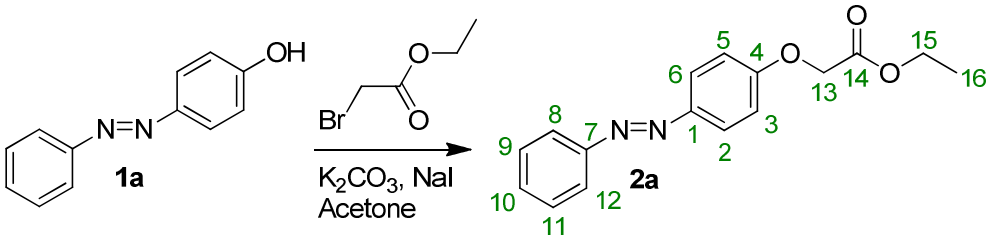

4-Phenylazophenol (**1a**, 0.38 g, 1.90 mmol) was dissolved in acetone (silica dried, 60 mL), followed by potassium carbonate (1.658 g, 11.9 mmol) and the mixture was warmed until dissolution occurred. To this stirred solution, ethyl bromoacetate (0.125 mL, 3.75 mmol) and sodium iodide (0.29 g, 1.9 mmol, in 4.0 mL acetone) were then added. The reaction mixture was heated under reflux for 16 h. The solvent was removed *in vacuo* to give an orange solid. This was subsequently extracted into diethyl ether (3 x 40 mL) from water (40 mL); before drying the combined extracts with magnesium sulphate, filtering and removal of the solvent *in vacuo*. The resultant solid was purified by column chromatography (50/50 diethyl ether/light petroleum (40-60)) to give an orange solid (**2a**, 0.31 g, 90 %).

MP: 66 ^{O}C (Lit [321]: 70 ^{O}C).

^{1}H NMR (MeOD, δ/ppm): 1.26 (t, *J*=7.1 Hz, 3H, H_{16}), 4.23 (q, *J*=7.1 Hz, 2H, H_{15}), 4.77 (s, 2H, H_{13}), 7.05 (d, *J*=9.0 Hz, 2H, $H_{3,5}$),

7.39 - 7.53 (m, *J*=7.5 Hz, 3H, $H_{9\text{-}11}$), 7.83 (dd, *J*=8.2, 1.7 Hz, 2H, $H_{8,12}$), 7.87 (d, J=9.2Hz, 2H, $H_{2,6}$).

^{13}C NMR (MeOD, δ/ppm): 14.6 (C_{16}), 62.6 (C_{15}), 66.4 (C_{13}), 116.2 ($C_{3,5}$), 123.7 ($C_{8,12}$), 125.8 ($C_{2,6}$), 130.3 ($C_{9,11}$), 131.9 (C_{10}), 148.9 (C_1), 154.17 (C_7), 162.1 (C_4), 170.6 (C_{14}).

IR (ν/cm^{-1}): 3068 (C-H aromatic), 2937 (C-H), 1726 (C=O), 1600 (C=C aromatic), 1495 (N=N), 1149 (C-N), 1077 (C-O).

MS (ES$^+$, MeOH, m/z): 285.2 (14.5 %, $[M+H]^+$), 307.1 (64.4 %, $[M+Na]^+$), 323.1 (2.62% $[M+K)^+$), 339.2 (18.7 %, $[M+Na+MeOH]^+$).

No comparative spectroscopic literature was found.

12.3.3 Phenylazophenoxyacetic acid (3a) [322]

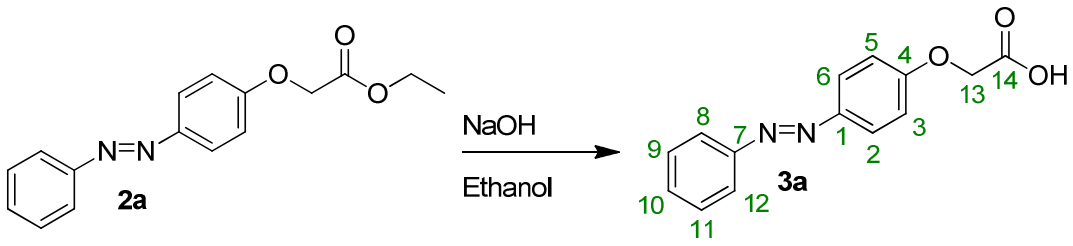

Ethyl (4-phenylazophenoxyacetate) (**2a**, 0.28 g, 0.971 mmol) was dissolved in ethanol (40 mL). To this, an aqueous solution of sodium hydroxide (0.056 M, 40 mL) was added before heating the mixture under reflux for 3 hours. The reaction mixture was acidified (conc. HCl) before it was extracted with diethyl ether (3 x 60 mL). The combined extracts were dried with magnesium sulphate, filtered and the solvent was removed *in vacuo* to yield a yellow solid (**3a**, 0.26 g, >99 %).

MP: 180 ^{O}C (Lit [322]: 184 ^{O}C).

^{1}H NMR (MeOD, δ/ppm): *trans*: 4.72 (s, 2H, H_{13}), 7.04 (d, *J*=9.0 Hz, 2H, $H_{3,5}$), 7.37 - 7.54 (m, 3H, $H_{9\text{-}11}$), 7.81 (dd, *J*=8.1, 1.4 Hz, 2H, $H_{8,12}$), 7.87 (d, *J*=9.0 Hz, 2H, $H_{3,6}$).

cis: 4.63 (s, 2H, H_{13}), 6.75 – 6.95 (m, 6H, $H_{2,3,5,6,8,12}$), 7.21 (t, 1H, *J*=8.0 Hz, H_{10}), 7.87 (t, 2H, *J*=8.0 Hz, $H_{9,11}$).

^{13}C NMR (MeOD, δ/ppm):	*trans:* 66.1 (C_{13}), 116.2 ($C_{3,5}$), 123.7 ($C_{8,12}$), 125.8 ($C_{2,6}$), 130.3 ($C_{9,11}$), 131.9 (C_{10}), 148.8 (C_1), 154.2 (C_7), 162.1 (C_4) 172.3 (C_{14}).
IR (ν/cm^{-1}):	3068 (C-H aromatic), 2915 (C-H), 2700 broad (O-H), 1706 (C=O), 1602, 1582 (C=C aromatic), 1501 (N=N), 1143 (C-N), 1085 (C-O).
MS (ES$^+$, MeOH, m/z):	256.2 (4.9 % $[M]\cdot^+$), 257.1 (67.9 % $[M+H]^+$), 279.1 (95.2 %, $[M+Na]^+$), 295.1 (4.5% $[M+K]^+$), 311.1 (100.0 %, $[M+Na+MeOH]^+$).
MS (ES$^-$, MeOH, m/z):	255.2 (6.7 %, $[M-H]^-$), 256.1 (1.0 %, $[M]\cdot^-$).
UV-vis (λ_{max} / nm)	320.5, 450.5 (cis), 342.0 (trans).
HRMS (ES$^+$)	calcd. for $C_{14}H_{13}N_2O_3$ $(M+H)^+$ 257.0921, found 257.0918. calcd. for $C_{14}H_{12}N_2O_3Na$ $(M+Na)^+$ 279.0740, found 279.0737.

No comparative spectroscopic literature was found.

12.3.4 4-(4-Nitrophenyl)azophenol (1b)

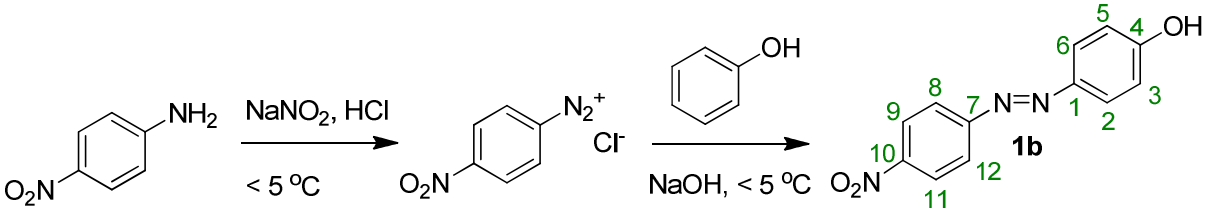

Freshly distilled 4-nitroaniline (2.96 g, 21.4 mmol) was dissolved in a solution of concentrated hydrochloric acid (9.0 mL, 0.295 mol) and water (200 mL). This was cooled (<5 °C) before subsequent dropwise addition of a solution of sodium nitrite (1.65 g, 23.8 mmol) in water (15.0 mL) until this was in excess. The mixture was then stirred for 30 minutes, before the addition of phenol (1.99 g, 21.2 mmol) in an aqueous solution of sodium hydroxide (1.0 M, 10 mL). This mixture was then stirred for a further 30 minutes, before filtering off the product as a solid which was washed with cold water and dried *in vacuo* to yield a terracotta solid (**1b**, 4.79 g, 93 %) which was not further purified.

MP: decomposition at 170 ^{O}C (Lit [323]: 207 ^{O}C).

^{1}H NMR (MeOD, δ/ppm): 6.94 (d, J=9.0 Hz, 2H, $H_{3,5}$), 7.87 (d, J=9.0 Hz, 2H, $H_{2,6}$), 7.97 (d, J=9.2 Hz, 2H, $H_{8,12}$), 8.36 (d, J=9.2 Hz, 2H, $H_{9,11}$).

^{13}C NMR (MeOD, δ/ppm): 117.1 ($C_{3,5}$), 124.2 ($C_{8,12}$), 125.9 ($C_{9,11}$), 127.0 ($C_{2,6}$), 147.7 (C_1), 149.7 (C_{10}), 157.7 (C_7), 163.7 (C_4).

IR (ν/cm^{-1}): 3381 (O-H), 3112 (C-H aromatic), 1584, 1603 (C=C aromatic), 1456 (N=N), 1135 (C-N), 1100 (C-O).

MS (ES^{+}, MeOH, m/z): 282.1 (100.0 %, $[M+K]^{+}$).

MS (ES^{-}, MeOH, m/z): 242.2 (100.0 %, $[M-H]^{-}$).

This is consistent with reported data [323].

12.3.5 Ethyl[4-(4-nitrophenyl)azophenoxyacetate] (2b)

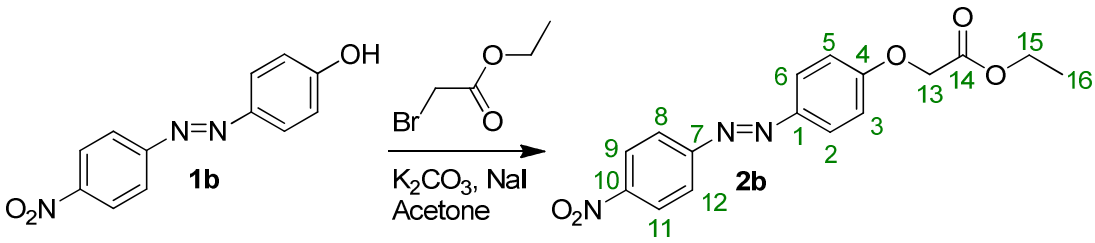

4-(4-Nitrophenyl)azophenol (**1b**, 4.69 g, 19.3 mmol) was dissolved in acetone (silica dried, 100 mL), followed by potassium carbonate (5.34 g, 38.5 mmol) and the solution was warmed until everything had dissolved. To this stirred solution ethyl bromoacetate (2.10 mL, 20.3 mmol) and sodium iodide (2.92 g, 19.5 mmol, in 4.0 mL acetone) were added. The reaction mixture was heated under reflux for 16 hours. The solvent was then removed *in vacuo* to give a brown solid. This was subsequently extracted into diethyl ether (4 x 200 mL) from water (600 mL) before drying the combined extracts with magnesium sulphate, filtering this off and removing the solvent *in vacuo*. The resultant solid was purified by column chromatography (50/50 diethyl ether / light petroleum (40-60)) to give a brown solid (**2b**, 2.88 g, 45 %).

MP: 138 – 139 ^{O}C (Lit [322]: 150.5 ^{O}C).

^{1}H NMR ($CDCl_3$, δ/ppm): 1.33 (t, *J*=7.1 Hz, 3H, H_{16}), 4.32 (q, *J*=7.0 Hz, 2H, H_{15}), 4.74 (s, 2H, H_{13}), 7.06 (d, *J*=9.0 Hz, 2H, $H_{3,5}$), 7.98 (d, *J*=9.2 Hz, 2H, $H_{8,12}$), 8.01 (d, *J*=9.0 Hz, 2H, $H_{2,6}$), 8.38 (d, *J*=9.0 Hz, 2H, $H_{9,11}$).

^{13}C NMR ($CDCl_3$, δ/ppm): 14.1 (C_{16}), 61.6 (C_{15}), 65.4 (C_{13}), 115.1 ($C_{3,5}$), 123.2 ($C_{8,12}$), 124.7 ($C_{9,11}$), 125.1 ($C_{2/6}$), 125.5 ($C_{2/6}$), 147.5 (C_1), 148.3 (C_{10}), 155.9 (C_7), 161.2 (C_4), 168.2 (C_{14}).

IR (ν/cm^{-1}): 2897, 3107 (C-H aromatic), 2909 ([C]C-H), 2847 ([O]C-H), 1755 (C=O), 1585, 1601 (C=C aromatic), 1499 (N=N), 1140 (C-N), 1082 (C-O).

MS (ES^+, MeOH, m/z): 330.2 (4.1 %, $[M+H]^+$), 352.2 (98.5 %, $[M+Na]^+$), 384.2 (56.6% $[M+Na+MeOH]^+$), 681.4 (100.0 %, $[2M+Na]^+$).

MS (ES^-, MeOH, m/z): 328.1 (11.0 %, $[M-H]^-$).

HRMS (ES^+) calcd. for $C_{16}H_{15}N_3O_5Na$ $(M+Na)^+$ 352.0904, found 352.0910.

No comparative spectroscopic literature was found.

12.3.6 4-(4-Nitrophenyl)azophenoxyacetic acid (3b) [322]

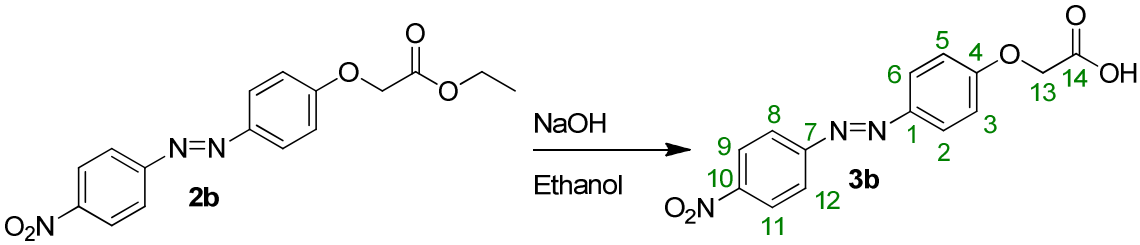

Ethyl[4-(4-nitrophenyl)azophenoxyacetate] (**2b**, 0.103 g, 0.313 mmol) was dissolved in ethanol (100 mL). To this, an aqueous solution of sodium hydroxide (0.042 M, 15 mL) was added before leaving the mixture to stir for 16 hours. The reaction mixture was then acidified (conc. HCl) before it was extracted into diethyl ether (3 x 60 mL), dried with magnesium sulphate, filtered and the solvent removed *in vacuo* to give a yellow solid (**3b**, 0.09 g, >99 %).

MP: decomposed at 175 ^{O}C (Lit [322]: 236 ^{O}C).

^{1}H NMR (MeOD, δ/ppm): *trans:* 4.75 (s, 2H, H_{13}), 7.09 (d, *J*=9.0 Hz, 2H, $H_{3,5}$), 7.97 (d, *J*=9.2 Hz, 2H, $H_{8,12}$), 8.00 (d, *J*=9.0 Hz, 2H, $H_{2,6}$), 8.37 (d, *J*=9.2 Hz, 2H, $H_{9,11}$).

cis: 4.63 (s, 2H, H_{13}), 6.75 – 6.95 (m, 6H, $H_{2,3,5,6,8,9,11,12}$).

^{13}C NMR (MeOD, δ/ppm): *trans:* 72.0 (C_{13}), 116.0 ($C_{3,5}$), 124.0 ($C_{8,12}$), 125.6 ($C_{2,6}$), 126.3 ($C_{9,11}$), 142.6 (C_1), 149.1 (C_{10}), 157.2 (C_7) 159.0 (C_4), 179.7 (C_{14}).

IR (ν/cm^{-1}): 3108 (C-H aromatic), 2912 ([C]C-H), 2845 ([O]C-H), 1704 (C=O), 1580, 1600 (C=C aromatic), 1496 (N=N), 1138 (C-N), 1070 (C-O).

MS (ES$^+$, MeOH, m/z): 301.2 (30.6 % $[M]\cdot^+$), 302.3 (6.7 % $[M+H]^+$), 324.2 (9.3 %, $[M+Na]^+$), 333.3(5.6 % $[M+MeOH]\cdot^+$), 340.2 (2.2 % $[M+K]^+$), 356.1 (9.3 %, $[M+Na+MeOH]^+$).

MS (ES$^-$, MeOH, m/z): 300.1 (16.3 %, $[M-H]^-$).

UV-vis (λ_{max} / nm) 367.5 (cis), 370.0 (trans).

HRMS (ES$^+$) calcd. for $C_{14}H_{12}N_3O_5$ $(M+H)^+$ 302.0771, found 302.0766.

No comparative spectroscopic literature was found.

12.3.7 4-(4-Methoxyphenyl)azophenol (1c)

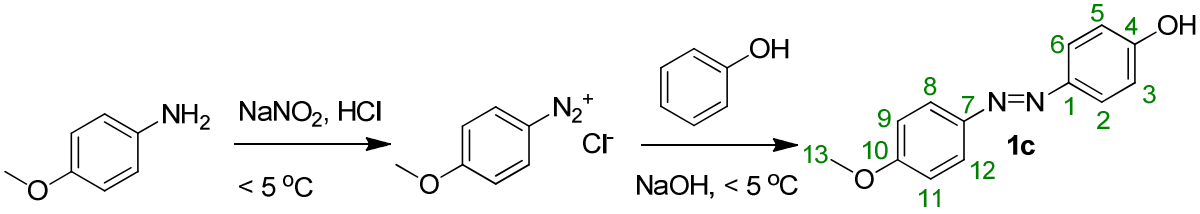

Freshly distilled 4-anisidine (1.04 g, 8.42 mmol) was dissolved in a mixture of concentrated hydrochloric acid (3.35 mL, 40.6 mmol) and water 10 mL). This was cooled (<5°C) before subsequent dropwise addition of a solution of sodium nitrite (2.80 g, 40.6 mmol) in water (25.0 mL) until this was in excess. The mixture was stirred for 30 minutes, before the addition of phenol (3.8167 g, 40.6 mmol) in an

aqueous solution of sodium hydroxide (1.71 g) and sodium carbonate (4.499 g) in water (50 mL). The mixture was then stirred for 1 hour, before neutralising with hydrochloric acid, and the resultant precipitate was filtered and the filtrate washed with cold water. The precipitate was dissolved into ether and the organic solution was washed with dilute hydrochloric acid and water. The organic phase was dried with magnesium sulphate, filtered and the solvent removed *in vacuo* to give an orange solid (**1c**, 1.81 g, 97 %).

MP: 132 – 133 ^{O}C (Lit [324]: 149.8 ^{O}C)

^{1}H NMR (MeOD, δ/ppm): 3.86 (s, 3H, H_{13}) 6.90 (d, *J*=9.0 Hz, 2H, $H_{9,11}$) 7.03 (d, *J*=9.2 Hz, 2H, $H_{3,5}$) 7.76 (d, *J*=9.0 Hz, 2H, $H_{8,12}$) 7.82 (d, *J*=9.2 Hz, 2H, $H_{2,6}$)

^{13}C NMR (MeOD, δ/ppm): 56.2 (C_{13}), 115.4 ($C_{9,11}$), 116.8 ($C_{3,5}$), 125.3 ($C_{8,12}$), 125.6 ($C_{2,6}$), 147.7 (C_1), 148.4 (C_7), 161.7 (C_4), 163.3 (C_{10}).

IR (*v*/cm^{-1}): 3411 (O-H), 3026 (C-H aromatic), 2953 (C-H), 1582, 1595 (C=C aromatic), 1436 (N=N), 1149 (C-N), 1014 (C-O)

MS (ES^{-}, MeOH, m/z): 227.2 (100.0 %, [M-H]$^{-}$)

This is consistent with reported data [324].

12.3.8 Ethyl [4-(4-methoxyphenyl)azophenoxyacetate] (2c)

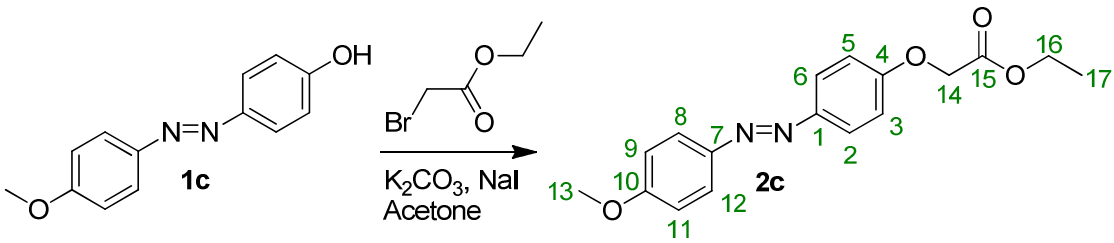

4-(4-Methoxyphenyl)azophenol (**1c**, 1.77 g, 7.78 mmol) was dissolved in acetone (silica dried, 50 mL), potassium carbonate (2.18 g, 15.7 mmol) was added and the solution was warmed until everything had dissolved. To this stirred solution ethyl bromoacetate (0.82 mL, 7.88 mmol) and sodium iodide (2.338 g, 15.6 mmol, in 4.0 mL acetone) were added. The reaction mixture was heated under reflux for 16

hours. The solvent was removed *in vacuo* to give a yellow solid. This was subsequently extracted into diethyl ether (5 x 50 mL) from water (250 mL). The organic layer was dried with magnesium sulphate and filtered and the solvent was removed *in vacuo*. The resultant solid was purified by column chromatography (50/50 diethyl ether / light petroleum (40-60)) to give a yellow solid (**2c**, 1.29 g, 53 %).

MP: 103 – 105 ^{O}C (No comparative literature)

^{1}H NMR ($CDCl_3$, δ/ppm): 1.32 (t, *J* = 7.2 Hz, 2H, H_{17}), 3.89 (s, 2H, H_{13}), 4.30 (q, *J* = 7.1 Hz, 2H, H_{16}), 4.70 (s, 1H, H_{14}), 7.02 (dd, *J* = 9.1, 2.8 Hz, 4H, $H_{3,5,9,11}$), 7.89 (dd, *J* = 9.1, 1.4 Hz, 4H, $H_{2,6,8,12}$).

^{13}C NMR ($CDCl_3$, δ/ppm): 14.2 (C_{17}), 55.5 (C_{13}), 61.5 (C_{16}), 65.5 (C_{14}), 114.2 ($C_{3,5}$), 114.9 ($C_{9,11}$), 124.3 ($C_{2,6}$), 124.4 ($C_{8,12}$), 147.0 (C_1), 147.7 (C_7), 159.6 (C_4), 161.7 (C_{10}), 168.5 (C_{15}).

IR (ν/cm^{-1}): 3069 (C-H aromatic), 2937, 2977 (C-H), 1758 (C=O), 1579, 1599 (C=C aromatic), 1437 (N=N), 1149 (C-N), 1027 (C-O).

MS (ES^+, MeOH, m/z): 315.2 (100.0 %, $[M+H]^+$), 337.2 (55.9 %, $[M+Na]^+$), 353.2 (5.2 % $[M+K]^+$), 369.2 (18.7 %, $[M+Na+MeOH]^+$).

HRMS (ES^+) calcd. for $C_{17}H_{19}N_2O_4$ $(M+H)^+$ 315.1339, found 315.1343.
calcd. for $C_{17}H_{18}N_2O_4Na$ $(M+Na)^+$ 337.1159, found 337.1155.

No comparative spectroscopic literature was found.

12.3.9 4-(4-Methoxyphenyl)azophenoxyacetic acid (3c)

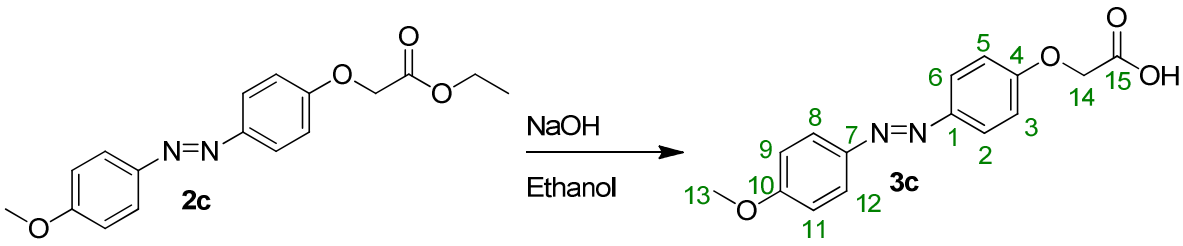

Ethyl [4-(4-methoxyphenyl)azophenoxyacetate] (**2c**, 1.33 g, 4.23 mmol) was dissolved in ethanol (100 mL). To this, an aqueous solution of sodium hydroxide (0.38 g in 100 mL water, 0.095 M) was added before leaving the mixture to stir for 16 hours. The reaction mixture was acidified (conc. HCl, 4 mL) before the solvent was removed *in vacuo*. The resultant orange solid was dissolved in water and extracted into diethyl ether (4 x 60 mL), the solute was dried with magnesium sulphate, filtered and the solvent was then removed *in vacuo* to give a yellow solid (**3c**, 1.23 g, >99 %).

MP: 182 – 183 ^{O}C (No comparative literature)

^{1}H NMR (DMSO-d_6, δ/ppm): *trans:*3.85 (s, 3H, H_{13}) 4.79 (s, 2H, H_{14}), 7.09 (d, J = 9.0 Hz, 2H, $H_{9,11}$) 7.10 (d, J = 9.0 Hz, 2H, $H_{3,5}$) 7.83 (d, J=9.0 Hz, 2H, $H_{8,12}$) 7.84 (d, J=9.0 Hz, 2H, $H_{2,6}$)

^{1}H NMR (MeOD, δ/ppm): *cis*: 3.70 (s, 3H, H_{13}), 4.55 (s, 2H, H_{14}), 6.75 – 6.95 (m, 6H, $H_{2,3,5,6,8,12}$).

^{13}C NMR (DMSO-d_6, δ/ppm): 55.6 (C_{13}), 64.8 (C_{14}), 114.6 ($C_{3,5}$), 115.1 ($C_{9,11}$), 124.1 ($C_{8,12}$), 124.2 ($C_{2,6}$), 146.3 (C_7), 146.6 (C_1), 159.96 (C_4), 161.57 (C_{10}), 169.9 (C_{15}).

IR (ν/cm^{-1}): 3419, 3515 (O-H), 2998 (C-H aromatic), 2972 (C-H), 1704 (C=O), 1579, (C=C aromatic), 1437 (N=N), 1144 (C-N), 1018 (C-O).

MS (ES^{+}, MeOH, m/z): 287.2 (16.9 % $[M+H]^{+}$), 309.2 (25.7 %, $[M+Na]^{+}$), 325.1 (2.5 % $[M+K]^{+}$), 341.2 (15.3 %, $[M+Na+MeOH]^{+}$) 572.6 (29.6 % $[2M]\cdot^{+}$).

MS (ES^{-}, MeOH, m/z): 285.2 (18.3 %, $[M-H]^{-}$).

UV-vis (MeOH, λ_{max} / nm) 444.0 (cis), 356.0 (trans).

HRMS (ES^+) calcd. for $C_{15}H_{15}N_2O4$ $(M+H)^+$ 287.1026, found 287.1027.

No comparative spectroscopic literature was found.

12.3.10 4-(4-Methoxyphenyl)azophenoxyacetyl chloride (4)

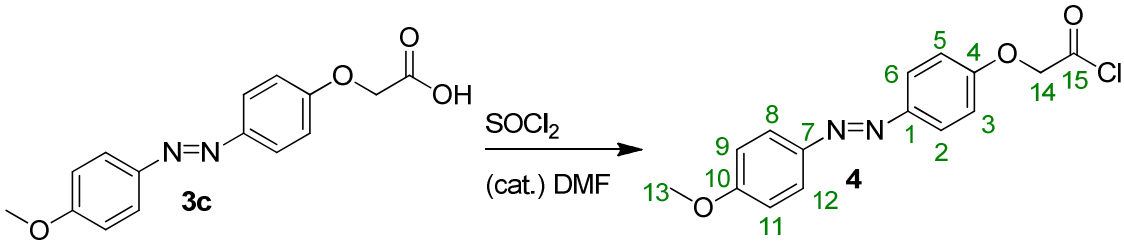

4-(4-Methoxyphenyl)azophenoxyacetic acid (**3c**, 0.110 g, 0.359 mmol) was dissolved in thionyl chloride (5 mL, 68.5 mmol) under nitrogen, and several drops of dimethylformamide were added. The solution was then refluxed overnight. The remaining thionyl chloride was removed by distillation under vacuum (50 °C), and the resulting red solid (**4**) was dried under vacuum (assumed quantitative yield and used immediately without further purification).

MP: 164 – 165^{O}C (No comparative literature)

MS (ES^+, MeOH, m/z): 301.2 (32.8 %, $[N+H]^+$), 323.2 (100.0 %, $[N+Na]^+$), 339.2 (5.9 % $[N+K]^+$), 355.2 (26.2 %, $[N+Na+MeOH]^+$), 623.4 (17.2 %, $[2N+Na]^+$).

N represents the molecular ion for methyl [4-(4-methoxyphenyl)azophenoxyacetate] formed from the reaction of 4-(4-Methoxyphenyl)azophenoxyacetyl chloride (**3c**) with the methanol MS solvent. The formation of the methyl ester was not seen with samples of **3c** and its presence can be used as an indicator for the successful synthesis of **4**.

12.3.11 Poly(methyl methacrylate) (hydroxyethyl methacrylate), P(MMA)(HEMA) (49:51) (5) [223]

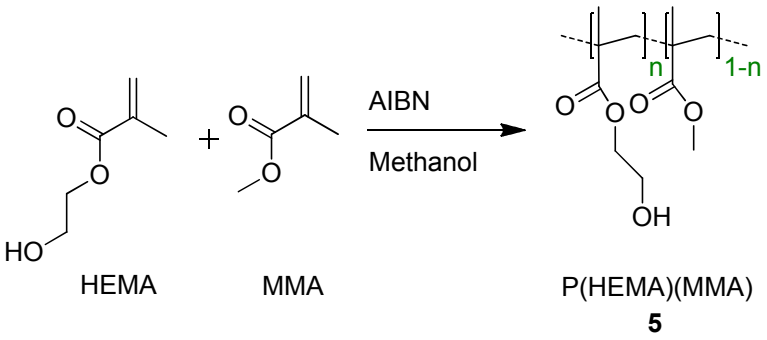

A mixture of methyl methacrylate (MMA, 0.89 mL, 8.3 mmol) and hydroxyethyl methacrylate (HEMA, 0.94 mL, 7.5 mmol) was dissolved in methanol (6.0 mL) and stirred under a slow stream of nitrogen at 60 ºC for 30 minutes prior to the addition of azobisisobutyronitrile (AIBN, 0.05 g, 0.316 mmol). The reaction was then stirred overnight before heating at 60 ºC for 24 hours. The viscous solution was poured into diethyl ether (200 mL) to yield a white precipitate. The cloudy solution was centrifuged before decanting the eluent. The solid was dissolved in methanol and precipitated from diethyl ether a further two times, before the white solid was dried under vacuum (**5**, 1.59 g, 88 %).

^{1}H NMR (MeOD, δ/ppm): 0.92 and 1.10 (br.s., 6H, -CH_3), 1.96 (br.s., 4H, -CH_2) 3.65 (br.s., 3H, -OCH_3) 3.80 and 4.07 (br.s., 2H, -CH_2CH_2-).

^{13}C NMR (DMSO-d_6, δ/ppm): 16.2 (CH_3), 18.5 (CH_3), 44.0 (Cα), 44.3 (Cα), 51.6 (OCH_3), 53.6 ($C\beta H_2$), 58.5 (CH_2OH), 66.3 (OCH_2), 176.3 (C(O)), 177.3 (C(O)).

IR: ν/cm^{-1} 3500 (broad, O-H), 2991 (C-H), 2948 (C-H), 1716 (C=O).

UV-vis (MeOH, λ_{max}/nm) 215.

GPC (expressed as 'PMMA equivalent' molecular weight recorded in N,N'-dimethylacetamide with 0.01 M lithium bromide) M_w: 190,500, M_N: 65,200 with a calculated polydispersity of 2.9.

This is consistent with reported data [223].

12.3.12 Poly(methyl methacrylate) (hydroxyethyl methacrylate) (4-(4-methoxyphenyl) azophenoxyacetylethyl methacrylate), P(MMA)(HEMA)(Azo-HEMA) (49:46:5) (6)

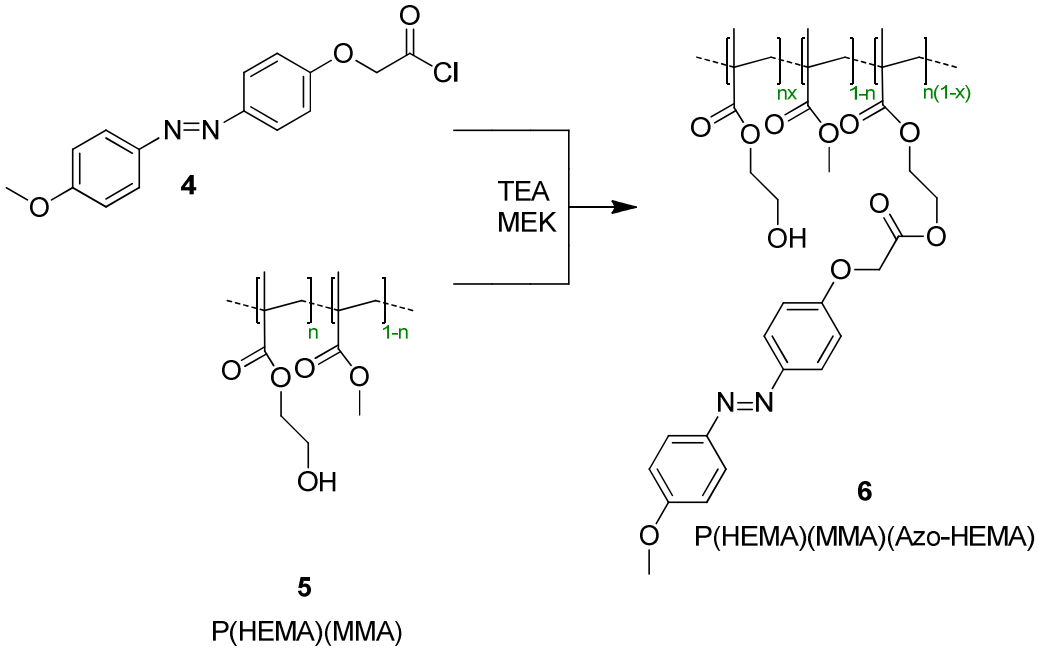

P(MMA)(HEMA) (**5**, 1.00 g, 7.72 mmol of HEMA) was dissolved in 2-butanone (12.0 mL) under a slow stream of nitrogen and triethylamine (TEA, 1.89 mL. 14 mmol) was then added to give a colourless solution. 4-(4-Methoxyphenyl)azophenoxyacetyl chloride (**4**, 0.40 g, 1.4 mmol) was dissolved in 2-butanone (4.0 mL) to give an orange solution and this was then added to the stirred polymer solution, instantaneously forming an orange precipitate. After stirring for 36 hours the viscous solution was poured into diethyl ether (150 mL) to yield a caramel precipitate. This was centrifuged and decanted before trituration in water (50 mL) to leave an orange solid. This was dissolved in 2-butanone (150 mL), centrifuged and precipitated from diethyl ether a further two times. The resultant orange solid was dried under vacuum (**6**, 0.84 g, 62 %).

^{1}H NMR (DMSO-d_6, δ/ppm): 0.76 and 0.90 (br.s., 4.26H, -CH_3), 1.78 (br.s., 1.98H, -CH_2) 3.53 (br.s., 3.0H, -OCH_3, -CH_2CH_2-) 3.90 (br.s., 1.30H, -CH_2CH_2-), 4.80 (br.s., 0.54H, -OH) 7.12 (br.s., 0.25H, Ar-H) 7.85 (br.s., 0.25H, Ar-H).

^{13}C NMR (DMSO-d_6, δ/ppm): 16.21 (CH_3), 18.3 (CH_3), 44.0 (Cα), 44.3 (Cα), 51.6 (OCH_3), 53.5 ($C\beta H_2$), 55.6 ((Azo) OCH_3), 58.5

(CH_2OH), 66.3 (OCH_2), 114.5 ((Azo) Ar), 115.1 ((Azo) Ar), 124.0 ((Azo) Ar), 124.2 ((Azo) Ar), 161.6 ((Azo) C(O)), 176.3 (C(O)), 177.0 (C(O)).

IR (ν/cm^{-1}): 3500 (broad, O-H), 2992 (C-H), 2949 (C-H), 1718 (C=O), 1598 (C=C).

UV-vis (2-butanone, λ_{max}/nm): 356, 447.

GPC (expressed as 'PMMA equivalent' molecular weight recorded in N,N'-dimethylacetamide with 0.01 M lithium bromide) M_w: 301,500, M_N: 90,850 with a calculated polydispersity of 3.3.

For deposition of a sub-micron film of **6** onto a surface, a 100 μL solution of this polymer (32.5 mg / mL in 2-butanone) was spun at 1800 rpm for 40 s.

No comparative spectroscopic literature was found.

12.3.13 Poly(dimethylsiloxane) ((3-aminopropyl)methylsiloxane) ((4-(4-methoxyphenyl) azophenoxyacetamidopropyl)methylsiloxane), (50:45:5) (7)

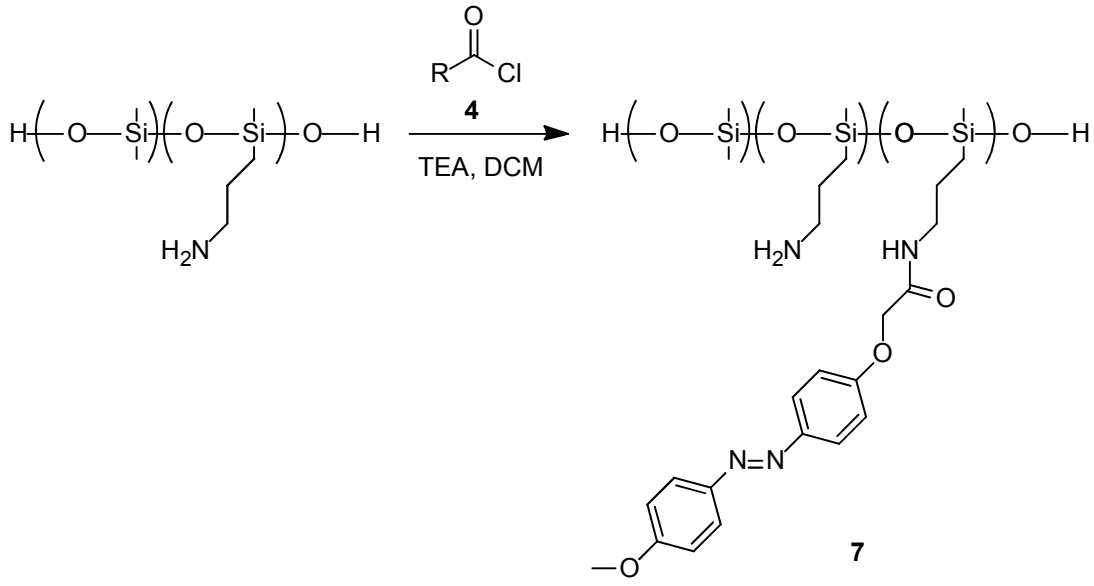

4-(4-Methoxyphenyl)azophenoxyacetyl chloride (**4**, 0.30 g, 1.1 mmol) was dissolved in distilled dichloromethane, giving a red solution. To this solution poly(dimethylsilane)((3-aminopropyl)methylsilane) (0.83 g, ~ 4mmol amine sites) and triethylamine (0.90 mL, 6.5 mmol) were added and the mixture was left to stir overnight. The organic mixture was washed with water (100 mL). The resultant

organic layer was dried with magnesium sulphate and the solvent removed *in vacuo* to give a yellow solid (0.22 g). This solid was redissolved in ethanol, followed by the addition of light petroleum (40-60) until precipitation occurred (**7**, 0.08 g, 6 %)

^{1}H NMR (MeOD-d_4, δ/ppm): 0.00 (br.s, 86H, Si-CH_3) 6.90 (d, *J*=4.3 Hz, 4H, Ar-H) 7.75 (d, *J*=4.0 Hz, 4H, Ar-H).

Other peaks could not be isolated due to the polymeric nature of the compound, however these key peaks allowed the amount of functionalisation to be estimated.

IR (ν/cm^{-1}): 3500 (broad, N-H), 2958 (C-H), 2908 (C-H), 1724 (C=O), 1605 (C=C), 1577 (C=C), 1254 (C-O), 1001 (C-O).

UV-vis (2-butanone, λ_{max}/nm): 353, 444.

No comparative spectroscopic literature was found.

12.3.14 4-Methoxybenzoyl chloride (8)

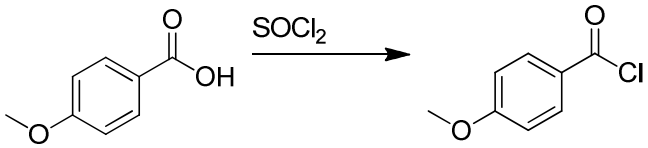

8

4-Methoxybenzoic acid (0.152 g, 1.0 mmol) was refluxed in thionyl chloride (5 mL, 68.5 mmol) overnight under nitrogen. The remaining thionyl chloride was removed by distillation under vacuum (50 °C), before drying the colourless liquid (**8**) under vacuum (assumed quantitative yield and used immediately without further purification).

MP: liquid (Lit [325]: 22 °C).

MS (ES$^+$, MeOH, m/z): 167.2 (8.3 %, $[N+H]^+$), 199.1 (7.1 %, $[N+H+MeOH]^+$), 205.1 (6.3 % $[N+K]^+$), 221.2 (2.6 %, $[N+Na+MeOH]^+$), 387.2 (8.5 %, $[2N+Na+MeOH]^+$).

MS (ES$^-$, MeOH, m/z): 165.0 (6.9 %, $[N-H]^-$).

Where N represents the molecular ion for methyl (4-methoxybenoate) formed from the reaction of 4-methoxbenzoyl chloride with the methanol MS solvent. The

formation of the methyl ester was not seen with samples of 4-methoxybenzoic acid and so this can be used as an indicator for successful synthesis of **8**.

12.3.15 4-Acetyl-4'-methoxydiphenyl (9)

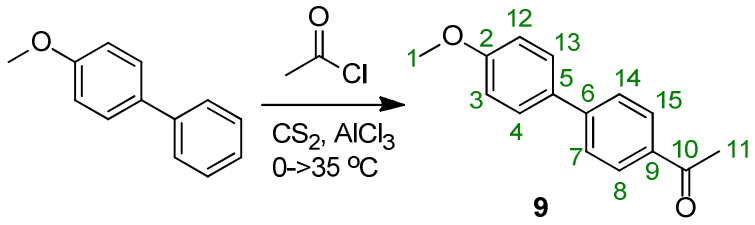

9

4-Methoxybiphenyl (2.00 g, 10.9 mmol) was dissolved in carbon disulphide (silica dried, 20 mL) under an inert atmosphere. Aluminium chloride (1.70 g, 12.8 mmol) was added below 5 °C, followed by acetyl chloride (1.00 mL, 14.0 mmol) over 10 minutes. The reaction mixture was slowly warmed to 35 °C and was then stirred for an hour, before heating to reflux for a further 30 minutes. The mixture was cooled and ice-cold hydrochloric acid (conc., 1.0 mL) was added dropwise to decompose the yellow-green complex. Steam was passed under the surface of the solution to remove the solvent and to complete the decomposition until a cream precipitate was formed. This was extracted into dichloromethane (3 x 50 mL), the combined organic extracts were dried with magnesium sulphate and the solvent removed under reduced pressure to give a cream solid. Trituration under ice of the solid with diethyl ether (2 x 15 mL) yielded an off-white solid that upon crystallisation from isopropanol formed plate-like crystals (**9**, 0.92 g, 37 %)

MP: 150 – 152 ^{O}C (Lit [326]: 152 ^{O}C)

^{1}H NMR ($CDCl_3$, δ/ppm): 2.63 (s, 3H, H_{11}), 3.87 (s, 3H, H_1), 7.01 (d, J = 8.8 Hz, 2H, H_3), 7.59 (d, J=9.0 Hz, 2H, H_4), 7.65 (d, J=8.5 Hz, 2H, H_7), 8.01 (d, J=8.5 Hz, 2H, H_8).

^{13}C NMR ($CDCl_3$, δ/ppm): 26.58 (C_{11}), 55.4 (C_1), 114.4 (C_3) 126.6 (C_8) 128.3 (C_4) 128.9 (C_7) 132.2 (C_5) 135.3 (C_9) 145.3 (C_6) 159.9 (C_2) 197.7 (C_{10}).

IR (ν/cm^{-1}): 3038 (C-H aromatic), 2959 (C-H), 1672 (C=O), 1577, 1596 (C=C aromatic), 1031 (C-O).

MS (ES^+, MeOH, m/z): 227.2 (3.1 %, $[M+H]^+$), 249.2 (72.0 %, $[M+Na]^+$), 281.2 (100.0 %, $[M+Na+MeOH]^+$), 475.4 (34.8 % $[2M+Na]^+$).

This is consistent with reported spectroscopic data [326].

12.3.16 4-Methoxydiphenyl-4'-carboxylic acid (10)

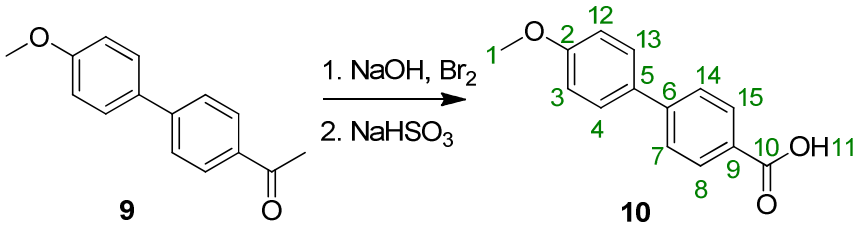

A sodium hypobromite solution was prepared by addition of bromine (0.25 mL, 4.83 mmol) to an aqueous solution of sodium hydroxide (5.0 mL, 3.8 M) below 5 °C.

This was added slowly to a solution of 4-acetyl-4'-methoxydiphenyl (**9**, 0.25 g) in dioxane (25 mL). The solution was warmed to room temperature before leaving to react for a further hour. Subsequent treatment with sodium bisulphite (0.38 g, 3.73 mmol), followed by hydrochloric acid (conc., <5 mL) precipitated a white solid. This was extracted into diethyl ether (3 x 70 mL), the solution was dried with magnesium sulphate and the solvent was removed under reduced pressure. Crystallisation from a mixture of diethyl ether and light petroleum (60 – 80) yielded colourless crystals (**10**, 0.18 g, 72 %).

MP: 239 – 240 ^{O}C (Lit [327]: 248 – 249 ^{O}C)

^{1}H NMR (DMSO-d_6, δ/ppm): 3.81 (s, 3H, H_1), 7.04 (d, J = 8.8 Hz, 2H, H_3), 7.68 (d, J=8.8 Hz, 2H, H_4), 7.73 (d, J=8.5 Hz, 2H, H_7), 7.98 (d, J=8.5 Hz, 2H, H_8), 12.81 (br. s., 1H, H_{11}).

^{13}C NMR (DMSO-d_6, δ/ppm):55.2 (C_1), 114.5 (C_3), 126.0 (C_7), 128.1 (C_4), 128.9 (C_9), 129.9 (C_8), 131.2 (C_5), 143.9 (C_6), 159.5 (C_2), 167.2 (C_{10}).

IR (ν/cm^{-1}): 3065 (C-H aromatic), 2953 (C-H), 2670 (broad, O-H), 1674 (C=O), 1599 (C=C aromatic), 1033 (C-O).

MS (ES^+, MeOH, m/z): 229.3 (19.3 %, $[M+H]^+$), 251.2 (36.7 %, $[M+Na]^+$), 261.3 (30.6 % $[M+H+MeOH]^+$), 267.3 (11.8 %, $[M+K]^+$), 283.3 (11.8 %, $[M+Na+MeOH]^+$), 299.3 (5.7 %, $[M+K+MeOH]^+$), 457.4 (6.2 %, $[2M+H]^+$), 479.4 (34.4 %, $[2M+Na]^+$).

MS (ES^-, MeOH, m/z): 227.2 (100.0 %, $[M-H]^-$),

This is consistent with reported spectroscopic data [328].

12.3.17 4-Methoxydiphenyl-4'-carbonyl chloride (11)

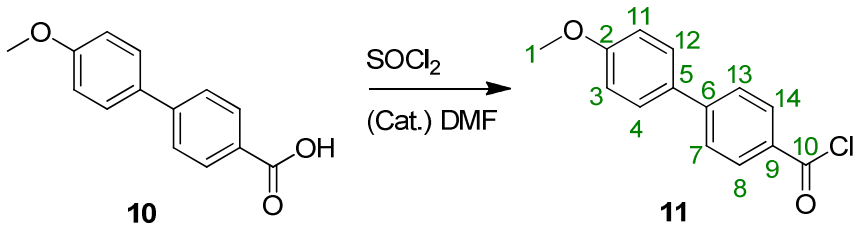

4-Methoxydiphenyl-4'-carboxylic acid (**10**, 0.099 g, 0.44 mmol) was refluxed in thionyl chloride (10 mL, 137 mmol) overnight under nitrogen, in the presence of several drops of catalytic dimethylformamide. The remaining thionyl chloride was removed by distillation under vacuum (50 °C), before drying the pale pink solid (**11**) under vacuum (assumed quantitative yield and used immediately without further purification).

MP: 94 – 96°C (Lit [329]: 100 °C).

MS (ES^+, MeOH, m/z): 243.2 (14.7 %, $[N+H]^+$), 265.2 (48.2 %, $[N+Na]^+$), 281.2 (9.2 % $[N+K]^+$), 297.2 (100.0 %, $[N+Na+MeOH]^+$), 507.3 (60.2 %, $[2N+Na]^+$).

Where N represents the molecular ion for methyl (4-methoxydiphenyl-4'-carboxylate) formed from the reaction of 4-methoxydiphenyl-4'-carbonyl chloride, **10**, with the methanol MS solvent. The formation of the methyl ester was not seen with samples of 4-Methoxydiphenyl-4'-carboxylic acid and its presence can be used as an indicator for successful synthesis of **11**.

12.3.18 4'-Acetylbenzo-15-crown-5 (12) [298, 299]

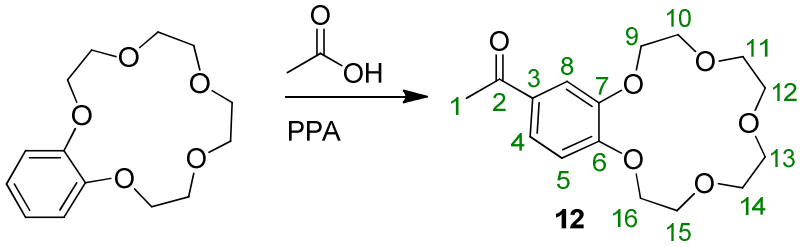

Benzo-15-crown-5 (0.27 g, 1.00 mmol) was dissolved in polyphosphoric acid (6.0 mL) followed by dropwise addition of acetic acid (0.10 mL, 1.75 mmol), this was heated for 1.5 hours at 60 ^{O}C. Once complete, the polyphosphoric acid was quenched with water (30 mL) after which the product was extracted into chloroform (3x40 mL), the combined extracts were dried and the solvent was removed *in vacuo* to give a white solid (**12**) (0.32 g, >99 %).

MP: 93 – 94 ^{O}C (Lit [298]: 94-95 ^{O}C).

^{1}H NMR ($CDCl_3$): 2.55 (s, 3H, H_1), 3.77 (d, *J*=2.8 Hz, 8H, H_{11-14}), 3.93 (ddd, *J*=8.4, 4.4, 4.3 Hz, 4H, $H_{10,15}$), 4.20 (dd, *J*=4.4, 3.1 Hz, 4H, $H_{9,16}$), 6.86 (d, *J*=8.3 Hz, 1H, H_5), 7.51 (d, *J*=2.0 Hz, 1H, H_8), 7.56 (dd, *J*=8.5, 2.0 Hz, 1H, H_4).

^{13}C NMR ($CDCl_3$): 26.2 (C_1), 68.7 – 69.4 (C_{11-14}), 70.4 (C_{15}), 70.4 (C_{10}), 71.2 ($C_{9,16}$), 111.8 (C_8), 112.8 (C_5), 123.5 (C_4), 130.7 (C_3), 148.8 (C_7), 153.5 (C_6), 196.7 (C_2).

IR (ν/cm^{-1}): 2962 (C-H aromatic), 2906, 2858 (C-H alkyl), 1666 (C=O), 1593, 1582 (C=C aromatic), 1012 (C-O).

MS (ES$^+$, MeCN, m/z): 311 (5.5 %, $[M+H]^+$), 328 (8.2 %, $[M+NH_4]^+$), 333 (100.0 %, $[M+Na]^+$), 349 (2.4 %, $[M+K]^+$).

This is consistent with the reported data [298].

12.3.19 4'-Carboxybenzo-15-crown-5 (13) [298, 300]

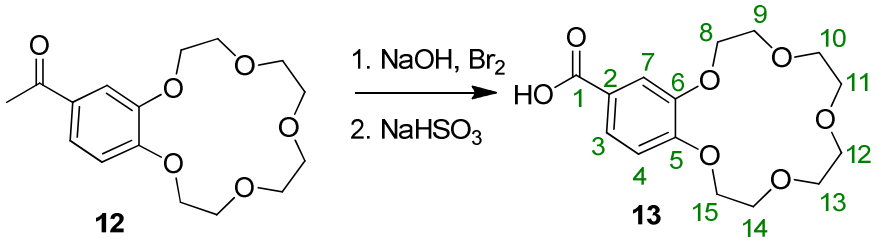

To a stirred solution of sodium hydroxide (2.65 g, 66.3 mmol) in water (19 mL) maintained below 10 ^{O}C, bromine (0.20 mL, 3.90 mmol) was added dropwise. 4'-Acetylbenzo-15-crown-5 (**12**, 0.29 g, 0.919 mmol) was then added with vigorous stirring. After 4 hours, sodium bisulphite (1.12 g, 9.33 mmol) was added to quench the reaction mixture which resulted in immediate decolourisation. The reaction mixture was filtered, washed with chloroform (3 x 25 mL) and acidified to pH 3 (conc. HCl, <8 mL). The aqueous mixture was subsequently extracted with dichloromethane (3 x 25 mL). The combined extracts were dried with magnesium sulphate and the solvent was removed *in vacuo* to give a white solid (**2**) which was crystallised from ethanol (**13**, 0.27 g, 94 %).

MP: 185.0 – 185.5 ^{O}C (Lit [298]: 185-186 ^{O}C).

^{1}H NMR ($CDCl_3$): 3.62 (s, 8H, $H_{10\text{-}13}$), 3.69 - 3.86 (m, 4H, $H_{9,14}$), 4.09 (ddd, *J*=9.0, 4.4, 4Hz, 4H, $H_{8,15}$), 7.02 (d, *J*=8.6 Hz, 1H, H_4), 7.43 (d, *J*=2.0 Hz, 1H, H_7), 7.55 (dd, *J*=8.4, 1.8 Hz, 1H, H_3), 12.68 (br. s., 1H, H_{acid}).

^{13}C NMR ($CDCl_3$): 68.3 – 68.8 ($C_{10\text{-}13}$), 69.6 (C_{14}), 69.7 (C_9), 70.5 – 70.6 ($C_{8,15}$), 112.3 (C_4), 113.8 (C_7), 123.1 (C_3), 123.4 (C_2), 147.9 (C_6), 152.4 (C_5), 167.0 (C_1).

IR (ν/cm^{-1}): 2930 (C-H aromatic), 2854 (C-H alkyl), 16681 (C=O), 1587, 1582 (C=C aromatic), 1053 (C-O).

MS (ES^+, MeOH, m/z): 330 (3.9 %, $[M+NH_4]^+$), 335 (100.0 %, $[M+Na]^+$), 349 (1.3 %, $[M+K]^+$).

MS (ES^-, MeOH, m/z): 311 (100.0 %, $[M-H]^-$).

This is consistent with the reported data [298].

12.3.20 4'-(Chlorocarbonyl)benzo-15-crown-5 (14) [301]

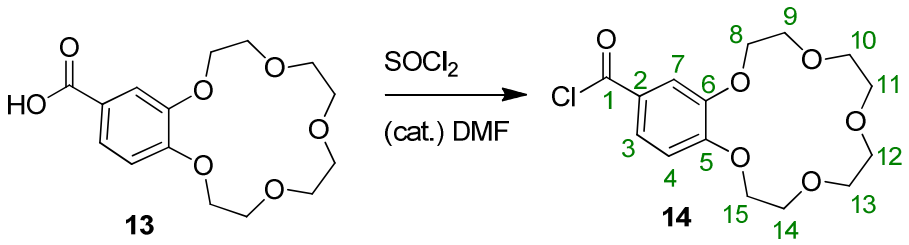

4'-Carboxybenzo-15-crown-5 (**13**, 0.0512 g, 0.164 mmol) was refluxed in thionyl chloride (5.0 mL, 68.5 mmol) containing several drops of catalytic dimethylformamide for 24 hours under nitrogen. The remaining thionyl chloride was removed by distillation under vacuum (50 °C), before drying the cream residue (**14**) (assumed quantitative conversion and the product was used immediately without further purification).

MS (ES^+, MeCN, m/z): 331 (51.3 %, $[M+H]^+$), 353 (6.5 %, $[M+Na]^+$), 369 (1.6 %, $[M+K]^+$).

MS (ES^+, MeOH, m/z): 331 (7.5 %, $[M+H]^+$), 330 (3.9 %, $[M+NH_4]^+$), 353 (4.6 %, $[M+Na]^+$), 369 (3.1 %, $[M+K]^+$).

335 (51.1 %, $[N+Na]^+$), 349 (18.4 %, $[N+K]^+$).

MS (ES^-, MeOH, m/z): 311 (61.9 %, $[N-H]^-$, not seen in MeCN ES^- samples).

N represents the molecular ion for 4'-carboxybenzo-15-crown-5 (1**3**). While mass spectrometry samples in acetonitrile shows only the acid chloride, those collected in methanol show decomposition back to the carboxylic acid. The methyl ester was not detected.

12.4 Surface Functionalisation

Early attempts at surface functionalisation were carried out *in situ* adapting traditional laboratory techniques. Exposure of the surfaces of interest to the atmosphere was minimised to avoid contamination, with samples being used immediately or stored under the appropriate distilled solvent. Physical contact with the surface was assumed to destroy any functionalisation present, with the sample cleaned and the procedure of functionalisation repeated. While it was shown with

the fluorescein functionalised surfaces that the chemistry was much more robust than this would imply, this ensured reproducibility between samples.

12.4.1 (3-Aminopropyl)silane functionalised surface (15) [266]

Two distinct methods were used to functionalise the surface with (3-aminopropyl)triethoxysilane. The first, Method A, was found to cause polymerisation of the silane in some circumstances, leading to the development of Method B. Method B was later adapted for use within the microfluidic flow cell, to give Method C.

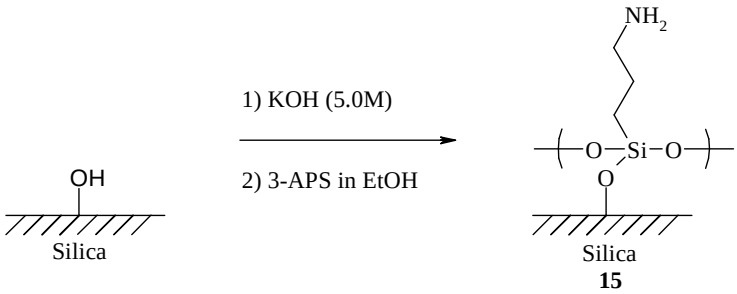

15

Method A:

A solution of (3-aminopropyl)triethoxysilane (0.10 mL) in a water/ethanol (10/90 v/v, 20 mL) solution was left to hydrolyse for 2 hours. The silica sample was cleaned in an aqueous solution of potassium hydroxide (2.5 M) for 20 minutes; after which it was washed with copious amounts of water.

The silica sample was immersed in the solution of (3-aminopropyl)triethoxysilane for 5 minutes. The surface was then washed with copious methanol and water.

Method B:

The silica sample was cleaned by sequential sonication for 20 minutes per step, in:

i. deionised water
ii. 50 % acetone / 50 % deionised water
iii. acetone
iv. 50 % acetone / 50 % deionised water
v. deionised water

(Tantalum pentoxide at this stage required washing in piranha solution for 30 minutes).

The sample was transferred to an aqueous solution of potassium hydroxide (5.0 M) for 3 hours; after which it was washed with copious amounts of water. The sample was rinsed in water (3x) and then in distilled ethanol (3x).

The silica sample was removed from ethanol, dried under nitrogen and immersed in a solution of (3-aminopropyl)triethoxysilane in ethanol (10 %v/v) for 16 hours. The surface was then washed with copious ethanol and water (as above).

Contact angle 53 ± 4 ° (Lit [275]: 52 ± 2 °)

Method C:

Within the microfluidic flow cell each individual step can be concatenated into a automated recipe that will be applied sequentially to the surface. The typical recipe used to clean and functionalise the surface was derived from Method B, as follows:

i.	deionised water	-	30 minutes
ii.	acetone	-	30 minutes
iii.	deionised water	-	30 minutes
iv.	potassium hydroxide (5.0 M)	-	60 minutes
v.	deionised water	-	20 minutes
vi.	methanol/ethanol	-	80 minutes
vii.	10 % 3-APS in methanol/ethanol	-	720 minutes
viii.	methanol/ethanol	-	80 minutes

Methanol or ethanol could be equally used, with the solvent choice dependent on the dynamic range of the Bragg sensor. The two alcohol washes allowed for the change in the effective index to be calculated, allowing the success of the surface functionalisation to be ascertained.

12.4.2 Gold functionalised surface [207, 273]

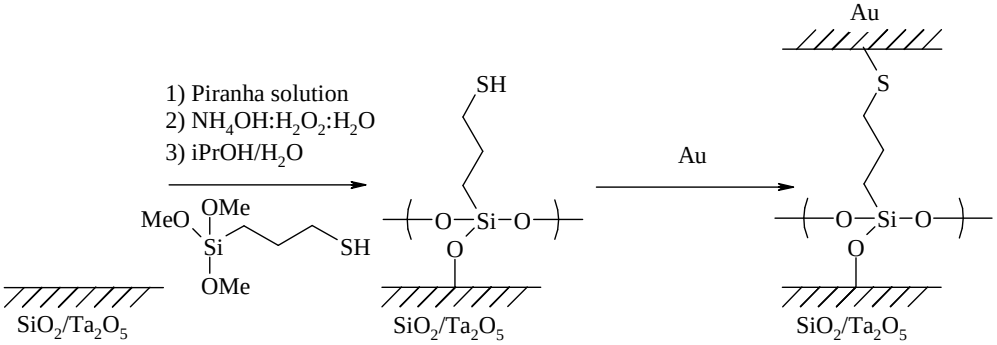

The sample surface was cleaned in "piranha solution" (4 mL) for 15 minutes after which it was rinsed in water and transferred to a solution of NH_4OH:H_2O_2:H_2O (1:1:4, 3 mL) for a further 15 minutes. The sample was then thoroughly washed with water.

(3-Mercaptopropyl)trimethoxysilane (5 mL) was refluxed in a mixture of isopropanol and water (40:1, 205 mL). Into this mixture was suspended the freshly cleaned surface for 10 minutes, after which it was removed, rinsed with isopropanol and baked for 10 minutes at ~100 °C. This procedure was repeated a further two times before the surface was finally cleaned vigorously with isopropanol.

Gold was deposited onto the functionalised surface to a depth of 50 nm. Adhesion was tested using cellulose tape:

Adhesion:	Silica	– 100 %	(bare silica – 0 %)
	Tantalum pentoxide	– 100 %	

12.4.3 A generic approach to a functionalised surface [207]

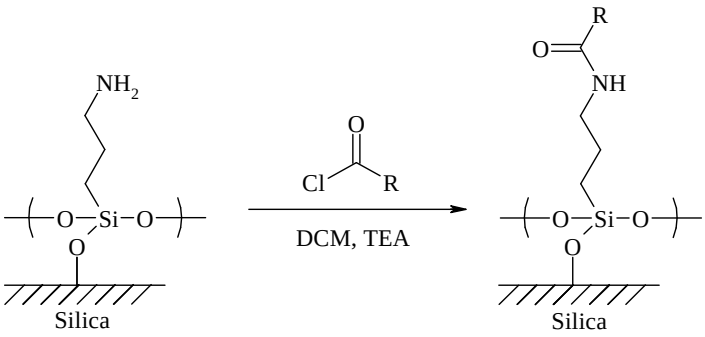

15

Bench-top (glass slide):

An excess of the desired acid chloride was dissolved in dichloromethane (20 mL). The pre-aminated silica sample (**14**) was immersed in the solution after which triethylamine (1 equiv.) was added and the sample left to react overnight. The success of the surface functionalisation was interrogated by changes in the contact angle with water droplets (1.0 μL).

Microfluidic (Bragg sensor):

An excess of the desired acid chloride (~ 50 mg) was dissolved in either dichloromethane or methylethylketone (80 mL), to this was added triethylamine (<0.01 mL).

The pre-aminated surface (**15**), mounted within the microfluidic flow cell was then sequentially exposed to the following solutions:

i. methanol/ethanol - 80 minutes
ii. acid chloride solution - 720 minutes
iii. methanol/ethanol - 80 minutes

The success of the surface functionalisation was interrogated by the change in the Bragg wavelength between the two alcohol steps.

12.5 Fabrication and Characterisation of a Bragg Grating Sensor

While the optical fabrication and characterisation processes have been detailed in Chapters 3 and 5, a brief overview is included below, focusing upon the experimental procedure rather than the underlying photonics.

12.5.1 UV written planar waveguides

6” wafers were fabricated by flame hydrolysis deposition (FHD) by the Centre for Integrated Photonics (CIP, Ipswich) with this wafer diced into practical sizes ready for use, with typical dimensions of 10 x 20 mm or 10 x 40 mm.

Prior to UV writing, the diced wafer was hydrogen loaded to enhance the available photosensitivity. This was achieved through storing the samples within a ≥120 bar hydrogen atmosphere at room temperature, for a minimum of three days. Upon removal from the hydrogen cell, samples were stored in liquid nitrogen to prevent out diffusion prior to the UV writing process.

The desired pattern of waveguides and Bragg gratings were written into the core of the silica-on-silicon wafer by controlling the modulation of a pair of focussed, interfering UV beams. This process was fully automated with the pattern and pulsing of the lasers determined by prewritten ‘G-code’. The UV power applied was determined by the maximum stable laser power output that could be achieved,

typically 48-59 mW. The required fluence (20 kJ cm^{-2}) was then controlled using the sample translation speed through the G-code.

12.5.2 Characterisation set-up

The Bragg gratings are monitored during etching, reaction and further experiments using the following set-up:

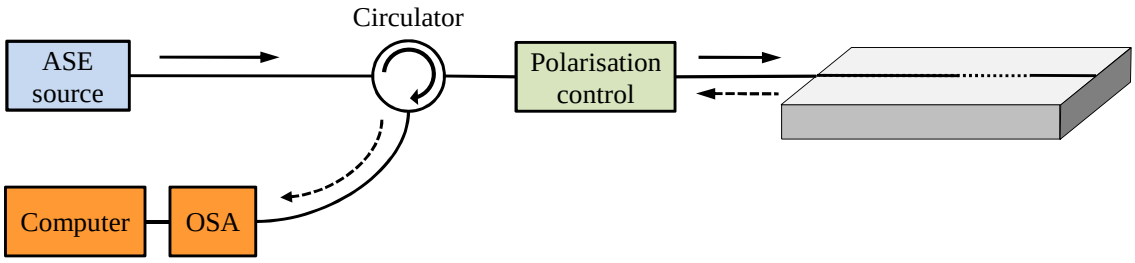

Fig. 12.1 Schematic of the optical characterisation set-up using standard telecomm analysis equipment.

A broadband ASE (amplified stimulated emission) source was used to analyse the sensor. This was linked by fibre to a polarisation maintaining (PM) polariser. The PM polariser was used to polarise the input light to an orientation aligned to one of the principle axes of the PM fibre with a suppression orthogonal polarisation mode of 30 dB (1000:1). From this point the signal is transmitted through PM fibre, minimising changes in polarisation from movement of the fibre during measurements. This is necessary as the peak wavelength of the transverse magnetic (TM) and transverse electric (TE) modes are different and any switch between will produce an anomalous shift in the sensor output. For the purposes of these experiments the TE mode typically was selected as this has been shown through modelling to have a higher sensitivity in the presence of a high-index overlayer. The circulator allows the reflected signal to be directed to the optical spectrum analyser (OSA) which was controlled remotely, via a PC running Labview.

12.5.3 "Pigtailing" a planar waveguide

Each device typically contained several copies of the desired waveguide for redundancy. This allowed for any defects in the substrate to be avoided or for waveguide properties to be varied to optimise the device to the desired application, these typically could include the fluence of the laser, Bragg wavelength or grating length. The spectrum for each waveguide on the device was acquired and the

waveguide that exhibited the best Bragg peak resolution and intensity was selected. The best waveguide was then selected for subsequent “pigtailing”.

A “pigtail” in this context, is a length of single mode fibre optic cable with an optical connector on one end (FC), while the other is bare fibre. The bare end is pre-mounted into a silicon V-groove with comparable dimensions to the silicon substrate. This increased surface area allows the pigtail to be bonded to the edge of the device. The optical fibre was aligned with the end of the waveguide with a visible He-Ne laser, before maximising the detected output with the ASE source and OSA, the joint was made permanent by gluing with index matching, UV-curing optical grade glue Dymax Ultra Light-Weld High T_g Optical Adhesive: OP-4-20632 (n = 1.55) and reinforcing with Dymax OP-60LS. Further reinforcement was achieved through encasing the fibre and pigtail in a short piece of heat-shrinkable PTFE tube.

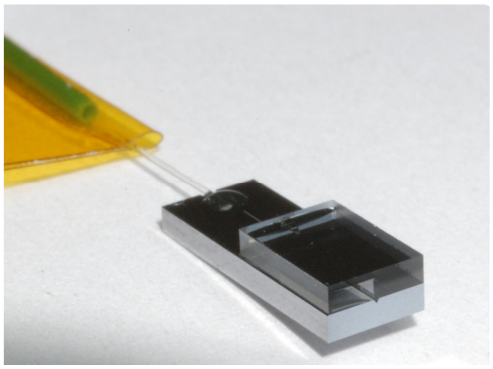

Fig. 12.2 A polarisation maintaining pigtail, showing the optical fibre with the silicon v-groove.

12.5.4 Etching a well into the optical device

The region to be etched was located above the sensor grating. This area was covered with a mask fabricated from an adhesive polyimide tape, exposing only the etched region. The end facet of the device was protected with a thin layer of the Dymax glue used to attach the pigtail.

The etch solution (conc.HF/conc.HCl/H_2O, 4/3/9 v/v, 8 mL) was prepared; the peak Bragg wavelengths of the pigtailed, masked sample were monitored in real time during emersion in the etch solution for ~18 minutes. When the sensor peak wavelength had shifted by 1 – 1.2 nm, the device was immediately washed with copious amount of deionised water and dried. This shift has been refined to

correspond to etching down to the core layer without significant loss of signal (~18 µm).

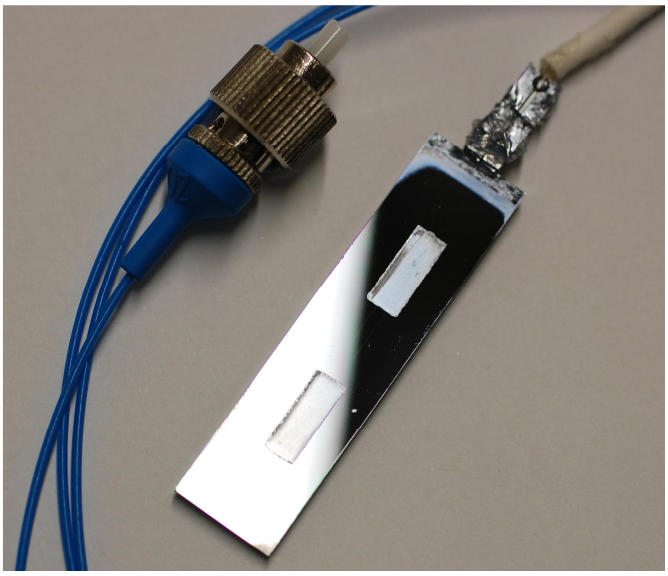

Fig. 12.3 A pigtailed Bragg grating sensor with two etched wells ready to be polished.

12.5.5 Polishing the well surface

The surface of the etched well was polished with a felt-ended handheld commercial polisher (Dremel 400 series digital rotary tool) with an alkali, colloidal silica solution (SF1) for 20 – 30 seconds. This was instantly washed with copious amounts of deionised water and dried. The process was repeated until the surface quality was sufficient.

12.5.6 Tantalum pentoxide overlayer

Tantalum pentoxide (typically 50 nm) was sputtered over the etched region. The pigtail was shielded with an aluminium mask that minimised exposure to just the sensor region. For "topless" wafers, the sample was sputtered without a mask before pigtailing, as a large step increase in overlayer would cause optical loss in the waveguide. Through comparison before and after sputter deposition, it was observed that the Bragg gratings increased in amplitude while the Bragg wavelength shifted to higher wavelength.

12.5.7 Microfluidic flow cell

The first generation flow cell was milled from aluminium, with a Kalrez O-ring, used to seal onto the sensor. This was found to work well, but the aluminium was

prone to etching by strong base. To overcome this a second generation was fabricated out of stainless steel that overcame this limitation.

The microfluidic flow was controlled by either a peristaltic pump (Masterflex C/L dual-channel variable speed pump) for a slow, continuous flow rate or a diaphragm pump (Bio-Chem Fluidics solenoid operated micro-pump, 130SP series) when a faster rate and computer control was required. To select the desired reagent, a PC controlled six-way valve (Cole-Parmer Manifold mixing solenoid valves, 6 inlet 1 outlet) was incorporated into the system. This was fully constructed from inert PTFE, within similar channel cross-sectional area to other components. Finally, to link these microfluidic components together a 400 µm bore ETFE pipe was used (Cole Parmer Chemfluor ETFE tubing, 0.016 x 1/16").

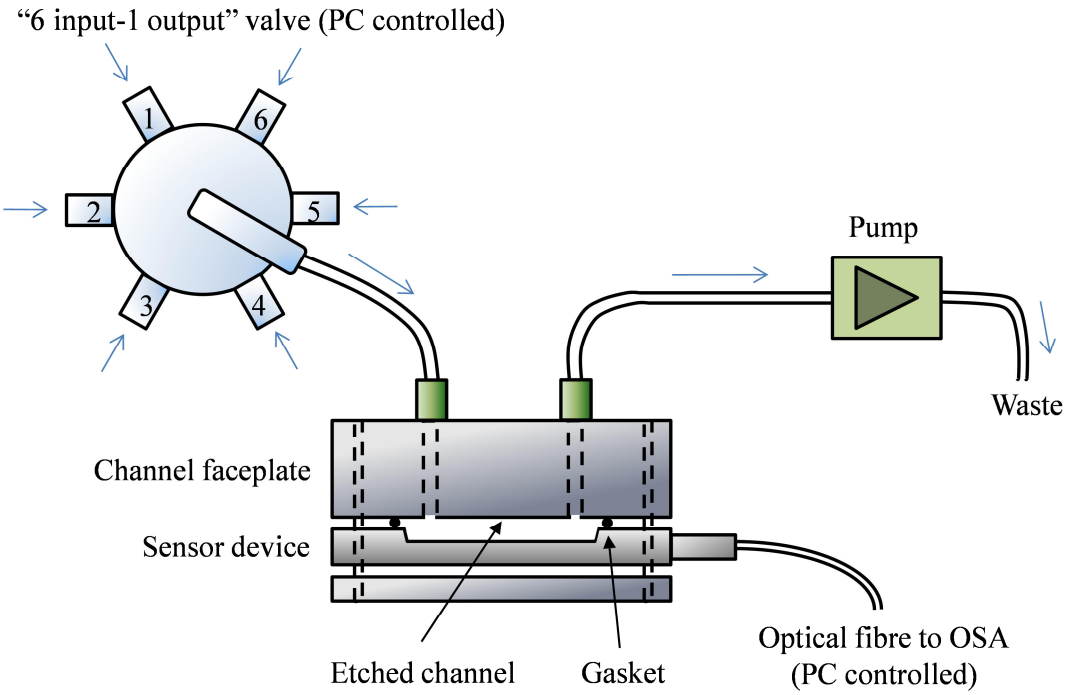

Fig. 12.4 A schematic of the microfluidic sensor network.

Appendix

Mathematical Operators

To aid with the understanding of the mathematical treatment of waveguides as introduced within Chapter 2, the following mathematical operators: "del", "curl" and "divergence" have been defined below. Further details can be found within the "Handbook of Mathematics for Engineers and Scientists" [330].

(i) In vector calculus, "del" is a vector differential operator, usually represented by ∇; it is defined as:

$$\nabla = \frac{\partial}{\partial x}\boldsymbol{i} + \frac{\partial}{\partial y}\boldsymbol{j} + \frac{\partial}{\partial z}\boldsymbol{k} \qquad (1)$$

where (***i,j,k***) are unit vectors in the respective directions (*x y,z*).

(ii) For the vector field "**a**(*x,y,z*) = P***i*** +Q***j*** + R***k***", the curl of **a** is then defined as the vector product of the del operator and the function:

$$curl\ \mathbf{a} = \nabla \text{ x } \mathbf{a}$$
$$\nabla \text{ x } \mathbf{a} = \left(\frac{\partial R}{\partial y} - \frac{\partial Q}{\partial z}\right)\boldsymbol{i} + \left(\frac{\partial P}{\partial z} - \frac{\partial R}{\partial x}\right)\boldsymbol{j} + \left(\frac{\partial Q}{\partial x} - \frac{\partial P}{\partial y}\right)\boldsymbol{k} \qquad (2)$$

which can be expressed as the determinant:

$$\nabla \text{ x } \mathbf{a} = \begin{vmatrix} \boldsymbol{i} & \boldsymbol{j} & \boldsymbol{k} \\ \frac{\partial}{\partial x} & \frac{\partial}{\partial y} & \frac{\partial}{\partial z} \\ P & Q & R \end{vmatrix} \qquad (3)$$

(iii) Similarly, the divergence of the vector field **a**(*x,y,z*) is defined as the scalar product of the del operator and the function:

$$div\ \mathbf{a} = \nabla \,.\, \mathbf{a}$$
$$\nabla . \mathbf{a} = \frac{\partial P}{\partial x} + \frac{\partial Q}{\partial y} + \frac{\partial R}{\partial z} \qquad (4)$$

References

1. *Chemical Sensors Forecasts for 2012 and 2017*. (The Freedonia Group, 2008).
2. S. E. Miller, AT&T Tech. J. **48** (7), 2059-2069 (1969).
3. M. Kawachi, Optical and Quantum Electronics **22** (5), 391-416 (1990).
4. M. Salib, L. Liao, R. Jones, M. Morse, A. Liu, D. Samara-Rubio, D. Alduino and M. Paniccia, Intel Technology Journal **8** (2), 143-160 (2004).
5. J. Aldred, in *The Guardian (online article www.guardian.co.uk)* (London, 2008).
6. S. Sathanur, in *www.telecomasia.net* (2010).
7. M. Broersma, in *eWeek Europe (www.eweekeurope.co.uk)* (2010).
8. G. A. Thomas, B. I. Shraiman, P. F. Glodis and M. J. Stephen, Nature **404** (6775), 262-264 (2000).
9. K. Okamoto, *Fundamentals of Optical Waveguides*, 2nd ed. (Elsevier, 2006).
10. M. G. Xu, L. Reekie, Y. T. Chow and J. P. Dakin, Electron. Lett. **29** (4), 398-399 (1993).
11. S.-M. Lee, K.-C. Ahn and J. S. Sirkis, KSME Int. J. **15** (3), 309-319 (2001).
12. G. Boisde and A. Harmer, *Chemical and biochemical sensing with optical fibers and waveguides*. (Artech House, Boston, 1996).
13. J. R. Casas and P. J. S. Cruz, Journal of Bridge Engineering **8** (6), 362-373 (2003).
14. H.-N. Li, G.-D. Zhou, L. Ren and D.-S. Li, Opt. Eng. **46** (5), 054402 (2007).
15. S.-L. Tsao and C.-P. Peng, Microw. Opt. Techn. Lett. **30** (5), 321-322 (2001).
16. K. Kincade, Laser Focus World **42** (2), 63-67 (2006).
17. C. Nylander, J. Phys. E Sci. Instrum. **18** (9), 736 (1985).
18. W. J. Lough and I. W. Wainer, *High performance liquid chromatography: fundamental principles and practice*. (Springer, 1995).

19. J. W. Jorgenson and K. D. Lukacs, Anal. Chem. **53**, 1298-1302 (1981).
20. R. Lucklum, C. Behling and P. Hauptmann, Anal. Chem. **71** (13), 2488-2496 (1999).
21. F. M. Ch. Battiston, J.-P. Ramseyer, H. P. Lang, M. K. Baller, C. Gerber, J. K. Gimzewski, E. Meyer and H.-J. Guntherodt, Sensor. Actuat. B-Chem. **77** (1-2), 122-131 (2001).
22. E. Bakker and M. Telting-Diaz, Anal. Chem. **74** (12), 2781-2800 (2002).
23. X. T. Zhou, J. Q. Hu, C. P. Li, D. Ma, C. S. Lee and S. T. Lee, Chem. Phys. Lett. **369** (1-2), 220-224 (2003).
24. A. D. Kersey, M. A. Davis, H. J. Patrick, M. LeBlanc, K. P. Koo, C. G. Askins, M. A. Putnam and E. J. Friebele, J. Lightwave Technol. **15** (8), 1442-1463 (1997).
25. P. V. Lambeck, Meas. Sci. Technol. **17** (8), R93-116 (2006).
26. S. Balslev, A. M. Jorgensen, B. Bilenberg, K. B. Mogensen, D. Snakenborg, O. Geschke, J. P. Kutter and A. Kristensen, Lab. Chip. **6** (2), 213-217 (2006).
27. R. Daw and J. Finkelstein, Nature **442** (7101), 367-367 (2006).
28. X. Fan, I. White, S. Shopova, H. Zhu, J. Suter and Y. Sun, Anal. Chim. Acta **620** (1-2), 8-26 (2008).
29. D. Psaltis, S. R. Quake and C. Yang, Nature **442**, 381-386 (2006).
30. R. M. Parker, J. C. Gates, M. C. Grossel and P. G. R. Smith, Sensor. Actuat. B-Chem. **145** (1), 428-432 (2010).
31. R. M. Parker, J. C. Gates, M. C. Grossel and P. G. R. Smith, Appl. Phys. Lett. **95** (17), 173306 (2009).
32. R. M. Parker, J. C. Gates, M. C. Grossel and P. G. R. Smith, Electron. Lett. **46** (5), 358-359 (2010).
33. R. M. Parker, J. C. Gates, H. L. Rogers, P. G. R. Smith and M. C. Grossel, J. Mater. Chem. **20**, 9118-9125 (2010).
34. A. Ghatak and Thyagarajan, *Introduction to fibre optics*. (Cambridge Univeristy Press, 2000).
35. K. Kawano and T. Kitoh, *Introduction to Optical Waveguide Analysis: Solving Maxwell's Equations and Schrodinger Equation*. (John Wiley and Sons, 2001).
36. M. Marz, *Integrated Optics: design and modeling*. (Artech House, 1994).
37. C. Holmes, PhD thesis, Univeristy of Southampton, 2010.

38. I. J. G. Sparrow, PhD thesis, Univeristy of Southampton, 2005.
39. F. Mesa, M. J. Freire, R. Marques and J. D. Baena, Phys. Rev. B **72** (23), 235117 (235116 pages) (2005).
40. V. Lucarini, J. J. Saarinen, K.-E. Peiponen and E. M. Vartiainen, *Kramers-Kronig Relations in Optical Materials Research*. (Springer, 2005).
41. R. P. Feynman, *The Feynman Lectures on Physics*, 2 ed. (Addison Wesley, 2005).
42. M. V. K. Chari and S. J. Salon, *Numerical Methods in Electromagnetism*. (Academic press, New York, 2000).
43. P. Hammond and J. K. Sykulski, *Engineering Electromagnetism: Physical Process and Computation*. (Oxford Univeristy Press, Oxford, 1999).
44. E. Schweig and W. B. Bridges, IEEE T. Microw. Theory **32** (5), 531-541 (1984).
45. K. Bierwirth, N. Schulz and F. Arndt, IEEE T. Microw. Theory **34** (11), 1104-1114 (1986).
46. M. S. Stern, IEE P-Optoelectron. **135** (1), 56-63 (1988).
47. C. Yeh, S. B. Dong and W. Oliver, Pure. Appl. Opt. **46** (5), 2125-2129 (1975).
48. A. S. Sudbo, Pure. Appl. Opt. **2** (3), 211 (1993).
49. A. S. Sudbo, IEEE Photonics Tech. L. **5** (3), 342-344 (1993).
50. C. Kittel, *Introduction to solid state physics*, 8th ed. (Wiley, 2004).
51. S. W. James and R. P. Tatam, Meas. Sci. Technol. **14** (5), R49-R61 (2003).
52. T. Erdogan, J. Lightwave Technol. **15** (8), 1277-1294 (1997).
53. Y. J. Rao, Optics and Lasers in Engineering **31** (4), 297-324 (1999).
54. A. Himeno, K. Kato and T. Miya, IEEE J Sel. Top. Quant. **4** (6), 913-924 (1998).
55. Y. P. Li and C. H. Henry, IEE P-Optoelectron. **143** (5), 263-280 (1996).
56. M. R. Poulsen, P. I. Borel, J. Fage-Pedersen, J. Huebner, M. Kristensen, J. H. Povlsen and K. Rottwitt, Opt. Eng. **42** (10), 2812-2834 (2003).
57. R. A. Soref, P IEEE **81** (12), 1687-1706 (1993).
58. G. D. Emmerson, PhD thesis, University of Southampton, 2003.
59. S. P. Watts, PhD thesis, University of Southampton, 2002.
60. M. Kawachi, M. Yasu and T. Edahiro, Electron. Lett. **19** (15), 583-584 (1983).

61. P. Tandon and H. Boek, J. Non-Cryst. Solids **317** (3), 275-289 (2003).
62. J. C. Gates, Optoelectronics Research Centre, University of Southampton.
63. M. Svalgaard, PhD thesis, Univeristy of Denmark, 1997.
64. R. F. Bunshah, IEEE T. Plasma Sci. **18** (6), 846-854 (1990).
65. G. Grand, J. P. Jadot, S. Denis, S. Valette, A. Fournier and A. M. Grouillet, Electron. Lett. **26** (25), 2135-2137 (1990).
66. C. H. Henry, R. F. Karzarinov, H. J. Lee, K. J. Orlowsky and L. E. Katz, Appl. Optics **26** (13), 2621-2624 (1987).
67. M. V. Bazylenko, M. Gross, P. M. Allen and P. L. Chu, IEEE Photonics Tech. L. **7** (7), 774-776 (1995).
68. K. O. Hill, Y. Fujii, D. C. Johnson and B. S. Kawasaki, Appl. Phys. Lett. **32** (10), 647 (643 pages) (1978).
69. B. S. Kawasaki, K. O. Hill, D. C. Johnson and Y. Fujii, Opt. Lett. **3** (2), 66-68 (1978).
70. D. K. W. Lam and B. K. Garside, Appl. Optics **20** (3), 440-445 (1981).
71. D. P. Hand and P. S. J. Russell, Opt. Lett. **15** (2), 102-104 (1990).
72. G. Meltz, W. W. Morey and W. H. Glenn, Opt. Lett. **14** (15), 823-825 (1989).
73. M. J. Yuen, Appl. Optics **21** (1), 136-140 (1982).
74. R. Kashyap, G. D. Maxwell and D. L. Williams, Appl. Phys. Lett. **62** (3), 214-216 (1993).
75. T. E. Tsai and D. L. Griscom, International Workshop on Photoinduced Self-Organization effects in Optical Fiber 1 **1516**, 14-28 (1991).
76. D. L. Williams, S. T. Davey, R. Kashyap, J. R. Armitage and B. J. Ainslie, Electron. Lett. **28** (4), 369-371 (1992).
77. M. Douay, W. X. Xie, T. Taunay, P. Bernage, P. Niay, P. Cordier, B. Poumellec, L. Dong, J. F. Bayon, H. Poignant and E. Delevaque, J. Lightwave Technol. **15** (8), 1329-1342 (1997).
78. A. Wootton, B. Thomas and P. Harrowell, J. Chem. Phys. **115** (7), 3336-3341 (2001).
79. L. Zheng, J. C. Lambropoulos and A. W. Schmid, J. Non-Cryst. Solids **347** (1-3), 144-152 (2004).
80. P. J. Lemaire, R. M. Atkins, V. Mizrahi and W. A. Reed, Electron. Lett. **29** (13), 1191-1193 (1993).

81. P. J. Lemaire, Opt. Eng. **30** (6), 780-789 (1991).
82. J. Stone, J. Lightwave Technol. **5** (5), 712-733 (1987).
83. M. Svalgaard, Electron. Lett. **35** (21), 1840-1842 (1999).
84. M. Lancry, P. Niay and M. Douay, Opt. Express **13** (11), 4037-4043 (2005).
85. H. Sorensen, J. Canning and M. Kristensen, Opt. Express **13** (7), 2276-2281 (2005).
86. M. Fokine and W. Margulis, Opt. Lett. **25** (5), 302-304 (2000).
87. A. Canagasabey and J. Canning, Opt. Express **11** (13), 1585-1589 (2003).
88. J. Canning, A. Canagasabey and N. Groothoff, in *Microwave and Optoelectronics Conference, IMOC. Proceedings of the 2003 SBMO/IEEE MTT-5 International* (Brazil, 2003), Vol. 2, pp. 973-976.
89. E. A. Chandross, C. A. Pryde, W. J. Tomlinson and H. P. Weber, Appl. Phys. Lett. **24** (2), 72 (73 pages) (1974).
90. M. Svalgaard and M. Kristensen, Electron. Lett. **33** (10), 861-863 (1996).
91. D. O. Kundys, J. C. Gates, S. Dasgupta, C. B. E. Gawith and P. G. R. Smith, IEEE Photonics Tech. L. **21** (13), 947-949 (2009).
92. M. Olivero and M. Svalgaard, Opt. Express **13** (21), 8390-8399 (2005).
93. SU8 is a product of MicroChem Corp., further information may be found at *http://www.microchem.com/products/su_eight.htm*.
94. M. Gnan, H. M. H. Chong and R. M. De La Rue, Proceedings of 12th European Conference on Integrated Optics, Grenoble **FrA1-5**, 310-313 (2005).
95. K. M. Davis, K. Miura, N. Sugimoto and K. Hirao, Opt. Lett. **21** (21), 1729-1731 (1996).
96. G. D. Marshall, M. Ams and M. J. Withford, Opt. Lett. **31** (18), 2690-2691 (2006).
97. S. Nolte, M. Will, J. Burghoff and A. Tuennermann, Appl. Phys. A-Mater. **77** (1), 109-111 (2003).
98. G. D. Emmerson, S. P. Watts, C. B. E. Gawith, V. Albanis, M. Ibsen, R. B. Williams and P. G. R. Smith, Electron. Lett. **38** (24), 1531-1532 (2002).
99. C. B. E. Gawith, G. D. Emmerson, S. G. McMeekin, J. R. Bonar, R. I. Laming, R. B. Williams and P. G. R. Smith, Electron. Lett. **39** (14), 1050-1051 (2003).

100. G. D. Emmerson, C. B. E. Gawith, S. P. Watts, R. B. Williams, P. G. R. Smith, S. G. McMeekin, J. R. Bonar and R. I. Laming, IEE P-Optoelectron. **151** (2), 119-122 (2004).
101. C. R. Giles, J. Lightwave Technol. **15** (8), 1391-1404 (1997).
102. D. W. Lubbers and N. Opitz, Zeitschrift Fur Naturforchung C **30**, 532-533 (1975).
103. O. S. Wolfbeis, Anal. Chem. **80** (12), 4269-4283 (2008).
104. A. Brecht and G. Gauglitz, Biosens. Bioelectron. **10** (9-10), 923-936 (1995).
105. G. Gauglitz, Sensors Update **1** (1), 1-48 (1996).
106. F. Baldini, A. N. Chester, J. Homola and S. Martellucci, *Optical chemical sensors*. (Springer, Dordrecht, 2004).
107. C. McDonagh, C. S. Burke and B. D. MacCraith, Chem. Inform. **39** (18) (2008).
108. P. V. Lambeck, J. van Lith and J. W. M. Hoekstra, Sensor. Actuat. B-Chem. **113** (2), 718-729 (2006).
109. R. G. Heideman and P. V. Lambeck, Sensor. Actuat. B-Chem. **61** (1-3), 100-127 (1999).
110. B. Lee, Optical Fiber Technology **9** (2), 57-79 (2003).
111. J. Homola, S. S. Yee and G. Gauglitz, Sensor. Actuat. B-Chem. **54** (1-2), 3-15 (1999).
112. I. Pockrand, J. D. Swalen, J. G. Gordon II and M. R. Philpott, Surf. Sci. **74** (1), 237-244 (1978).
113. J. G. Gordon II and S. Ernst, Surf. Sci. **101** (1-3), 499-506 (1980).
114. C. Nylander, B. Liedberg and T. Lind, Sensor. Actuator. **3**, 79-88 (1982).
115. B. Liedberg, C. Nylander and I. Lundstrom, Sensor. Actuator. **4**, 299-304 (1983).
116. B. Liedberg, C. Nylander and I. Lundstrom, Biosens. Bioelectron. **10** (8), i-ix (1995).
117. S. A. Maier, *Plasmonics: Fundamentals and Applications*. (Springer, New York, 2007).
118. M. A. Ordal, L. L. Long, R. J. Bell, S. E. Bell, R. R. Bell, R. W. Alexander Jr and C. A. Ward, Appl. Optics **22** (7), 1099-1119 (1983).
119. T. Liebermann and W. Knoll, Colloid. Surface. A. **171** (1), 115-130 (2000).

120. J. Kneipp, H. Kneipp and K. Kneipp, Chem. Soc. Rev **37** (5), 1052-1060 (2008).
121. C. Hubert, L. Billot, P.-M. Adam, R. Bachelot, P. Royer, J. Grand, D. Gindre, K. D. Dorkenoo and A. Fort, Appl. Phys. Lett. **90** (18), 181105 (181103 pages) (2007).
122. A. M. Moran, J. Sung, E. M. Hicks, R. P. van Duyne and K. G. Spears, J. Phys. Chem. B **109** (10), 4501-4506 (2005).
123. H. E. deBrujin, R. P. H. Kooyman and J. Greve, Appl. Optics **31** (4), 440-442 (1992).
124. R. P. H. Kooyman, H. Kolkman, J. van Gent and J. Greve, Anal. Chim. Acta **213**, 35-45 (1988).
125. E. M. Yeatman, Biosens. Bioelectron. **11** (6-7), 635-649 (1996).
126. J. Homola, Sensor. Actuat. B-Chem. **41** (1-3), 207-211 (1997).
127. J. Homola, I. Koudela and S. S. Yee, Sensor. Actuat. B-Chem. **54** (1-2), 16-24 (1999).
128. A. A. Kolomenskii, P. D. Gershon and H. A. Schuessler, Appl. Optics **36** (25), 6539-6547 (1997).
129. T. M. Chinowsky, L. S. Jung and S. S. Yee, Sensor. Actuat. B-Chem. **54** (1-2), 89-97 (1989).
130. N. J. Walker, Science **296**, 557-559 (2002).
131. R. C. Jorgensen and S. S. Yee, Sensor. Actuat. B-Chem. **12** (3), 213-220 (1993).
132. R. C. Jorgensen and S. S. Yee, Sensor. Actuat. A-Phys. **43** (1-3), 44-48 (1994).
133. P. V. Lambeck, Sensor. Actuat. B-Chem. **8** (1), 103-116 (1992).
134. J. Homola, J. Ctyroky, M. Skalsky, J. Hradilova and P. Kolarova, Sensor. Actuat. B-Chem. **39** (1-3), 286-290 (1997).
135. C. R. Lavers and J. S. Wilkinson, Sensor. Actuat. B-Chem. **22** (1), 75-81 (1994).
136. R. D. Harris and J. S. Wilkinson, Sensor. Actuat. B-Chem. **29** (1-3), 261-267 (1995).
137. C. Mouvet, R. D. Harris, C. Maciag, C. Luff, J. S. Wilkinson, J. Piehler, A. Brecht, A. Gauglitz, R. Abuknesha and G. Ismail, Anal. Chim. Acta **338** (1-2), 109-117 (1997).

138. J. Ctyroky, J. Homola and M. Skalsky, Electron. Lett. **33** (14), 1246-1248 (1997).
139. M. N. Weiss, R. Srivastava and H. Groger, Electron. Lett. **32** (9), 842-843 (1996).
140. R. Srivastava, M. N. Weiss, H. Groger, P. Lo and S. F. Luo, Sensor. Actuat. A-Phys. **51** (2-3), 211-217 (1996).
141. E. G. Ruiz, I. Garcez, C. Aldea, M. A. Lopez, J. Mateo, J. Alonso-Chamarro and S. Alegret, Sensor. Actuat. A-Phys. **37-38**, 221-225 (1993).
142. S. Miwa and T. Arakawa, Thin Solid Films **281-282** (1-2), 466-468 (1996).
143. A. Abdelghani, J. M. Chovelon, N. Jaffrezic-Renault, C. Ronot-Trioli, C. Veillas and H. Gagnaire, Sensor. Actuat. B-Chem. **39** (1-3), 407-410 (1997).
144. M. Niggemann, A. Katerkamp, M. Pellmann, P. Bolsmann, J. Reinbold and K. Cammann, Sensor. Actuat. B-Chem. **34** (1-3), 328-333 (1996).
145. R. P. Podgorsek, T. Sterkenburgh, J. Wolters, T. Ehrenreich, S. Nischwitz and H. Franke, Sensor. Actuat. B-Chem. **39** (1-3), 349-352 (1996).
146. B. Chadwick and M. Gal, Appl. Surf. Sci. **68** (1), 135-138 (1993).
147. B. Chadwick, J. Tann, M. Brungs and M. Gal, Sensor. Actuat. B-Chem. **17** (3), 215-220 (1994).
148. G. J. Ashwell and M. P. S. Roberts, Electron. Lett. **32** (22), 2089-2091 (1996).
149. C. Granito, J. N. Wilde, M. C. Petty, S. Houghton and P. J. Iredale, Thin Solid Films **284-285**, 98-101 (1996).
150. J. Van Gent, P. V. Lambeck, R. J. Bakker, T. J. Popma, E. J. R. Sudholter and D. N. Reinhouldt, Sensor. Actuat. A-Phys. **26** (1-3), 449-452 (1991).
151. C. C. Jung, S. B. Saban, S. S. Yee and R. B. Darling, Sensor. Actuat. B-Chem. **32** (2), 143-147 (1996).
152. T. M. Chinowsky, S. B. Saban and S. S. Yee, Sensor. Actuat. B-Chem. **35** (1-3), 37-43 (1996).
153. B. H. Ong, X. Yuan and S. C. Tjin, Fiber. Integrated. Opt. **26** (4), 229-240 (2007).
154. G. R. Quigley, R. D. Harris and J. S. Wilkinson, Appl. Optics **38** (28), 6036-6039 (1999).
155. R. G. Heideman, R. P. H. Kooyman and J. Greve, Sensor. Actuat. B-Chem. **10** (3), 209-217 (1993).

156. B. J. Luff, J. S. Wilkinson, J. Piehler, U. Hollenbach, J. Ingenhoff and N. Fabricus, J. Lightwave Technol. **16** (4), 583-592 (1998).

157. B. Sepulveda, J. Sanchez del Rio, M. Moreno, F. J. Blanco, K. Mayora, C. Dominguez and L. M. Lechung, J. Opt. A-Pure Appl. Opt. **8** (7), S561-S566 (2006).

158. A. Bearzotti, C. Caliendo, E. Verona and A. D'Amico, Sensor. Actuat. B-Chem. **7** (1-3), 685-688 (1992).

159. B. Guha, A. Gondarenko and M. Lipson, Opt. Express **18** (3), 1879-1887 (2010).

160. R. Slavik, J. Homola and E. Brynda, Biosens. Bioelectron. **17** (6-7), 591-595 (2002).

161. K. T. Kim, H. S. Song, J. P. Mah, K. B. Hong, K. Im, S.-J. Baik and Y.-I. Yoon, IEEE Sens. J. **7** (12), 1767-1771 (2007).

162. S. K. Khijwania, V. S. Tiwari, F.-Y. Yeuh and J. P. Singh, Sensor. Actuat. B-Chem. **125** (2), 563-568 (2007).

163. W. Cao and Y. Duan, Sensor. Actuat. B-Chem. **119** (2), 363-369 (2006).

164. H. Dacres and R. Narayanaswamy, Talanta **69** (3), 631-636 (2006).

165. I. Zilbermann, E. Meron, E. Maimon, L. Soifer, L. Elbaz, E. Korin and A. Bettelheim, J. Porphyr. Pthalocya. **10** (1), 63-66 (2006).

166. F. J. F. Martin, J. C. C. Rodriguez, J. C. A. Anton, J. C. V. Perez, I. Sanchez-Barragan, J. M. Costa-Fernandez and A. Sanz-Medel, IEEE T. Instrum. Meas. **55** (4), 1215-1221 (2006).

167. I. Sanchez-Barringan, J. M. Costa-Fernandez, A. Sanz-Medel, M. Valledor, F. J. Ferrero and J. C. Campo, Anal. Chim. Acta **562** (2), 197-203 (2006).

168. S. Tao and T. V. S. Sarma, Opt. Lett. **31** (10), 1423-1425 (2006).

169. S. Trupp, A. Schweitzer and G. J. Mohr, Microchim. Acta **153** (3-4), 127-131 (2006).

170. N. Liu, J. Hui, C. Sun, J. Dong, L. Zhang and H. Xiao, Sensors **6** (8), 835-847 (2006).

171. M. Consales, A. Crescitelli, S. Campopiano, A. Cutola, M. Penza, P. Aversa, M. Giordano and A. Cusano, IEEE Sens. J. **7** (7), 1004-1005 (2007).

172. H. J. Patrick, A. D. Kersey and F. Bucholtz, J. Lightwave Technol. **16** (9), 1606-1612 (1998).

173. H. J. Patrick, G. M. Williams, A. D. Kersey, J. R. Pedrazzani and A. M. Vengsarkar, IEEE Photonics Tech. L. **8** (9), 1223-1225 (1996).
174. A. Othonos and K. Kalli, *Fiber Bragg gratings - Fundamentals and Applications in Telecommunications and Sensing*. (Artech House, Boston, 1999).
175. M. Song, S. B. Lee, S. S. Choi and B. Lee, Optical Fiber Technology **3** (2), 194-196 (1997).
176. M. G. Xu, J.-L. Archambault, L. Reekie and J. P. Dakin, Electron. Lett. **30** (13), 1085-1087 (1994).
177. V. Vali and R. W. Shorthill, Appl. Optics **15** (5), 1099-1100 (1976).
178. K. Bohnert, P. Gabus, J. Nehring and H. Brandle, J. Lightwave Technol. **20** (2), 267-276 (2002).
179. G. Meltz, S. J. Hewlett and J. D. Love, P. SPIE **2836**, 342-350 (1996).
180. W. Ecke, K. Usbeck, V. Hagemann, R. Mueller and R. Willsch, P. SPIE **3555** (457-466), 457 (1998).
181. V. Bhatia and A. M. Vengsarker, Opt. Lett. **21** (9), 692-694 (1996).
182. Z. Zhang and J. S. Sirkis, in *Proceedings of the 12th international Conference on Optical Fibre Sensors* (Williamsburg, USA, 1997), pp. 294-297.
183. R. Falciai, A. G. Mignani and A. Vannini, P. SPIE **3555**, 447-450 (1998).
184. F. Ouerghi, W. Belhadj, F. Abdelmalek, M. Mejatty and H. Bouchriha, Thin Solid Films **485** (1-2), 176-181 (2005).
185. C. Wochnowski, M. Abu-El-Qomsan, W. Pieper, K. Meteva, S. Metev, G. Wenke and F. Vollertsen, Sensor. Actuat. A-Phys. **120** (1), 44-52 (2005).
186. C. Wochnowski, M. T. Kouamo, W. Pieper, K. Meteva, S. Metev, G. Wenke and F. Vollertsen, IEEE Sens. J. **6** (2), 331-339 (2006).
187. K. J. Kim and M. C. Oh, IEEE Photonics Tech. L. **20** (4), 288-290 (2008).
188. T. Pustelny, I. Zielonka, C. Tyszkiewicz, P. Karasinski and B. Pustelny, Opto-electron. Rev. **14** (2), 161-166 (2006).
189. V. M. N. Passaro, R. Loiacono, G. D'Amico and F. De Leonardis, IEEE Sens. J. **8** (9), 1603-1611 (2008).
190. D. Runde, S. Brunken, C. E. Ruter and D. Kip, Appl. Phys. B-Lasers O. **86** (1), 91-95 (2007).
191. I. J. G. Sparrow, G. D. Emmerson, C. B. E. Gawith and P. G. R. Smith, Sensor. Actuat. B-Chem. **107** (2), 856-860 (2005).

192. I. J. G. Sparrow, G. D. Emmerson, C. B. E. Gawith, P. G. R. Smith, M. Kaczmarek and A. Dyadyusha, Appl. Phys. B-Lasers O. **81** (1), 1-4 (2005).
193. X. Dai, S. J. Mihailov, C. L. Callender, C. Blanchetiere and R. B. Walker, Meas. Sci. Technol. **17** (7), 1752-1756 (2006).
194. A. V. Dotsenko, A. L. Diikov and T. A. Vartanyan, Sensor. Actuat. B-Chem. **94** (1), 116-121 (2003).
195. H. Nishiyama, Y. Hirata, I. Miyamoto and J. Nishii, Appl. Surf. Sci. **253** (15), 6550-6554 (2007).
196. I. J. G. Sparrow, P. G. R. Smith, G. D. Emmerson, S. P. Watts and C. Riziotis, Journal of Sensors **2009**, 607647 (2009).
197. K. Kato and Y. Kitano, J. Oceanogr. Soc. Japan **24** (4), 147-152 (1968).
198. T. A. Dickinson, J. White, J. S. Kauer and D. R. Walt, Nature **382**, 697-700 (1996).
199. N. A. Rakow and K. S. Suslick, Nature **406**, 710-713 (2000).
200. A. Goodey, J. J. Lavigne, S. M. Savoy, M. D. Rodriguez, T. Curey, A. Tsao, G. Simmons, J. Wright, S.-J. Yoo, Y. Sohn, E. V. Anslyn, J. B. Shear, D. P. Neikirk and J. T. McDevitt, J. Am. Chem. Soc. **123** (11), 2559-2570 (2001).
201. *www.stratophase.com*.
202. B. Snow, Optoelectronics Research Centre, University of Southampton.
203. C. Iliescu, J. Jing, F. E. H. Tay, J. Miao and T. Sun, Surf. Coat. Tech. **198** (1-3), 314-318 (2005).
204. Z. Zhao, B. K. Tay and G. Yu, Appl. Optics **43** (6), 1281-1285 (2004).
205. U. Huebner, R. Boucher, W. Morgenroth, J. Kunert, H. Roth, H.-G. Meyer, T. Glaser and S. Schroeter, Microelectron. Eng. **78-79**, 422-428 (2005).
206. C. Christensen, R. deRaus and S. Bouwstra, J. Micromech. Microeng. **9** (2), 113-118 (1995).
207. R. De Palma, W. Laureyn, F. Frederix, K. Bonroy, J.-J. Pireaux, G. Borghs and G. Maes, Langmuir **23** (2), 443-451 (2007).
208. D. B. Asay and S. H. Kim, J. Phys. Chem. B **109** (35), 16760-16763 (2005).
209. R. Kohli and K. L. Mittal, *Developments in Surface Contamination and Cleaning: Fundamentals and Applied Aspects*. (William Andrew, New York, 2008).
210. Z. Zhang, P. Zhao, G. Sun, G. Xiao and Y. Wu, IEEE Photonics Tech. L. **19** (24), 1958-1960 (2007).

211. X. Dai, S. J. Mihailov and R. B. Walker, Meas. Sci. Technol. **19** (4), 045302 (045305 pages) (2008).
212. K.-I. Tsunoda, A. Nomura, J. Yamada and S. Nishi, Appl. Spectrosc. **44** (1), 163-165 (1990).
213. L. Eldada, Rev. Sci. instrum. **75** (3), 575-593 (2004).
214. H. G. Limberger, N. Hong Ky, D. M. Constantini, R. P. Salathe, C. A. P. Muller and G. R. Fox, IEEE Photonics Tech. L. **10** (3), 361-363 (1998).
215. S. Y. Kim, S. B. Lee, S. W. Kwon, S. S. Choi and J. Jeong, Electron. Lett. **34** (1), 104-105 (1998).
216. L. Cruz, A. Diez, M. V. Andres, A. Segura, B. Ortega and L. Dong, Electron. Lett. **33** (3), 235-236 (1997).
217. M. Le Blanc, S. Y. Huang, M. M. Ohn and R. M. Measures, Electron. Lett. **30** (25), 2163-2165 (1994).
218. M. Sun, W. Que and X. J. Hu, J. Sol-gel Sci. Techn. **50** (3), 415-420 (2009).
219. P. S. Ramanujam, S. Hvilsted, F. Ujhelyi, P. Koppa, E. Lorincz, G. Erdei and G. Szarvas, Synth. Met. **124** (1), 145-150 (2001).
220. S. H. Barley, A. Gilbert and G. R. Mitchell, J. Mater. Chem. **1**, 481-482 (1991).
221. R. Lausten, P. Rochon, M. Ivanov, P. Cheben, S. Janz, P. Desjardins, J. Ripmeester, T. Siebert and A. Stolow, Appl. Optics **44** (33), 7039-7042 (2005).
222. H. Rau, Angew. Chem. Int. Ed. **12** (3), 224-235 (1973).
223. J.-S. Koo, P. G. R. Smith, R. B. Williams, M. C. Grossel and M. J. Whitcombe, Chem. Mater. **14** (12), 5030-5036 (2002).
224. N. Wazzan, PhD Thesis, University of Edinburgh, 2009.
225. M. Ueda, H.-B. Kim and K. Ichimura, Chem. Mater. **6**, 1771-1775 (1994).
226. C. Z. Tan and J. Arndt, J. Phys. Chem. Solids **61** (8), 1315-1320 (2000).
227. C. Z. Tan, J. Non-Cryst. Solids **238** (1-2), 30-36 (1998).
228. C. Z. Tan and J. Arndt, Physica B **229** (3-4), 217-224 (1997).
229. C. Z. Tan, J. Arndt and H. S. Xie, Physica B **252** (1-2), 28 (1998).
230. C. Z. Tan and J. Arndt, J. Non-Cryst. Solids **242** (2-3), 149 (1998).
231. M. Sparks, J. Appl. Phys. **42**, 5029 (1971).
232. J. Schroeder, J. Non-Cryst. Solids **40** (1-3), 549-566 (1980).

233. R. B. Sosman, *The Properties of Silica*. (Chemical Catalog Company, New York, 1927).
234. K. Schroeder, W. Ecke, R. Mueller, R. Willsch and A. Andreev, Meas. Sci. Technol. **12** (7), 757-764 (2001).
235. D. A. Pereira, O. Frazao and J. L. Santos, Opt. Eng. **43**, 299-304 (2004).
236. R. C. Kamikawachi, I. Abe, A. S. Paterno, H. J. Kalinowski, M. Muller, J. L. Pinto and J. L. Fabris, Opt. Commun. **281** (4), 621-625 (2008).
237. J. Lee, C. Hahn, B. Wang, K. Reichard, D. Ditto, D. Glista, Q. Wang and S. Yin, Opt. Commun. **258** (2), 184-492 (2006).
238. G. D. Emmerson, C. B. E. Gawith, I. J. G. Sparrow, R. B. Williams and P. G. R. Smith, Appl. Optics **44** (24), 5042-5045 (2005).
239. G. W. Yoffe, P. A. Krug, F. Ouellette and D. A. Thorncraft, Appl. Optics **34** (30), 6859-6861 (1995).
240. K. Iga and A. Kokubun, *Encyclopaedic handbook of integrated optics*. (CRC Press, 2005).
241. Y. Inoue, A. Kaneko, F. Hanawa, H. Takahashi, K. Hattori and S. Sumida, Electron. Lett. **33** (23), 1945-1946 (1997).
242. R. Roy and E. F. Osborn, J. Am. Chem. Soc. **71** (6), 2086-2095 (1949).
243. C.-B. Kim and C. B. Su, Meas. Sci. Technol. **15** (9), 1683-1686 (2004).
244. A. N. Chryssis, S. S. Saini, S. M. Lee and M. Dagenais, IEEE Photonics Tech. L. **18** (1), 178-180 (2006).
245. G. M. Whitesides, Nature **442**, 368-373 (2006).
246. J. P. Holman, *Heat transfer*. (McGraw-Hill, 2002).
247. Y. Fainman, L. P. Lee, D. Psaltis and C. Yang, *Optofluidics: Fundamentals, devices and applications*. (McGraw-Hill, 2010).
248. Labview is a product of National Instruments.
249. M. A. Unger, H. P. Chou, T. Thorsen, A. Scherer and S. R. Quake, Science **288** (5463), 113-116 (2000).
250. *www.smartfibres.com/FBG-interrogators*.
251. *www.kalrez.com*.
252. E. D. Katz, C. H. Lochmuller and R. P. W. Scott, Anal. Chem. **61** (4), 349 (1989).
253. F. G. Bessoth, A. J. deMello and A. Manz, Anal. Commun. **36**, 213-215 (1999).

254. B. J. Kirby, D. S. Reichmuth, R. F. Renzi, T. J. Shepodd and B. J. Wiedenman, Lab. Chip. **5** (2), 184-190 (2005).
255. *Jaiv Oorja: Biofuels Database*. (Shri Mata Vaishno Devi Univeristy, Katra).
256. J. V. Herraez and R. Belda, J. Solution Chem. **35** (9), 1315-1328 (2006).
257. R. J. Jimenenz Rioboo, M. Philipp, M. A. Ramos and J. K. Kruger, Eur. Phys. J. E **30** (1), 19-26 (2009).
258. J. C. Love, L. A. Estroff, J. K. Kriebel, R. G. Nuzzo and G. M. Whitesides, Chem. Rev. **105** (4), 1103-1169 (2005).
259. J. Sagiv, J. Am. Chem. Soc. **102** (1), 92-98 (1980).
260. E. J. Nemanick, P. T. Hurley, L. J. Webb, D. W. Knapp, D. J. Michalak, B. S. Brunschwig and N. S. Lewis, J. Phys. Chem. **110** (3), 14770-14778 (2006).
261. J. M. Buriak, Chem. Commun., 1051-1060 (1999).
262. S. S. Vegunta, J. N. Ngunjiri and J. C. Flake, Langmuir **25** (21), 12750-12756 (2009).
263. T. K. Mischki, R. L. Donkers, B. J. Eves, G. P. Lopinski and D. D. Wayner, Langmuir **22** (20), 8359-8365 (2006).
264. I. I. Slowing, B. G. Trewyn, S. Giri and V. S.-Y. Lin, Adv. Funct. Mater. **17** (8), 1225-1236 (2007).
265. S. L. Westcott, S. J. Oldenburg, T. R. Lee and N. J. Halas, Langmuir **14** (19), 5396-5401 (1998).
266. C. Perruchot, M. M. Chehimi, M. Delamar, E. Cabet-Deliry, B. Miksa, S. Slomkowski, M. A. Khan and S. P. Armes, Colloid. Polym. Sci. **278** (12), 1139-1154 (2000).
267. D. J. Macquarrie and S. E. Fairfield, J. Mater. Chem. **7** (11), 2201-2204 (1997).
268. M. L. Hair and C. P. Tripp, Colloid. Surface. A. **105** (1), 95-103 (1995).
269. S. D. Conzone and C. G. Pantano, Mater. Today **7** (3), 20-26 (2004).
270. L. T. Zhuravlev, Langmuir **3** (3), 316-318 (1986).
271. C. Wittmann, in *Topics in Current Chemistry* (Springer, 2005), Vol. 261.
272. X. Zhao and R. Kopelman, J. Phys. Chem. **100** (26), 11014-11018 (1996).
273. C. A. Goss, D. H. Charych and M. Majda, Anal. Chem. **63** (1), 85-88 (1991).
274. C. Malins, S. Fanni, G. Glever, J. Vos and B. D. MacCraith, Anal. Commun. **36**, 3-4 (1999).
275. D. G. Kurth and T. Bein, Angew. Chem. Int. Ed. **31** (3), 336-338 (1992).

276. P. Mela, S. Onclin, M. H. Goedbloed, S. Levi, M. F. Garcia-Parajo, N. F. van Hulst, B. J. Ravoo, D. N. Reinhouldt and A. van den Berg, Lab. Chip. **5** (2), 163-170 (2005).

277. H. Fujiwara, *Spectroscopic Ellipsometry: Principles and Applications*. (Wiley, 2007).

278. X. Guo, M. Myers, S. Xiao, M. Lefenfeld, R. Steiner, S. Tulevski, J. Tang, J. Baumert, F. Leibfarth, J. T. Yardley, M. L. Steigerwald, P. Kim and C. Nuckolls, PNAS **103** (31), 11452-11456 (2006).

279. S. S. Saini, C. Stanford, S. M. Lee, J. Park, P. DesShong, W. E. Bentley and M. Dagenais, IEEE Photonics Tech. L. **19** (18), 1341-1343 (2007).

280. J. L. Sessler, P. A. Gale and W.-S. Cho, *Anion Receptor Chemistry*. (Royal Society of Chemistry, 2006).

281. J.-M. Lehn, *Supramolecular Chemistry: Concepts and Perspectives*. (Wiley, 1995).

282. J. Vicens and V. Bohmer, *Calixarenes: a Versatile Class of Macrocyclic Compounds*. (Springer, 1990).

283. H. Bradl, *Heavy metals in the environment: origin, interaction and remediation*. (Academic Press, 2005).

284. Lenntech Water Treatment Solutions: *http://www.lenntech.com/periodic/elements/cu.htm*.

285. *ToxFAQS for Copper* (Agency for Toxic Substances and Disease Registry, DHHS, US Gov., 2004).

286. J. G. P. Espinola, S. F. Oliveira, W. E. S. Lemus, A. G. Souza, C. Airoldi and J. C. A. Moreira, Colloid. Surface. A. **166** (1-3), 45-50 (2000).

287. Y. Kim, I. Choi, S. K. Kang, J. Lee and J. Yi, Appl. Phys. Lett. **88** (1), 013113 (013113 pages) (2006).

288. Z. Wang, G. Wu, M. Wang and C. He, J. Mater. Sci. **44** (10), 2694-2699 (2009).

289. T. Kang, S. Hong, J. Moon, S. Oh and J. Yi, Chem. Commun., 3721-3723 (2005).

290. J. Stockel, J. Safar, A. C. Wallace, F. E. Cohen and S. B. Prusiner, Biochemistry **37** (20), 7185-7193 (1998).

291. H. Sigel and R. B. Martin, Chem. Rev. **82** (4), 385-426 (1982).

292. M. Algarra, M. V. Jimenez, E. Rodriguez-Castellon, A. Jimenez-Lopez and J. Jimenez-Jimenez, Chemosphere **59** (6), 779-786 (2005).
293. F. Vogtle, *Supramolecular Chemistry: An Introduction*. (Wiley, 1993).
294. C. J. Pedersen, J. Am. Chem. Soc. **89** (26), 7017-7036 (1967).
295. M. A. Bush and M. R. Truter, J. Chem. Soc. Perk. T. 2, 341-344 (1972).
296. Y. Takeda and T. Kumazawa, Bull. Chem. Soc. Jpn. **61** (3), 655-658 (1988).
297. M. Nakajima, K. Kimura and T. Shono, Anal. Chem. **55** (3), 463-467 (1983).
298. V. Percec, G. Johansson, J. Heck, G. Ungarb and S. V. Batty, J. Chem. Soc. Perk. T. 1, 1411-1420 (1993).
299. M. Tada, H. Hamazaki and H. Hirano, Bull. Chem. Soc. Jpn. **55**, 3865-3869 (1982).
300. M. Bourgin, K. H. Wong, J. Y. Hui and J. Smid, J. Am. Chem. Soc. **97** (12), 3462-3467 (1975).
301. L. H. Uppadine, J. E. Redman, S. W. Dent, M. G. B. Drew and P. D. Beer, Inorg. Chem. **40** (12), 2860-2869 (2001).
302. E. Wagner-Czauderna, A. Koczorowska and M. K. Kalinowski, J. Coord. Chem. **46** (3), 265-276 (1999).
303. P. R. Mallinson and M. R. Truter, J. Chem. Soc. Perk. T. 2, 1818-1823 (1972).
304. F. Arnaud-Neu, M.-J. Schwing-Weil, K. Ziat, S. Cremin, S. J. Harris and M. A. McKervey, New J. Chem. **15** (1), -3733 (1991).
305. J. S. Benco, H. A. Nienaber and W. G. McGimpsey, Sensor. Actuat. B-Chem. **85** (1-2), 126-130 (2002).
306. T. Hayashita, K. Kunogl, H. Yamamoto and S. Shinkai, Analyt. Sci. **13**, 161-166 (1997).
307. I. U. Vakarelski, C. E. McNamee and K. Higashitani, Colloid. Surface. A. **295** (1-3), 16-20 (2007).
308. A. Jenkins, PhD thesis, Univeristy of Southampton, 2010.
309. K. Fant, E. K. Esbjorner, A. Jenkins, M. C. Grossel, P. Lincoln and B. Norden, Mol. Pharm., in press (2010).
310. J. W. Lee, J. H. Kima, B.-K. Kima, J. H. Kimb, W. S. Shin and S.-H. Jin, Tetrahedron **62** (39), 9193-9200 (2006).
311. Z.-X. Guo and J. Yu, J. Mater. Chem. **12** (3), 468-472 (2002).

312. S. Antebi, P. Atrya, L. E. Manzer and H. Alper, J. Org. Chem. **67** (19), 6623-6631 (2002).
313. P. K. Jal, S. Patel and B. K. Mishra, Talanta **62** (5), 1005-1028 (2004).
314. N. A. J. M. Sommerdijk, E. R. H. van Eck and J. D. Wright, Chem. Commun., 159-160 (1997).
315. S. Sato, T. Murakata, T. Suzuki and T. Ohgawara, J. Mater. Sci. **25** (11), 4880-4885 (1990).
316. D. J. Wales, Optoelectronics Research Centre, University of Southampton.
317. M. Odabasoglu, G. Turgut and H. Kocaokutgen, Phosphorus Sulfur **152** (1), 27-34 (1999).
318. A. Ault, *Techniques and experiments for organic chemistry*, 4th ed. (University Science Books, 1976).
319. H. Iwamoto, M. Yoshimura, T. Sonoda and H. Kobayashi, Bull. Chem. Soc. Jpn. **56** (3), 796-801 (1983).
320. D. Jackson, PhD thesis, University of Southampton, 2008.
321. E. Woolfolke, E. Donaldson and M. Payne, J. Org. Chem. **27** (7), 2653-2655 (1962).
322. V. Ettel and J. Myska, Collect. Czech. Chem. C. **23** (7), 1341-1345 (1958).
323. M. L. Rahman, C. Tschierske, M. Yusoff and S. Silong, Tetrahedron Lett. **46** (13), 2303-2306 (2005).
324. J. Kim and B. M. Novak, Macromolecules **37** (22), 8286-8292 (2004).
325. J. F. Norris, E. V. Fasce and C. J. Staud, J. Am. Chem. Soc. **57** (8), 1415-1420 (1935).
326. T. Thiemann, K. Umeno, J. Wang, Y. Tabuchi, K. Arima, M. Watanabe, Y. Tanaka, H. Gorohmaru and S. Mataka, J. Chem. Soc. Perk. T. 1, 2090-2110 (2002).
327. L. F. Fieser and C. K. Bradsher, J. Am. Chem. Soc. **58** (9), 1738-1741 (1936).
328. F. Homsi, K. Hosoi, K. Nozaki and T. Hiyama, J. Organomet. Chem. **624** (1-2), 208-216 (2001).
329. A. Burawoy and E. Spinner, J. Chem. Soc., 2557-2563 (1955).
330. A. D. Polyanin and A. V. Manzhirov, *Handbook of Mathematics for Engineers and Scientists*. (Chapman and Hall / CRC, 2007).